Modelling the physiology of Spiral Ganglion Neurons

Doctoral Thesis in Linguistics

Matthieu Recugnat

Supervisor: Prof. David McAlpine

Asso. Supervisor: Dr Jaime Undurraga

Department of Linguistics

Faculty of Human Sciences

Macquarie University

Sydney, July 12, 2019

To Pauline

Statement of Originality

This work has not previously been submitted for a degree or diploma in any university. To the best of my knowledge and belief, the thesis contains no material previously published or written by another person except where due reference is made in the thesis itself.

Date: 8/04/2019

Matthieu Recugnat

Lay Abstract

Through the electrical stimulation of the peripheral auditory brain, Cochlear Implant (CI) have been successful in restoring some sense of hearing to inviduals with severe to profound hearing loss. However, variablity in CI users speech understanding requires a better comprehension of the deaf inner ear under electrical stimulation to improve. Here, modelling studies employing computational models of the Spiral Ganglion Neurons (SGNs), forming the Auditory Nerve (AN), under electrical stimulation are presented. Our modelling studies have produced predictions for SGN populations health evaluation and stimulation strategy optimizations that can help reduce the variablity in speech understanding for CI users.

Abstract

The efficiency of electrical stimulation in cochlear implantation with a CI depends critically on the state of the nerve fibers interfacing with the array of electrodes inserted into the inner ear. Neural morphology and degeneration, ionic channels, electrode position and stimulus polarity and shape have all demonstrated to be important factors of the response of SGNs to electrical stimulus. Previous modelling and human studies have shown that some underlying interactions in electrical stimulation of the AN could be at the origin of patient performance variability that could not be explained by CI candidacy factors alone.

In this thesis, a biophysical model of the human SGN, that includes voltage-gated hyperpolarization-activated cation (HCN) and low threshold potassium voltaged-gated delayed-rectifier potassium (KLT) channels, was used to model single neuron and population responses to different stimulus conditions and strategies. The results show that healthy SGNs which have preserved peripheral processes prefer cathodic leading stimulation while SGNs with degenerated peripheral processes prefer anodic leading. Also, another degree of degeneration was modelled by partially removing myelin on the peripheral process, resulting in altered spike latencies which could in turn destroy benefits of bilateral CI hearing. Interesting phenomenon of "cathodic blocking" and "spike-rate adaptation blocking" that could explain non-monotonic loudness growth functions were also introduced.

Further, population simulations were produced to model Electrically evoked Compound Action Potential (ECAP) responses and pulse train responses. The results show that ECAPs for various polarities and stimulation levels could be used as an assessment tool for neural health and predictions of best stimulation strategies. However, the results also showed that the ECAP responses were often decorrelated from the ability of a neuron population to encode pulse train stimulations.

Overall, the thesis presents interesting results with regards to how best to design patient-oriented stimulation strategies. By evaluating the neural health using ECAP and pulse train ECAPs, and performance of individual patients with regards to pulse shapes, preferred polarity and pulse rate, stimulation strategies could be designed beyond the typical thresholds and Most Comfortable Level (MCL). This might create an opportunity to reduce the CI user variability in performance that is currently observed.

Acknowledgements

"From London to Sydney": it could have been the title of a romantic movie about research. Instead, it symbolises the past 4.5 years of my life, and looking back at all the turns that were taken to get this thesis out, I can safely say this was a ride I'll remember. From the half desks of the "PhD" room at UCL's Ear Institute to the large-windowed shared-space of the Australian Hearing Hub at Macquarie University, I've enjoyed (almost) every steps of this long journey. With so many places comes many people to remember and thank for the role, small and big, they've played in this thesis.

First, I'd like to thank my supervisor, Prof. David McAlpine for his constant belief in me and in the project, although over the past 4.5 years our relationship has grown beyond supervision, into something I believe is more a mix of mentorship and friendship. However, It is safe to say that our relationship has been sometimes unconventional, and I'm not talking about the color of his suits: it is more that I've come to be somewhat critical as to David's ability to use computers. For my defense, computers seem to always fault when he uses them... a problem which I have come to learn is called PEBCAK ("Problem Exists Between Chair And Keyboard."). However, what David lacked in computer skill, he made up in his ability to surround himself with highly technical people, such as Jess (his wife who I thank for waiting a bit longer to give birth and kept David available to me!) and Jaime Undurraga.

Interestingly, the relationship between Jaime and I followed the opposite direction of the one with David: from friendship to clairvoyant, "unofficial", supervision. Jaime, it is pretty clear that this thesis would not exist without your unvaluable input and patience over the past 3.5 years. Countless discussions and ideas that have helped me stay on track and work smarter. For all these conversations, explanations, attention to detail and your patience, I thank you.

Thank you to Fabrice, Nick, Kelly, Lyndsey, Heivet, Jason, Remi, Javi and all the people from the lab that made the days brighter, the beers cooler and the AC warmer.

Also, it is important to mention that this thesis was undertaken with the assistance of resources and services from the National Computational Infrastructure (NCI), which is supported by the Australian Government. It has become pretty clear to me that this thesis wouldn't have existed without the 150k+ of computational hours made possible thanks to NCI and its people.

Perhaps the only sad thought I will have upon submitting this work, is that the

person that started all of this for me, around 5 years ago, will never be able to read it. But for all you've done for me, and for your communicative love of research, I will forever be in your debt Jonathan Laudanski.

Of course, I'd like to thank my parents and family, especially my grand-parents, who have always believed in me and pushed me forward, even when I didn't know where to go. Thanks mom and dad for providing love, support, and a bit of structure to my sometimes unsettled personna, and to always be there when it counted.

Finally, there would be no thesis for sure if it had not been for the unconditional love and support of my wife, Pauline Paoli, who was here for each hoop and hurdle that needed jumping and to who I'll always be thankful. If "From London to Sydney" was a movie, she would be the main character, tagging along with me all the way. In the end, you trully were the most important piece of this puzzle, from our shared apartment in London (1 bathroom for 5 bedrooms!!), to our beloved village of Balmain. You are my light inside the tunnel, and I'm grateful that you shared this journey, and hopefully many MANY others, with me.

Table of Contents

List of Figures

List of Tables

List of Abbreviations

AB	Advanced Bionics
AGF	Amplitude Growth Function
AN	Auditory Nerve
AP	Action Potential
ARP	Absolute Refractory Period
BEM	Boundary Element Model
BM	Basilar Membrane
BP	Bipolar
CAP	Compound Action Potential
CBCT	Cone Beam Computed Tomography
CF	Characteristic Frequency
CI	Cochlear Implant
CIS	Continuous Interleaved Sampling
CN	Cochlear Nucleus
DR	Dynamic Range
EABR	Electrically evoked Auditory Brainstem Response
ECAP	Electrically evoked Compound Action Potential
FE	Firing Efficiency
FH	Frankenhaeuser Huxley
GSEF	Generalised Schwarz Eikhof Frijns
HCN	voltage-gated hyperpolarization-activated cation
HH	Hodgkin-Huxley
HSR	High Spontaneous Rate
IHC	Inner Hair Cell
IPG	Inter-Phase Gap
K	Potassium

KLT	voltaged-gated delayed-rectifier potassium
Kv	voltaged-gated high-threshold inactivating potassium
LSR	Low Spontaneous Rate
MCB	Myelinated Cell Body
MCL	Most Comfortable Level
MP	Monopolar
MSR	Medium Spontaneous Rate
Na	fast activating sodium
NCI	National Computer Infrastructure Australia
NH	Normal Hearing
NSRD	Normalized spike rate decrement
OHC	Outer Hair Cell
PSR	Pseudomonophasic-Ramped
PSS	Pseudomonophasic-Square
PSTH	Post-Stimulus Time Histogram
RMP	Resting Membrane Potential
RRP	Relative Refractory Period
RS	Relative Spread
SD	Standard Deviation
SE	Schwarz Eikhof
SEF	Schwarz Eikhof Frijns
SF	Scaling Factor
SFAP	Single Fibre Action Potential
SGN	Spiral Ganglion Neuron
SOE	Spread of Excitation
SYM	Symmetric
SYMR	Symmetric-Ramped
SYMS	Symmetric-Square
TP	Tripolar
UMCB	Unmyelinated Cell Body

VCN	Ventral Central Nucleus

1 General Introduction

Cochlear Implants (CIs) are the single most successful sensory prosthetic device, helping restore hearing function in people with severe to profound hearing loss. Although many reasons can cause a normal ear to become non-functional, most hearing impairment pathologies related to the inner ear can be overcome using CIs. Over the past four decades or so, research has made CIs increasingly efficient at stimulating the Auditory Nerve (AN), to the point that some CI recipients perform as well as Normal Hearing (NH) patients in terms of speech understanding, at least in quiet listening conditions. Nevertheless, many listening situations prove to be extremely challenging to CI users, in particular the "cocktail party" scenarios, where high levels of background noise make it difficult to follow conversation. In such scenarios, CI users generally perform very poorly indeed. In general, although NH listeners can understand speech when the level of the background noise is greater than that of the speech, CI users require speech to be much louder than the background noise to comprehend it.

To determine some of the possible causes of this poor performance and how it could be improved, we first need to understand the principles of CIs and how it differs from normal hearing.

1.1 Normal Hearing

In normal hearing, a series of mechanical, electrical and chemical processes transduce acoustic waves that reach the ears into electrical pulses (Action Potentials (APs)) that propagate through the auditory nerve to the central auditory pathways. Fig. 1.1 represents a schematic view of the normal ear and its components.

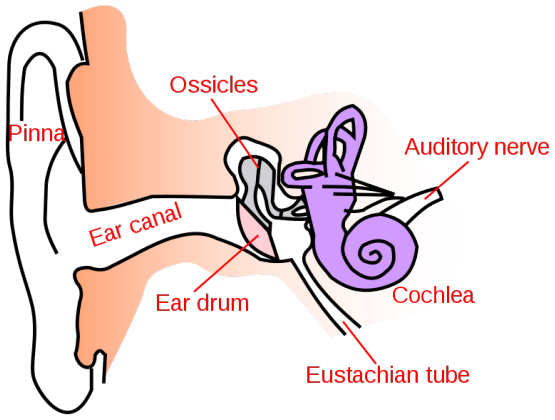

Figure 1.1: Detailed diagram of the human ear anatomy. From Wikipedia contributors (2003)

1.1.1 Outer and middle ear

Acoustic waves enter the ear through the pinna, the most external part of the ear. These waves travel through the ear canal to reach the tympani membrane which leads to the first frequency modifications - filtering - due to the acoustic properties of these structures. This filtered mechanical signal cause the ear bones (ossicles) in the middle ear to vibrate and in turn pass on the vibrations - with a higher gain introduced by the ossicles - into the cochlea.

1.1.2 The cochlea

The cochlea is a spiralled liquid-filled three-parted cavity, called scalae, named: the scala vestibuli, the scala media and the scala tympani. While both the scala vestibuli and scala media are located above the organ of Corti where lives the hearing hair cells, the scala tympani is located below it (Hatsushika et al., 1990). The received vibrations, that originate from the ossicles, make the liquid move and displace the basilar membrane. Because of its gradual changes in stiffness and size along the cochlea, the basilar membrane resonates at higher frequencies on the base of the cochlea and lower frequencies towards the apex of the cochlea. This causes different places of the basilar membrane to vibrate depending on the frequency components of the incoming sound which creates a specific place-frequency filter for the received signal.

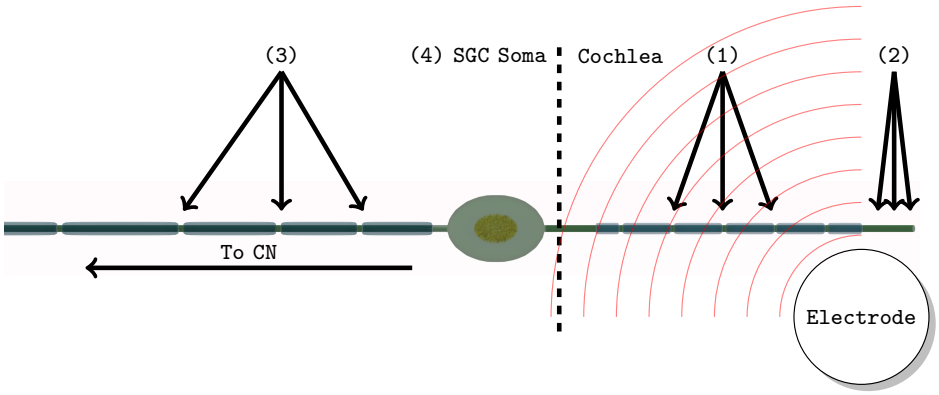

Figure 1.2: Detailed diagram of the SGN and a schematic stimulating electrode. From Undurraga, Carlyon, Wouters, et al. (2013a)

Two types of hair cells can be found along the cochlea to transduce the acoustic vibrations into neural spikes: the Inner Hair Cells (IHCs) and the Outer Hair Cells (OHCs). The IHCs transduce the basilar membrane movements at specific locations of the cochlea into neural spikes. The specific place of excitation along the basilar membrane and the alignment of IHCs account for what is known as the place-code for frequency. IHCs are located on the Organ of Corti and run longitudinally through the cochlear spiral. This distribution ensures that each IHC encodes for a specific frequency: due to the mechanics of the Basilar Membrane (BM), high frequencies are encoded in the most basal turn and low frequency in the most apical turn. Each IHC is activated according to the intensity of the vibration at their specific position, translating for the temporal and intensity fluctuations of the received signal at a specific frequency. Each IHC is innervated by 5 to 20 Spiral Ganglion Neurons (SGNs) (in humans) (Nayagam et al., 2011). SGNs synapses trigger APs depending on the concentrations of neurotransmitters released by the IHC.

1.2 Auditory Nerve Fibres

1.2.1 Single SGN

SGNs are bipolar myelinated neurons with a hyperpolarized cell membrane that initiate and conduct APs from their most distal end towards the Cochlear Nucleus (CN), the obligatory first stage of neural processing in the auditory brain. Initiation

and travel of APs rely on the presence of voltage-dependent ionic channels located along the SGN on the cell body and at regions along the axon either side of the cell body called nodes of Ranvier. The SGN membrane behaves as a leaky capacitor; myelin sheets insulating the SGN behave as capacitors while the nodes of Ranvier and their ionic channels - with a relatively high probability of being in an 'open state' - tend to allow current to flow through them, effectively creating a leak. When an AP is elicited in a node of Ranvier, the neighboring membrane charges and its potential increases; when the opening probability of the ionic channels decreases after it's reached its maximum potential, the membrane will then discharge which would saltate the AP to the next node of Ranvier. As shown in Fig. 1.2, SGNs have their most peripheral end synapsing with a single IHC in the Organ of Corti, whilst the cell body is contained within the spiral ganglion. Finally, its central axon is part of the cochlear nerve. Although some morphometric parameters of the SGN have not been studied systematically, parameters such as the length of the peripheral process have been shown to differ along the length of the cochlea. This is mainly due to the loose nature of the location of the SGNs in the modiolus (Spoendlin and Schrott, 1989; Finley et al., 1990). The peripheral end - i.e. the end synapsing with the IHC - has been measured to be between 1.5 mm and 2.3 mm in length with diameters ranging from 0.8 µm to 2 µm. The human peripheral axon often contains 5 nodes of Ranvier and 6 myelinated internodes (Spoendlin and Schrott, 1989; Finley et al., 1990). The neuron cell body, also called the soma, is spherical and its diameter can range between 20 µm and 30 µm in diameter. Most studies report that the cell bodies of human SGN are partially myelinated (e.g. Spoendlin and Schrott, 1989; Finley et al., 1990; Rattay, Lutter, et al., 2001). Finally, the central axon of SGNs is of variable length and synapses with one or more neurons located within the CN. The diameter of the central axon is usually twice as large as that of the peripheral axon (Spoendlin and Schrott, 1989; Finley et al., 1990).

1.2.2 Types of auditory nerve neurons

The complement of SGNs connected to an IHC has a distribution of characteristics that can be divided in 3 groups: Low Spontaneous Rate (LSR) fibres, whose spontaneous activity (i.e. in the absence of sound stimulation) is below 0.5 spikes/s

, Medium Spontaneous Rate (MSR) fibres, with spontaneous rates in the range 0.5 to 18 spikes/s and High Spontaneous Rate (HSR) fibres, with rates greater than 18 spikes/s (Schmiedt, 1989). The spontaneous rate of SGNs is also related to their threshold for sound activation. HSR SGNs show lower thresholds for generating APs at rates higher than the spontaneous firing rate than LSR SGNs. This difference in spontaneous rate and threshold is mainly attributed to variations in morphological properties of the SGNs: HSR SGNs have large diameters (Frijns, Mooij, et al., 1994; Rattay, Lutter, et al., 2001) and thus, higher concentrations of ionic channels than LSR SGNs. Variability in the distribution of morphological parameters distribution within a population ensures a wide range of coding for different frequencies and intensities.

1.2.3 Action Potentials

Figure 1.3 describes a typical AP. When subjected to strong depolarizing levels of neurotransmitters concentration, the SGN membrane depolarizes quickly causing the opening probability of ionic channels to increase and, in turn, to trigger an AP if the depolarization is strong enough. The membrane depolarization potential required to trigger an AP is known as the threshold: thresholds are SGN specific and can vary over time because of the time dependence of ionic channels dynamics. After depolarization the neuron enters the repolarization phase: activating ionic (sodium) channels close and inactivating channels (potassium) open to repolarize the cell membrane. Inactivating channels being slow to close, the potential overshoots into the refractory period. The activating channels then reopens to finally bring the cell membrane back to its Resting Membrane Potential (RMP).

1.2.4 Ionic Channels

The different types of voltage dependent ionic channels found at the nodes of Ranvier and on the SGN cell body are responsible for generating the firing patterns of SGNs. Activating ionic channels which help the neuron membrane to quickly depolarize creating an AP and inactivating ionic channels which hyperpolarize the membrane back to its resting potential and regulating ionic channels.

With changing membrane potential, ionic channels open or close according to

their intrinsic dynamics. The fast activating sodium (Na) channels are responsible for the fast depolarization of the membrane potential and are the main driver for AP activation. They are called fast because of the short time-constant required for them to open. When fully opened, they bring the membrane potential up to its peak (Hodgkin and Huxley, 1952). Upon reaching the peak membrane potential, the opening probability of Na channels starts decreasing and the ionic channels enter a recovery state. The voltaged-gated high-threshold inactivating potassium (Kv) channels maintain, or return the cell membrane to, the RMP. This can happen either after reaching the AP peak or after a sub-threshold event. For example, after the membrane has reached its peak due to the opening of Na channels, Kv channels open and return the membrane potential to its hyperpolarized state (Hodgkin and Huxley, 1952).

Similar to Kv channels, voltaged-gated delayed-rectifier potassium (KLT) channels are inactivating and act to stabilize the RMP over time (Negm and Bruce, 2014; Boulet, 2016). Finally, voltage-gated hyperpolarization-activated cation (HCN) channels mediate the Na and Kv ionic channels over longer periods of time to regulate overall SGN activity (Negm and Bruce, 2014; Boulet, 2016).

1.2.5 Refractoriness, Accommodation, Spike-rate Adaptation, and Facilitation

When subjected to a long term stimulus, SGNs will see their intrinsic dynamic properties change. These changes reflect the states called refractoriness, accommodation, spike-rate adaptation, and facilitation. The ***refractoriness*** represents a period of time in which SGNs will be in a recovery phase and thus will not be able to fire. The overall refractory period can be broken down in 2 parts: 1/ the Absolute Refractory Period (ARP) and 2/ the Relative Refractory Period (RRP). Ionic channels cannot reopen until the refractory period is over, more specifically the ARP (Negm and Bruce, 2014; Boulet, 2016). KLT channels are long-term rectifying channels that are thought to explain the refractoriness of SGNs. This is due to the long recovery time constant of ionic channels underlying the firing of APs (Crozier and Davis, 2014). Neural ***spike-rate adaptation*** is defined as the change in neural responsiveness over time to a constant stimulus. In other words, the neuron

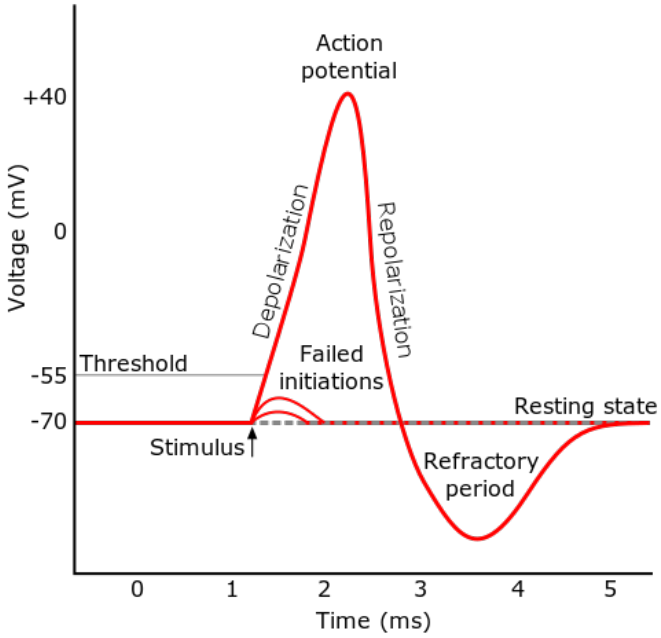

Figure 1.3: Illustration of a typical action potential. The membrane potential starts at the RMP −70 mV. A stimulus raises the membrane potential to −55 mV at 1 ms (the threshold potential). After the stimulus, the membrane potential rapidly rises to a peak potential of 40 mV at time = 2 ms. The potential then drops and overshoots to −90 mV at 3 ms, and finally the resting potential of −70 mV is reestablished at 5 ms. From Wikipedia contributors (2007)

ability to fire and firing pattern can be time-dependent and is strongly related to the stimulus intensity and duration. This is explained by two mechanisms: first, the accumulation of after-hyperpolarization due to the presence of HCN channels; second, the extracellular accumulation of Potassium (K) ions over time (Boulet, 2016). ***Accommodation*** represents the behaviour of neurons when subjected to slowly rising stimulus. APs are usually generated when the neuron membrane is rapidly depolarized following a stimulating event that opens activating ionic channels. In neural accommodation, a slow depolarization induces a gradual increase in the opening probability of activating channels, which is offset by the gradual increase in opening probability of inactivating channels. Effectively, this causes the SGN membrane to never reach threshold, disabling the neuron to fire an AP (Boulet, 2016). Finally, ***facilitation*** can be defined as the firing of an AP following one or more sub-threshold acoustic events which elevate the membrane potential to near threshold, facilitating the triggering of an AP. This is possible when two or more sub-threshold acoustic events are only separated by a short time gap (Cartee, Van Den Honert, et al., 2000a,b; Miller, Abbas, and Robinson, 2001; Cartee, Miller, et al., 2006).

The first sound depolarizes the membrane enough to increase the opening probability of activating ionic channels but not enough to elicit an AP. If the second pulse is close in time to the first stimulus, it then builds on the existing activating currents and this time the SGN membrane is depolarized enough to elicit an AP (van den Honert and Stypulkowski, 1987; Finley et al., 1990).

1.2.6 Cochlear Neural Filter

The cochlear neural filter is defined as the filtering process that occurs due to the mechanics of the peripheral ear, from acoustic signals arriving at the pinna to the generation of APs by the SGNs. As it represents the transduction of acoustic waves in the environment into electrical events, it acts as entry point for neural-encoded signals and is effectively the first filtering system of incoming signals. In the normal-functioning cochlea, it is considered that the distribution of SGNs along the tonotopy gradient of the BM constitutes the very first encoding of the mechano-transduced signal. Different SGNs with different physiological and morphological properties

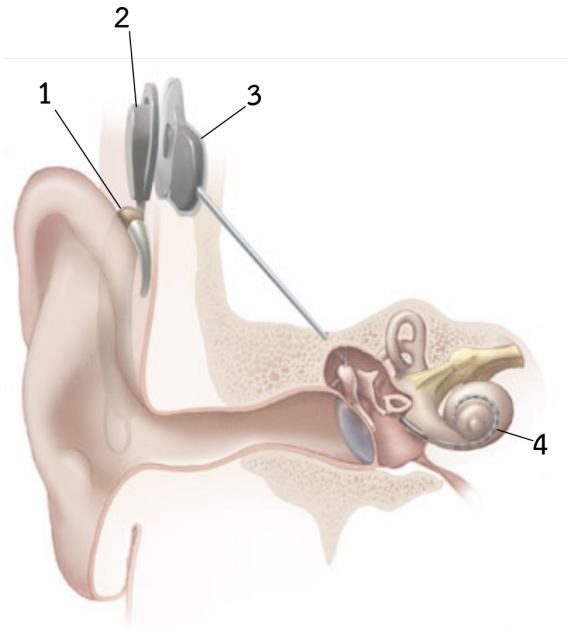

Figure 1.4: Schematic representation of a typical CI used for AN electrical stimulation using electrodes inserted in the cochlea. From Wikipedia contributors (2005)

synapse with the same IHC and, because of this variability, the output signal from a population of SGNs synapsing with a single IHC varies in response to the same input signal according to the pattern and magnitude of synaptic currents generated in each. This process is believed to be the stem reason for the finesse of the cochlear filter encoding of sounds.

1.3 Cochlear Implants

Hearing loss can be caused by many different reasons, including genetic causes, infections, particularly viral infections, trauma, acoustic overexposure or congenital and acquired sensorineural diseases causing neural damage in the peripheral ear. Most commonly, we know from Hinojosa and Marion (1983) that the most common cause for profound hearing loss is due to loss of IHCs rather than SGNs. For this reason, CIs employ electrical stimulation to bypass the NH mechanisms of mechano-transduction to directly stimulate remaining SGNs.

In order to bypass the mechanical periphery of the auditory pathway, CIs encode

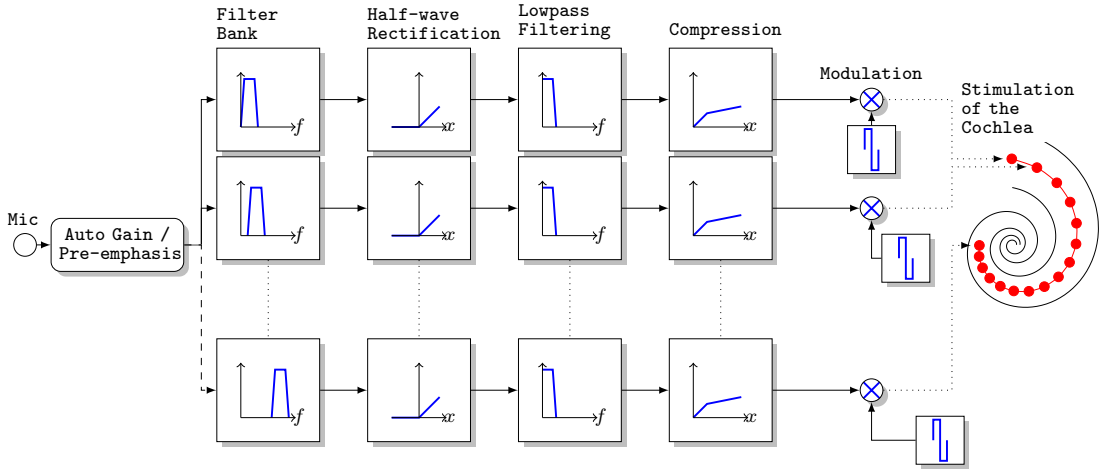

Figure 1.5: Diagram of a multichannel CI operation from Microphone sound capture to electrode stimulation. From Undurraga (2013)

environment sounds into electrical stimuli. Fig. 1.4 shows a typical CI configuration. Generally, CIs are made of two parts: the external part comprising the sound processor (1) which captures external sounds using microphones, and converts them to a series of electrical pulses. These electrical pulses are transmitted by radio frequency waves to the internal part of the implant via the antenna (2). The internal part, which requires surgical insertion, consists of a receiver-stimulator (3) placed under the skin that receives and interprets the information to generate the electrical pulses, which are sent to an electrode array (4). The electrode array is surgically inserted directly along the length the cochlea, which can occur in the scala tympani or scala media. Electrode arrays contain between 10 and 24 electrodes along their length, and by positioning these along the length of the cochlea, different subpopulations of SGNs can be stimulated depending on the frequency of the encoded sound.

Fig. 1.5 represents a diagram of how a multichannel CI functions using the Continuous Interleaved Sampling (CIS) strategy. In order to transduce sounds reaching the microphones of the device into electrical pulses, multichannel CIs use the CIS strategy which constructs a non overlapping stimulation map from input sounds (Wilson et al., 1991). External sound is captured by the microphone and then passed through a compression stage. Compression occurs in CIs when the

amplitude, and sometimes also frequency, range from an external sound is too broad to be represented efficiently by the device. Effectively, compression shifts amplitude, and sometimes frequency, closer together in a way that allows the original sound to be interpreted and stimulated via the CI. The output of this compression is then fed to a filter bank to separate the signal into different continuous frequency bands, mimicking the natural filtering performed by the basilar membrane. The filter bank is usually logarithmic or near-logarithmic, spanning the 250 Hz to 5500 Hz. There can be as many filters as there are electrodes, also called channels. The envelope of each filter output is detected by performing a half-wave rectification and lowpass filtering with 200 Hz or 400 Hz cutoff frequency (Loizou, 1998). The extracted envelope is then compressed on a logarithmic scale in order to map the wide input Dynamic Range (DR) of the envelope (about 50 dB) into the narrow electrical DR of the patients which ranges typically between 6 dB and 20 dB (e.g. Zeng and Shannon, 1992; Zeng, 2002). Finally, the amplitude envelopes extracted after compression are used to modulate trains of Symmetric (SYM) charge-balanced pulses presented at a fixed rate. Importantly, in the CIS strategy, stimuli are presented in a non-overlapping sequence to avoid stimulation of two or more channels at the same time (Fig. 1.5). It is often granted that by reducing channel interaction this method has helped increase speech intelligibility in CI users. However, it should be noted that Wilson et al. (1991) was using more channels for CIS than the compared encoding technique.

1.3.1 Modes of stimulation

Electrodes can be configured in different ways to allow current to flow across them, thereby forming an electrical channel. For example, in Monopolar (MP) mode (the most common configuration), a channel is constituted by an active intracochlear electrode and an external return (or ground) electrode usually located on the implanted aspect of the implant casing, or a separate electrode contact. In Bipolar (BP) mode both active and return electrodes (constituting a channel) are intracochlear electrodes that can be separated by N electrodes (BP + N). In Tripolar (TP) mode a channel consists of one active electrode and two intracochlear return electrodes. Although, in theory, the more complex modes of stimulation

might provide greater control over the stimulation, practically they underperform in terms of patient outcome measures (i.e. place-specificity) when compared to monopolar mode (Macherey, Van Wieringen, et al., 2006; Carlyon, Van Wieringen, et al., 2005; Carlyon, Long, et al., 2008; Carlyon, MacHerey, et al., 2010; Rattay, Lutter, et al., 2001). Thus, there is a need to study and understand better how the electrode-to-nerve interface behaves when subjected to electrical stimulus from one or more electrodes.

1.3.2 Pulse shape and polarity

Although any arbitrary pulse could be theoretically used, CIs have traditionally employed biphasic, symmetric charge-balanced pulses. Monophasic pulses have been found to cause long term damage to the cochlea due to electrolysis (Loeb et al., 1983). This has been counterbalanced thanks to the charge-balanced biphasic pulse which consists of two phases of equal magnitude but opposite polarity. Thus the charge injected by the first phase is removed by the second opposite polarity phase. Other types of pulse shapes are increasingly being assessed for use in stimulation strategies. As shown in Fig. 1.6, asymmetrical pulses—with a short duration and a high amplitude phase followed or preceded by a long duration but low amplitude phase (with the same charge as the high phase)—can be safely used as an alternative to symmetric biphasic pulses. Fig. 1.6 subplot A shows a typical biphasic symmetrical pulse. The pulse represented in subplot B is called Alternate monophasic. Mainly, this pulse shape uses monophasic pulses presented at fixed interval but with alternating polarities, which causes the charge to be balanced although the pulses are monophasic. Subplot C shows a Pseudo Monophasic Anodic pulse. This pulse uses a short but intense eliciting pulse and is followed by a long but low intensity discharge phase. It is thought that because of SGN properties such as refractoriness, adaptation, accommodation, and facilitation, as well as the general physiological status of the AN, the polarity of the main high-amplitude phase is critical in effective stimulation of SGNs (Macherey, Van Wieringen, et al., 2006; Undurraga, 2013).

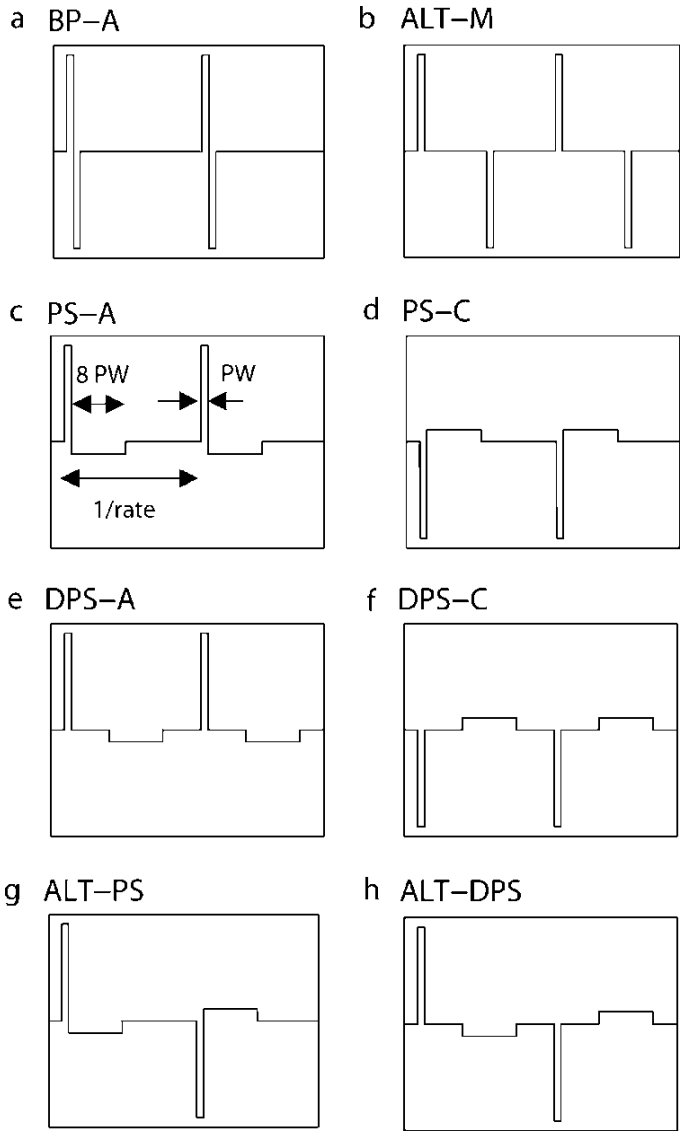

Figure 1.6: Figure showing different temporal pulse shapes that can be used for electro-stimulation of the AN. From Macherey, Van Wieringen, et al. (2006)

1.3.3 Limitations of Cochlear Implant

Although electrical stimulation in CI is very effective at stimulating neurons, the overall performance of CIs is highly variable across patients of any aetiology or age. Many potential reasons for this exist, such as electrode array insertion position, pre-lingual vs post lingual deafness of patient or accurate stimulation startegy fitting. But one explanation can be found in the variability of SGN survival in the hearing-impaired and the health of the remaining population available for stimulation. To this end, variable spread of current within the cochlea, refractoriness and adaptation are some of the problems derived from use of CIs in unhealthy populations of SGNs that account for part of the variability in performance.

The efficiency of electrical stimulation in CIs depends critically on the state of the nerve fibres interfacing with the array of electrodes inserted into the inner ear, the so called 'electrode-neuron interface'. Current research in the field focuses on improving that interface; biologically through increased 'bio-mimicking' of electrical stimulation strategies, pharmacologically with neuro-trophic or -protective drug coatings applied to the electrode array, or through parallel advances in signal processing (Rattay, Lutter, et al., 2001; Macherey, Van Wieringen, et al., 2006; O'Brien, 2016) . Understanding how such techniques could maximise the neural output of stimulated SGNs is key to improving CI outcomes. However, this endeavour is challenging because of limited access to physiological human data - most data have been obtained from physiological investigations of implanted animal models (Frijns, Mooij, et al., 1994; Frijns, de Snoo, et al., 1995; Frijns, De Snoo, et al., 1996; Rattay, Lutter, et al., 2001; Miller, Abbas, and Robinson, 2001) and computational models (Rattay, Lutter, et al., 2001; Macherey, Van Wieringen, et al., 2006; Joshi et al., 2017).

1.3.3.1 Spread of excitation

Due to the nature of the stimulus, CIs tend to stimulate much larger numbers of SGNs than would be stimulated in the normal ear. Despite the number of electrodes available for stimulation (between 20 and 24 on average), multiple studies have shown that only 7 to 8 independent channels could be used simultaneously in practice (Holmes et al., 1987; Dorman, Dankowski, et al., 1989; Dorman, Loizou, et al.,

2000; Friesen et al., 2001). This effect is explained by the high recruiting efficiency of electrical pulses. Because the electrical pulse sent is more effective than the natural synaptic current emitted by IHC, it recruits the majority of the stimulating electrode neighbouring SGN population regardless of the SGN physiological and morphological properties. This Spread of Excitation (SOE), often attributed to the spread of current in the cochlea due to the conductive properties of the perylimph, provides for insufficient spatial selectivity of individual electrode channels, as well as channel interaction found in CI users. Several approaches to solve this interaction issue have been undertaken: some have tried to physically change the shape of the stimulating electrodes or the shape of the electrode array itself; others have tried to develop techniques to reduce the distance between the array and the excitatory elements; finally, some have also tried to develop current focus techniques using multiple electrodes, two or more such as BP, simultaneously in order to produce focused current stimulation patterns.

1.3.3.2 Stochasticity

Another limiting factor in cochlear implantation is stochasticity, or more accurately the lack of it. Because of such an efficient recruiting mechanism of SGNs, electrical stimulation induces a loss of stochasticity; SGNs now respond in synchrony regardless of their intrinsic properties which dramatically reduces the chances for a fine signal encoding (Frijns, Mooij, et al., 1994; Rattay, Lutter, et al., 2001; Carlyon, Van Wieringen, et al., 2005; Carlyon, Long, et al., 2008; Macherey, Van Wieringen, et al., 2006). To overcome part of those problems, researchers have developed stimulation strategies based on stimulus pulse shape and current focusing with bipolar or multipolar techniques using multiple electrodes. However, their effectiveness still remains to be proven, as they have only shown limited improvements when compared to the traditional biphasic-monopolar stimulation strategy (Frijns, Mooij, et al., 1994; Rattay, Lutter, et al., 2001; Carlyon, Van Wieringen, et al., 2005; Carlyon, Long, et al., 2008; Macherey, Van Wieringen, et al., 2006).

1.3.3.3 Polarity effects

Polarity effects are an inherent problem of extracellular electrical stimulation of neurons. The normal mechanism by which neurons allow for initiation of APs subsequent to synaptic current input requires them to have their external membrane hyperpolarized initially (i.e. this is their 'resting state'). After hearing loss, SGNs can be partially and sometimes totally degenerated. The surviving neuron population can be composed of SGNs with different degrees of degeneration. Partial degeneration is defined as a decrease of myelination or partial to total loss of the SGNs' peripheral processes whilst the cell body and central process are still functional. Such types of partial degeneration leave room for electrical stimulation of the SGN, as the cell body and central axon can still propagate an AP. However, total degeneration will not allow electrical stimulation as SGNs are entirely removed. This is why polarity effects need to be understood. In the case of NH, the healthy SGN will elicit APs when the level of the synaptic stimulus exceeds the SGN's specific threshold. The synaptic phenomenon will almost exclusively elicit APs at the synaptic terminal of the SGN. This accounts for very predictable latencies and expected changes in spiking probability according to the level of the synaptic input. Mainly, the SGN firing will become more synchronous as the input level increases.

When it comes to extracellular stimulation, the SGNs are subjected to an external electrical field produced by a CI electrode. The electrical field in turn will depolarize the SGN and elicit an AP. However, in the case of extracellular stimulation, the AP does not necessarily start at the synaptic terminal. This can be due to two different phenomena: first, the electrical field could be such that the depolarization is stronger at an active node of Ranvier that is located further along the neuron; second, the SGN could be morphologically degenerated, which would shift the initiation point further along the neuron (Rattay, Lutter, et al., 2001; Macherey, Van Wieringen, et al., 2006; Undurraga, van Wieringen, et al., 2010; Undurraga, 2013; Joshi et al., 2017). This shift in the site of initiation of APs could explain the variability found in CI performance. As a result, assuming that each implanted patient have different degrees of SGN population survival, it can thus be said that the same stimulation strategy would recruit SGNs more or less effectively according to the neurons' health at the vicinity of the stimulating electrodes. This source of patient variability helps

explain why it is common to see stimulation strategies that are successful for some patients but not others. This proves to be a major challenge for the design of a device and stimulation strategy that would be efficient for every CI user. It also means that in order to regain performance for CI users, one would have to design a more personalised process to fit the device to better suit the surviving neuron profile of each CI user. The ability to predict the surviving SGN profile could be a key factor in the design for a personalised fitting process.

All of these effects of electrical stimulation and their implications for the performance of CI users need to be closely understood. Single SGN behaviour and the underlying membrane mechanisms are thought to explain how neurons will respond to trains of electrical pulses according to their intrinsic refractoriness, spike-rate adaptation, accommodation and facilitation properties. But, more complex representation of the cochlear filter, in the form of populations of neurons, also requires investigation in order to understand how non-homogeneous distributions of physiological properties influence electrical hearing. Such experiments are hard to implement, both *in vitro* and *in vivo*, due to obvious experimental constraints. A computational modelling approach has then been often preferred to analyse such problems. Sec. 1.4 will look at different computational model approaches that have been developed over the years.

1.4 Computational Models

Different research groups have proposed variable techniques to such end; they can be divided into two model types, phenomenological and physiological models.

1.4.1 Phenomenological Models

Phenomenological models use the measured probability of spiking of characterised neurons to clamped or extracellular stimulation to determine how they might react to specific stimulation strategies, i.e. these models are based on a neuron's probability of firing according to a stimulus. These models then use the characterised neuron's firing probability in conjunction with simulated stimulations pulses integrated over time, which are called 'integrate-and-fire' models. Macherey, Van Wieringen, et al. (2006) presented a phenomenological model that aimed to understand the

impact of alternative pulse shapes compared to the classic biphasic Monopolar (MP) stimulations. Their findings with the model were then used as guidance in conducting a similar study in human CI users where it was found that asymmetrical pulses could elicit lower thresholds and increased electrical dynamic ranges. More recently, Joshi et al. (2017) studied the effects of polarity using a cat SGN phenomenological model with two spike initiation sites, one at the peripheral axon and one at the central axon. They assumed that: (i) the peripheral axon of SGNs is excited by the cathodic charge, inhibited by the anodic charge, and exhibits longer spike latencies than the central axon; (ii) the central axon is excited by the anodic charge, inhibited by the cathodic charge, and exhibits shorter spike latencies than the peripheral axon. The model correctly predicted effects of different stimulus pulse shapes, stimulation pulse rates, and level on the neural response patterns.

These models have proved successful in revealing the underlying dynamics contributing to AP timing and latency, often related to the site of excitation and state of the cell membrane. However, such models lack the fundamental biophysical properties of nerve fibres and are thus less effective in predicting neuron behaviours such as refractoriness, adaptation, accommodation and spike-rate adaptation, key factors when modelling the electrically stimulated SGN.

1.4.2 Physiological Models

Physiological models aim to mimic as closely as possible a neuron's electrical behaviour when it is subjected to a stimulus. They are designed to represent AP according to underlying physiological properties to account for all properties of neurons. To do so, physiological models include ionic channel dynamics and geometric parameters that impact directly on the firing patterns of those neurons. Over the years, models of SGNs have been used successfully to explore the underlying dynamics of the electrically stimulated SGN. In their seminal work, Hodgkin and Huxley (1952) were able to characterise the dynamics of sodium and potassium ionic channels present on the cell membrane of a squid giant axon. These voltage-gated ionic channels are the current source that allows the propagation of APs along the axons and dendrites of neurons. The dynamics of such ionic channels can be described by voltage related differential equations. Inheriting from the Hodgkin-Huxley (HH)

equations, many models have been developed over the past two decades to better understand how SGN morphology, degeneration and ionic channels dynamics impact on the behaviour of SGN under electrical stimulation. Single SGN models are highly valuable in helping understand the basics of neural excitation patterns when subjected to synaptic and extracellular stimuli. Although some models have been found to be successful in predicting the nerve fibre behaviour, the biophysical parameters as well as the morphological parameters used to model those SGNs have been found to differ across studies. Key biophysical parameters for modelling SGNs include the type of ionic channels modelled, their dynamics and concentration, the related conductivity, but also the cell membrane characteristics accounting for leakage current, such as degree of myelination and membrane capacitance (Frijns, de Snoo, et al., 1995; Rattay, Lutter, et al., 2001; Rattay, Potrusil, et al., 2013; Smit, Hanekom, van Wieringen, et al., 2010; Badenhorst et al., 2016, 2017; Kalkman, Briaire, and Frijns, 2016). Together with SGN morphology, these parameters should account for features such as threshold, refractoriness, accomodation, spike-rate adaptation and facilitation.

These models have been found successful in predicting the behaviour of healthy, as well as unhealthy, neurons when subjected to electrical stimulation in the form of injected current or external electrical potentials.

1.4.3 Biophysical models of the SGN

1.4.3.1 Ionic channel models

One of the first biophysical models of SGN was developed by Frijns, Mooij, et al. (1994), a compartment model of neural excitation of mammalian SGNs derived from measurements from rat and cat sciatic nerve from Schwarz and Eikhof (1987) called the Schwarz Eikhof (SE) equations. The Schwarz Eikhof Frijns (SEF) model, a multiple non-linear node model of myelinated fibres with nodes obeying the SE equations, mainly differs from other amphibian derived models because it accounts for mammalian specific properties. Although the AP shapes are essentially similar between mammal and amphibian nerve fibres, the behaviour of mammalian neuron is driven by far fewer active potassium channels in the nodal area and the repolarization of the SGN's membrane is due mainly to a relatively large leak

conductance. Although it was initially developed to account for most of mammalian nerve fibres behaviour, Frijns, Mooij, et al. specified that the focus for this model was the electrically stimulated cochlea. The model has since been used in different studies including Frijns, de Snoo, et al. (1995), Frijns, Briaire, and Grote (2001), and Briaire and J. H. Frijns (2005) with different parameters. Ionic channels dynamics equations for the Frijns, de Snoo, et al. (1995) were taken from a previous study by Frijns, Mooij, et al. (1994). The SEF — similarly to the HH or Frankenhaeuser Huxley (FH) models — defines the current at a node as being the sum of voltage-related sodium and potassium channels, and leak current from the membrane capacitance and voltage. The main differences between these models are that the SEF uses physiologically ranged ionic concentrations, and that the resting potential is computed using the Goldman and Albus (1968) equations that allow the RMP to be computed from the presence of ionic channels and the concentration of ions inside and outside the SGN. The original SEF model was extended to represent the fundamental characteristics of mammalian nerve fibres in general.

The Rattay, Lutter, et al. (2001) model adapts the 'warm' HH equations for potassium and sodium ionic channels as well as the membrane induced leak current. The equations describe the voltage-related gating of ionic channels present on the membrane of the SGN. Two modifications are applied to the HH equations. First, the density of channels on the nodes of Ranvier is multiplied by 10 to reflect a 10-fold density increase compared to the squid giant axon. Second, because the original measurements were made at 6.3 °C, the gating processes were multiplied by a factor of 12 to account for the temperature difference and make them more realistic for 'warm' mammalian SGNs. The equations presented by HH represented a deterministic opening and closing of the ionic channels. This means that those equations don't usually account for spontaneous spiking rates or stochasticity. This behaviour is due to the presence of current fluctuation in the node regions. Such fluctuation is thought to be induced by intrinsic noise of ionic channel that Rattay, Lutter, et al. (2001) added to their set of equations. Verveen and Derksen (1965) reported that the noise was correlated to deviations from the RMP and that this noise increases when the neuron is depolarized compared to when it is hyperpolarized. In order to represent the noise in a computational tractable manner, Rattay, Lutter, et al. (2001) chose to use the technique of Rubinstein (1995) where noise currents

are considered proportional to the square root of the number of sodium channels within a compartment. The noise current can be represented as follows:

$$I_{noise} = gauss \times k_{noise} \times (A_n \times g_{Na})^{\frac{1}{2}} \tag{1.1}$$

where $gauss$ is a Gaussian noise current term (mean=0, S.D=1) that changes value at each computational step, A_n is the node membrane area in ^{2}, g_{Na} is the maximum Sodium channel specific conductivity per unit area, and k_{noise} is a noise constant between compartments $^{-1/2}$

Negm and Bruce (2014) recently presented a model comprising a single node of Ranvier that implements KLT and HCN ionic channels. The model was derived from equations adapted from a study by Rothman (2003) who developed a model of Ventral Central Nucleus (VCN) neurons using those same ionic channels. Historically based on deterministic sets of equations for sodium and potassium channels, previous models of the ionic channels of SGN have provided valuable yet limited description of real neural membranes. Indeed, as mentioned previously, Verveen and Derksen (1965) reported large stochastic membrane fluctuations that would better explain SGN responses. Subsequently, Bruce et al. (1999) showed that a stochastic model of the electrically stimulated AN would better represent experimental responses. Other HH models were then developed which included forms of stochastic processing to better match experimental data.

In addition, several studies (Hossain et al., 2005; Yi et al., 2010) have shown that Type I SGN neurons, like VCNs, contain both KLT and HCN channels. These KLT and HCN channels are considered partly responsible for the experimentally observed refractoriness and spike-rate adaptation properties of neurons in general. Because previous models of the SGN ionic channel dynamics didn't include such equations, this model represents a considerable improvement, revealing specific mechanisms of response properties of SGNs. Negm and Bruce (2014) observed that the addition of KLT and HCN dynamics in the HH model for SGN was efficient in explaining more of the refractoriness, spike-rate adaptation and accommodation properties usually observed in animal data. Previous models that only included sodium and potassium high threshold channels showed poor representation of these properties, an important limitation when it comes to modelling electrical stimulation.

By introducing KLT and HCN ionic channels, the model is able to produce more accurate predictions of the current refractoriness, facilitation, accomodation and spike-rate adaptation state of SGNs under electrical stimulation. In the scope of CI, this prediction could help explain the underlying differences in SGN recruitment.

Smit, Hanekom, and Hanekom (2009) developed a nodal model based on a set of kinetics equation using adapted HH equations to better fit temperature dependence shown in experimental data. This nodal model was effective in eliciting APs in better agreement with human APs both in terms of amplitude and duration. Furthermore, in a following-up study Smit, Hanekom, van Wieringen, et al. (2010) proposed two different distributions of sodium channels based on observations made in previous studies (Smit, Hanekom, and Hanekom, 2008; Smit, Hanekom, and Hanekom, 2009) where the population of sodium channels could be subdivided in activating and permanent, or persistent, components. Permanent channels are channels that remain open all the time, and are not subject to change in membrane potential. Activating, or transient, channels are voltage-gated i.e. their activity is dependent on membrane potential at that specific point in time. Smit, Hanekom, van Wieringen, et al. (2010) tested two configurations: first, ionic channel configuration was set with 100% activating channels. Second, the population was divided in 2.5% permanent channels and 97.5% activating channels. They established that the second configuration that includes persistent channels accounted better for data obtained from human listeners because of the accurate prediction of the non-monotonic threshold behaviour for pulse rates higher than 1000 pps. In addition, Smit, Hanekom, van Wieringen, et al. chose not to include fast potassium ionic channels under the assumption that such channels do not activate as they are mostly located under the myelin sheaths at the vicinity of the internode.

Overall, models including more complete ionic channels dynamics have been shown actively to adapt threshold levels of the SGN and characterize better the observed properties of SGNs therefore, the modelling of these ionic channels in more realistic model may offer better understanding of the electrically stimulated AN.

1.4.3.2 Morphology of the SGN

As shown in Fig. 1.7, different models have used different morphological representations of the SGN. When first presented by Frijns, Mooij, et al. (1994), the morphological parameters used for their model were based on guinea pig and cat measurements. A bipolar neuron was divided into a compartment model (shown in Fig. 1.7). The peripheral process was divided into 7 compartments, 4 nodes of Ranvier compartments and 3 internode myelinated compartments. The internodes were all assigned a length of 175 µm and the nodes were all 1 µm long, except for the postsynaptic compartment, which was 10 µm. The peripheral terminal had a diameter of 3 µm corresponding to a HSR type SGN. A central process was divided into variable number of compartments dependent on its position on the 3D representation of the cochlea. The lengths of internodes varied along the axon. The parameters used for this publication along with parameters from other models are summarized in Table 1.1.

In a more recent study by Briaire and J. H. Frijns (2005), the morphological parameters for the SGN were adapted to more closely represent the human SGN. Essentially, a long pre-somatic compartment was added, matching the pre-somatic compartment used in another study by Rattay, Lutter, et al. (2001). The rationale for this extra compartment, as reported by Rattay, Lutter, et al., was to allow for the AP to saltate the current consuming soma compartment. Due to its large size, the soma acts like a large capacitance that needs to be charged before it allows the AP to continue propagating. Additional node and internode compartments were also added to the peripheral axon. In 2005, Briaire and J. H. Frijns modified and extended the Generalised Schwarz Eikhof Frijns (GSEF) model to match human morphology more closely and examine the contribution of individual neurons in Electrically evoked Compound Action Potentials (ECAPs). The ECAP is an objective measure of neural recruitment in response to an electrical stimulus. As such, ECAPs represent the contribution of a population of SGNs to an electrical pulse (Undurraga, van Wieringen, et al., 2010; Undurraga, Carlyon, Macherey, et al., 2012). To achieve this, Briaire and J. H. Frijns (2005) modified the guinea pig model from Frijns, Mooij, et al. (1994) and adapted the morphological parameters of the SGN to mimic more closely human physiology, and combined it with a 3D volume conduction

model of the human cochlea they previously reported (Briaire and J. H. M. Frijns, 2000). Briaire and J. H. Frijns reported that the main morphological modifications occurred at the level of the peripheral process, and in the demyelinated parts of the SGN, the main differentiating characteristics of human SGNs when compared with other mammals. Because of the lack of histological data available, they accounted for these changes in morphology by implementing measures previously reported by Rattay, Lutter, et al. (2001). Furthermore, to understand the role of the pre-somatic and somatic regions, the authors described two conditions. The first condition was described as the Unmyelinated Cell Body (UMCB) were both pre-somatic and somatic compartments were set with active membranes. The second condition was defined as the Myelinated Cell Body (MCB) condition where both pre-somatic and somatic compartments were insulated by myelin sheets.

Although the model described by Rattay, Lutter, et al. (2001) contained specifications for both cat and human SGN morphology, we will only focus on the human description of their work. The model developed by Rattay, Lutter, et al. is based on the HH equations with some modified parameters to fit the biophysics of SGN in humans. They described two types of human SGN morphology: a standard human cell and a short cell. The peripheral axon of the SGN is modelled with 7 peripheral demyelinated nodes of Ranvier compartment, 5 peripheral myelinated internode compartments all with a diameter of 1 µm. The post-synaptic and pre-somatic were given lengths of 10 µm and 100 µm respectively. All other nodes of Ranvier on the peripheral process have a length of 2.5 µm. Noting that human internodal lengths were not systematically reported, they chose lengths that were published in a study by Finley et al. (1990). The peripheral internodes are considered to have 40 layers of insulating myelin. The central axon was modelled with 15 nodes of Ranvier compartments and 14 myelinated internode compartments with a 2 µm diameter across compartments. The first node of Ranvier compartment on the central axon was given a 5 µm length. All other node of Ranvier compartments on the central axon were given a 2.5 µm length. Internode compartments were all given a length of 500 µm. The central internodes are considered to have 80 layers of insulating myelin. Both peripheral and central axons were connected by 1 partially myelinated soma compartment with 30 µm diameter with 3 layers of insulating myelin. The second type of SGN, called short human-SGN, was an altered version of the long

human-SGN where peripheral nodes P2, P3, and P4 were removed. Rattay, Lutter, et al. reported that the main issue to be overcome with simulations of the human SGN is for the stimulated AP to propagate past the soma. The morphology of the SGN, the distribution of nodes length along the peripheral axon of the neuron, the strength of currents inside the neuron as well as the soma diameter and insulation were all considered parameters to the success of an AP propagating over the soma to the central axon. It appears that changes to those parameters would modify the somatic delay. Furthermore, Rattay, Lutter, et al. reported that in the case of a human SGN model, even small variations in SGN geometry could cause the loss of a propagating AP. In addition, the study showed that the fluctuations in ion channel current was a source of variability in the AP latency.

The Negm and Bruce (2014) model represents a single node. Thus, no morphometry parameters were reported. Instead, they used nodal conductivities related to the number of channels that have been reported in the literature. The number of sodium, potassium high threshold, potassium low threshold, and hyperpolarizing cation channels for a normal node of Ranvier were defined as 1000, 166, 166 and 100 respectively.

1.4.3.3 Electrical field distribution

In order to account for the three-dimensional distribution of the electrical current resulting from the electrical pulse trains, the model was subsequently combined with Boundary Element Models (BEMs). These models aimed to represent the stimulation of neuron populations in different regions of the cochlea when subjected to different electrical pulses. In their 1995 report, Frijns, de Snoo, et al. used a combination of two sub-models. The first model employed was a rotational symmetric model of the cochlea. This BEM was used to compute electrically induced potentials at different electrode positions. This model was combined with their previously developed GSEF model for neural excitation. The aim of this two parts model of the cochlea was to compare modelled Input/Output (I/O) response curves with animal data from guinea pig. For the BEM component, a cross section of the cochlea was modelled using 41 quadratically curved elements through 72 mesh points. The cross section was then rotated around a central modiolar axis. This created a toroidal

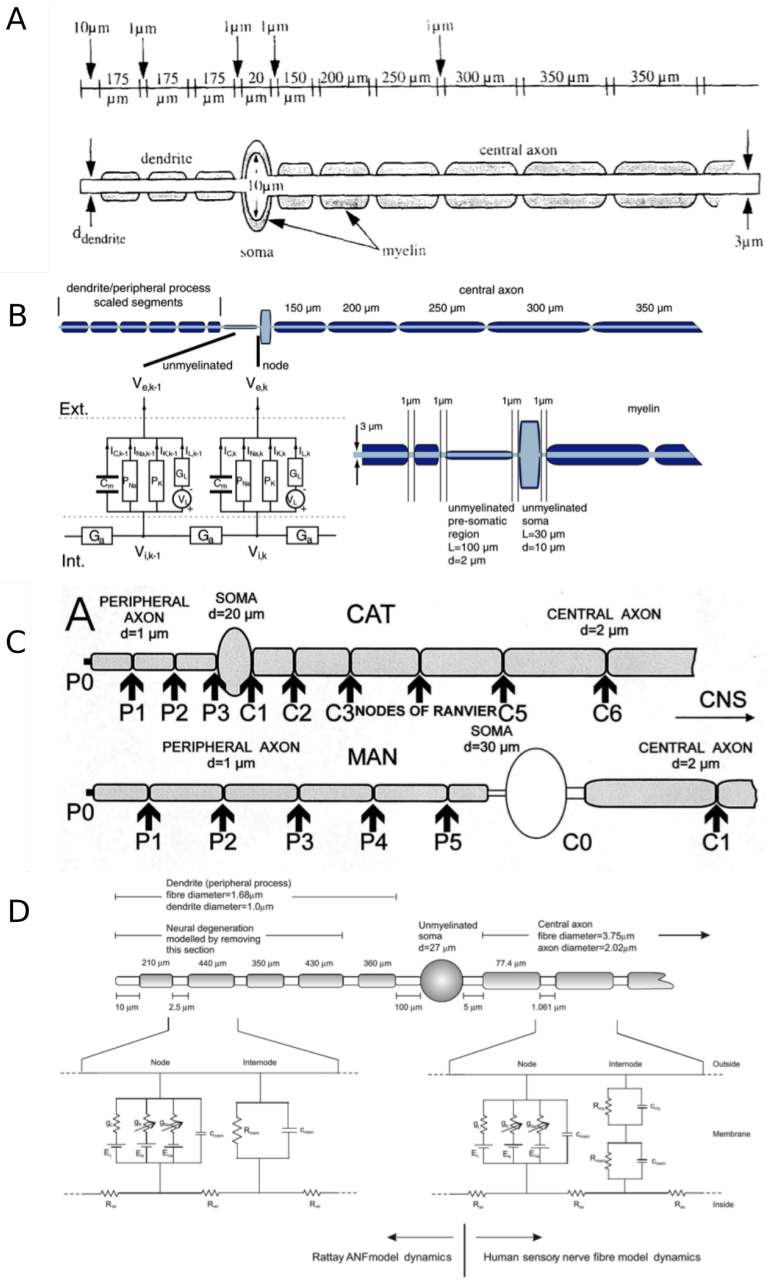

Figure 1.7: Morphological schematics from different publications. A) Frijns, Mooij, et al. (1994), B) Briaire and J. H. Frijns (2005), C) Rattay, Lutter, et al. (2001), D) Smit, Hanekom, van Wieringen, et al. (2010)

structure containing a total of 2240 elements and 4194 nodes. The main assumption of this model was that the cochlear turn was entirely contained in bone instead of projecting in an air-filled bulla, as is the case in guinea pigs. In addition, the model didn't account for tissue capacitive effects but instead considered impedances of all media in the cochlea to be purely resistive. It was considered that this simplification was supported by the work reported by Spelman et al. (1982) where they found that potentials in the scala tympani are virtually frequency independent up to 12.5 kHz. Finally, tissue conductivities used in the BEM were adopted from the study by Finley et al. (1990) who compiled values from several authors. With this model, Frijns, de Snoo, et al. (1995) were able to produce excitation patterns from electrical stimuli generated by varied electrode positions. It enabled them to establish the effect of stimuli in different turns of the cochlea on neurons. The I/O curves were then derived from the excitation patterns for specific electrical pulses at different electrode positions.

In their study, Briaire and J. H. Frijns (2006) simulated 299 equally spaced neurons along the entire length of the 3D modelled human cochlea. As a result, each fibre represented a group of 100 actual nerve fibres. For each neuron, a Single Fibre Action Potential (SFAP) was computed by adding the contribution of the current at each node of Ranvier along the SGN as a function of time. ECAPs were then computed by summation of each SFAP at a given stimulation site in the cochlea. Interestingly, Briaire and J. H. Frijns (2006) reported that simulated ECAPs showed stimulation artefacts similar to those reported in experimentally measured data. Stimulation artefacts are the effects of the stimulation potential on the measured potential. Usually, the measure that is recorded is much smaller than the artefact of stimulation, which makes the measure unusable. Thus, all simulated ECAPs had to undergo artefact removal to account for the effect of the extracellular stimulation artefacts evident on SFAPs and thus on the simulated ECAPs. For technical and computational practicality, subtraction of a scaled artefact was chosen to compute clean ECAPs. The scaled-artefact technique uses an artefact measured from a sub-threshold stimulus and is then scaled to a supra-threshold size. From their simulated ECAPs, Briaire and J. H. Frijns (2006) concluded that the modifications made to the GSEF and compartment model weren't enough to successfully represent human recorded ECAPs. The main outcome reported from the simulations of ECAPs using

this model was that the largest contribution observed came from the cell body in the UMCB. Briaire and J. H. Frijns (2006) suggested that this contribution could be explained by the lack of leak element in the model which would account for the under contribution of the other compartments of the SGN. Another plausible cause for the mismatch between human recordings and the modelled ECAPs is that the GSEF model kinetics are based on animal kinetics which make the AP shape different from the expected shape of a human AP. Thus, they concluded that human model-kinetics would have to be tested.

In a following up study, Rattay, Potrusil, et al. (2013) presented the single SGN model combined with a 3D spiralled model of the cochlea. By simulating 18 neurons positioned along the cochlea and calculating the corresponding potentials they were able to study some aspect of polarity effects. The study outcomes were reported as travelling waves and threshold levels for each SGN according to their position relative to the stimulating electrode. They reported that the model could make simple predictions on the effect of stimulation polarity on threshold as a function of distance from the electrode. In their 2001 study, Hanekom developed a 2-parts 3D Firing Efficiency (FE) model of the human cochlea. The first part of the model was a 3D spiralled FE model accounting for the morphological and tissue properties of the human cochlea based on a previous study by Finley et al. (1990). The main specificity of the FE model was that it included two electrode carriers in the cross section of the cochlea, allowing any electrode configuration to be represented. From this model, they derived conductive potentials for varying modes of stimulation in the electro-stimulated cochlea to be imputed in the neurally active part of the model.

1.4.3.4 Effects of stimulus and pulse shapes

In their study, Rattay, Lutter, et al. (2001) used an ***activation function*** to represent the direct influence of extracellular stimulation. This tool was reported previously by Rattay (1999), and helps explain the impact of extracellular stimulation on responses of neurons of arbitrary shape. The tool assumes an infinite homogeneous

extracellular medium. The extracellular potential can then be represented as:

$$V_e = \rho_e \times \frac{I_{electrode}}{4\pi r} \tag{1.2}$$

Where ρ_e =0.3 kΩ is set to be the mean resistivity of the extracellular medium. r is the distance between a point of interest and the center of the electrode. Under these assumptions, the potential at a point along the SGN is considered to be proportional to 1/r.

The stimulus shape used to calculate Ve were either monophasic or biphasic symmetric. For the extracellular stimulation, Rattay, Lutter, et al. used a simplified representation of the upper end of the basal turn. The same representation was used for both the long and short version of the SGN model. Simulations with the two types of SGN model inform as to how morphological difference across neural population can contribute to the latency and threshold differences that account for the complexity of neural encoding. They found that cathodic pulses were more efficient than anodic pulses, if the neurons were in a healthy physiological state. This because the proximity of the peripheral end of the axon to the extracellular electrode eliciting an AP in the peripheral process was more effective in depolarizing the SGN, than was an anodic pulse. Anodic pulses were generally found to have higher thresholds for spike initiation, with the initiation site lying closer to, or even beyond, the soma when the intensity of stimulation was increased. This has been shown to have major impact on firing patterns when stimulating degenerated SGNs; cathodic pulses became inefficient at generating APs and high intensity anodic monophasic pulse or anodic first biphasic pulses were found to elicit APs. Rattay, Lutter, et al. explained that this phemenomenon was caused by the lack of cathodic-preferred site of excitation. The degenerated SGN being missing its peripheral element, SGNs were now exclusively initiated at a central position on the axon, thus favouring anodic stimulation.

In their 2001 study, Hanekom employed the field potentials measured for different stimulation modes using the FH model to activate SGN models distributed along 90 segments represented by the 3D cochlear model. Those 90 segments potentials were then used as input for 90 active neuron models. In their study, Smit, Hanekom, van Wieringen, et al. (2010) reused the Hanekom (2001) FH conduction model with

their new modified HH model combined with the compartment parameters reported by Rattay, Lutter, et al. (2001). With this new model combining the morphologic parameters from Rattay, Lutter, et al. (2001) and new equations for the neural membrane dynamics, Smit, Hanekom, van Wieringen, et al. studied the effect of different pulse shapes on threshold levels for the simulated SGNs. Using pulses first defined by Van Wieringen et al. (2005) and van Wieringen, Macherey, et al. (2008), the authors computed the electric potentials at 12 separate locations in the 3D modelled cochlea. The calculated potentials were then used as input for the active neuron model. Results were presented in the form of predicted threshold for each stimulation configuration of pulse and electrode position. With this model, the authors were able to predict temporal characteristics relative to different pulse shapes. The model was also successful in predicting the behaviour of threshold levels as a function of pulse rate, which wasn't possible with previous models.

1.4.3.5 Effects of SGN degeneration

In their 2006 study, Briaire and J. H. Frijns extended the Briaire and J. H. Frijns (2005) model to study the effects of peripheral process degeneration, and electrode position in the cochlea, on the measurement of ECAPs (Briaire and J. H. Frijns, 2006, 2005). They made several predictions on the effect of electrode position on the simulated ECAP. Differences in selectivity between basal and apical electrodes placed laterally or medially compared to the modiolus: (i) the basal electrodes were observed to be more selective when placed medially in the scala tympani (relative to the organ of Corti) whilst more apical electrodes were more selective when placed laterally; (ii) lower threshold levels for basal electrodes placed medially compared to laterally but these benefits were less clear for more apical electrodes. This is similar in both degenerated and non-degenerated configurations, as reported in their previous study, with a difference in threshold level benefit; non-degenerated SGNs showed a 9 to 15 dB benefit in threshold levels where only 3 dB benefit was observed for degenerated SGNs. Additionally, Briaire and J. H. Frijns (2006) observed that comparison between ECAPs in non-degenerated and degenerated SGNs could help explain the subjective percept of electrical stimuli in patients with no recorded ECAPs. It is thought that some degenerated populations generate such small ECAP

that they would be hard to measure in patients although they elicit a perceived response.

The model by Rattay, Lutter, et al. (2001) was further studied to explain the effect of myelination, morphometry and synaptic current strength on spike conduction (Rattay, Potrusil, et al., 2013). The model developed in 2001 was used with a small modification where the temperature was lowered from 29 °C to 27 °C (Rattay, Lutter, et al., 2001; Rattay, Potrusil, et al., 2013). Although this study did not focus on extracellular stimulation, the modifications made to the model and findings related to morphometry and myelination are interesting in the context of the modelling of SGN degeneration. They reported that a '1/2 ratio' existed between the diameter of the peripheral and the central processes. Moreover, they concluded that this ratio was an important factor in the successful delivery of APs to the CN. Also, the specific myelination of human Type I SGN seems to favour the constant spike conduction time in each frequency region of the cochlea, meaning that myelination plays a central role in the latency profile of SGN responses. Finally, the importance of morphometry for CI is related to the possible elicitation of multiple sites of excitation in the case of electrically stimulated SGNs. This phenomenon is thought to account for the difference in threshold of polarity pulses observed in humans and animals, with anodic-first pulses exciting at lower levels than cathodic-first ones in humans and the opposite for most *in vivo* animal models. It is important to note that although this effect is mostly true at suprathreshold and comfortable levels, it hasn't been shown to hold at threshold levels in humans (Macherey, Van Wieringen, et al., 2006; Undurraga, van Wieringen, et al., 2010; Undurraga, Carlyon, Macherey, et al., 2012; Undurraga, 2013; Joshi et al., 2017).

1.4.3.6 Effects of electrode placement

Hanekom (2001) used the technique presented by Frijns, De Snoo, et al. (1996) in which they truncated the guinea pig SGN model from the 4 initial nodes and internodes to start the cell at its pre-somatic terminal. This shifted the end of the neuron to be located inside the modiolus and was used as a model of a degenerated SGN. Also, they assumed that although guinea-pig SGNs are morphologically different to human SGNs, the threshold difference that resulted would be within the

diversity of variation observed across human CI users. To evaluate the efficiency of electrode placement and configuration as well as the efficiency of pulse polarity in generating APs, Hanekom (2001) reported results in the form of threshold levels, the potential amplitude required to stimulate an AP, and spectral selectivity information in the form of SOE profiles. By compiling the excitation profiles of neuron models according to electrode configurations Hanekom and colleagues were able to predict the effects of stimulation strategies on dynamic range and spectral-selectivity.

More recently, Kalkman, Briaire, Dekker, et al. (2014) extended the volume conduction model from Briaire and J. H. Frijns (2006) to study the effect of electrode placement on pitch. They reported several findings impacting the stimulation-electrode placement: (i) neural recruitment with electrical stimulation is a three-dimensional process; excitation regions expand in apical and basal directions, as well as penetrate deep into the spiral ganglion. (ii) at equal loudness, certain differences between the spatial excitation patterns of various multipoles cannot be simulated in a model containing linearly aligned neurons of identical morphology. They concluded that introducing variability in the neural spatial distribution of somas is essential in modelling SOE.

1.5 Thesis outline

This chapter reviews the most influencial research of multiple groups that have spent the past two decades extensively studying the various effects of morphology, myelination, ionic channels distribution and dynamics on electrical stimulation by CIs and, the effect of stimulation strategies at the level of single, or population of, SGNs. Unequivocally, SGN morphology has a major impact on the efficiency of electrical stimulation. Different morphologies, e.g. the difference between cat and human SGNs, can change the entire properties of propagating APs. Latency, somatic delay and site of excitation are in part responsible for the encoding of the neural signal. The model proposed by Rattay, Lutter, et al. (2001) includes a morphology element that has since been used in most physiologically based models of SGNs: adding a long, demyelinated pre-somatic compartment to the morphology of the SGN seems key for the successful propagation of APs over the cell body. Such an element of SGN morphology is not found in other species and was later added in

other models (Frijns, Mooij, et al., 1994; Hanekom, 2001). The other particularity of the human SGN morphology is the length of its peripheral process. This plays an important role when it comes to modelling degeneration of the peripheral process and in explaining the causes of changes in spike latency. In the case of degeneration, Rattay, Lutter, et al. (2001), Frijns, Mooij, et al. (1994) and other studies (Hanekom, 2001; Smit, Hanekom, van Wieringen, et al., 2010; O'Brien, 2016) have used a technique that simply truncates the 4 initial nodes of the SGN in order to simulate the peripheral process loss. As demonstrated in all of these studies, the truncated SGNs will behave differently in terms of polarity sensitivity and initiation site. This shows major effects on APs latency, as a result of the shift from the peripheral to central axon of the APs initiation site . In turns, this could help explain some of the neural encoding problems in electrical stimulations in CIs.

Ionic channels have also been thoroughly studied over the past two decades. Their role as the engine of AP propagation in the nodes of Ranvier makes the understanding of their behaviour a key element in the successful simulation of physiologically based models of electrical stimulation. From the studies assessed in this review, two different approaches are apparent. The first, developed by Frijns, Mooij, et al. (1994) employs mammalian-derived equations initially reported by Schwarz and Eikhof (1987), and ensures that models are compliant with the dynamics of warmed blooded animals, such as guinea pigs or humans. As it was developed using data obtained from guinea pigs, the equations had to be adapted and fitted to better represent human data. However, the model was limited by the lack of leak currents and the absence of stochasticity. The alternative approach taken by Rattay, Lutter, et al. (2001) et al as well as Negm and Bruce (2014) was to build on the seminal work from Hodgkin and Huxley (1952). Using equations they initially reported, Rattay, Lutter, et al. (2001) modified the HH model into a high density, warm HH model that was successful in predicting most aspects of the membrane dynamics observed in cats and other mammals. The main modifications compared to previous models was the increased density of ionic channels by a factor of ten, and the 12-fold increase in the gating processes, compared to the HH equations to account for the temperature difference between the cold squid giant axon and the human configuration. To overcome the absence of stochasticity of the HH model, Rattay, Lutter, et al. (2001) introduced a noise current that was

linked to the density of sodium channels. Although the technique was successful in restoring current fluctuations and impact the distribution of firing latencies, the stochasticity induced didn't generate spontaneous firing. The main limitation observed from the studies presented in this review is the lack of explanation when it comes to refractoriness, facilitation, accommodation and spike-rate adaptation of SGNs. None of the single SGN models presented seem to predict how SGN behave when subjected to train of pulses, which is the form of stimulation normally applied for clinical use. The nodal model presented by Negm and Bruce (2014), introducing KLT and HCN ionic channels, is an advance on this and seems to predict more of those aspects.

Finally, the various stimulation strategies that were studied show how important electrode configuration and pulse shape are in the neural encoding of signals in CIs. Population models developed from the single-SGN models in combination with 3D-volume models of the cochlea have helped to explain how stimulation strategies could impact SOE, shifts in threshold levels, and neural recruitment. As shown in many of the studies, pulse shape can have a major impact in reducing threshold levels and therefore generating a greater electrical dynamic range. In a recent study, Smit, Hanekom, van Wieringen, et al. (2010) showed that both polarity and pulse shape, associated with the neural degeneration could, in fact, explain much of the reported variability in CI candidates. Although they've been successful in predicting some of the spectral selectivity and threshold levels in the cochlea, population models are still limited by the lack of variability in the distribution of the physiological and morphological parameters, and is often lacking the SGN density required for proper study of SOE.

1.5.1 Aims

Increasing efforts have been made to determine those properties responsible for the neural encoding of electrical stimuli in CI. Physiological models are now able to predict to a relatively high level the behaviour of single SGNs. However, there is still a need to improve on those models. By moving towards physiological constraints relevant to the human inner ear, computational models could help understand better the impact of complex stimulation strategies on neural encoding. A better match

with properties of spike-rate adaptation, refractoriness, accommodation, facilitation and stochasticity is still required if models are to successfuly predict SGN responses to electrical stimulation pulse trains as produced by CIs. Finally, the increasingly precise information available concerning the behaviour of SGN populations in human CI users, due to better measurement techniques, will provide for more precise models. This is key to the development of novel stimulation strategies adapted and fitted to meet the specific needs of each individual CI users.

To summarize, the literature shows a breadth of knowledge on tools for the modelling of SGNs with features of facilitation, refractoriness, accomodation and spike-rate adaptation. However, what appears to be missing is a model which combines all those features at once with a human-like morphology. From Smit, Hanekom, van Wieringen, et al. (2010) and Rattay, Lutter, et al. (2001), an effective cable equation model with a human morphology can be derived with features of refractoriness, accomodation and facilitation. In addition, Negm and Bruce (2014) and Boulet (2016) introduced ionic channels, HCN and KLT that show features of spike-rate adaptation. One aim of this thesis is to combine the knowledge from those studies to produce a SGN cable-equation model with human-like morphology that would present all the expected features of refractoriness, facilitation, accomodation and spike-rate adaptation.

Also, the available literature on population of SGNs, with or without conduction models, seems to mostly focus on the excitation across the entire cochlea. Given the important amount of computational ressources required to simulate those, the compromise of a low spatial resolution for SGN excitation is often required. In this thesis, the aim will be to focus the population modelling to a high-density subpopulation of SGNs. This subpopulation model would allow for more accurate predictions on local excitation patterns.

The main aim of this thesis, then, is to develop more realistic, physiologically based, models of single and populations of SGNs. These models will be used to demonstrate that stimulation strategies adapted to specific patient profiles could provide better encoding of speech information by restoring important temporal and spatial information or, by minimizing unwanted temporal and spatial interactions of electrical stimulation. In Chapter 2 I will present the general methods that were used to develop the model used in all subsequent chapters.

This thesis also aims to explore how a pulse shape designed according to the physiological properties of SGN and leveraging the mechanism of accommodation can help restore some sense of stochasticity and increase the spatial selectivity of electrical stimulation. To achieve this, Chapter 3 will examine an implementation of an extended version of the Rattay, Lutter, et al. (2001) model and the effects of the addition of ionic channels such as those of Rothman (2003) and Negm and Bruce (2014). The historical Rattay, Lutter, et al. (2001), and more recent Rothman (2003), models and modified versions of these models will be compared in full single SGN models. Models of single SGNs will be developed in response to extracellular stimulation. Extracellular potentials will comprise several temporal pulse shapes and leading phase polarity, to evaluate the polarity effect on the dynamics of ionic channels, and the initiation and propagation of APs. Introducing new types of ionic channels will help model more closely the behaviour of SGNs. By doing so, more complex pulse shapes that leverage from the subthreshold properties of the SGN, such as ramp pulses, could be developed (Ballestero et al., 2015).

In Chapter 4 I will examine how degeneration and demyelination of SGNs modifies responses to electrical stimulation. Physiologically healthy and unhealthy SGNs differ in the distribution of morphological and physiological parameters along their length. Thus, the response of unhealthy and healthy SGNs will be specific for any one degeneration profile. Using the single-SGN model developed in Chapter 3, different degeneration profiles and pulse shapes with varying leading polarities will be evaluated to reveal the key features for effective degenerated-SGN electrical stimulation.

Chapter 5 will examine a fully parametrized model of a sub-population of SGNs. The aim of this chapter is to determine the impact on responses of SGNs with different morphological and physiological parameters, in response to several typical and atypical pulse shapes. By changing the distribution of morphological and physiological parameters in a population of SGNs in close proximity—mimicking the encapsulated auditory nerve—I will assess how this population of SGNs behaves when subjected to the same external, electrical-stimulation. 1500 SGNs will be simulated according to three profiles: 1/ healthy; 2/ demyelinated, and; 3/ degenerated distribution. Differences in responses for the three profiles will be compared when subjected to the different stimulation pulses and polarities.

Finally, Chapter 6 focuses on evaluating the effectiveness of novel pulse shapes, in particular asymmetrical (Macherey, Van Wieringen, et al., 2006; Van Wieringen et al., 2005; van Wieringen, Macherey, et al., 2008) and ramped pulse shapes. Asymmetrical and ramped pulse shapes are designed to bring a new dimension to coding and stochasticity in the electrical encoding of sound signals. Leveraging ionic channel dynamics, accommodation properties of SGNs and electrical diffusion properties, these atypical pulse shapes are thought to help improve CI performance and reduce inter-patient variability in outcomes by increasing stimulation strategy personalization. As such, it can be theorised that ramped pulses or asymmetrical pulses, using different coding paradigms, could show lower thresholds of excitation and/or better power consumption. Using the complex model developed and validated in Chapter 3, Chapter 4 and Chapter 5, I will evaluate the efficacy of these atypical pulse shapes in healthy and unhealthy single and populations SGNs.

Table 1.1: Summary of Morphology parameters

Parameter	units	Rattay, Lutter, et al. (2001)	Bruce et al. (1999)	Brown	Smit, Hanekom, and Hanekom (2009)	Frijns, De Snoo, et al. (1996)
Node length	μm	2.5		1.3	1.061	1
Node diameter	μm	1	2-4	0.8	1-2	2-3
Node area	nm^2				50	
Presoma node length	μm	100			100	1-100
Post soma node length	μm	5			5	1
Post synaptic node length	μm	10			10	10
Internode length	μm	75-500		100	77-440	175-350
Number of Myelin sheets (P/C)		40/80				
Specific membrane capacitance	$\mu F/cm^2$	1			1	2.8
Total nodal membrane capacitance	pF		0.0714	0.0327	1.4	0.189
Intracellular resistivity	$\Omega \cdot cm$	50		50		0.025
Total nodal membrane resistivity	$M\Omega$		1953.49			
Sodium channel density	μm^2		1000/node			700-2000
Sodium specific conductance	S/cm^2	0.12		0.05	0.64	
Sodium nodal conductance	pS		25690			
Kv specific conductance	S/cm^2	0.036		0.015	0.06	
Kv nodal conductance	pS		8300			
KLT specific conductance	S/cm^2			0.002		
KLT nodal conductance	pS		2158			
Leak specific conductance gL	S/cm^2	0.0003		0.0002	0.0575	
Leak Reversal potential	mV	-54.6		-63		

Sodium Reversal potential	mV	55	66	50
Potassium reversal potential	mV	-75	-88	-80
Membrane Resting Potential	mV	-65	-78	-88
Gating process multiplicator		12		
Channel Density multiplicator		10		

2 General Methods

In this thesis, the compartment model first developed by Rattay, Lutter, et al. (2001) will be used to simulate single and populations of electrically-stimulated human Spiral Ganglion Neurons (SGNs). The aim is to study the differences in the responses of SGNs as a function of stimulus, morphology and other physiological properties.

Morphological parameters of interest in this thesis are related to electrode position and the different degrees of degeneration that can affect SGNs, such as loss of their peripheral processes or demyelination following hearing loss. As mentioned in Chapter 1, a breadth of literature exists reporting different approaches to the modelling of electrically-stimulated human and mammalian SGNs (Rattay, Lutter, et al., 2001; Rattay, Potrusil, et al., 2013; Hanekom, 2001; Smit, Hanekom, van Wieringen, et al., 2010; Frijns, de Snoo, et al., 1995; Briaire and J. H. Frijns, 2006; Badenhorst et al., 2017; Kalkman, Briaire, and Frijns, 2016).

This chapter presents the methods and framework used to model the human SGN throughout this thesis as well as the general physiological and morphological parameters that were used to represent each SGN. Study-specific modifications to the model will be specified in each subsequent chapter.

First, the compartment model used for simulating healthy and unhealthy SGNs will be described. Then, a description of spike detection techniques and the solving methods for simulations will be detailed. Finally, validation of the proposed implementation of the model will be presented.

2.1 SGN Models

2.1.1 Compartment Model

As shown in Fig. 2.1, the morphology of the human SGN employed in this thesis is represented by a bipolar neuron. The peripheral process is composed of seven

nodes of Ranvier, named with a P and numbered from 0 to 6, e.g. P0, while the central process has fifteen nodes, named with a C and numbered from 0 to 14, e.g. C0. All nodes of Ranvier are separated by long internodes. Peripheral and central processes are connected by the cell body, or soma. The soma and all internodes are myelinated but the number of myelin sheaths varies for each structure.

To model the SGN, the morphology presented here was segmented into compartments: each node of Ranvier, internode and soma is represented by a compartment. Furthermore, the NEURON software that was used for the simulations enables subdivision of compartments into segments, dramatically increasing the spatial precision of the predictions.

Previous studies have shown the importance of the spatial distribution of these compartments relative to a realistic cochlea when applying extracellular stimulation (Rattay, Lutter, et al., 2001; Boulet, 2016; Badenhorst et al., 2017; O'Brien, 2016; Mino et al., 2002). As shown in Fig. 2.2, SGNs in the human cochlea wrap around the electrode, due to their natural curvature along the modiolus. This is thought to account for several polarity effects observed *in vivo* that cannot be accounted for by neural degeneration only (Rattay, Lutter, et al., 2001; Rattay, Potrusil, et al., 2013; Hanekom, 2001; Smit, Hanekom, van Wieringen, et al., 2010; Frijns, de Snoo, et al., 1995; Briaire and J. H. Frijns, 2006; Badenhorst et al., 2017). To represent the curvature of the modiolus, the compartments were positioned following a curved line with the shape of the SGN. Geometrical parameters of the neuron and spatial coordinates are based on Rattay, Lutter, et al. (2001), Rattay, Potrusil, et al. (2013), and Smit, Hanekom, van Wieringen, et al. (2010) and details are given in Table 2.1. The specific peripheral and central internode lengths that were used for this thesis were taken from Smit, Hanekom, van Wieringen, et al. (2010) as Rattay, Lutter, et al. (2001) did not report them systematically. Other physical properties for the nodes and internodes are shown in Table 2.2.

2.1.2 Modelling degeneration

The properties of SGNs undergoing degeneration, due to trauma or other aetiologies, may change depending of the degree of peripheral degeneration. This can range from partial peripheral loss of myelin sheaths to the complete loss of the peripheral

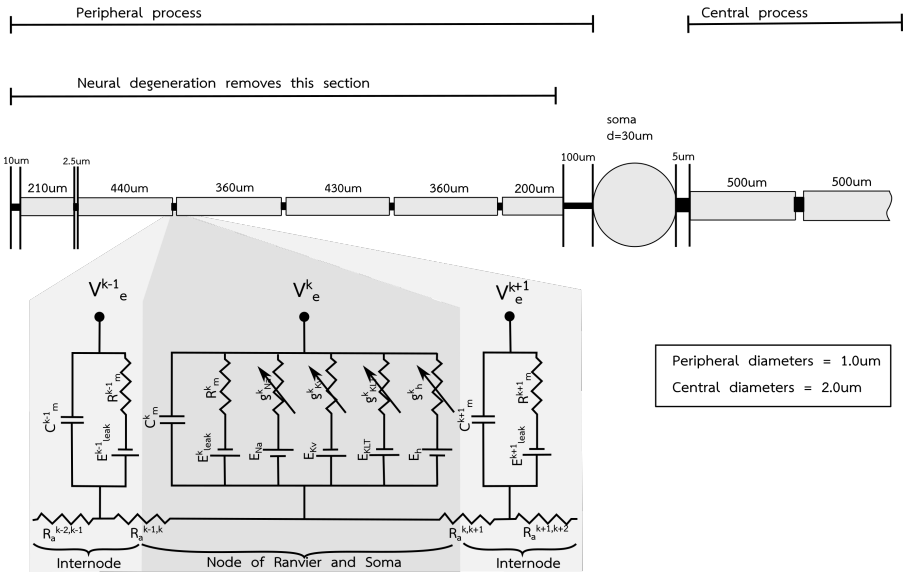

Figure 2.1: Morphology of the Type I SGN in human, based on Rattay, Lutter, et al. (2001) and Rattay, Potrusil, et al. (2013), and the corresponding circuit model. The upper portion of the figure shows the SGN geometry. The peripheral nodes of Ranvier are denoted by P0–P6 whereas the central nodes are called C0–C14. All internodes between nodes C0–C14 have the same length. The lower portion shows a segment of the circuit model at node P2 and the surrounding internodes. Starting at the left is one internodal compartment, followed by the nodal compartment including all ion channels and finally, to the right, is another internodal compartment.

process.

In most cases, extracellular stimulation targets SGNs that have started degenerating, i.e. partial degeneration, or have already lost their peripheral process, i.e. fully degenerated (Rattay, Lutter, et al., 2001; Rattay, Potrusil, et al., 2013; O'Brien, 2016; Boulet, 2016; Frijns, Mooij, et al., 1994). However, little is known about the effects of neural degeneration and electrical stimulation in the human SGN, and the development of a realistic model of degeneration of the SGN would be highly beneficial to our understanding of how electrical hearing is influenced by different degrees of SGN degeneration.

In this thesis, three types of neurons similar to Rattay, Lutter, et al. (2001) are defined: first, a healthy human SGN; second, a partially demyelinated SGN, where the term 'partially' refers to the loss of myelin sheaths at the peripheral process level; and finally, a fully degenerated SGN where the peripheral process was truncated at node P6. These three different SGNs allow for a realistic model representation of most expected cases of SGN health *in vivo*. The healthy SGN is as described in Fig. 2.1 and closely matches previous studies (Rattay, Lutter, et al., 2001; Rattay, Potrusil, et al., 2013; Hanekom, 2001; Smit, Hanekom, van Wieringen, et al., 2010).

Demyelination can occur over time and usually drives a change in threshold and latency of firing of SGN to electrical stimulation (Kroon et al., 2017; O'Brien, 2016; Boulet, 2016; Miller, Abbas, and Robinson, 2001). The demyelinated SGN loses its conductive properties as the myelin sheaths are lost. SGN demyelination is a progressive phenomenon that can take years in humans or weeks in animals, and is a consequence of hair cell loss (Ylikoski et al., 1974; Spoendlin, 1975; Ramekers et al., 2014). As such, demyelination essentially becomes a continuum where any number of myelin sheats would be relevant. Here, the demyelinated SGN was modelled by removing half of the myelin sheaths found on the peripheral process of healthy human SGNs (40 sheaths), matching previous studies (Rattay, Lutter, et al., 2001; Rattay, Potrusil, et al., 2013).

Finally, the degenerated SGN was modelled by removing the peripheral process of the neuron, with the exception of the pre-somatic node of Ranvier compartment. In this condition, the SGN's soma was maintained at the same distance from the stimulating electrode as the healthy neuron to present a realistic scenario. This model of degeneration was previously used by Rattay, Lutter, et al. (2001), Smit,

Hanekom, van Wieringen, et al. (2010), and Badenhorst et al. (2017) and has shown to be effective in explaining some animal data (Miller, Abbas, and Robinson, 2001; Javel and Viemeister, 2000).

Table 2.1: Summary of Morphology parameters. Peripheral (P), central (C), and internodoes (Int) parameters are indicated for each model, respectively.

Parameter	Model	Compartment	Value	units	Reference
Node of Ranvier					
Node length	all	all except P0, P6, C0	2.5	μm	Rattay, Lutter, et al. (2001)
		P0	10	μm	
		P6 (presoma)	100	μm	
		C0	5	μm	
Node diameter	all	peripheral	1	μm	
		central	2	μm	
Internode					
Internode length	healthy and demyelinated	peripheral	210	μm	Smit, Hanekom, van Wieringen, et al. (2010)
	all	central	500	μm	
		P-Int 0	210	μm	
		P-Int 1	440	μm	
		P-Int 2	360	μm	
		P-Int 3	430	μm	
Number of Myelin sheaths (P/C)	healthy		40/80		Rattay, Lutter, et al. (2001)
	demyelinated		20/80		
Number of Myelin sheaths soma	all		3		
Specific membrane capacitance			1	$\mu F/cm^2$	
Intracellular resistivity			50	$\Omega \cdot cm$	
Sodium Reversal potential		all	66	mV	Rothman (2003)

Potassium potential	reversal	all	-88	mV	
Membrane Potential	Resting	all	-65	mV	Rattay, Lutter, et al. (2001)
Gating multiplicator	process	all	12		
Channel multiplicator	Density	all except soma	10		

2.1.3 Electrode Positions

Dimensions of the scala tympani were systematically reported by Hatsushika et al. (1990) and were found to be between 1 and 1.5 mm high and 1.5 to 2 mm wide on average. The stimulating electrode was represented as a sphere and given a diameter of 480 µm. Three different electrode positions matching those presented by Rattay, Lutter, et al. (2001) were used for this study: a 'high position', a 'mid position', and a 'low position' where the electrode was placed 200 µm, 500 µm, and 800 µm under the synaptic node compartment (P0), respectively. These three positions (shown in Fig. 2.2) represent an approximation of the possible positions that electrode arrays can take in the scala tympani. For all three positions, the electrode was always located at a fixed x-axis distance of 720 µm from the soma. This distance, as well as the y-axis positions, were assumed from Rattay, Lutter, et al. (2001) as they did not report them systematically. For this situation, it is assumed that tissues between the electrode and the SGN were of homogeneous conductivity.

2.1.4 Ionic currents and channel distribution

As shown in Chapter 1, SGNs, and neurons in general, are subjected to the complex mechanics of ionic channels to generate Action Potentials (APs). In the seminal work by Hodgkin and Huxley (1952), the two main types of ionic channels, i.e voltaged-gated high-threshold inactivating potassium (Kv) and fast activating sodium (Na), were modelled based on measurements from the generation of APs in the squid giant axon. This basic mod of activation and inactivation of ionic channels has been used and adapted to account for many features of SGN activity such as refractoriness and facilitation (Rattay, 1999; Rattay, Lutter, et al., 2001; Smit, Hanekom, van Wieringen, et al., 2010). However, some fundamental properties

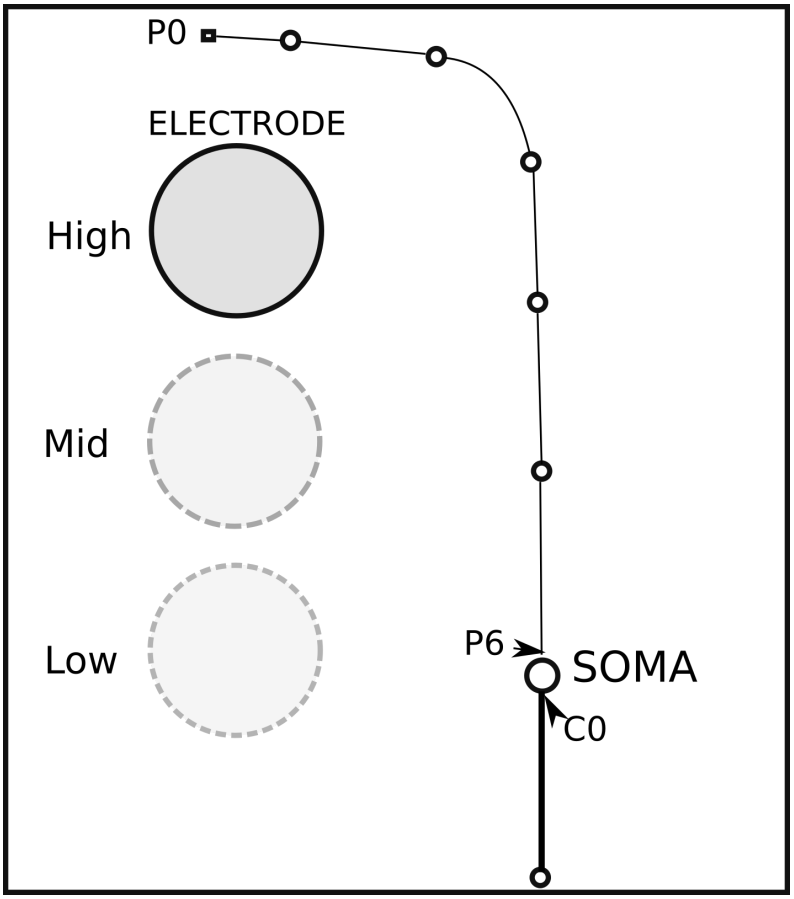

Figure 2.2: Position of a human primary auditory neuron relative to a round stimulating electrode. P0 indicates the first node of the peripheral process. P6 indicates the presomatic node compartment. C0 indicates the first node on the central process.

of SGN activity such as accommodation and adaptation cannot be accounted for by these channels alone. Several physiological studies of SGNs and other types of neurons, e.g. neurons in the Ventral Central Nucleus (VCN), have demonstrated the existence of additional channels - voltaged-gated delayed-rectifier potassium (KLT) and voltage-gated hyperpolarization-activated cation (HCN) channels - that account for adaptation and accommodation (Hossain et al., 2005; Adamson et al., 2002; Rothman, 2003). Recent studies by Boulet (2016) and Negm and Bruce (2014) have shown the benefits of including KLT and HCN ionic channels in addition to the usually modelled Kv and Na ionic channels, derived from the seminal work from Hodgkin and Huxley (1952). In general, addition of these channels to the models help to explain properties of spike-rate adaptation and accommodation which are observed *in vivo* but that weren't correctly modelled by previous ionic channel models (Zhang et al., 2007; Boulet, 2016; Negm and Bruce, 2014).

A recent study Boulet (2016) highlighted the effects of the different distributions of ionic channels distribution on a feline SGN compartment model, pursuing the efforts from the single node study by Negm and Bruce (2014). Based on these studies, similar distributions of the Kv, Na, KLT and HCN ionic channels in a more morphologically realistic model of the human SGN were implemented in this thesis.

From the validation that was performed for each ionic channel models (see Sec. 2.2), two distributions of ionic channels that will be used throughout this thesis are defined: the first distribution will only implement the Hodgkin-Huxley (HH) Na and Kv ionic channels equations, similarly to previously reported studies Rattay, Lutter, et al. (2001) and Rattay, Potrusil, et al. (2013) and will be called the **"HH"** distribution, where HH is the origin of the ion channel used; the second distribution, called **"HH+HCN+KLT"** will find KLT channels co-located with the HH channels, Na, Kv, and HCN channels placed in the first node as well as the pre and post somatic compartments. The ionic channel locations chosen for the "HH+HCN+KLT" distribution were based on previous studies (Boulet, 2016; Hossain et al., 2005; Adamson et al., 2002). A complete set of the equations to be solved for each compartment in the model is presented in Appendix 2.A.

Table 2.2: Summary of ionic channel distributions, This table presents the different specific conductances for each ion channel ($g_m bar$) where m is the type of ionic channel, e.g Na. The table indicates the conductance used for each distribution model (e.g HH or HH+HCN+KLT) and for which compartment of the cell.

Channel m	Model	Compartments	Specific Conductance g_{mbar} (S/cm^2)	Reference
Na	all models	all nodes except soma	1.32	Rattay, Potrusil, et al. (2013)
		Soma	0.132	
Kv	all models	all nodes except soma	0.3375	
		Soma	0.03375	
KLT	HH only	all nodes	0.0	Boulet (2016)
	HH+HCN+KLT only	all nodes except soma	0.013	
		Soma	0.0013	
HCN	HH only	all nodes	0.0	
	HH+HCN+KLT only	P0, P6, C0	0.013	
		Soma	0.0013	
Leak	all models	all nodes except Soma	0.003	Rattay, Lutter, et al. (2001)
		Soma	0.0003	

2.1.5 Stochasticity

The normal human SGN is naturally subject to stochastic noise that finds its source in small fluctuations in the SGN membrane potential. These fluctuations can be due to temperature-induced ionic channel activity, local ionic gradient generated by synaptic activity, or activity in neighbouring SGNs (Verveen and Derksen, 1968; Hales et al., 2004). This means that the modelling of the response of human SGNs in a more realistic way requires the incorporation of stochastic membrane fluctuations. However, literature shows how challenging it can be to represent correctly the noise element of mammalian SGNs (Boulet, 2016; Rattay, Lutter, et al., 2001; Frijns, De Snoo, et al., 1996; Badenhorst et al., 2016).

Because stochastic noise has been shown to depend on both the dendritic diameter and membrane potential of SGNs, Badenhorst et al. (2016) extended the technique

introduced in Rattay, Lutter, et al. (2001) that required the computation of an additional stochastic current injected at each node of Ranvier alongside with other ionic currents. Badenhorst et al. (2016) reported a multi-step method for the estimation of a voltage-dependent current noise injected in the active compartments of the modelled SGN.

In this study, I used a simplification of the technique proposed by Badenhorst et al. (2016) which injects a stochastic voltage-dependent noise current, proportional to the concentration of Na channels.

2.1.5.1 Firing Efficiency

When subjected to stochasticity, different ionic channel distributions are known to change the response properties of SGNs. Stochastic SGN responses are typically represented by a discharge probability function, also called a Firing Efficiency (FE) curve. FE curves encapsulate the ability of a SGN — with a specific set of morphological and physiological properties — to fire under different stimulation conditions. Each curve represents the probability of a spike(s) occuring in response to a given stimulus amplitude. For each stimulus condition and SGN model, a first-pass estimate of the deterministic threshold was found. Then, a 6 dB range around the deterministic threshold (± 3 dB) was divided in 40 intensities presenting 120 repetitions of the same stimulation level. Data were subsequently used to fit and estimate the two parameters (σ and θ) of equation Eq. 2.1:

$$FE = \frac{1}{2}(erf\left(\frac{x-\theta}{\sqrt{2}\sigma}\right)+1) \tag{2.1}$$

where x is the stimulation level, σ is the function spread, and θ represents the threshold, or 50% FE.

In this study, the Relative Spread (RS) was defined as $RS = \frac{\sigma}{\theta}$ in a similar way as in previous animal and modelling studies (Verveen and Derksen, 1968; Shepherd and Javel, 1997; Boulet, 2016; Badenhorst et al., 2016, 2017).

While σ and θ have been shown to vary with pulse width, the RS remains constant across the pulse widths ranging from 100 µs to 3 ms (Rubinstein, 1995; Verveen, 1962). In other words, regardless of the ionic model being simulated, RS remains constant for a fixed electrode position and a fixed pulse width (Badenhorst et al.,

2016, 2017).

2.1.5.2 Noise current term

From Badenhorst et al. (2016) the noise current term for the n node is represented as follows:

$$I_{noise,n} = GAUSS \cdot \frac{k_{fact} \cdot 10^{-8}}{\sqrt{A_n \cdot g_{Na}}} \tag{2.2}$$

where A_n is the node surface (in cm^3), g_{Na} is the specific Na channel concentration (in S/cm^3), k_{fact} is a constant and $GAUSS$ is a random Gaussian value between 0 and 1. The value 10^{-8} is included so that $k_{fact} > 1$ in all simulations.

Furthermore, Badenhorst et al. (2016) defined k_{fact} as:

$$k_{fact} = \frac{V_{RMS,n}}{m_{VK}} \tag{2.3}$$

where $V_{RMS,n}$ is the expected noise voltage for a specific node of Ranvier (n) and membrane potential level, and m_{VK} is voltage and diameter dependent.

To compute the V_{RMS} of a node as a function of membrane potential, Verveen and Derksen (1968) derived an equation based on measured data. Because this voltage RMS is node diameter dependent, I will call it $V_{RMS,0}$ with 0 indicating this RMS values related to the original node size from Verveen and Derksen (1968). It can be computed using:

$$V_{RMS,0} = 0.549e^{0.0137V_{mem}} \tag{2.4}$$

where V_{mem} is the neuron's membrane potential.

However, as the $V_{RMS,0}$ computed in Eq. 2.4 corresponds to the node size of the large neuron used by Verveen and Derksen (1968), it needs to be scaled for smaller neuron diameters. Following Badenhorst et al. (2016), $V_{RMS,0}$ was scaled to any compartment n diameter using:

$$V_{RMS,n} = V_{RMS,0} \times \frac{\sqrt{A_0}}{\sqrt{A_n}} \tag{2.5}$$

where A_0 is the node area from Verveen and Derksen (1968) and A_n being the area of the scaled compartment.

Badenhorst et al. (2016) also reported that the noise current derived from Eq. 2.2 was generally too small to produce the previously measured Dynamic Range (DR) from Shepherd and Javel (1997). For this reason, Badenhorst et al. (2016) further added a Scaling Factor (SF) to Eq. 2.2 in order to allow for greater noise to be injected, dependent on the SGN properties. The new noise current term can then be written as:

$$I_{noise,n} = GAUSS \cdot \frac{k_{fact} \cdot 10^{-8}}{\sqrt{A_n \cdot g_{Na}}} \cdot SF \tag{2.6}$$

where SF is model dependent.

2.1.5.3 Simplified Badenhorst et al. (2016) procedure

In the scope of this thesis, only one morphology will be used for the modelled SGN, therefore modelling only one axon diameter. One of the requirements from the Badenhorst et al. (2016) procedure was to first compute a m_{vk} gradient that would allow to derive the k_{fact} value for any neuron diameter. Because this is not needed in the present case, a simplified procedure that only computes the m_{vk} value corresponding to this thesis' SGN morphology is proposed.

This simplified procedure uses the same steps as reported by Badenhorst et al. (2016):

1. Only once
    a) Calculate the expected reference V_{RMS}, or $V_{RMS,0}$, at a SGN's Resting Membrane Potential (RMP) using Eq. 2.4
    b) Calculate the V_{RMS} scaled to the compartment n size, i.e. $V_{RMS,n}$, with compartment n area A_n using Eq. 2.5
    c) Empirically find the k_{fact} value with model simulations for which the compartment's measured V_{RMS}, or simulated $V_{RMS,n}$, at RMP (here $-65\,\text{mV}$) equals the $V_{RMS,n}$ derived in step b)
    d) Derive m_{vk} from Eq. 2.3 with the k_{fact} value from step c) and $V_{RMS,n}$ from step b)
2. Every time step

a) Compute k_{fact} using Eq. 2.3 with the desired $V_{RMS,n}$ from Eq. 2.4 and Eq. 2.5 at the membrane potential V_{mem} for this time step and for each nodal compartment n.

b) Use Eq. 2.6 to evaluate the noise current term for this time step

2.1.6 AP detection and location

Precise and robust detection of APs and their initiation site is key to studying the effects of cell physiology on the extracellularly stimulated SGN. Usually, single-spike detection can be achieved by tracking the threshold crossing of the SGN's membrane potential. However, this technique can come short in more complex situations, e.g pulse-train stimulation where shifts in membrane potential over time can make threshold-crossing detection non-trivial — due to the fluctuations in membrane potential. When subjected to repetitive stimulation, the membrane potential of SGNs will be variable, making difficult to detect APs and measure spike initiation timing precisely.

A more robust marker of the firing of SGNs can be found in the gating of Na currents, combining the activating and inactivating properties of the ionic channel. These currents are the main driving force of APs and can be used to determine spike firing time robustly. In this thesis, a technique based on this principle that was previously presented by Boulet (2016) was implemented, using the m^3h gating product to detect the initiation of an AP. Fig. 2.3 represents a typical m^3h probability plotted as a function of time. The orange trace in the left panel plots the development of m^3h as a function of time, and how a successful AP can be detected from it when compared to an unsuccessful stimulation (blue trace). From the orange trace, one can measure the duration of the gating time relative to the m^3h product, called λ, that is necessary for generation of an AP. Further, this λ value can be computed for a range of stimulus parameters, covering the various possibilities of λs that would relate to successful AP generation. Here, 20 repetitions were simulated over 200 intensity steps between 0 and 1000 µA to establish the distribution of λ for each of the two models, i.e "HH" and "HH+HCN+KLT". Finally, the range of λ values was clustered to find the shortest λ value from the highest mean cluster which indicates a precise estimation of the minimum λ value, or threshold λ, required

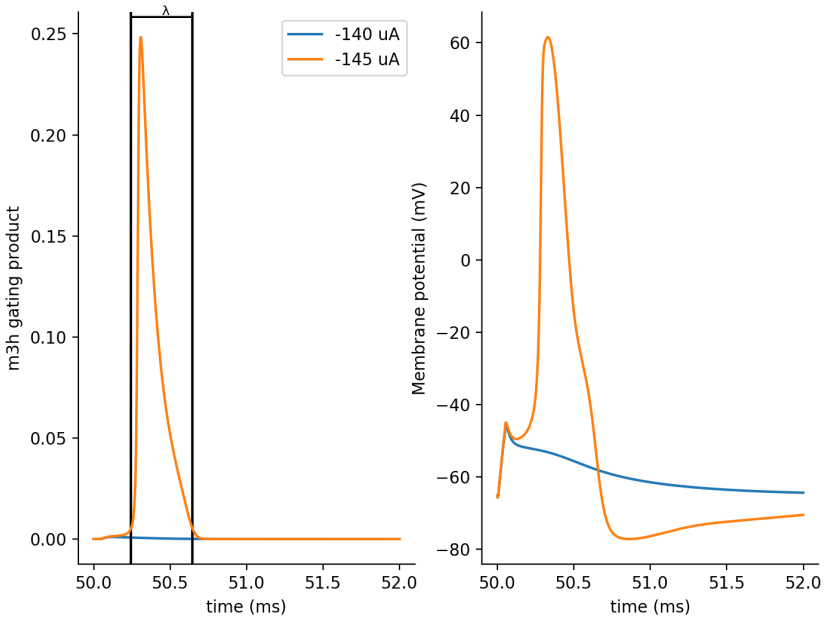

Figure 2.3: Spike-detection from Na gating. Left panel shows the m^3h gating product for the Na ionic channels plotted as a function of time. Right panel shows the membrane potential plotted as a function of time. The orange trace indicates a successful AP and the blue trace indicates a below threshold stimulation. Traces were obtained presenting a monophasic cathodic stimulus at an amplitude of 140 µA and 145 µA,for the unsuccessful and successful simulations respectively.

for an AP to be elicited. Using this minimal λ value, APs were then detected by determining wether the λ value of a stimulated SGN was above or below the threshold λ value. The m^3h product technique proved to be a robust marker for AP as it typically remains stable with varying membrane potential (Boulet, 2016).

2.1.7 Software and computing ressources

The software was programmed in Python 3.6 and uses the NEURON Yale library (Hines and Carnevale, 2003). The step size for the computations in NEURON was set to be 1 µs. The solver followed the Crank-Nicholson Exponential technique as implemented by the NEURON software to compute the membrane current and potential at each iteration. This thesis was undertaken with the assistance of

resources and services from the National Computational Infrastructure (NCI), which is supported by the Australian Government.

2.2 Model validation

In order to validate the new model implementation, simulations were performed to compare results reported in previous computational (Rattay, Lutter, et al., 2001; Rattay, Potrusil, et al., 2013; Badenhorst et al., 2016; Boulet, 2016) or animal studies (Zhang et al., 2007; Shepherd and Javel, 1997).

In this section, the aim is to validate two elements of the model: 1) the set of equations for Na and Kv ionic channel from Rothman (2003) with equations adapted from the original HH equations for VCN channel kinetics, and the original HH equations for Na and Kv used by Rattay, Lutter, et al. (2001) can be interchanged for a SGN model without unreasonable difference in the output predictions; 2) the inclusion of the HCN and KLT channels using the equations from Rothman (2003) does induce extra and meaningful spike-rate adaptation.

First, to validate the equations for Na and Kv channels, single pulse FE curves were simulated at the three electrode positions for the two sets of Na and Kv equations mentioned previously: the original HH equations as described in Rattay, Lutter, et al. (2001) were used as control; and the equations from Rothman (2003) were used as a test condition. The same conductances and morphological parameters, as described in Table 2.1 and Table 2.2, were used for both sets of equations. Temperature factors for the original HH equations were set to the values introduced in Rattay, Lutter, et al. (2001) (warmed to 29 °C), while the Rothman (2003) equations were warmed up from 22 to 37 °C to account for kinetic shifts between VCN and SGN ionic channels. This difference in temperature shift comes from the nature of the ionic channel equations kinetics that were introduced for SGN modelling by Rattay, Lutter, et al. (2001) and VCN modelling by Rothman (2003). Essentially, the Rattay, Lutter, et al. (2001) ionic channels kinetics were already adapted for SGN simulations while the kinetics of the Rothman (2003) needed to be increased because of the slower nature of VCNs.

The model was stimulated using monophasic pulses with 100 µs phase duration for both anodic and cathodic polarities to match the Rattay, Lutter, et al. (2001)

study. The results of the model using both sets of equations and the noise term described in Sec. 2.1.5 are compared to determine whether or not the equations of Rothman (2003) constitute a valid alternative to the original HH equations previously employed by Rattay, Lutter, et al. (2001), Rattay, Potrusil, et al. (2013), and Smit, Hanekom, van Wieringen, et al. (2010).

Second, the Rothman (2003) equations for KLT and HCN channels were added to the now validated set of Na and Kv channels equations from Rothman (2003) in order for the model to simulate increased spike-rate adaptation. The addition of the KLT and HCN created a need for validation of greater spike-rate adaptation in their presence. Three model configurations were tested for this validation: the "HH" model with the ionic conductances from Rattay, Lutter, et al. (2001) as a control for the limited adaptation case; the "HH+HCN+KLT" model using HCN and KLT concentrations from Boulet (2016) to test the hypothesis that additional KLT and HCN channels can induce additional spike-rate adaptation; and, the "HH+HCN+KLT" model with strong, i.e. a 4-fold, concentration increase to control for conductance parameters that would induce "over-adaptation", i.e. effectively shutting down AP activity. Because adaptation is most meaningful at the site of excitation of APs, but also to reduce stimulus interactions (and to compare with previous studies), models were stimulated with the cell placed in a straight line configuration, presenting pulse trains at two intensity levels, and using three different pulse-rates. The latest allowing to evaluate Post-Stimulus Time Histograms (PSTHs) responses and establish the presence of spike-rate adaptation.

All validations in this chapter were performed using the healthy SGN morphology in a bent configuration for the single-pulse responses and in a straight configuration for the purposes of validating the effects of adaptation.

2.2.1 Noise current and Scaling Factor (SF) value

Prior to characterising the simulated SGN responses, the model-specific SF value to be used in Eq. 2.6 had to be defined in order to provide the desired amount of noise. As mentioned in Sec. 2.1.5.1, the RS of a FE response, defined as $RS = \frac{\sigma}{\theta}$, will be used to quantify the right amount of noise (Badenhorst et al., 2016; Boulet, 2016). From previous animal and computational models, it appears that a realistic

RS value would range between 0.02 and 0.04 (Shepherd and Javel, 1997; Badenhorst et al., 2016, 2017; Verveen and Derksen, 1968).

The ionic-model specific SF values were found by linear interpolation of RS from simulations of each ionic model using a range of empirical SF values (2.0, 4.0 and 6.0). Fig. 2.4 shows an example of the FE curves for 100 µs biphasic, cathodic-first stimulus at a high (200 µm) electrode position for the "HH" model.

In order to produce the desired RS for the two simulated models, i.e. the "HH" and "HH+HCN+KLT" models, SFs of 3.0 and 6.0 were interpolated for the "HH" and "HH+HCN+KLT" models, respectively. The necessary SF value for the "HH+HCN+KLT" model was predicted to be higher than for the "HH" model: because the "HH+HCN+KLT" model incorporates additional ionic channels that aim to maintain the RMP, thresholds are predicted to increase. As a result, with an increased threshold (θ) the ratio $RS = \frac{\sigma}{\theta}$ indicates that a greater spread (σ) and thus a greater level of noise would be needed to preserve a constant RS. This is achieved by increasing the SF between 3.0 and 6.0 for the "HH+HCN+KLT" model. These healthy SGN benchmarked SF values will be applied to all subsequent versions of the "HH" and "HH+HCN+KLT" models as it is assumed that the noise mechanisms are independent of neural degeneration and electrode placement (Rattay, Lutter, et al., 2001; Badenhorst et al., 2016, 2017).

2.2.2 Single pulse response

Fig. 2.5 shows responses from the two sets of equations that both represent the "HH" model presented earlier: 1) the original equations for the Na and Kv ionic channels from Rattay, Lutter, et al. (2001) and derived from Hodgkin and Huxley (1952) that will be used as control the "Rattay" condition; 2) the Rothman (2003) equations for Na and Kv ionic channels the "Rothman" condition. For both conditions, the morphology was implemented to mimic Rattay, Lutter, et al. (2001), using the internodal lengths from Smit, Hanekom, van Wieringen, et al. (2010) as explained in Sec. 2.1.1. All parameters are summarized in Table 2.1 and Table 2.2.

In order to validate the two sets of equations for the "HH" model, simulations using 100 µs monophasic, cathodic and anodic, single-pulse stimuli were conducted using either sets of equations. The equations were considered to be validated if the

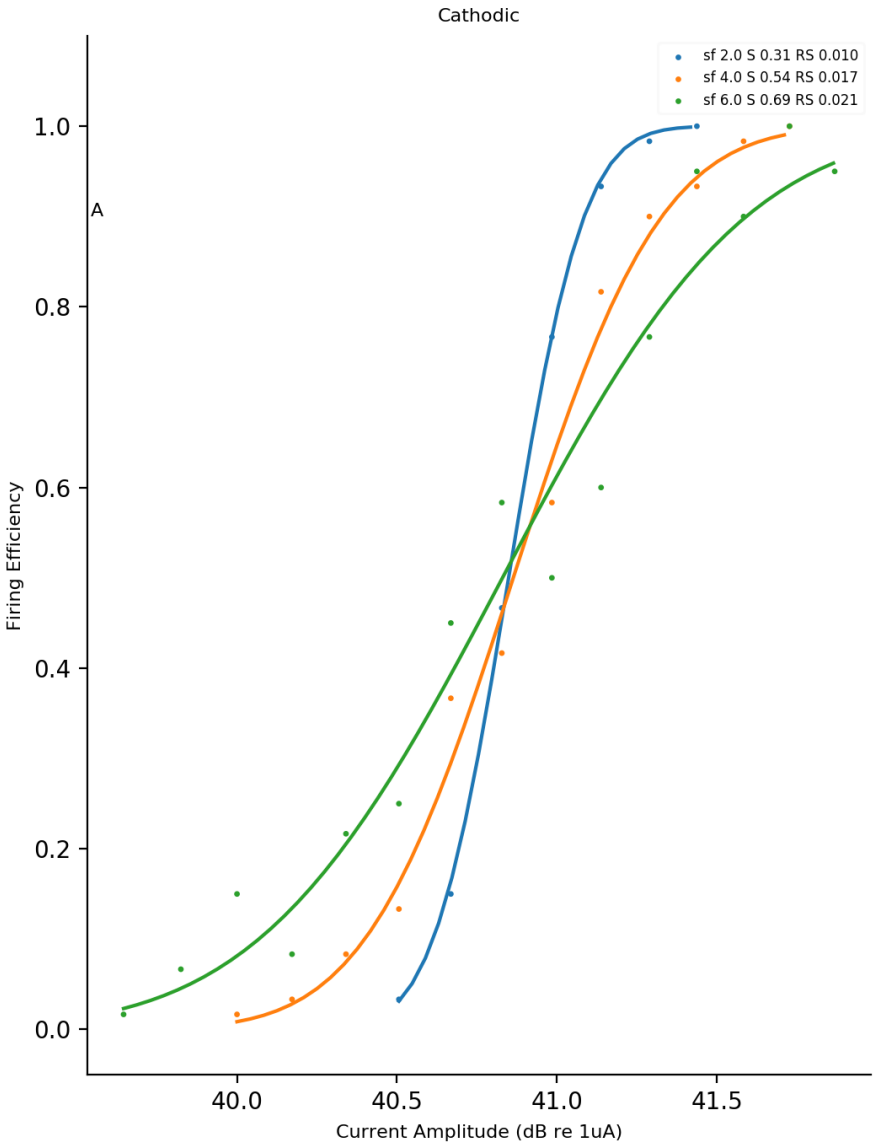

Figure 2.4: FE curves in response to 100 µs cathodic-first single biphasic pulse for different SF coefficients using the "HH+HCN+KLT" model. Each curve represents the response for a specific SF value. A 6.0 SF value was interpolated for this example generating the 0.02 RS value.

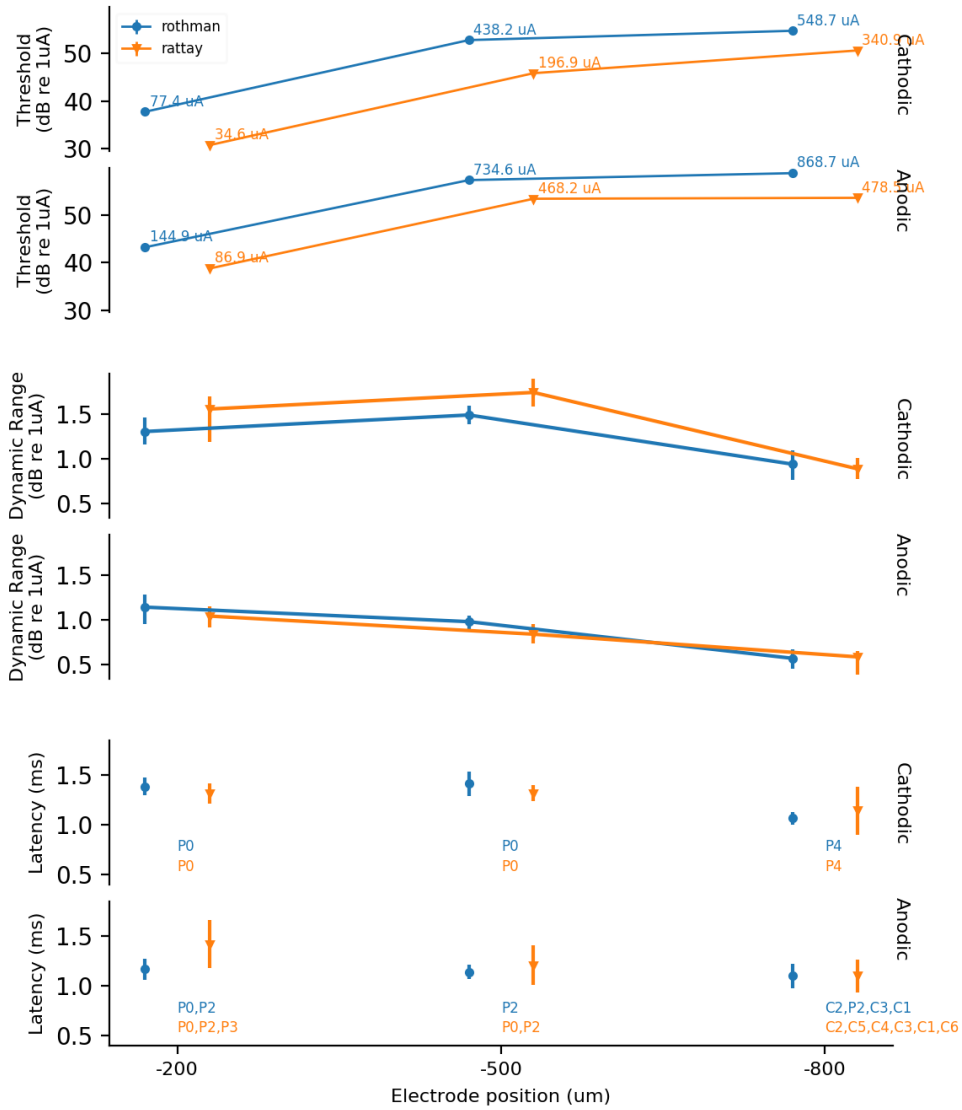

Figure 2.5: Validation of Na and Kv ionic channels using the "warmed" HH equations from Rattay, Lutter, et al. (2001) compared to the equations from Rothman (2003) shifted to 37 °C. Top panels show the modelled thresholds (50% FE) for the three electrode positions to cathodic and anodic for monophasic pulse shapes (100 µs pulse width). Error bars for the Threshold and DR panels indicate the confidence interval of the measured value when randomly bootstrapped over 300 iterations. The error bars on the latency panel indicate 1 standard deviation interval from the set of latencies collected.

thresholds from Rattay, Lutter, et al. (2001) were a close match and if the measured DR corresponds with Rattay, Lutter, et al. (2001) and in the range of mammalian DRs reported in Shepherd and Javel (1997).

First, the top panel of Fig. 2.5 shows the thresholds for the two sets of equations at the three specified electrode positions, where thresholds are defined as the 50% point on the measured FE curve for each model at each electrode position and stimulus polarity. Confidence intervals for both thresholds and DRs were calculated through random data bootstrapping over 300 iterations. The confidence intervals are depicted with error bars in Fig. 2.5.

For cathodic pulses, 34.6 µA, 196.9 µA and 340.9 µA thresholds were measured for the "HH" model using the control "Rattay" equations at 200 µm, 500 µm and 800 µm electrode positions, respectively. The "HH" model using the "Rothman" equations showed slightly higher thresholds with 77.5 µA, 438.4 µA, and 548.5 µA at 200 µm, 500 µm and 800 µm electrode positions, respectively. This can be compared with the thresholds reported by Rattay, Lutter, et al. (2001) where, in the cathodic case, 60 µA, 260 µA and 540 µA thresholds were measured at distances (from the electrode) of 200 µm, 500 µm and 800 µm, respectively.

Similarly, in the anodic case, 86.9 µA, 468.2 µA, and 478.5 µA thresholds were measured for the "Rattay" equations at 200 µm, 500 µm and 800 µm electrode positions, respectively. The "Rothman" equations showed higher thresholds again, with 144.9 µA, 734.5 µA, and 869.0 µA at 200 µm, 500 µm, and 800 µm electrode positions, respectively. This can be compared with the thresholds reported by Rattay, Lutter, et al. (2001) where, in the anodic case, 130 µA, 720 µA and 780 µA thresholds were measured at distances of 200 µm, 500 µm and 800 µm respectively.

Another aspect that requires comparison between the two models is the ratio between anodic and cathodic thresholds. Rattay, Lutter, et al. (2001) reported ratios of 2.17, 2.70 and 1.44 for 200 µm, 500 µm and 800 µm respectively. In this study, the ratios were 1.87, 1.67 and 1.58 for the "Rothman" equations, and 2.52, 2.38 and 1.40 for the "Rattay" equations for 200 µm, 500 µm and 800 µm, respectively. The observed differences in threshold ratios are explained by small implementation differences, e.g morphology parameters and gating dynamics differences between the "Rattay" and "Rothman" equations for ionic channels.

Second, the mid panel of Fig. 2.5 shows the change in DR with electrode position

and stimulus polarity. Shepherd and Javel (1997) and Javel and Viemeister (2000) reported SGN DRs in cat in the range 0.79 to 4 dB. Here, the measured DR varied across conditions but was confined to the range 0.8 to 1.8 dB. It was noted in Javel and Viemeister (2000) that, although DRs between 1 dB and 4 dB are common in electrical stimulation, they are much smaller than those to acoustic stimulation, which often span 15 to 30 dB at a neuron's Characteristic Frequency (CF).

Furthermore, the bottom panel of Fig. 2.5 shows the latency, variance and electrode position as a function of electrode position and stimulus polarity. Latencies ranged from 1.0 to 1.5 ms, and were systematically shorter for centrally elicited APs, i.e. time between pulses and spikes at node of Ranvier 'C14' were shorter for central sites of excitation. Although latencies weren't systematically reported by Rattay, Lutter, et al. (2001), the data here match closely previously reported values, with latencies in the range 1.0 to 1.5 ms close to threshold.

Finally, sites of excitations did match the previously reported data from Rattay, Lutter, et al. (2001): in the cathodic condition, all sites of excitation were peripheral to the soma for both the "Rattay" and "Rothman" sets of equations. However, more variability was observed in the "Rattay" condition, specifically at low electrode positions, with the site of excitation jumping between P2 and P4, while they were fixed at P4 in the "Rothman" condition. This trend was also noticed in the anodic conditions, where the "Rattay" equations systematically showed greater variability in site at which excitation was generated, compared to the "Rothman" equations. In this regard, the "Rothman" equations are more consistent with previous reports from Rattay, Lutter, et al. (2001) than my implementation of the "Rattay" equations.

Although the thresholds and anodic-versus-cathodic ratios are not perfectly matching with Rattay, Lutter, et al. (2001), the two models presented here closely mimic the behaviour reported in previous studies. While the "Rattay" equations showed the closest match in ratios with the presented morphology when compared to Rattay, Lutter, et al. (2001), the thresholds from the "Rothman" equations were closer. In addition to the thresholds, both DRs and latencies were in the range reported previously (Javel and Viemeister, 2000; Shepherd and Javel, 1997; Rattay, Lutter, et al., 2001).

The mismatches observed can be explained by multiple factors:

1. because of the lack of systematic report of morphology parameters in Rattay, Lutter, et al. (2001), the morphology parameters employed in this thesis were taken from Smit, Hanekom, van Wieringen, et al. (2010). Those might have been slightly different from the values initially used in Rattay, Lutter, et al. (2001). This could explain differences in thresholds and latencies as interactions and AP travelling time will be different;

2. the spatial precision in the model presented here was considerably increased when compared to Rattay, Lutter, et al. (2001), as extracellular potentials in that study were computed at the center of each compartment, whilst here the compartments were subdivided into 11 segments effectively increasing spatial precision by 11-fold;

3. the computational solver time-step was reduced from 2.5 µs to 1 µs;

4. a narrow dynamic range of approximatively 1 dB was measured for a specific SF value used to compute the noise current term. The SF, being a model specific parameter, was chosen to achieve a 0.02 RS value. However, SF could be increased to yield greater RS and DR values.

To summarize:

1. Cathodic and anodic thresholds were in the range of previously reported studied (Rattay, Lutter, et al., 2001; Rattay, Potrusil, et al., 2013; Frijns, de Snoo, et al., 1995; Javel and Viemeister, 2000).

2. Cathodic thresholds were systematically lower than anodic thresholds, similar to Rattay, Lutter, et al. (2001).

3. DRs were found to be relatively narrow, but still in the range reported by previous studies *in vivo* and computational studies (Rattay, Lutter, et al., 2001; Badenhorst et al., 2017; Javel and Viemeister, 2000; Shepherd and Javel, 1997).

4. Latencies, measured as the timing difference between stimulus onset and AP onset in compartment C14, had similar qualitative and quantitative behaviours for both models. All latencies are contained in the range 0.5-1.1 ms which is in

line with previous reports such as Rattay, Lutter, et al. (2001) and Badenhorst et al. (2017).

2.2.3 Spike-rate adaptation

The rationale behind the inclusion of KLT and HCN ionic channels in the model presented in this thesis was to introduce features of spike-rate adaptation into the SGN response. To validate the presence of spike-rate adaptation, pulse train responses were stimulated at two intensity levels, 50% FE and 80% FE, on a straight cell, to replicate more closely the previously reported studies of Boulet (2016) and Zhang et al. (2007). Three conditions were simulated for this validation: the previously introduced "HH" and "HH+HCN+KLT", as well as a *strong* adaptor concentration condition in which the KLT and HCN conductances were increased 4-fold. The rationale for using the *strong* adaptor conductances is to compare the "HH+HCN+KLT" model with normal conductances with an over-adapting condition. Doing so helps to validate the "classification" of the spike-rate adaptation implementation proposed here, i.e. differentiate the proposed model between a "strong" or "weak" adaptor model.

Using wide bins, PSTH were fitted to single-exponential functions to quantify the modelled adaptation as first described in Zhang et al. (2007). Quality of fits was assessed by computing the R^2 value: the single-exponential function (Eq. 2.7) systematically was more effective at fitting the data than the double-exponential function. Thus, subsequent references to the R^2 value will be with regard to the single-exponential function fit.

$$s(t) = A_{ss} + A_{dec} \cdot e^{-t/\tau_{adapt}} \tag{2.7}$$

where t was evaluated at the centre of the wide-bin intervals (Zhang et al., 2007).

PSTHs were evaluated for: 1) small bin widths of 1 ms employed for visual interpretation, and 2) variable-width bins defined by the intervals 0–4 ms, 4–12 ms, 12–24 ms, 24–36 ms, 36–48 ms, 48–100 ms, 100–200 ms, and 200–300 ms (Zhang et al., 2007).

The Normalized spike rate decrement (NSRD), was calculated as the difference between the response rate evoked in the intervals 0–12 ms and 200–300 ms, and

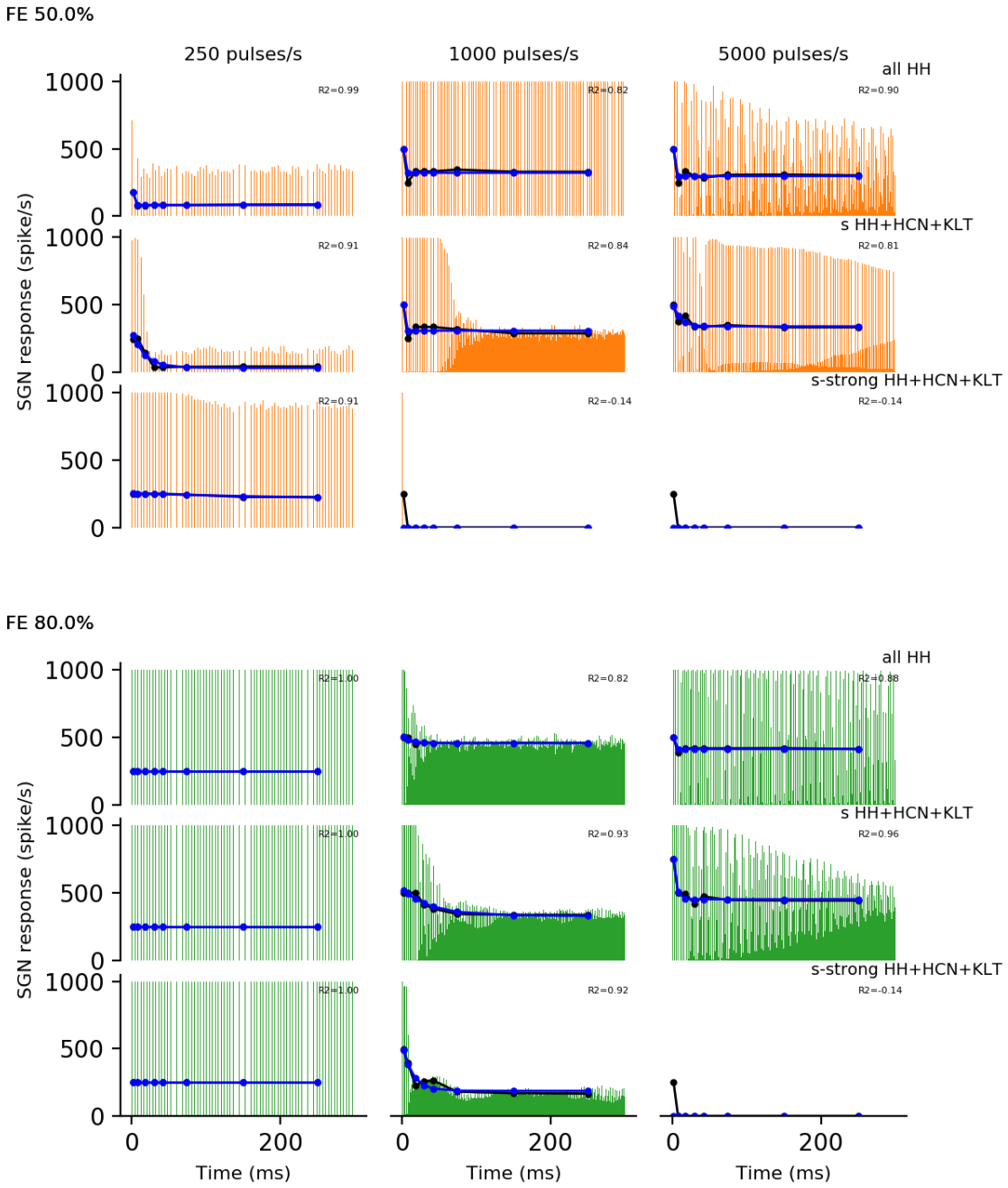

Figure 2.6: PSTH of the simulated healthy SGN response to 300 ms pulse trains at 250, 1000 and 5000 pulses/s for the two ionic channel models described in Sec. 2.1.4, "HH+HCN+KLT" having the additional "strong" set of conductances. Top panel represents 50% FE intensity and bottom panel shows 80% FE simulations.

then divided by the response rate during the 0–12 ms interval (Zhang et al., 2007), resulting in values between 0 (no adaptation) and 1 (fully adapted).

In total, 15 out of the 18 PSTH responses presented in Fig. 2.6 showed response fits with R^2 values above 0.81, meaning the fits were well fitted. The three remaining fits gave negative R^2 values due to the lack of activity of the SGN in that condition. Overall, the fits for the PSTH responses were between good and exact, with the exception of responses with no, or very low, activity. The top panel in Fig. 2.6 shows responses to 50% FE, whilst the bottom panel shows responses to 80% FE intensity. "HH" simulations at higher pulse rates showed little spike-rate adaptation, most likely due to the onset effect of the pulse train and Relative Refractory Period (RRP) effects. Although this was observed for both intensities examined, spike-rate adaptation was lower for the higher-intensity stimulation intensity in the "HH" model. This is in accordance with Boulet (2016) who reported only little spike-rate adaptation for models without HCN and KLT channels.

In comparison, the "HH+HCN+KLT", as well as its *strong* version, showed the predicted stronger effects of spike-rate adaptation at pulse rates of 1000 and 5000 pulses/s.

In addition, spike-rate adaptation increased in the *strong* model, to the extent that spiking activity beyond the initial spiking was completely blocked in some conditions.

Although for this thesis the set of KLT and HCN concentrations that was defined as normal was preferred—in order to generate a relatively high rate of activity—it is interesting to note that the *strong* conductances for the "HH+HCN+KLT" model could be used as a model of spike-rate adaptation blocking.

The τ_{adapt} and NSRD values were used to quantify the spike-rate adaptation created by the different models. Fig. 2.7 shows the τ_{adapt} and NSRD from the responses previously shown in Fig. 2.6. NSRDs ranged from 0 to 0.85, except for the *strong* model where NSRDs values of 1 were found in response to 1000 and 5000 pps for stimulation at both 50% and 80% FE. NSRDs for the "HH+HCN+KLT" were systematically higher than those of the "HH" model, consistent with the fact that the additional ionic channels increased spike-rate adaptation. In their study, Zhang et al. (2007) classified the SGNs according to the measured amount of spike-rate adaptation at 5000 pps: NSRD above 0.9 would mean strong adaptation,

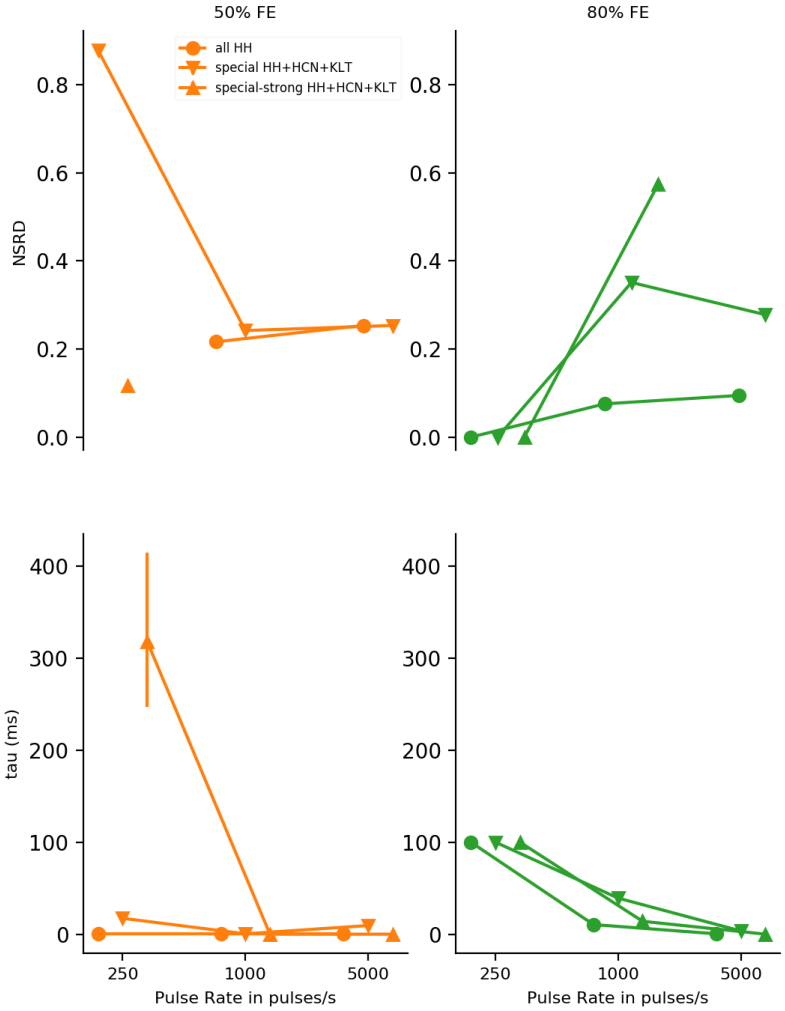

Figure 2.7: τ_{adapt} and NSRD of the modelled SGN response to 300 ms pulse trains at 250, 1000 and 5000 pulses/s for the three ionic channel models described in Sec. 2.1.4. Top panel shows the NSRD responses and bottom panel shows τ_{adapt} values as a function of pulse rate. The orange color codes for 50% FE simulations and green color codes for 80% FE.

whilst values in range from 0.25 to 0.9, would be considered weak adaptors. In this thesis, and according to the adaptor classification of Zhang et al. (2007), the "HH+HCN+KLT" at 5000 pps generated a NSRD of 0.3, classifying the modelled SGN as only weakly adapting.

In addition, τ_{adapt} values for all models ranged between 0 ms and 150 ms, except for the *strong* model at 50% FE and 250 pps condition which showed a much larger value (around 300 ms). Zhang et al. (2007) reported for the single-exponential model fits that τ_{adapt} had a mean of 74.6 ms with Standard Deviation (SD) of 44.8 ms at 250 pps, a mean of 49.9 ms ($\pm$ 39.9 ms) at 1000 pps, and a mean of 40.0 ms ($\pm$ 32.2 ms) at 5000 pps. With values confined to the range 5 to 140 ms across conditions, the τ_{adapt} values for the "HH+HCN+KLT" are within the range reported *in vivo* in animal studies, indicating that the model correctly encapsulates some dimension of spike-rate adaptation.

In summary, it was demonstrated that:

1. Models containing HCN and KLT channels show increased spike-rate adaptation (Negm and Bruce, 2014; Boulet, 2016).

2. The "HH+HCN+KLT" condition is consistently more adapted than the "HH" model (Boulet, 2016).

3. NSRD and τ_{adapt} in the model presented here are comparable to those of animal data reported by Zhang et al. (2007).

2.3 Conclusions

This chapter presented the general methods employed in this thesis to model responses of SGNs to electrical stimulation. An implementation of the human SGN model was defined and validated against previous animal and computational models. The model successfully demonstrated both stochastic and spike-rate adaptation features. The two configurations of the "HH+HCN+KLT" models that included additional ions channels, i.e. normal and strong conductances, demonstrated mild and very strong adaptation levels respectively. Based on these outcomes, two ionic channel distributions will be employed throughout the rest of the thesis: the "HH"

model with all nodes containing Na and Kv channels, which will serve as a control model, and the "HH+HCN+KLT" model with KLT channels co-located with Kv and additional HCN channels in the post-synaptic as well as pre- and post-somatic nodes of Ranvier. The normal conductances were preferred over the strong conductances as the *strong* configuration shows over-adaptating responses, effectively reducing the amount of data available in terms of spiking activity.

Both models were validated against previous animal and modelling studies, and were found to be constistent with these.

Appendix

2.A Ionic channels equations

$$C_m \frac{dV}{dt} = i_{leak} + i_{Na} + i_{Kv} + i_{KLT} + i_h + I_{noise} \tag{2.8}$$

2.A.1 Sodium channels

$$i_{Na} = g_{Nabar} m^3 h (E_{Na} - V) \tag{2.9}$$

$$\frac{dm}{dt} = \alpha_m (1 - m) - \beta_m m \tag{2.10}$$

$$\frac{dh}{dt} = \alpha_h (1 - h) - \beta_h h \tag{2.11}$$

$$\alpha_m = \frac{-0.1(V + 40)}{\exp(\frac{-(V+40)}{10} - 1)} \tag{2.12}$$

$$\beta_m = 4 \exp(\frac{-(V + 65)}{18}) \tag{2.13}$$

$$\alpha_h = 0.07 \exp(\frac{-(V + 65)}{20}) \tag{2.14}$$

$$\beta_h = \frac{1}{\exp(\frac{-(V+35)}{10}) + 1} \tag{2.15}$$

2.A.2 High-threshold potassium channels

$$i_{Kv} = g_{kbar} n^4 (E_{Kv} - V) \tag{2.16}$$

$$\frac{dn}{dt} = \alpha_n (1 - n) - \beta_n n \tag{2.17}$$

$$\alpha_n = \frac{-0.01(V+55)}{\exp(\frac{-(V+55)}{10}) - 1} \tag{2.18}$$

$$\beta_n = 0.125 \exp(\frac{-(V+65)}{80}) \tag{2.19}$$

2.A.3 Hyperpolarised-cation channels

$$i_h = g_{hbar} r (E_h - V) \tag{2.20}$$

$$\frac{dr}{dt} = \frac{r_\infty - r}{r_\tau} \tag{2.21}$$

$$r_\infty = \frac{1}{1 + \exp(\frac{V+76}{7})} \tag{2.22}$$

$$r_\tau = \frac{100000}{237 \exp(\frac{V+60}{12}) + 17 \exp(\frac{-(V+60)}{14}) + 25} \tag{2.23}$$

2.A.4 Low threshold potassium channels

$$i_{KLT} = g_{KLTbar} w^4 z (E_K - V) \tag{2.24}$$

$$\frac{dw}{dt} = \frac{w_\infty - w}{w_\tau} \tag{2.25}$$

$$\frac{dz}{dt} = \frac{z_\infty - z}{z_\tau} \tag{2.26}$$

$$w_\infty = \frac{1}{(1 + \exp(\frac{-(V+48)}{6}))^{0.25}} \tag{2.27}$$

$$z_\infty = z_{ss} + \frac{1. - z_{ss}}{1 + \exp(\frac{V+71}{10})} \tag{2.28}$$

$$w_\tau = \frac{100}{6 \exp(\frac{V+60}{6}) + 16 \exp(\frac{-(V+60)}{45}) + 1.5} \tag{2.29}$$

$$z_\tau = \frac{1000}{\exp(\frac{V+60}{20}) + \exp(\frac{-(V+60)}{8})} + 50 \tag{2.30}$$

3 Modelling the physiology of a single, healthy Spiral Ganglion Neuron (SGN)

3.1 Introduction

Compartment models of the SGN have been successfully used to study the impact of extracellular electrical stimulation generated by Cochlear Implants (CIs) (Rattay, Lutter, et al., 2001; Rattay, Potrusil, et al., 2013; Frijns, de Snoo, et al., 1995; Briaire and J. H. Frijns, 2006; Boulet, 2016; Hanekom, 2001; Malherbe et al., 2016; Smit, Hanekom, van Wieringen, et al., 2010; Negm and Bruce, 2014; Badenhorst et al., 2016). Such models are key in understanding the behaviour of the Auditory Nerve (AN) when subjected to an electrical stimulus. Physiological models aim to study the behaviour of SGNs at a higher level of complexity than single-compartment models, and these models are therefore mostly multi-compartment cable-equation models, equipped with features of ionic channel developed from single-node models (Frijns, Mooij, et al., 1994; Rattay, Lutter, et al., 2001; Hanekom, 2001; Boulet, 2016). In comparison to single-node models, the more complex compartment models of SGNs can be used to study how SGNs behave when subjected to an electrical stimulus in various morphological or spatial situations (Frijns, de Snoo, et al., 1995; Rattay, Lutter, et al., 2001; Hanekom, 2001; O'Brien, 2016; Boulet, 2016).

Compartment models have been extensively used to model the electrical stimulation of nerves by subjecting the compartments to a range of electrical stimuli. With each compartment behaving according to Kirchoff's law, the complex system can be simplified into solvable electrical equations. Compartments are used to simplify the complexity of structural models that involve varying shapes or physical attributes such as mechanical or electrical properties. For SGNs, the use of compartment models is useful as it allows for simplification of a complex electrical and structural model into simple elements. Each node of Ranvier and internode, becomes a compartment with its own electrical properties. The elements of the SGN can also

be considered as sections in which each section of the SGN can be represented by one or more segments. The number of segments depends on the morphological and electrical properties of the section being modelled as well as the numerical precision required for that section. For example, Boulet (2016) subdivided the soma of the modelled cat SGN into 9 segments for greater precision. This is particularly relevant as its larger diameter, and its central role in the transport of Action Potentials (APs), makes it an important part of the SGN, where great numerical precision could be significant to achieve good accuracy. In this thesis, sections consisted of 11 segments for the nodes of Ranvier and internodes and 51 for the soma, ensuring an accurate level of spatial specificity.

Healthy SGN models are composed of a peripheral and central axon separated by the soma (Frijns, de Snoo, et al., 1995; Rattay, Lutter, et al., 2001; Hanekom, 2001; Smit, Hanekom, van Wieringen, et al., 2010; Boulet, 2016). Previous models of healthy SGNs have been used to explain some aspects of refractoriness and polarity effects observed in human CI users (Frijns, de Snoo, et al., 1995; Rattay, Lutter, et al., 2001; Hanekom, 2001). However, those models have been unsuccessful at explaining other effects of electrical stimulation, including: accommodation, facilitation, and spike-rate adaptation.

Rothman (2003) and Negm and Bruce (2014) found evidence that such effects could be in part explained by the presence of two ionic channel types voltaged-gated delayed-rectifier potassium (KLT) and voltage-gated hyperpolarization-activated cation (HCN), not represented by the Hodgkin-Huxley (HH) or Generalised Schwarz Eikhof Frijns (GSEF) equations often used to model SGNs (Frijns, de Snoo, et al., 1995; Rattay, Lutter, et al., 2001; Hanekom, 2001). Instead, those sets of equations use a single type of sodium activation, fast activating sodium (Na), and a single type of potassium inactivation, voltaged-gated high-threshold inactivating potassium (Kv), ionic channels. Because the KLT and HCN ionic channels are thought to change thresholds levels dynamically, and overall sustain responses when a SGN is subjected to trains of electrical pulses, they are closely related to the phenomenon of refractoriness, accommodation, spike-rate adaptation and facilitation. Moreover, the compartment model developed by Negm and Bruce (2014) using modified equations from Rothman (2003) already demonstrated some features of spike-rate adaptation and facilitation.

Perceptual and listening performance by CI users remains highly variable and the reasons for this variability are still to be explained. At least one explanation of this variability is attributed to parameters such as the health of SGNs, the position of electrode contacts relative to the SGN population, current spread within the cochlea, and factors related to the CI device itself, including the shape and rate of electrical pulses, and specifics of the stimulation strategy employed (e.g. monopolar vs multipolar). Further, understanding the basic features of healthy SGNs could be relevant in the present and future context of neural regeneration. By means of a more realistic compartment model of the human SGN, the aim of this thesis is to understand how the physiology of the electrically stimulated SGNs contributes to, explains, and predicts some of the variability in listening outcomes in CI users. With these predictions, it may be possible to establish which stimulation strategy is best suited for specific profiles of neural health and electrode positions within the cochlea. In this chapter, a model of a healthy SGN that will be subjected to different stimulation paradigms, including various pulse rates as well as monophasic and biphasic pulse shapes, is presented and characterized. First, the impact of HCN and KLT ionic channels on SGN responses will be examined, and then the hypothesis that the implementation of the previously described (see Chapter 2) ionic channels impact responses of an electrically stimulated SGN to different polarity and pulse-shapes, will be tested.

3.2 Methods

Employing the model presented in Chapter 2, a healthy SGN in response to monophasic and biphasic pulses presented in monopolar mode is modelled in this chapter. Stimulations were performed for various combinations of parameters: 2 types of pulse shapes (monophasic and biphasic) x 2 polarities (anodic and cathodic) x 3 positions (high, mid, low) x 2 ionic models.

3.2.1 Stimulus

Both single pulses and pulse trains were used. The pulse-width was fixed to 50 µs and a 1 µs interphase interval was added for biphasic pulses. Both monophasic and biphasic pulse-shapes were studied in this chapter. The study of monophasic

pulse shapes in this thesis has two main benefits: 1) it allows for the exploration of parameters which are not ethically acceptable in humans; 2) it shades light on the effects of the discharge phase of biphasic pulses by its absence. Biphasic pulses were symmetric, where the first phase was either anodic or cathodic followed by a second phase of opposite polarity with the same amplitude. Pulse-rates of 250, 1000 and 5000 pps were used for all models. Each condition was repeated 10 times and both average and confidence intervals (obtained by means of bootstrapping methods) reported.

3.2.2 Ionic channel models

Two ionic channel models, both previously defined in Chapter 2, were tested: 1) the "HH" model using the Na and Kv channels equations from Rothman (2003); 2) the "HH+HCN+KLT" model, including HCN and KLT channel equations from Rothman (2003). All conductances and temperature shifts were reported in Chapter 2.

3.2.3 SGN Morphology

In this chapter, a healthy human SGN was modelled, according to the morphology previously employed in other studies (Rattay, Lutter, et al., 2001; Rattay, Potrusil, et al., 2013; Smit, Hanekom, van Wieringen, et al., 2010). For details refer to Chapter 2.

3.3 Results

Characterisation of SGN responses under different stimulation configurations is critical to understand the overall behaviour of the healthy human single SGN compartment-model presented here. The healthy human SGN was modelled for 3 electrode positions under both single and trains of electrical pulses using biphasic and monophasic pulse-shapes for cathodic and anodic polarities. First were examined responses to single pulses, that provide important insights into the model's ability to reveal basic features of the electrically stimulated SGN such as threshold shifts, polarity sensitivity and stochasticity. Next, responses to trains of electrical pulses were examined, to simulate a single healthy SGN subjected to stimulation more

typical of actual CI stimulation. All results presented here are summarised in the Appendices 3.B.1 and 3.C.1.

3.3.1 Single Pulse Responses

As ionic channel configurations generate different voltage dependent characteristics, the overall threshold of the SGN can change depending on ionic model distributions (Boulet, 2016; Negm and Bruce, 2014). In addition, the SGN also behaves differently when subjected to different pulse shapes and polarities (Rattay, Lutter, et al., 2001; Rattay, Potrusil, et al., 2013; Smit, Hanekom, van Wieringen, et al., 2010). Here, the model-dependent properties for a single human healthy SGN when subjected to single-pulse stimulation were examined.

3.3.1.1 Thresholds for single pulse stimulation

As previously explained (in Chapter 2) stochastic SGN responses are typically represented by a discharge probability function, also called the Firing Efficiency (FE) curve. FE curves encapsulate the ability of a SGN — with a specific set of morphological and physiological properties — to generate APs under different stimulation conditions. Fig. 3.3.1 shows a summarised representation of the modelled FE curves for all configurations.

Overall, it was observed that monophasic and biphasic pulses thresholds had similar behaviours and were almost identical between ionic channel models for most conditions: the "HH" ionic channel model showed lower or equal thresholds when compared to the "HH+HCN+KLT" model, for both the high and mid electrode positions, and for both polarities. A maximum single-pulse threshold difference (measured at 50% FE) of 1 dB between the "HH" and"HH+HCN+KLT" models was reported for the healthy SGN in the monophasic conditions.

This is contrasted with the lower position configuration, where thresholds were identical for all conditions between the two ionic channel models. Thresholds to biphasic pulses were systematically higher than to monophasic pulses, although a larger difference was observed in the anodic condition.

The differences in thresholds between ionic channels were never larger than 1 dB between all biphasic and monophasic conditions. Although the additional HCN

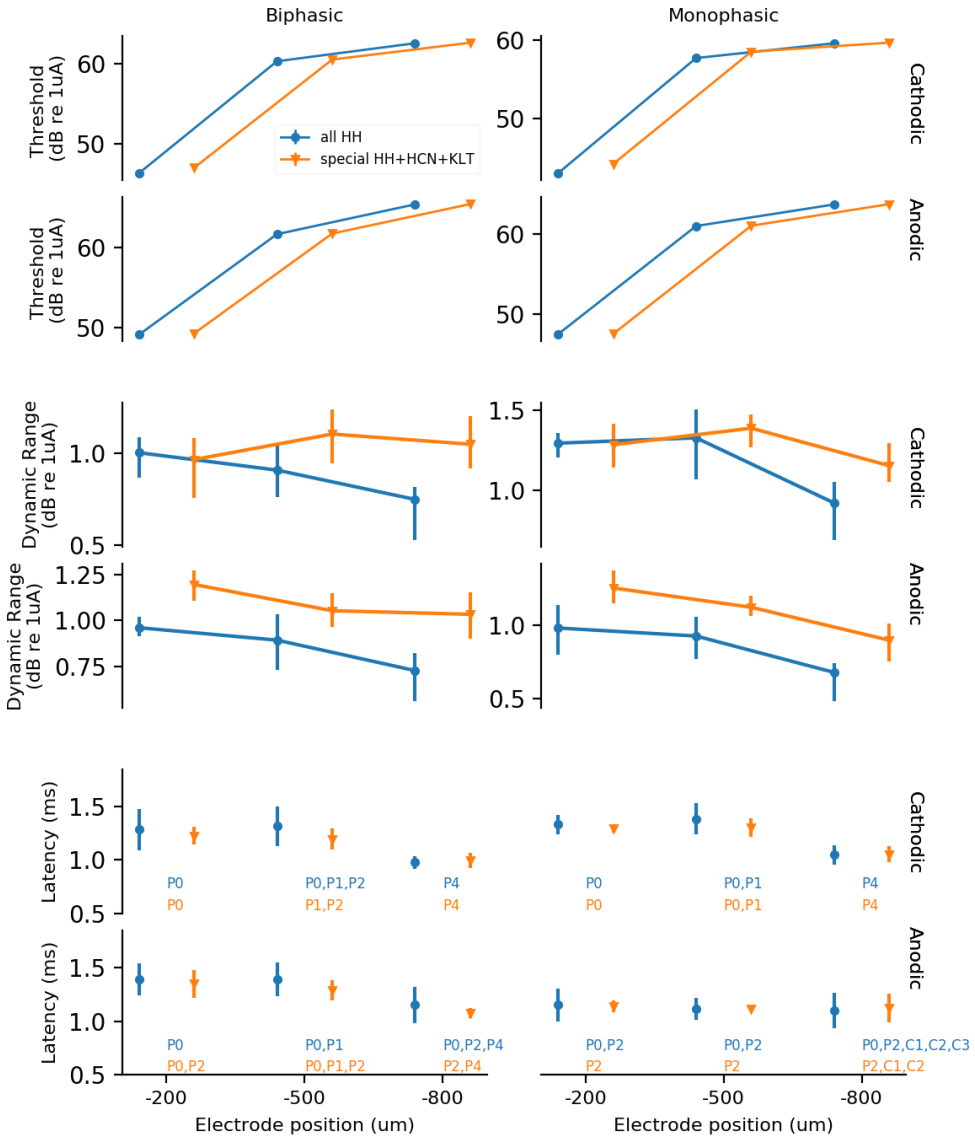

Figure 3.3.1: Summary of Firing Efficiency curves in response to monophasic and biphasic single pulse stimulus were modelled for a healthy SGN. The 50% FE, or threshold, Dynamic Range (DR) and latencies are recorded here. Different polarities, electrode positions and ionic distributions were tested to understand basic differences. Top panel shows the thresholds for both models, at 3 electrode positions, for monophasic and biphasic stimuli and for the two polarities. Mid panel shows the corresponding DRs for those conditions and bottom panel shows the corresponding latencies and observed site of excitations.

and KLT channels are known to increase threshold levels when compared to HH models (Boulet, 2016), the relatively small differences observed here are in line with conclusions from Chapter 2 with regards to the "HH+HCN+KLT" being a relatively weak adaptor and are in line with previous studies (Boulet, 2016; Zhang et al., 2007).

The thresholds for both pulse shapes and polarities increased by 10 dB from high to mid position and by 4 dB from mid to low position. In addition, cathodic thresholds were 4 dB lower than anodic thresholds whilst biphasic thresholds were 3 dB higher than monophasic thresholds.

3.3.1.2 Dynamic range for single pulse stimulation

DRs were measured as the range of activity between 10% and 90% FE as per Javel and Viemeister (2000). The middle panel in Fig. 3.3.1 plots the measured DRs for all the simulated conditions. Differences between the two ionic channel models were noticeable: the "HH+HCN+KLT" showed similar or higher DRs for all conditions. The DR values for the "HH+HCN+KLT" in the anodic case were systematically 0.25 dB higher than the "HH" condition. For the cathodic condition both pulse shapes (monophasic and biphasic) showed similar DRs for both models at the highest electrode position but a clear difference of 0.2 to 0.3 was observed at the mid and low electrode positions.

3.3.1.3 Spike latencies and excitation site for single pulse stimulation

The bottom panel of Fig. 3.3.1 plots latencies between stimulus onset and arrival time in C14, averaged over all simulation amplitudes. Latencies in the range 1 to 1.5 ms were evident, consistent with latencies reported in Rattay, Lutter, et al. (2001) for a healthy human SGN model, and with limited variability between ionic channel models and stimuli conditions. The latencies from biphasic stimulus and the "HH" model were relatively more variable than for the monophasic stimulus condition, shown by the error bars highlighting one standard deviation in the latencies, for both anodic and cathodic polarities.

The excitation sites along the SGN subjected to single pulse responses were also studied. High and mid electrode positions systematically proved to excite

the SGN peripherally (P0-P2), whilst at the low electrode position the site of excitation jumped to the central axon (P0-C3) for the monophasic anodic condition. Differences in the excitation site were also observed between ionic models: whilst the "HH+HCN+KLT" model showed relatively stable site of excitations in the high and mid electrode position, the "HH" model proved to be more fluctuating, i.e. the excitation sites varied between nodes P0-P2-P4-C1-C2-C3. However, low electrode positions generated large variations in the excitation sites for both ionic channel models, most likely due to the proximity of the electrode to the cell soma. Generally, lower electrode positions increasingly brought the site of excitation more centrally (usually nodes P4 and C1), accounting for the relatively shorter latencies observed for lower electrode positions.

3.3.2 Pulse-train Responses

Previous studies have reported the pulse train responses of SGNs in the form of Gaussian distributions or FE curves, similar to those from single pulse responses (Javel and Viemeister, 2000; Shepherd and Javel, 1997; Badenhorst et al., 2017). However, due to the complex stimulus interactions, the presence of the SGN peripheral process and, the additional ionic channels that were added in this thesis, the responses of the present SGN model to pulse-trains at different pulse rates and, for various electrode positions, were found to vary beyond a typical distribution with increasing stimulus intensity. As such, responses could not be fitted with Gaussian distributions or FE curves due to their non-monotonic behaviour. Instead, pseudo-FE curves were fitted on the first rising edge of the responses to insure homogeneity in the reported measures.

Here are first described the SGN responses and later the thresholds, DRs and latencies, when subjected to a range of stimulus conditions with the aim of understanding how these could help better predict the overall behaviour of a healthy auditory nerve neuron under extracellular electrical stimulation. To encourage brevity, the mechanisms responsible for the non-monotonicities above mentioned and referenced throughout Chapter 3 were further investigated in the Appendix 3.A.

Statistical relevance of the threshold levels, DR and latencies results for all

conditions was assessed by calculating the 95% confidence interval (indicated by error bars) and are summarized in Fig. 3.3.6, Fig. 3.3.7 and Fig. 3.3.8 respectively.

3.3.2.1 SGN spike-rate functions for monophasic pulses

Fig. 3.3.2 and Fig. 3.3.3 respectively show spike-rate curves and latencies of a single SGN subjected to monophasic pulse trains at 3 electrode positions (high, mid, low), three pulse rates (250, 1000, 5000 pps), and two stimulus polarities (anodic, cathodic). Results were obtained for a range of intensities spanning between 31 (35 µA) and 71 dB (3548 µA) in 40 steps of 1 dB.

Fig. 3.3.2 panels A and B show data for the high electrode position, C and D the mid position, and E and F the low electrode position. At the lowest pulse rate (250 pps), only small differences between ionic channel models were observed for both cathodic and anodic polarities and at all electrode positions.

The main difference for that condition was a relatively small shift in threshold (between 1 and 2 dB), with the "HH+HCN+KLT" model having a higher threshold than the "HH" model. In almost all conditions, spike-rate functions increased monotonically at this low stimulation rate. However, the cathodic pulses resulted in decreasing activity at 63 dB, until it completely stopped around 65 dB.

Note that although this non-monotonic spike-rate function was only observed for the cathodic pulses (Fig. 3.3.2 A), it does not mean that it wouldn't also occur in other conditions at higher intensities.

As shown in Fig. 3.3.2, higher stimulation rates (1000 and 5000 pps) resulted in complex non-monotonic spike-rate functions in which polarity, ionic model, and electrode position had strong effects on these functions. Three distinct patterns can be described from the SGN responses simulated: First, **monotonic growth** can be seen in all panels, except for panel A, at 250 pps. Second, several conditions (e.g A, B, C and E) produced **monotonic** spike-rate functions that initially increased with intensity until reaching a plateau over varying ranges of intensity, which was then followed by sharp decrease of activity at higher intensities. This pattern is shown in panel A (cathodic polarity, at 1000 pps for "HH" model, and at 5000 pps for both ionic models).

The last spike-rate pattern observed could be described as **bimodal**, where two

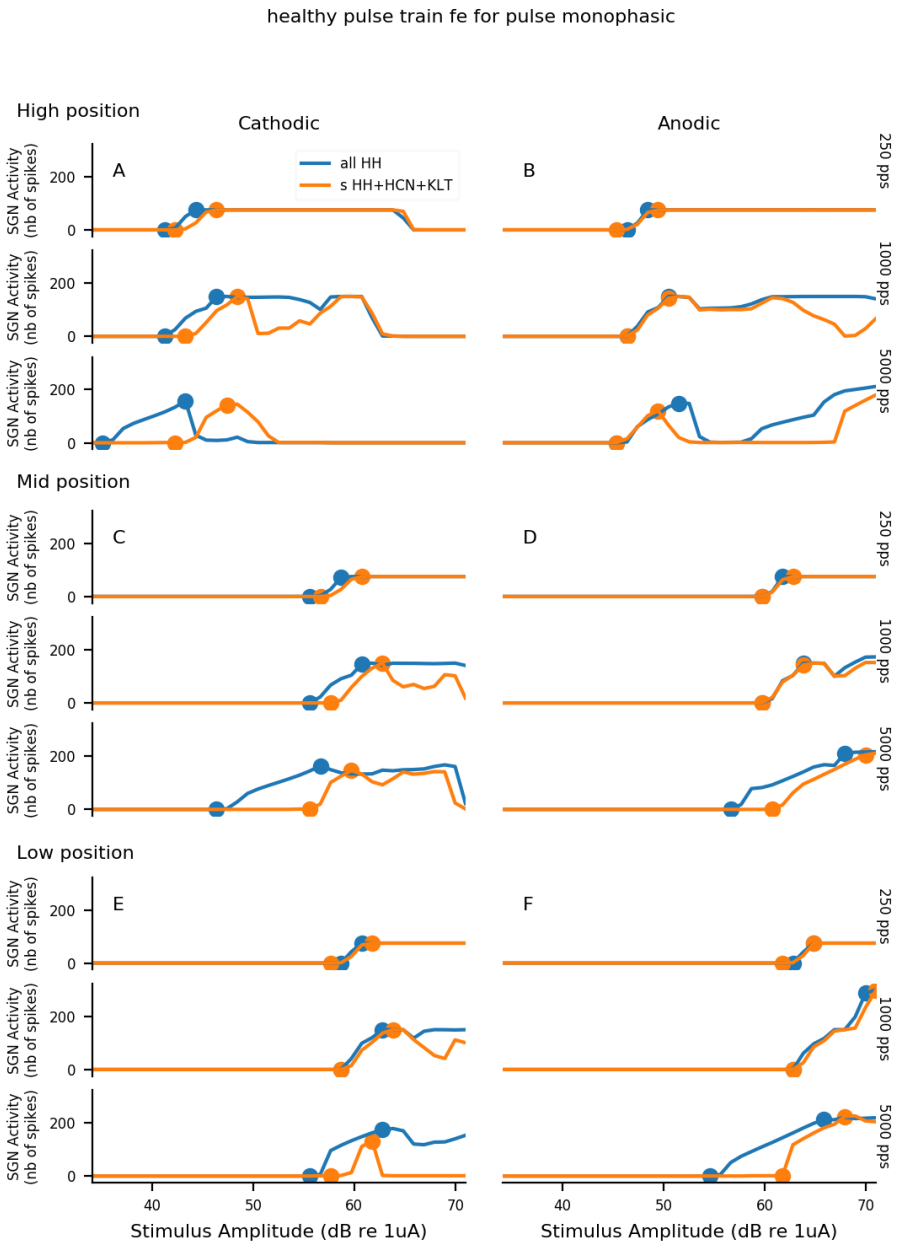

Figure 3.3.2: Monophasic pulse train response curves for healthy SGN. Response curves for a healthy SGN to 300 ms monophasic pulse trains as a function of stimulus amplitude, ionic model, electrode position, and polarity. Panels A and B for the high electrode position, C and D for the mid electrode position; E and F for the low electrode position. Left panel corresponds to the cathodic conditions whilst right panel to the anodic ones. Responses were calculated as the average SGN spike activity obtained from 50 independent simulations.

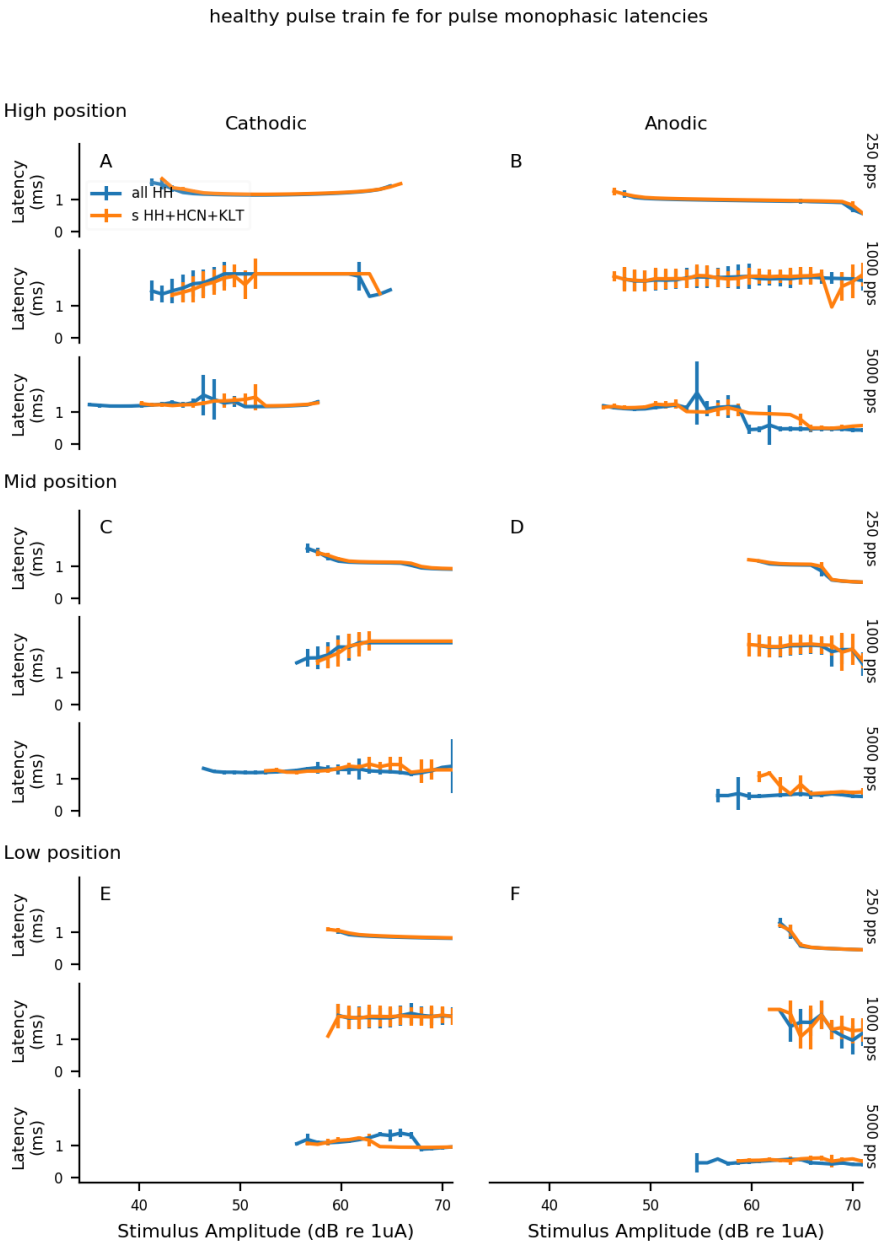

Figure 3.3.3: Monophasic pulse train latencies for healthy SGN. Response curves for a healthy SGN to 300 ms monophasic pulse trains as a function of stimulus amplitude, ionic model, electrode position, and polarity. Panels A and B for the high electrode position, C and D for the mid electrode position; E and F for the low electrode position. Left panel corresponds to the cathodic conditions whilst right panel to the anodic ones. Responses were calculated as the average SGN spike activity obtained from 50 independent simulations.

growth phases separated by a range of intensities generating less or no activity, were observed. This behaviour can be seen for the "HH+HCN+KLT" model using cathodic pulses at 1000 pps at the high electrode position (panel A) as well as for anodic pulses (panel B) at 5000 pps using both ionic models.

The mechanisms that explain these complex patterns has its origin in the multiple layers of polarity and morphology interactions as well as in the ionic channel dynamics of the models (see Appendix 3.A).

3.3.2.2 SGN spike-rate latencies for monophasic pulses

Interestingly, latencies for all conditions presented in Fig. 3.3.3 followed a similar pattern: latencies were found to be maximal at threshold levels, and decreased with increasing stimulating intensities (on average 0.1 ms) to then stabilise.

Large variability was observed in reduced activity and zones of no activity, most likely due to the instability of firing in these specific conditions. The most variability was observed for the 1000 pps condition for both cathodic and anodic polarities.

Overall, spike latencies were consistent with the excitation site of the spike. At points in the function generating high spike-rates, anodic pulses generated latencies that were, on average, 200 µs shorter than those generated by cathodic pulses, in agreement with the excitation site being relatively more central for anodic stimulation. These effects were independent of the ionic model, but not of the electrode position for which the excitation site changed from a more-peripheral to a more-central place as the electrode position was lowered (latencies increased from 200 to 400 µs shorter at lower electrode positions across all conditions).

3.3.2.3 SGN spike-rate functions for biphasic pulses

Fig. 3.3.4 and Fig. 3.3.5 respectively show spike-rate functions and latencies of a single SGN stimulated with biphasic pulse trains at 3 electrode positions (high, mid, low), three pulse rates (250, 1000, 5000 pps), and two stimulus polarities (anodic- and cathodic-first). Similar to the monophasic pulses, non-negligible differences and non monotonicity in the activity growth of the SGN were observed under biphasic stimulation. Differences between the modelled ionic channels were much less obvious in the biphasic pulse condition than for the monophasic. As for single

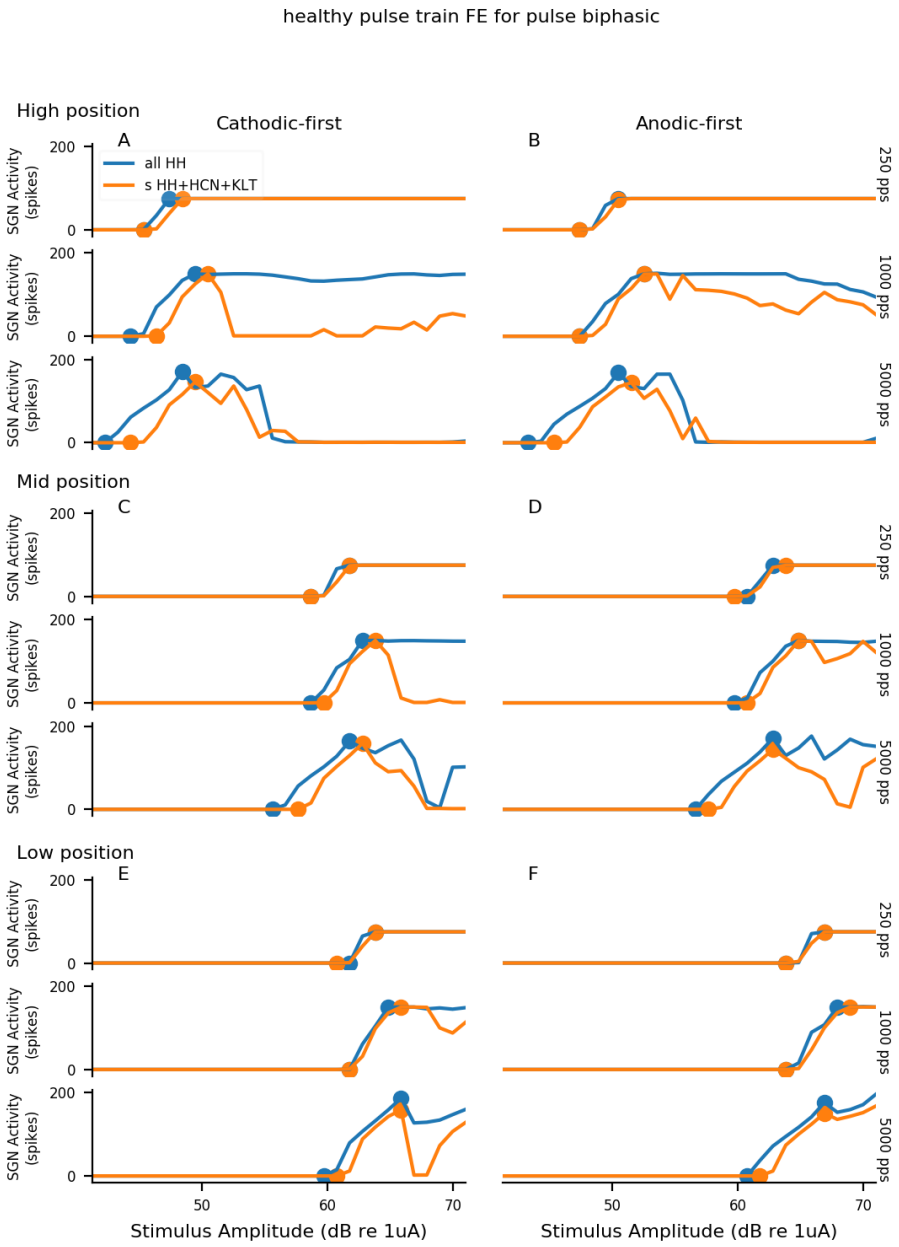

Figure 3.3.4: Healthy SGN responses to biphasic pulse trains. Spike-rate functions for a healthy SGN to 300 ms biphasic pulse trains as a function of pulse amplitude, ionic distribution, electrode position, and polarity. Left panels correspond to cathodic-first biphasic pulses whilst right panels were obtained using to anodic-first biphasic pulses. Electrode position is shown from top to bottom (high, middle, and low). Spike-rate functions were obtained by averaging 50 independent pulse train stimulations. Amplitude spike-rate and latencies are indicated in each panel (left-vertical axis) whilst the simulation rate is shown on the right-vertical axis.

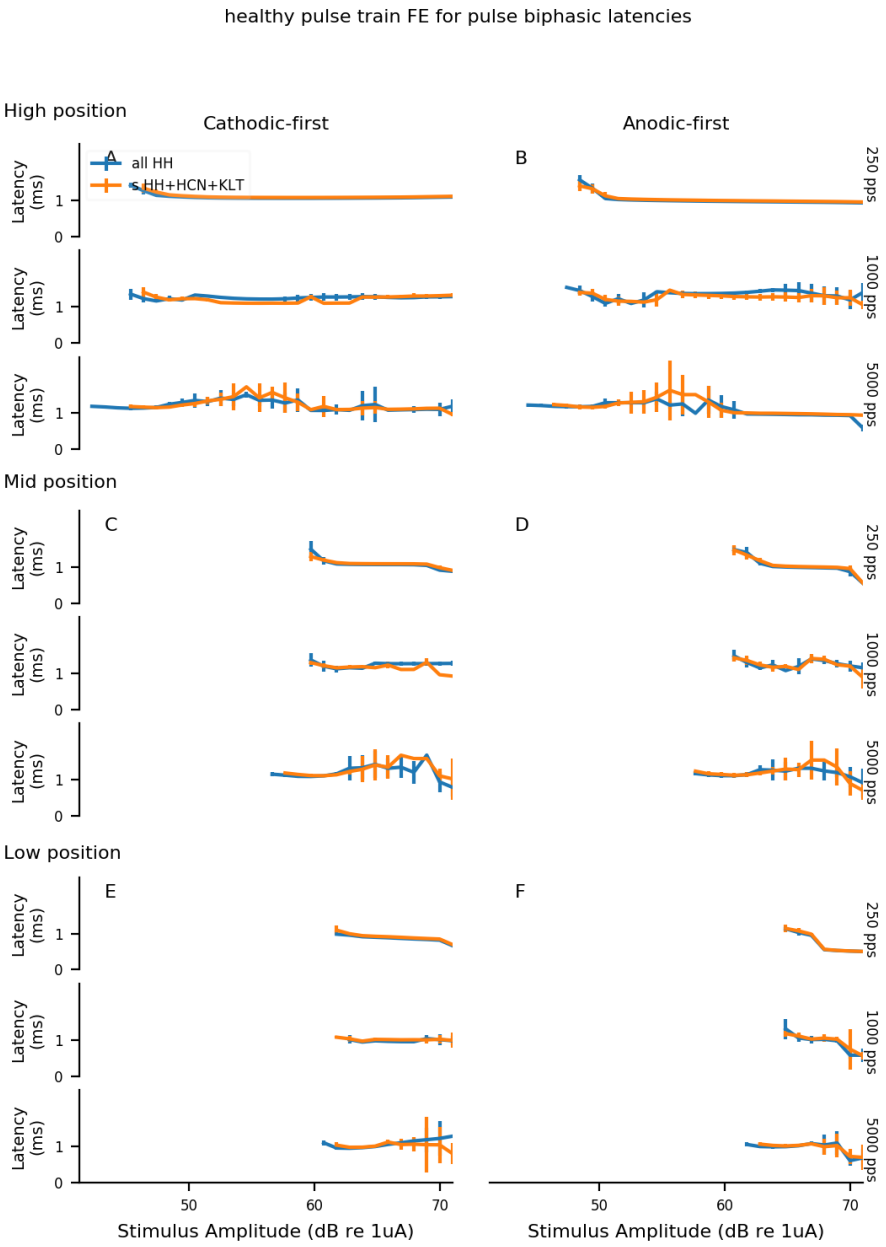

Figure 3.3.5: Healthy SGN responses to biphasic pulse trains. Spike-rate functions for a healthy SGN to 300 ms biphasic pulse trains as a function of pulse amplitude, ionic distribution, electrode position, and polarity. Left panels correspond to cathodic-first biphasic pulses whilst right panels were obtained using to anodic-first biphasic pulses. Electrode position is shown from top to bottom (high, middle, and low). Spike-rate functions were obtained by averaging 50 independent pulse train stimulations. Amplitude spike-rate and latencies are indicated in each panel (left-vertical axis) whilst the simulation rate is shown on the right-vertical axis.

pulse responses, the threshold shifts observed between the two ionic models were still present, although smaller than for monophasic conditions. In addition, both ionic models appear to track each other in terms of their modality: except for the 1000 pps condition for the high- and mid–electrode positions where the "HH+KLT+HCN" model activity decreased but not the "HH" model, the activity functions otherwise behaved similarly.

The 250 pps stimulus spike-rate functions were similar for both polarities and all electrode positions, except for the shift in threshold accounted for by the different electrode-to-SGN distance. In the case of higher pulse rates, the "HH+HCN+KLT" digressed the most from the typical Gaussian distribution e.g. panel A at 1000 pps where the "HH" model follows the typical growth and "HH+HCN+KLT" shows a unimodal pattern. This is also observed at 5000 pps at high- and mid–electrode positions for both models and polarities, as well as at 1000 and 5000 pps cathodic-first pulses for the "HH+HCN+KLT" model (in both mid- and low–electrode positions).

3.3.2.4 SGN spike-rate latencies for biphasic pulses

Similar to monophasic conditions, the latencies measured for biphasic stimulations (see Fig. 3.3.5) all followed a typical pattern: latencies were maximal at threshold levels and then slightly decreased with increasing spike-rate, until reaching a stable value.

Latencies in the anodic-first condition ranged from 0.67 to 1.34 ms with the cathodic-first condition showing latencies from 0.85 to 1.29 ms. The higher variability in the anodic-first latencies can be explained by the higher probability of APs being initiated at either a central or peripheral location, whilst the cathodic-first pulses are more likely to elicit APs peripherally due to the presence of the opposite-polarity phase.

Overall, the biphasic responses were more homogeneous across stimulation conditions and electrode positions, when compared to the monophasic conditions. Although both models often predict similar responses to different stimulus conditions, one of the most significant difference between the two ionic channel models was that the "HH+HCN+KLT" model showed supra-thresholds regions of 'no-activity' that were not always observed with the "HH" model. These differences are most likely

induced by spike-rate adaptation: when APs have to pass through nodes of Ranvier P0, P6, and C0, where KLT and HCN channels are located, they are subjected to larger spike-rate adaptation, in turns reducing the overall AP activity of the SGN.

3.3.2.5 Monophasic vs. Biphasic pulse train thresholds

Fig. 3.3.6 summarises the effect of different stimulus conditions on thresholds for the pulse-train responses presented in Fig. 3.3.2 and Fig. 3.3.4. As described earlier, because of the unimodal and non-monotonic activity patterns described previously, pseudo-FE curves using the first rising region of the spike-rate function were derived, i.e. the first monotonic region illustrated by the dots at the bottom and at the peak of the spike-rate function in Fig. 3.3.2 and Fig. 3.3.4. Using these pseudo-FE curves, thresholds were estimated as the 50% point of the pseudo-FE and DRs as difference between the intensities necessary to reach the 10% and 90% of the pseudo-FE curves, in agreement with single pulse responses characterized *in vivo* in animal models of CI (Javel and Viemeister, 2000). The results show that thresholds changed in similar ways at each electrode positions for all pulse-rates and ionic channel models.

Similar to single pulse stimulation, cathodic thresholds were systematically lower than anodic thresholds, for both monophasic and biphasic pulse shapes. From Fig. 3.3.6 panels A, B and C, it is evident that the largest significant effect on threshold across all monophasic conditions occurs at 5000 pps at the mid electrode position where the difference in thresholds between polarities was maximal.

In general, thresholds increased as the electrode was placed near the central axon away from the peripheral process i.e with lower electrode position.

The effect of pulse rate on thresholds was small yet significant, where 5000 pps pulses showed the lower thresholds than did other rates (about 1 dB). Psychophysical experiments in humans have shown decreasing thresholds with increasing pulse rates (about 10 dB for pulse rates increase from 100 to 800 pps) (Macherey, Van Wieringen, et al., 2006; Heffer et al., 2010). The data do not show such a decrease, likely because loudness perception relies on central processing mechanisms which are able to perform a temporal integration of SGN spikes (McKay, Lim, et al., 2013).

Although relatively small differences were observed between thresholds with respect to each electrode position, Fig. 3.3.6 (panel C) shows that the "HH"

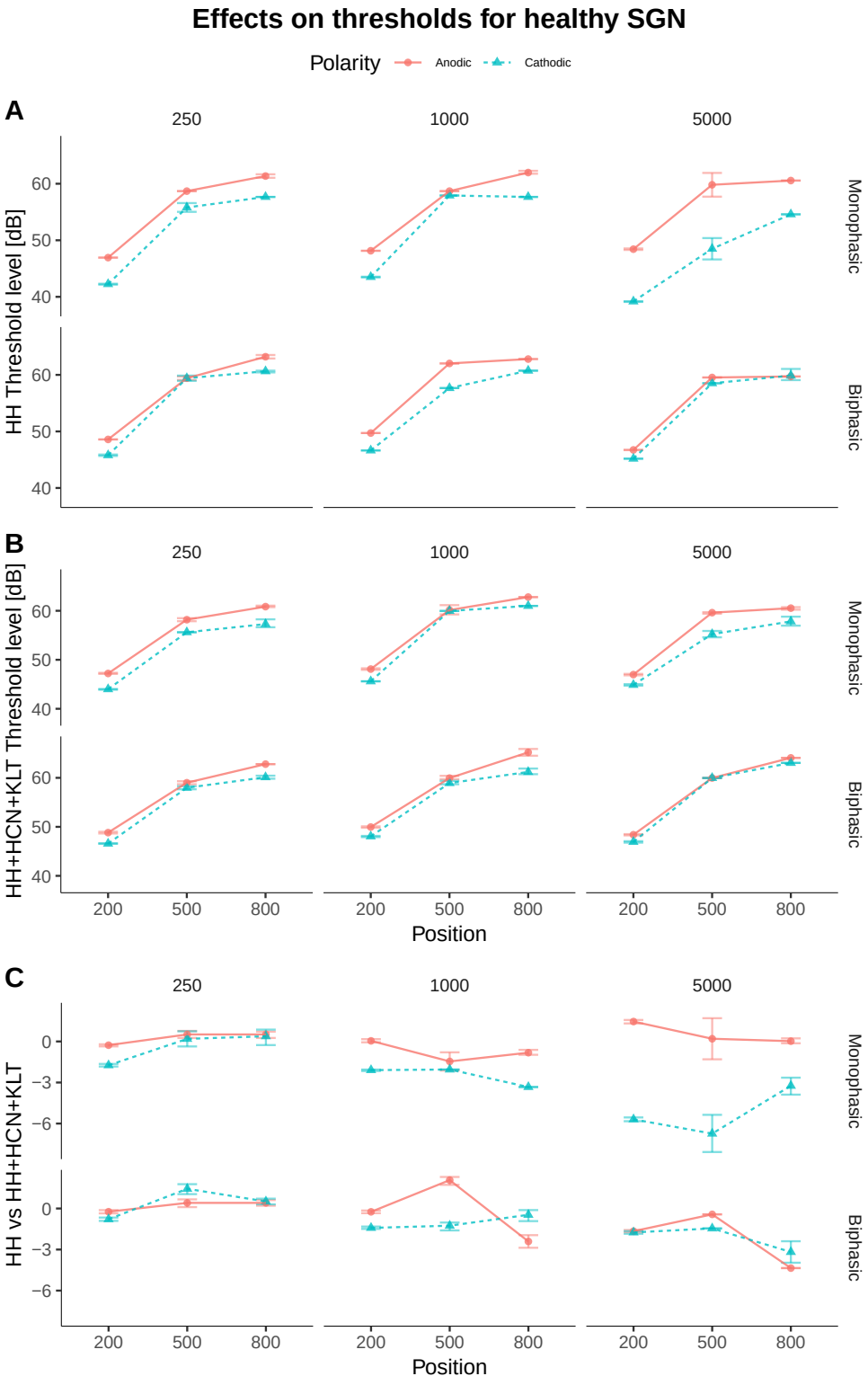

Figure 3.3.6: Threshold levels across models and stimulus conditions. A) threshold levels for the "HH" ionic model, B) the HH+HCN+KLT ionic model, C) the difference between the simulated threshold levels for the "HH" and "HH+HCN+KLT".

model generally had thresholds lower than, or at best equal to, thresholds in the "HH+HCN+KLT" model. This accords with single-pulse responses and previous studies showing that HCN and KLT channels typically increase threshold levels (Svirskis, 2004; Boulet, 2016; Negm and Bruce, 2014).

Overall, threshold values were found in the expected range: the 250 pps condition showed thresholds in the range of the single-pulse responses and, more importantly, in the range previously recorded *in vivo* (Shepherd and Javel, 1997). This is important, as 250 pps is a slow pulse rate that should allow the SGN to recover almost completely between pulses and behave with little or no evidence of refractoriness or adaptation. Thresholds ranged from 39 to 67 dB within all the simulated conditions, in line with other modelling studies (Rattay, Lutter, et al., 2001; Badenhorst et al., 2017).

3.3.2.6 Monophasic vs. Biphasic pulse train dynamic range

Fig. 3.3.7 summarises the effect of different stimulus conditions on DRs for the pulse-train responses presented in Fig. 3.3.2 and Fig. 3.3.4. DR values ranged from 0.37 to 10.74 dB across all conditions. Higher pulse-rate almost always showed larger DR than lower pulse rates, which is in line with previous literature (Skinner et al., 2000; Kreft et al., 2004; Boulet, 2016; Badenhorst et al., 2017). This suggests that increased DR observed at higher stimulation rates in humans may rise from increased neural DR together with temporal integration at higher levels in the auditory pathway.

While monophasic cathodic pulses proved to show relatively stable DR across electrode positions, anodic pulses showed greater DR variability at different electrode position for both ionic channel models. For example, the DR for the "HH" model at 5000 pps (Fig. 3.3.7) raised from 5 dB at the high electrode position up to 9 dB for both mid and low positions, whilst the DR for the "HH+HCN+KLT" model was 3 dB at the high position, 7.5 dB at the mid position, and 5 dB at the low position. Low stimulation rates (250 pps), on the other hand, showed stable DR values across electrode positions.

Similarly to threshold levels, the biphasic pulses DRs were stable across electrode when compared to the monophasic conditions (Fig. 3.3.7 A and B). More importantly, the simulations indicated almost systematically that biphasic pulses resulted in

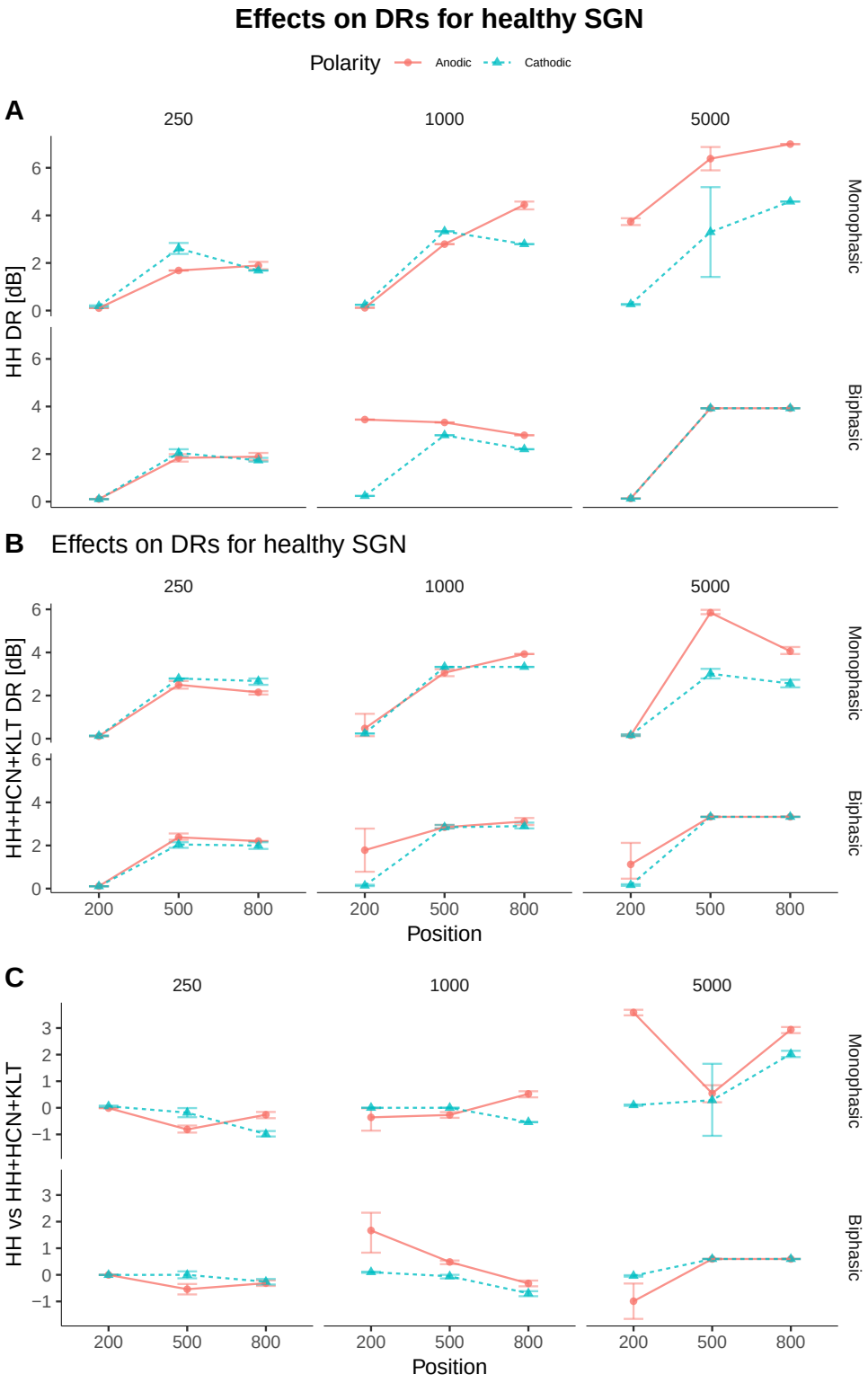

Figure 3.3.7: DR across models and stimulus conditions. A) DR for the HH ionic model, B) the HH+HCN+KLT ionic model, C) the difference between the simulated DRs for the HH and HH+HCN+KLT.

grater DRs as the pulse-rate increased. In addition, DR values were also found to be in the expected range: the 250 pps condition showed DR values in the range of the single pulse responses and more importantly in the range of previously recorded *in vivo* data (Shepherd and Javel, 1997). Also, it appears that although higher pulse rates did not noticeably and systematically lead to reduced thresholds, the DR values increased with increasing pulse-rate, which has been reported in previous animal studies (Miller, Abbas, and Robinson, 2001; Javel and Viemeister, 2000).

3.3.2.7 Monophasic vs. Biphasic pulse train latencies

Fig. 3.3.8 provides a summary of the recorded latencies over the range of intensities for all conditions presented in Fig. 3.3.3 and Fig. 3.3.5. Latencies ranged from 0.47 to 2.05 ms relative to C14 which is in the range of previously reported values (Rattay, Lutter, et al., 2001; Badenhorst et al., 2017; Frijns, de Snoo, et al., 1995).

For monophasic pulses, 1000 pps pulse trains showed relatively large latencies (1.4 to 2 ms) when compared to the other pulse rates. This effect is of interest as it could derive from the intrinsic properties of SGNs. This is in contrast with the 250 and 5000 pps which showed the shortest latencies for cathodic and anodic polarities (0.5 to 1.5 ms respectively). In the biphasic pulse-shape condition however, the low pulse-rate showed the shortest latencies, whilst the 1000 and 5000 pps pulse-rate conditions showed longer, and similar, latencies.

Polarity effects are expected to impact significantly latencies in monophasic conditions because of the preferred site of excitation moving centrally between cathodic and anodic polarities. This effect was however predicted to be minimal for biphasic conditions because of the counter-acting discharge phase. Fig. 3.3.8 panels A and B confirm that these predictions are true for both models. Monophasic stimulation latencies were significantly higher for cathodic polarities (more peripheral site of excitation) than anodic stimulation latencies. The largest difference was observed at 5000 pps (up to 500 µs) while both 250 and 1000 pps latency differences were similar (100 µs).

In all the simulated conditions, a small to no difference was noticed between the "HH" and "HH+HCN+KLT" models. Significant differences, highlighted in Fig. 3.3.8 panel C, were only found in anodic conditions for the mid-position electrode at

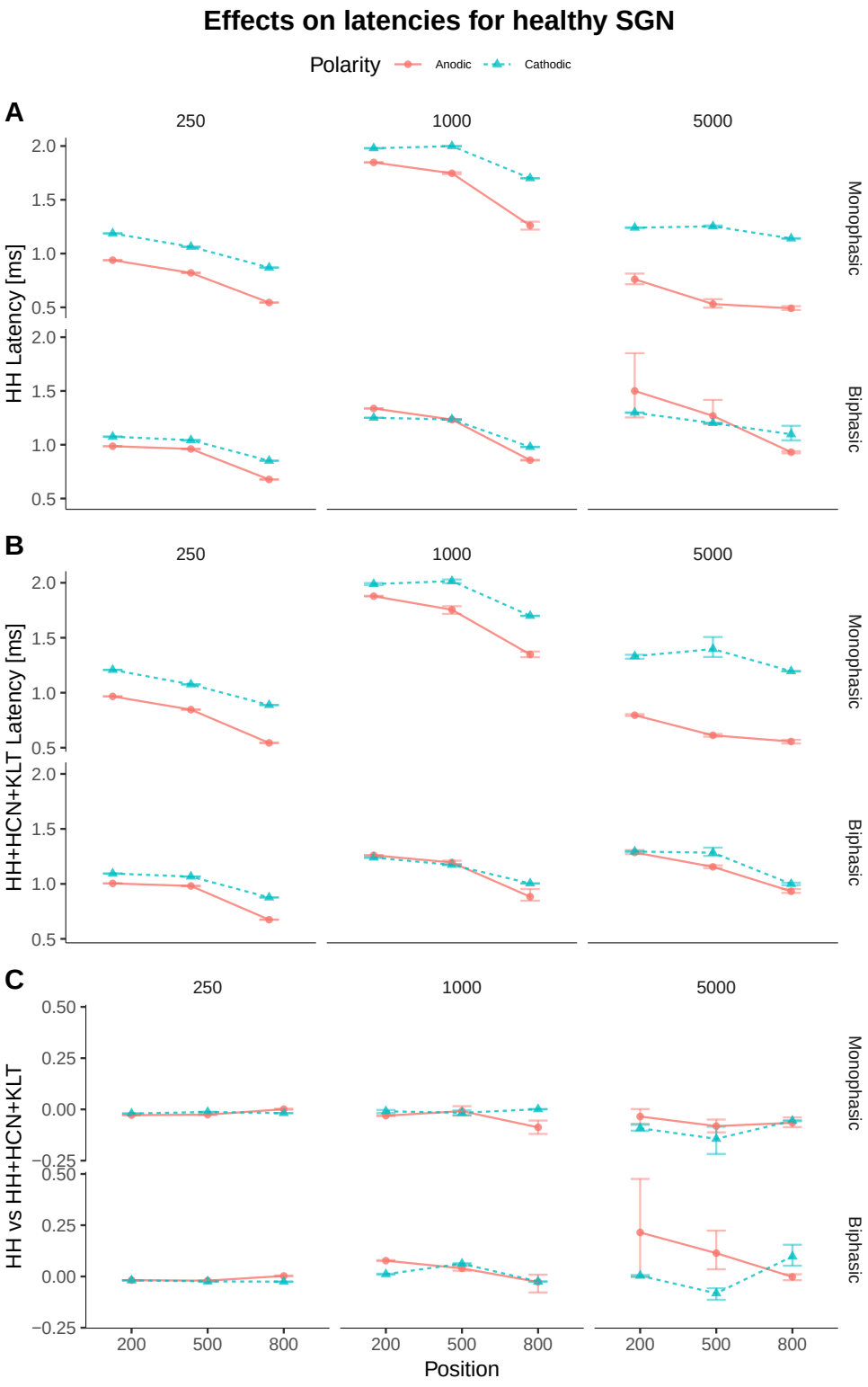

Figure 3.3.8: Latencies across models and stimulus conditions. A) Latencies for the HH ionic model, B) the HH+HCN+KLT ionic model, C) the difference between the simulated latencies for the HH and HH+HCN+KLT.

1000 pps for the monophasic condition and low-position electrode at 1000 and 5000 pps for the biphasic condition. The ionic model effects were smaller than 100 µs: in the monophasic anodic scenario the "HH" model was found to predict latencies that were 50 to 100 µs shorter than the "HH+HCN+KLT". However, in both the biphasic anodic and cathodic cases, the "HH" model was found to predict larger latencies for the mid-electrode and low-electrode positions respectively.

3.4 Discussion

In this Chapter was presented a computational model of an electrically stimulated healthy human SGN where different distributions of ionic channels, pulse shapes, and stimulation rates were investigated. Two ionic models were tested: the standard HH equations for Na and Kv, and a more complex and realistic model that included KLT and HCN ionic channels. By introducing KLT and HCN, the aim was to test the hypothesis that modelled AN responses would be closer to neural activity recorded *in vivo* in animal models than those generated by modelling AN responses using the complement of ionic channels based on HH models. CI stimulation strategies encode sounds by means of amplitude modulated pulse trains at rates where spike-rate adaptation and accommodation are important features to be expected in the SGN response, features underpinned by the properties of these additional channels.

In this study, it was observed that the introduction of KLT and HCN did change the preferred monophasic pulse-rate for highest DR at specific electrode positions and polarities. This indicates that KLT and HCN can impact encoding of monophasic electrical impulses at the level of single SGNs, making them important parameters to be considered when simulating responses of SGN to trains of electrical pulses. Although the effects of KLT and HCN with regards to threshold were also apparent for biphasic stimulations, the difference was not statistically significant (see Fig. 3.3.6 panel C).

Finally, responses to different pulse shapes were tested: polarity and pulse shape are known to play an important role in the efficacy of SGN recruitment in electrical stimulation, and are often considered as possible sources of the large variability in patient performance observed clinically (Undurraga, Carlyon, Wouters, et al., 2013a; Macherey, Carlyon, Chatron, et al., 2017). Here were investigated neural responses

at three arbitrary electrode positions, matching the positions first introduced in the study by Rattay, Lutter, et al. (2001). Additionally, both single pulse and pulse train stimulation, for monophasic and biphasic pulse shapes, in cathodic and anodic conditions were investigated.

3.4.1 Effects of KLT and HCN

For single pulses, the main observable difference is an upward shift in threshold for the model containing the additional channels, i.e. KLT and HCN. This can be explained by the low threshold inactivating properties of KLT and HCN which are in line with previous studies (Rothman, 2003; Negm and Bruce, 2014; Boulet, 2016). In response to trains, different behaviours can be observed depending on electrode position and pulse rate.

Due to spike-rate adaptation, one would have predicted that the “HH+HCN+KLT” would show lower activity at higher pulse rates but this was not observed. However, the “HH+HCN+KLT” is a weak adaptor model, possibly underestimating some effects of spike-rate adaptation.

One of the most interesting difference between the ionic channel models observed was in the FE using biphasic pulses at the high electrode position, and when using higher pulse rates (Fig. 3.3.4 A-D for 1000 pps and 5000 pps). First, at 1000 pps for the high- and mid-electrode positions, the "HH+HCN+KLT" model showed a unimodal spike-rate function. Moreover, the model predicted “no-activity” for the cathodic-first pulses beyond 52 dB, whereas the “HH” model predicted only small reductions in activity at much higher intensities. Second, a similar effect for the mid-electrode position on the spike-rate function was observed using anodic-first 5000 pps pulse trains, where the SGN also demonstrated a unimodal pattern; a “no-activity” region was observed at supra-threshold intensities.

Moreover, it is important to highlight the **bimodal** patterns that were reported in Fig. 3.3.2. These **bimodal** patterns indicate that, at least at the level of single SGNs, non-monotonic activity can be explained by complex stimulus interactions. The underlying mechanisms that can cause these non-monotonic responses hints at an explanation for non-monotonic loudness growth functions reported in humans by Macherey, Carlyon, Chatron, et al. (2017).

The aim of introducing the KLT and HCN ion channels was to achieve a more-realistic model of the human SGN. As mentioned in Chapter 2, the "HH+HCN+KLT" model presented here has been defined as a weak-adaptor model. The new ionic model presents variations in the predictions of activity that were noted for all electrode positions, and for all pulse-shapes and pulse-rates. This indicates that the model generates a closer approach and perspective to the electrically stimulated SGN *in situ*.

3.4.2 Effects of electrode position

Electrode position is highly variable in the implanted ears of human CI recipients, and depends on factors such as the surgical approach, electrode type, and the shape of the cochlea (Blamey et al., 1996). Previous studies using 3D volume conduction models combined with active SGN models, have underpinned the importance of electrode position in the efficiency of extracellular electro-stimulation (Rattay, Lutter, et al., 2001; Rattay, Potrusil, et al., 2013; Frijns, de Snoo, et al., 1995; Badenhorst et al., 2017). Moreover, electrode position is often directly related to the performance of a specific stimulation strategy in computational models (Rattay, Lutter, et al., 2001; Rattay, Potrusil, et al., 2013; Frijns, de Snoo, et al., 1995; Badenhorst et al., 2017). In this thesis, three arbitrary electrode positions were chosen: the high electrode position which placed the electrode near to the peripheral end of the SGN; the mid position which placed the electrode 300 µm below the high position; the low position which placed the electrode a further 300 µm below the mid position, closer to the central axon. Each of these positions is similar to the positions first introduced by Rattay, Lutter, et al. (2001), which match an implantation of the electrode array in *scala tympani*. Fig. 3.3.1 and Fig. 3.3.7 illustrate the main known effects of electrode position for single pulse response of healthy SGNs. Cathodic thresholds increase at lower positions, whilst anodic thresholds first increase between the high and mid position, and either decrease or stay stable between the mid and low positions (Rattay, Lutter, et al., 2001; Frijns, de Snoo, et al., 1995). This is particularly important given that electrode position can be directly related to the assessment of neural health: healthy SGNs will supposedly show lower thresholds for higher-electrode positions. Moreover, monophasic cathodic pulses presented at

the low-electrode position showed the largest sensitivity to the distribution of ionic channels. This indicates that the additional KLT and HCN channels have more effect when the electrode position is at a lower position which highly correlates with the difference in the preferred site of excitation. HCN channels were located at P0, P6 and C0 which means that more central initiation sites (after P4) would be more impacted by their presence. In addition, APs that started at P6 would be even further impacted due to the longer morphology of this node and its larger ionic channel concentration.

Finally, from Fig. 3.3.1, it can be concluded that the most important effect observed for electrode position is the shift in site of excitation. Higher electrode positions favour the most peripheral node (P0) as the site of initiation of APs whereas lower electrode positions shift the site of excitation more centrally. The main effect that can be derived from this phenomenon is a shift in AP latency, and with latency being an important factor in the temporal encoding of the signal, large differences between site of excitations can dramatically impact neural encoding.

3.4.3 Polarity effects

Perhaps the biggest polarity effect that was observed is the cathodic blocking effect at pulse rates higher than 1000 pps for both the biphasic and monophasic pulses (shown in Fig. 3.3.2 and Fig. 3.3.4). This phenomenon has been previously described (Rattay, 1989; Rubinstein and Rubinstein, 1993; Rattay, Lutter, et al., 2001; Macherey, Carlyon, Chatron, et al., 2017) as the result of counter-acting polarization along the SGN which resulted in blocking the elicitation of APs. Fig. 3.A.3 shows the hyperpolarization happening at higher levels of stimulation. Polarisation being highly dependent on electrode position, the observation of this effect is most likely limited by the arbitrary electrode positions that were chosen for this experiment. Different conditions of electrode position, SGN morphology and pulse shape would most likely bring different results. This is an interesting effect as the inactivity of the SGN at specific intensities above the measured threshold could have important implications in CI fitting. However, it is important to note that the cathodic blocking effects reported in Macherey, Carlyon, Chatron, et al. (2017) were observed at 100pps, a much lower pulse-rate when compared to the effects reported here.

This could be caused by multiple factors given that Macherey, Carlyon, Chatron, et al. (2017) observed this effect in human subjects while this chapter models a single neuron.

In addition to this phenomenon, it was also observed that polarity effects were larger at the high-electrode position, and for monophasic pulses. This is not surprising as monophasic pulses are known to highlight these effects; biphasic pulses also contain the counteracting polarity phase. These differences were not large (Fig. 3.3.4) for the threshold, probably as a result of the interaction between both phases of the pulses.

Finally, polarity effects for monophasic pulses were found to have an important impact on latencies as observed in Fig. 3.3.8. In the context of binaural CI implantation, designing stimulation strategies that allow for latencies to match in both neural pathways might be a key to reintroducing the cues necessary for binaural hearing. Differences as small as 100 µs could already interfere with binaural processing. The current model could be instructive in understanding how to reduce mismatches in latencies across the ears.

3.4.4 Effects of Stimulation Pulse Rate

Previous computational models and *in vivo* animal studies have shown the effects of pulse rate and ionic channel distributions on response properties of SGNs when subjected to extracellular stimulation (Negm and Bruce, 2014; Boulet, 2016; Miller, Abbas, and Robinson, 2001). Pulse train presented at around 1000 pps are commonly used in CI. Due to intrinsic properties (refractoriness, facilitation, and accommodation), higher pulse-rate can cause the SGN to enter different states, e.g. firing state or recovery state, within a pulse train, depending on its Absolute Refractory Period (ARP) and Relative Refractory Period (RRP) and threshold. In Fig. 3.3.6 it can be seen that thresholds generally decrease as pulse-rate increase. However, when compared with the evolution of DR illustrated in Fig. 3.3.6, lower thresholds don't always mean larger DRs. Further, with loudness perception being a function of the temporal integration of neural spikes, it is critical to design stimulation strategies that effectively encode pulse trains at the neural level.

The underlying mechanism for the difference in latencies was not systematically

studied in this thesis. However, the origin of these differences can be predicted to come from either the facilitation and refractoriness properties of the SGN, or the change in excitation site, both of which can be impacted by pulse rate (Boulet, 2016; Miller, Abbas, and Robinson, 2001). Latencies were higher for monophasic at 1000 pps than other pulse rates, most likely due to facilitation and refractoriness effects. This is an important feature to understand as the signal would be relatively distorted by such a difference in latencies and this must be taken into account when designing stimulations strategies.

Finally, the main pulse-rate effect observed is the blocking described in Appendix 3.A.1, where the continuous high pulse-rate stimulus caused the SGN to enter in a bistable equilibrium state. Although this is a major finding in the study presented here, its implications are mitigated by the restricted range of conditions over which it was observed. This effect will be tracked and reported if observed in other results presented in this study but further investigation into how it could be characterised were beyond the scope of this thesis.

Appendix

3.A Complex spike-count patterns

As shown in Sec. 3.3.2, pulse trains produced complex spike-rate functions that did not follow a monotonic function as a function of the intensity. These complex patterns were characterized as **unimodal** and **bimodal**, where spike-rate functions showed response minima at certain supra-threshold levels for multiple stimulation conditions. Three mechanisms causing these non-monotonic spike-rate functions were identified. These can be described as: 1) bistable state of the model, which is highly prominent at 5000 pps; 2) cathodic blocking, where part of the nodes of Ranvier became hyperpolarized due to complex stimulus interactions; and 3) spike-rate adaptation at P6, where high pulse-rates cause a threshold rise in this node preventing the passage of APs through the soma. It is a fair assumption to state that these mechanisms can occur individually or in combination, producing complex prediction scenarios. Although more obvious for monophasic (e.g. cathodic pulse-train at 1000 and 5000 pps in Fig. 3.3.2 A-C and E), those mechanisms were also seen with biphasic pulses (e.g Fig. 3.3.4 A-D and E).

3.A.1 Bi-stable state

Perhaps the most important mechanism explaining non-monotonous responses in this study is the bi-stable state of the gating equations of Na ionic channels gating equations. Put simply, when a SGN is stimulated at higher pulse-rates, e.g. 5000 pps, the h and m gates of the Na channel enter a stable state that is entrained by the continuous stimulus. The entrainment is explained by the repetitive nature of the stimulating signal: although the SGN does not necessarily fire for each stimulating pulse, each pulse does affect the SGN membrane potential. From a certain intensity level, often above threshold, and because the stimulating pulses happen very close together in time, the SGN's membrane does not have the time to recover and go

back to its Resting Membrane Potential (RMP) level.

Fig. 3.A.1 shows the progression of APs along a SGN in response to a 5000 pps pulse train in monophasic anodic stimulation mode, at the highest electrode position. Fig. 3.A.1 A and B show sub-threshold and suprathreshold events, respectively. When the electrode delivers a 48 dB current, APs are elicited at node P2. However, Fig. 3.A.1 C and D show two supra-threshold events where only the onset APs are elicited at P2 (panel C), or the initiation site jumps to a central node (panel D). This phenomenon is explained in terms of a bistable state induced by the high pulse-rate stimulus. In that state, shown in Fig. 3.A.2 and Fig. 3.A.1 at 55 and 60 dB, the m gate, i.e. activation gate, remains in an open state after the initial spike for the duration of the stimulus. Typically, following a spiking event, the activation gate should return to a near resting level but here it remains in an open, oscillatory state, never reaching rest. This is because the ongoing stimulus which continuously bounces the membrane potential and maintains it at a slightly depolarized level. At the same time, the h gate, i.e the inactivation gate, is shut down by the ongoing stimulus, effectively putting the SGN in a stimulus-entrained equilibrium from which it cannot generate APs. The n gate, being the only driver of the potassium inactiving channel, tracks the sodium-activating m gate when APs occur (see Fig. 3.A.2 second row). However, in the case of the bistable scenario (observed in Fig. 3.A.2 rows three and four), the n gate first opens at the pulse-train onset but never shuts.

This can be contrasted with Fig. 3.A.2 at 48 dB where the SGN generates APs efficiently at the same pulse-rate, with h and m gates reaching near resting levels after each spike.

Arguably, the mechanism described here is an important feature of the SGN model presented in this thesis. Although this phenomenon could theoretically be reproduced *in vitro* and *in vivo* in the laboratory for very high pulse-rates and controlled stimulation parameters, it would be unlikely to happen naturally due to the high complexity of environmental requirements and the high frequency of stimulation. As such, and due to the restricted number of conditions in which it has been observed in the course of this thesis, further investigations to further understand this phenomenon lie outside the scope of this study.

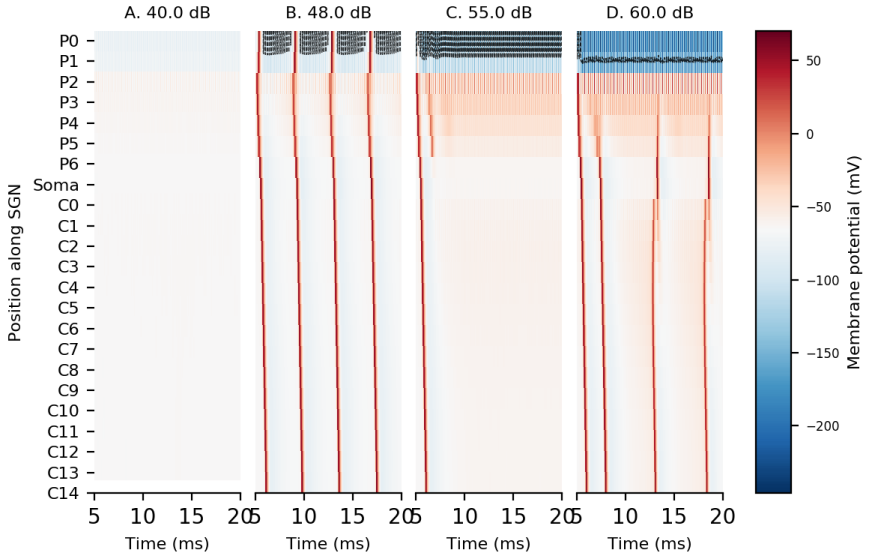

Figure 3.A.1: Bistable state travelling APs. Due to the high pulse-rate, the SGN membrane potential is depolarised at P2

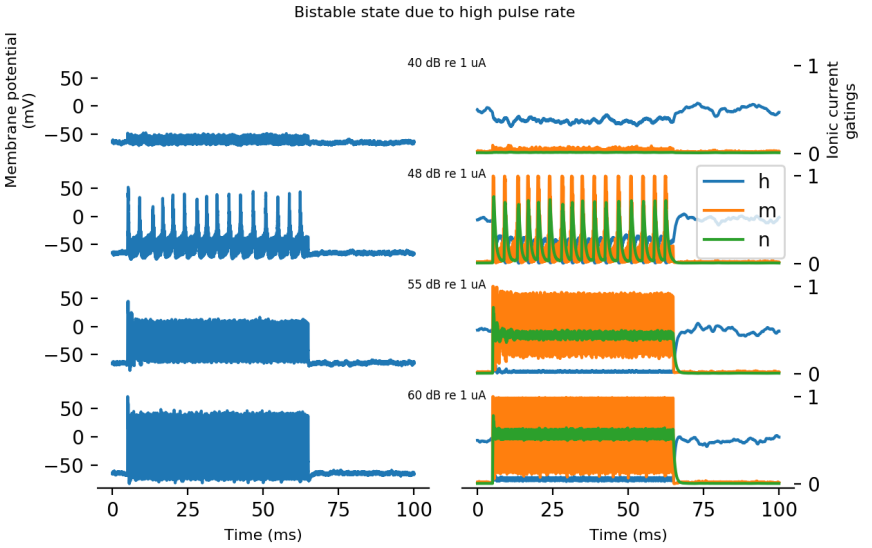

Figure 3.A.2: Bistable state illustration at node P2. Due to the high pulse-rate, the SGN membrane potential is depolarised at P2

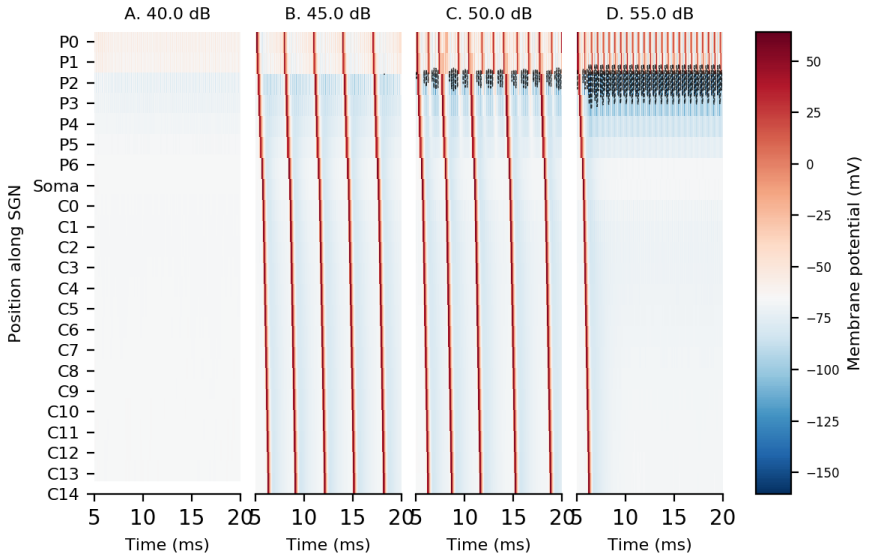

Figure 3.A.3: Cathodic blocking phenomenom. The cathodic blocking phenomenon happens when a node of Ranvier situated more centrally than the initial site of excitation is hyperpolarised by the stimulus. Due to the high pulse-rate (5000 pps) with monophasic, cathodic pulse shape and the "HH+HCN+KLT" model, the SGN membrane potential is depolarised at P2

3.A.2 Cathodic blocking

Cathodic blocking is a phenomenon that was previously introduced by Rattay (1989) and further observed by Rubinstein and Rubinstein (1993), Rattay, Lutter, et al. (2001), and Macherey, Carlyon, Chatron, et al. (2017) where the stimulus causes parts of the SGN's nodes of Ranvier to be hyperpolarized to such an extent that APs are unable to saltate through them. This mechanism is highlighted by the complex, bended morphology of the SGN in which nodes of Ranvier located further away from the depolarized excitation site become hyperpolarized.

Fig. 3.A.3 illustrates parts of the cathodic blocking that was observed in Fig. 3.3.2 and Fig. 3.3.4.

Fig. 3.A.3 A-D represent the 15 ms time window after stimulus onset (5 ms) from the response of a SGN to a pulse-train at 5000 pps for the "HH+HCN+KLT" ionic channel model, at the highest electrode position using monophasic cathodic pulses. Simulations were performed at four different levels, 40 dB, 45 dB, 50 dB and 55 dB,

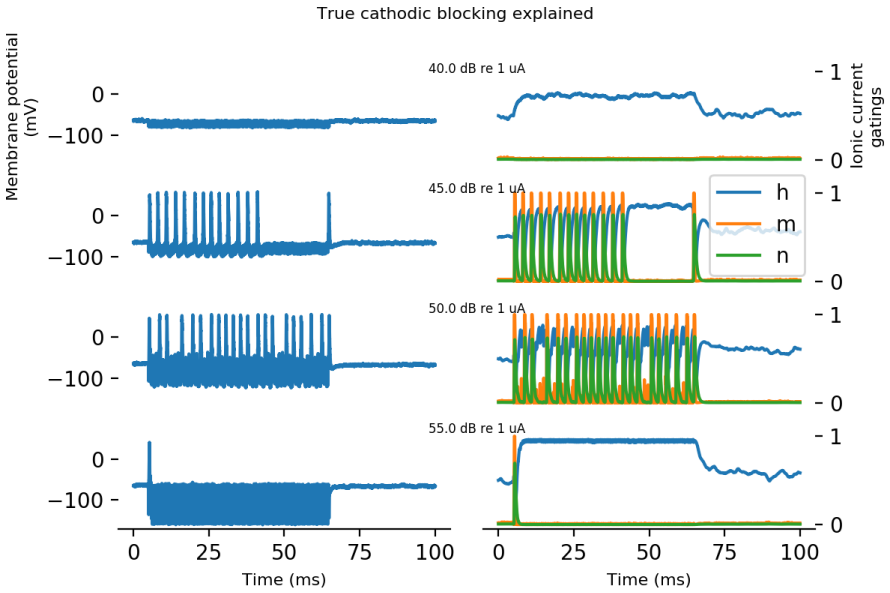

Figure 3.A.4: Cathodic blocking illustration at node P2. Due to the high pulse-rate (5000 pps) with monophasic pulse shape and the "HH+HCN+KLT" model, the SGN membrane potential is hyperpolarised, effectively blocking any spiking event from happening.

according to the pulse train response presented in Fig. 3.3.2 A.

For stimulation levels of 45 dB and 50 dB, APs were successfully elicited at the most peripheral node P0, sometimes simultaneously with P1. For these intensities, APs normally travel towards the most central node (C14) in a saltatory manner.

However, at 55 dB (Fig. 3.A.3 panel D) a different phenomenon was observed: nodes P2-P3 were seen to be overly hyperpolarized, shown by a dashed countour in Fig. 3.A.3 C-D, which blocked the APs that started in P0 from passing through. Fig. 3.A.4 shows the gating of Na and Kv ionic channels for sub-threshold and supra-threshold pulse-trains are simulated at node of Ranvier P2. The first row of Fig. 3.A.4 shows a typical sub-threshold event, where the m and n activating gates for Na and Kv respectively are left shut down and the Na-inactivating gate is strongly opened by the hyperpolarizing stimulus affecting the SGN membrane.

The two middle rows in Fig. 3.A.4 show typical APs being elicited due to a suprathreshold stimulus (Fig. 3.A.3 B-C) with gating recovery after each spike.

Finally, the last row from Fig. 3.A.4 illustrates the gating of the different ionic

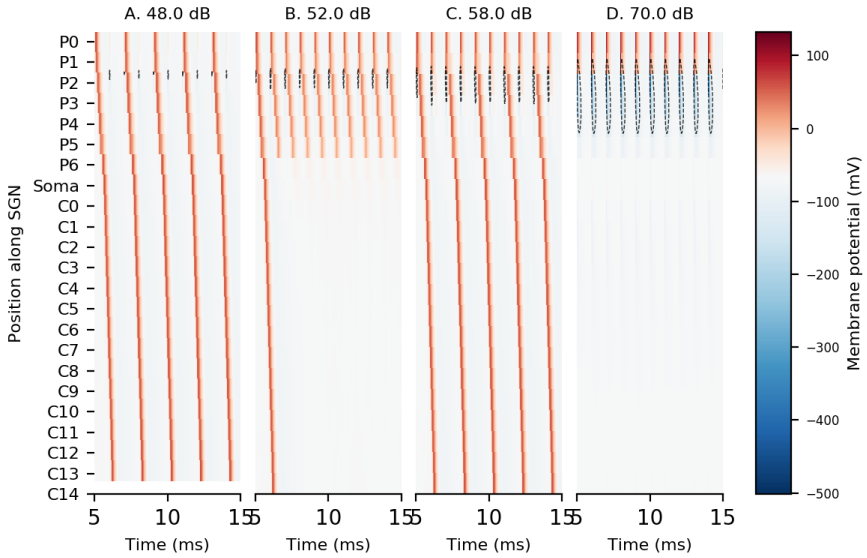

Figure 3.A.5: Spike-rate adaptation blocking. The spike-rate adaptation blocking phenomenon happens when a peripheral node of Ranvier situated more centrally than the initial site of excitation is adapted by the stimulus.

channels (see) Fig. 3.A.3 panel D), where strong hyperpolarisation at node P2 effectively blocks the gating activity.

Subjected to a strong cathodic pulse-train stimulus and, due to the position of node P2 from the electrode, the membrane potential is depolarised to an extent where h gates are wide open while m and n gates are wide shut. This causes the SGN to become unable to fire APs and blocks incoming spiking events from going through.

In this scenario, the growth in activity of the spiking response did not recover from the cathodic blocking phenomenon i.e. no activity at intensities beyond 55 dB. In addition, the "HH" model showed a similar response pattern, except for an overall 10 dB shift downwards.

3.A.3 Spike-rate adaptation

The third phenomenon previously introduced in this thesis (Sec. 3.3.2) is caused by the HCN and KLT ionic channels in node P6 and thus, most probably due to the spike-rate adaptation mechanism.

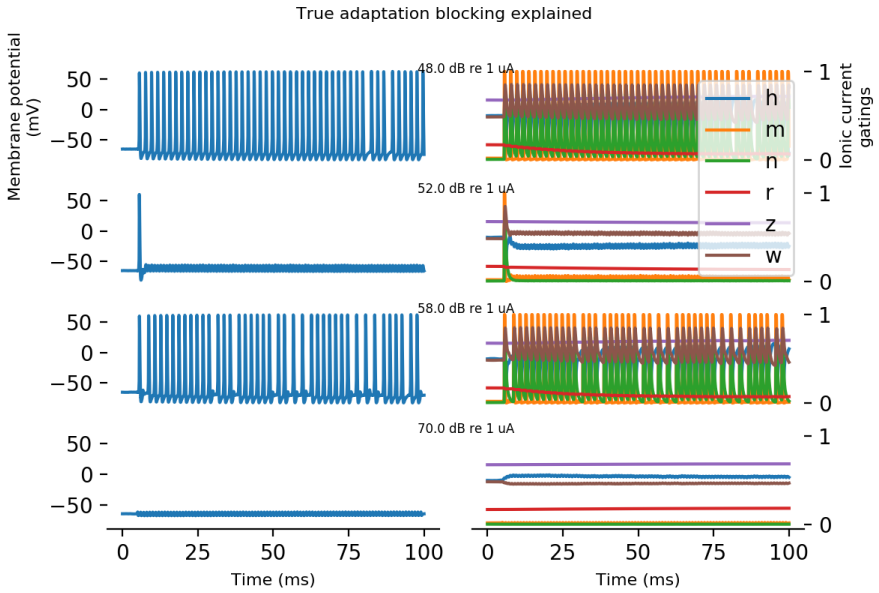

Figure 3.A.6: Spike-rate adaptation blocking at node of Ranvier P6. Due to the high pulse-rate, the SGN membrane potential is depolarised at P6

Fig. 3.A.5 A-D represent the 10 ms time window after stimulus onset (5 ms) from the response of a SGN to a pulse-train at 1000 pps for the "HH+HCN+KLT" model, at the highest electrode position using monophasic, cathodic pulses. Similar to Sec. 3.A.2, stimulations were performed at four different levels, 48 dB, 52 dB, 58 dB and 70 dB, according to the response to pulse trains presented in Fig. 3.3.2.

Although some hyperpolarization contours were noticed at 58 dB, APs at 48 dB and 58 dB were successfully elicited at the most peripheral node P0, sometimes simultaneously with P1, again successfully travelling towards C14. However, at 52 dB, yet a different phenomenon was observed: APs that were successfully elicited between P0 and P2 were blocked at node P6. A closer look at the ionic channel gatings at node P6 (Fig. 3.A.6) revealed that this blocking is due to the opening of the KLT channel activating gate w which is maintained in an open state by the ongoing stimulus. As a consequence of the strong w gate opening, the Na-activating gates stay closed for membrane current equilibrium, which brings the SGN into a state where APs cannot be generated. This is illustrated in the second row of Fig. 3.A.6, where all gates enter an equilibrium state after the initial event. Because this only happens in node P6 and not at P0 or C0 which also have KLT channels,

it is fair to assume that this mechanism is amplified by the large surface of this specific node, which causes the ionic current to be stronger at this particular node.

Finally, the ionic currents for intensities around 58 dB and below 70 dB became strong enough for P6 to elicit APs again. At 70 dB, the stimulus became too hyperpolarising at node P2 which caused a cathodic block, similar to the one explained in Appendix 3.A.2.

3.B Summary table single pulse responses

Table 3.B.1: Summary table single pulse responses healthy

Pulse type	Polarity	Model	Electrode position	Threshold	DR	Latency
Monophasic	Cathodic	HH	High	43	1.29	1.42
			Mid	58	1.33	1.63
			Low	60	0.93	1.14
		HH+HCN+KLT	High	44	1.28	1.28
			Mid	59	1.39	1.39
			Low	60	1.15	1.1
	Anodic	HH	High	47	0.98	1.15
			Mid	61	0.93	1.19
			Low	64	0.68	1.12
		HH+HCN+KLT	High	48	1.25	1.26
			Mid	61	1.13	1.15
			Low	64	0.89	1.15
Biphasic	Cathodic	HH	High	46	1.01	1.7
			Mid	60	0.9	1.43
			Low	63	0.75	1.22
		HH+HCN+KLT	High	47	0.98	1.31
			Mid	61	1.11	1.35
			Low	63	1.05	1.0
	Anodic	HH	High	49	0.96	1.56
			Mid	62	0.9	1.5
			Low	65	0.73	1.14
		HH+HCN+KLT	High	49	1.2	1.68
			Mid	62	1.04	1.35
			Low	65	1.03	1.15

3.C Summary table pulse train responses

Table 3.C.1: Summary table pulse train responses healthy SGN

Pulse type	Polarity	Model	Pulse rate	Electrode position	Threshold	DR	Latency
Monophasic	Cathodic	HH	250	High	43	1.17	1.19
				Mid	58	0.84	1.06
				Low	60	0.42	0.87
			1000	High	44	4.1	1.41
				Mid	58	4.14	1.47
				Low	61	2.53	1.68
			5000	High	39	7.07	1.24
				Mid	52	8.31	1.25
				Low	58	3.93	1.14
		HH+HCN+KLT	250	High	45	1.68	1.21
				Mid	59	1.68	1.08
				Low	60	1.33	0.89
			1000	High	46	3.17	1.39
				Mid	60	2.93	1.52
				Low	61	2.83	1.69
			5000	High	45	2.34	1.32
				Mid	57	2.14	1.32
				Low	60	1.32	1.2
	Anodic	HH	250	High	47	0.48	0.94
				Mid	61	0.77	0.82
				Low	64	0.77	0.54
			1000	High	48	2.89	1.79
				Mid	62	2.28	1.61
				Low	67	7.31	1.22
			5000	High	48	3.74	0.68
				Mid	62	10.68	0.49
				Low	60	9.25	0.47
		HH+HCN+KLT	250	High	48	1.37	0.97
				Mid	61	1.29	0.85
				Low	64	0.82	0.54
			1000	High	48	2.64	1.77
				Mid	62	2.54	1.61
				Low	67	6.58	1.28

			5000	High	47	2.2	0.8
				Mid	65	7.37	0.61
				Low	64	4.42	0.56
Biphasic	Cathodic	HH	250	High	46	0.73	1.08
				Mid	60	0.8	1.04
				Low	63	0.62	0.85
			1000	High	47	2.77	1.25
				Mid	61	2.52	1.24
				Low	63	1.47	0.98
			5000	High	46	5.36	1.29
				Mid	59	4.64	1.15
				Low	63	4.36	1.03
		HH+HCN+KLT	250	High	47	0.88	1.09
				Mid	61	0.87	1.07
				Low	63	0.72	0.88
			1000	High	48	2.45	1.24
				Mid	62	2.34	1.17
				Low	64	2.17	1.0
			5000	High	47	2.67	1.27
				Mid	60	3.46	1.19
				Low	63	2.6	0.97
	Anodic	HH	250	High	49	0.85	0.99
				Mid	62	0.73	0.96
				Low	65	0.7	0.68
			1000	High	50	3.31	1.34
				Mid	62	2.8	1.23
				Low	66	2.33	0.86
			5000	High	47	5.83	1.24
				Mid	60	5.4	1.18
				Low	64	5.32	0.93
		HH+HCN+KLT	250	High	49	0.86	1.0
				Mid	62	1.22	0.98
				Low	66	0.92	0.67
			1000	High	50	2.55	1.26
				Mid	63	2.42	1.2
				Low	66	2.44	0.85
			5000	High	48	3.15	1.23
				Mid	60	3.05	1.11

Low	64	3.21	0.92

4 Modelling the physiology of a single, unmyelinated or degenerated Spiral Ganglion Neuron (SGN)

4.1 Introduction

In Chapter 3, the complex interactions in the response of an electrically stimulated healthy SGNs were examined. In the deaf ear, the complexity of these interactions may be diverse, because of the different degrees of peripheral SGN degeneration that are related to deafness. The state of degeneration of SGN populations in the deaf ear is an important factor of Cochlear Implant (CI) performance (Pfingst et al., 2015; Shepherd and Javel, 1997). In addition, encoding of electrical signals is mostly affected by the ability of SGNs to elicit Action Potentials (APs) over a large range of amplitudes and varying timings. In that context, the effect of partial or total loss of the peripheral process could limit even more the ability to encode amplitude modulations and precise timing of an AP.

Typically, two levels of degeneration are reported: partial demyelination, which accounts for a loss of myelin sheaths on the peripheral process of the SGN; and full degeneration, where the peripheral process is completely absent (Kroon et al., 2017). Partial and full degeneration impact the electro-neuron interface differently. In the normal ear, the peripheral process innervates the Inner Hair Cell (IHC) which elicits an AP. Whenever the level of activity at the specific frequency is enough, large amounts of ions are released through mechano-chemical transduction into the synapse. The SGN then converts the received ions *via* chemo-electrical transduction which depolarizes the peripheral process (above threshold) at the synapse. In the implanted ear, however, elicitation of APs is induced directly at the membrane level by an electrical signal. As such, the quality of the electrode-neuron interface, defined by the health of the SGNs and their distance from the electrode, is a crucial factor in the performance of electrical stimulation. Electrode arrays are implanted inside scala tympani, aiming to place the electrodes as close as possible to the peripheral

process of SGNs (Gulya, 1996; O'Connell et al., 2016). However, loss of myelin reduces the electrical insulation of the SGN, effectively slowing down the travelling velocity of APs and increases the latency response relative to healthy neurons.

Understanding the impact of specific degeneration profiles of SGN populations would help to establish better stimulation strategies tailored for patient's specific needs. In order to better predict the effects of SGN loss of peripheral process, multiple models of the degenerated SGN have been studied. Most models consist of a healthy SGN model, similar to the model presented in Chapter 3, which physiological properties are then altered to simulate some degree of abnormality. To simulate partial demyelination, for example, the SGN's membrane capacitance is increased, which is equivalent to mimic the loss of myelin sheaths. In the full degeneration case, the entire peripheral section of the SGN is truncated to a single pre-somatic node (P6) while keeping a similar morphometrical disposition relative to the stimulating electrode.

Previous models of SGN degeneration have been used to explain the basic differences between healthy and unhealthy neurons, so as to understand the possible sources of variability that can be observed in listening performance by CI users.

From these models, the main finding is that partial demyelination doesn't affect thresholds but does modify AP latencies in proportions that can affect signal encoding (Rattay, Lutter, et al., 2001; Hanekom, 2001; Smit, Hanekom, van Wieringen, et al., 2010; Badenhorst et al., 2017). Moreover, full degeneration models indicate that SGN thresholds can increase significantly, depending on the pulse shape (Rattay, Lutter, et al., 2001), in agreement with data from CI users (Miller, Abbas, and Robinson, 2001; Macherey, Carlyon, Van Wieringen, et al., 2008; Undurraga, Carlyon, Macherey, et al., 2012). However, as the site of excitation is confined near the soma and the central axon, latencies are less impacted than in the partially demyelinated case (Miller, Abbas, and Robinson, 2001; Rattay, Lutter, et al., 2001; Rattay, Potrusil, et al., 2013).

In this Chapter, the impact that neural degeneration (full and partial) has on the Auditory Nerve (AN) will be examined. The "HH" model, similar to previous studies (Rattay, Lutter, et al., 2001; Hanekom, 2001; Smit, Hanekom, van Wieringen, et al., 2010; Badenhorst et al., 2017), and the "HH+HCN+KLT" model will be used to assess the effect of additional voltaged-gated delayed-rectifier potassium (KLT) and

voltage-gated hyperpolarization-activated cation (HCN) ionic channels.

Such neural degeneration models should match existing models of peripheral neural degeneration and better represent spike rate adaptation and accommodation.

4.2 Methods

This Chapter employs the model that was presented in Chapter 2 to model both partially demyelinated and fully degenerated SGNs in response to monophasic and biphasic monopolar pulse shapes. The electrode positions are as described previously (see Chapter 2). Stimulations were performed for various combinations of parameters: 2 pulse shapes (monophasic and biphasic) x 2 polarities (anodic and cathodic) x 3 positions (high, mid, low) x 3 pulse rates x 2 ionic models.

4.2.1 Stimulus

Both single pulses and pulse trains were used as in Chapter 3, all pulse width were fixed to 50 µs and a 1 µs interphase interval was added for biphasic pulses. As per Chapter 3, both monophasic and biphasic pulse-shapes were studied in this chapter. The study of monophasic pulse shapes in this thesis has two main benefits: 1) it allows for the exploration of parameters which are not ethically acceptable in humans; 2) it shades light on the effects of the discharge phase of biphasic pulses by its absence. Biphasic pulses were all symmetrical, with varying polarities. Pulse rates of 250, 1000 and 5000 pps were used for pulse trains simulations.

4.2.2 Ionic channel models

Two ionic channel models, both previously defined in Chapter 2, were tested: 1 the "HH" model presenting the warmed fast activating sodium (Na) and voltaged-gated high-threshold inactivating potassium (Kv) channels equations from Rothman (2003); 2 the "HH+HCN+KLT" channel model adding HCN and KLT channel equations from Rothman (2003). All conductances and temperature shifts are reported in Chapter 2.

4.2.3 SGN Morphology

Partially demyelinated and fully degenerated human SGNs were modelled according to the morphology previously used in similar studies (Rattay, Lutter, et al., 2001; Rattay, Potrusil, et al., 2013; Smit, Hanekom, van Wieringen, et al., 2010). Morphology parameters are reported in Chapter 2.

4.2.4 Degenerated and partially demyelinated model validation

Validation of the degenerated and partially demyelinated SGN was conducted by simulating these two conditions using single pulse stimulus with 0.1 ms pulse width to compare with the previous report by (Rattay, Lutter, et al., 2001).

4.2.4.1 Full degenerated SGN: single pulse response

Loss of the peripheral process causes dramatic changes to the SGN response, namely large thresholds increase and reduced Dynamic Range (DR) (Rattay, Lutter, et al., 2001). Rattay, Lutter, et al. (2001) reported that thresholds for their model of degeneration were −3200 µA, −2400 µA, −1900 µA for monophasic cathodic pulses, and 1500 µA, 1100 µA, 800 µA for monophasic anodic pulses, at −200, −500 and −800 µm electrode positions, respectively.

Fig. 4.2.1 shows the results of the simulations for the model, and is described for validation of the SGN degeneration models. The results for validation are presented in micro-amperes to enable comparison with Rattay, Lutter, et al. (2001) and the corresponding "dB re 1 µA" value is presented in parenthesis. However, further descriptions of results in Sec. 4.3 will be presented in "dB re 1 µA". First, thresholds for the "HH+HCN+KLT" model were −2790 µA (68 dB), −2067 µA (66 dB) and −1598 µA (64 dB) for cathodic and 1718 µA (64 dB), 1235 µA (62 dB), and 892 µA (59 dB) for anodic polarities, respectively at −200, −500 and −800 µm electrode positions. Thus, the corresponding anodic/cathodic ratios for the "HH+HCN+KLT" model were 0.61, 0.59, 0.56 at −200, −500, and −800 µm electrode positions, respectively.

Similarly, thresholds obtained with the "HH" model were −2416 µA (67.5 dB), −1789 µA (65 dB) and −1385 µA (62.8 dB) for cathodic and 1690 µA (64.5 dB),

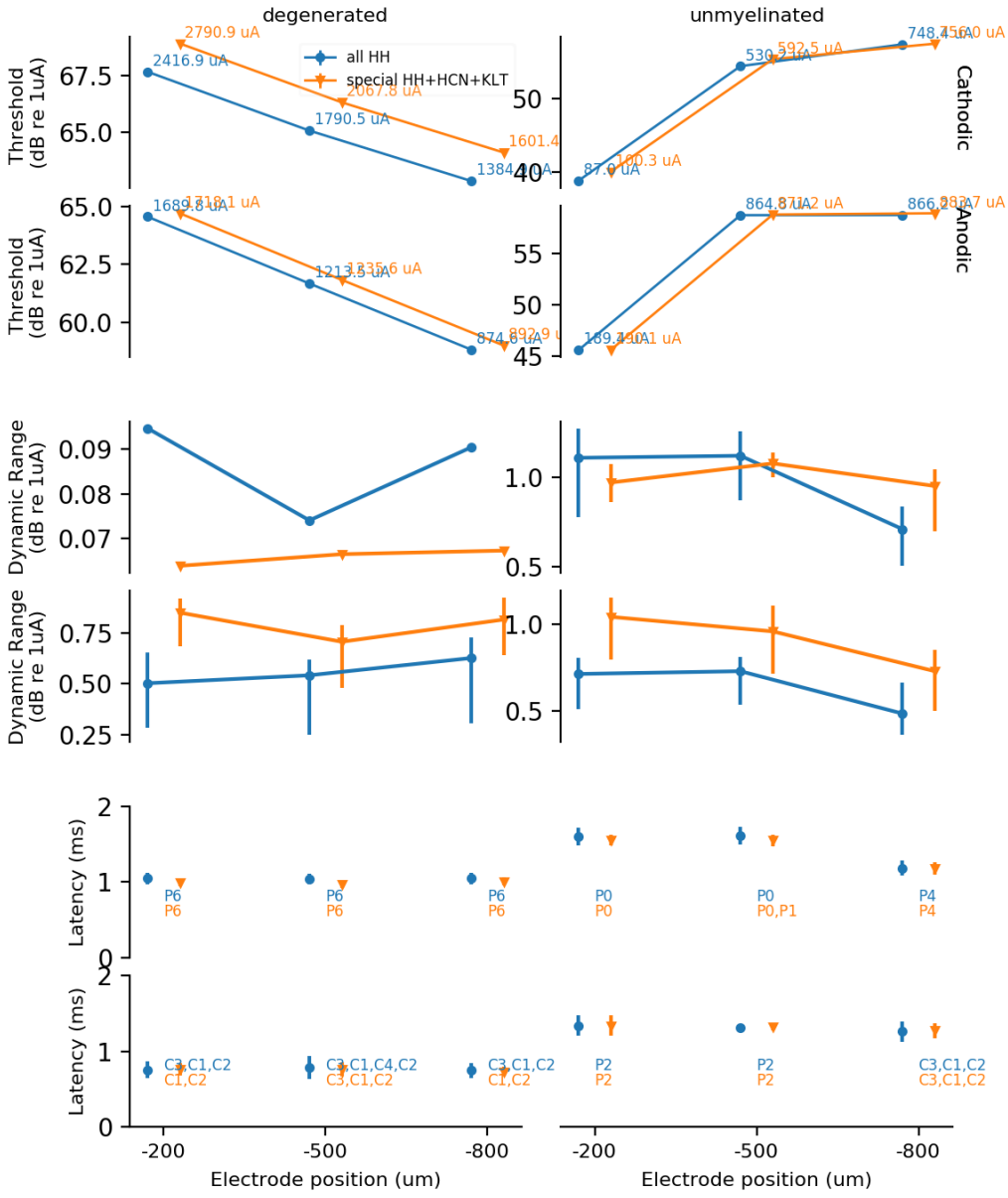

Figure 4.2.1: Validation for degenerated and partially demyelinated thresholds and DRs.

1213 µA (61.7 dB) and 874 µA (58.8 dB) for anodic polarities, giving anodic/cathodic ratios of 0.70, 0.67, 0.63 for −200, −500, and −800 µm electrode position, respectively.

Both models presented here show threshold and anodic/cathodic ratios that differ slightly from the previous study by Rattay, Lutter, et al. (2001). Although ratios from the "HH+HCN+KLT" model were higher than for the "HH" model, they followed a similar decreasing pattern with lowering electrode positions in addition to the quantitative values being consistent with those of Rattay, Lutter, et al. (2001). Again, the ratios and thresholds for the "HH" model are not perfectly matched to the values reported by Rattay, Lutter, et al. (2001) but lie in a similar range with average deviations of 25% for cathodic and 10% for anodic stimulations when compared to that study.

The difference in ratios compared to those of Rattay, Lutter, et al. (2001) seems to derive from a relatively small increase in anodic thresholds and a decrease in cathodic thresholds. Cathodic thresholds in our model were on average 14% smaller than in Rattay, Lutter, et al. (2001) whilst anodic threshold were 13% larger than in Rattay, Lutter, et al. (2001). These differences are most likely due to the small morphological and modelling differences outlined in Chapter 2, and these are responsible for the ratio being slightly higher in the model presented here.

The observed differences in thresholds are most likely explained by small differences in the parameters of the implemented model such as morphology and specific values of conductances. Overall, the current model of degeneration provides predictions consistent with previous reports.

In terms of DR, values ranged from 0.05 to 0.8 dB and were higher for the anodic stimulation polarity (0.5 to 0.8 dB) than for the cathodic conditions (0.05 to 0.1 dB). This contradicts previous reports from animal studies were the SGNs from deafened animals were found to have an equal or greater DR than the SGNs from undeafened animals (Sly et al., 2007). This effect might be explained by the fact that the fully degenerated SGN model presented has a preserved pre-somatic (P6) node of Ranvier, similar to the degeneration model of Smit, Hanekom, van Wieringen, et al. (2010), and which can interfere with the normal firing of the SGN.

Finally, a shift in latencies of between 0.2 and 0.5 ms was observed for the degenerated SGN model when compared to the healthy SGN model from Chapter 3. This can be explained by a shift in the site of excitation to a more central node of

Ranvier, the result of the absence of the peripheral process. This is in accordance with animal reports in guinea pigs Sly et al. (2007) and Ramekers et al. (2014) and with human Electrically evoked Auditory Brainstem Responses (EABRs) responses Undurraga, Carlyon, Wouters, et al. (2013b).

4.2.4.2 Partially demyelinated SGN: single pulse response

The myelin sheaths insulating the internodes, and partially the cell body of SGNs, play an important role in the transport of APs along the neuron. Its insulating properties allow for currents to flow along the SGN and strongly participate in the AP saltatory behaviour. When subjected to demyelination, the membrane capacitance of the SGN increases, which in turn slows down the travelling speed of the AP (Tagoe et al., 2014; Brown and Hamann, 2014).

For the purpose of this study, partial demyelination was modelled by removing half the number of myelin sheaths on the SGN peripheral process. Similar to the fully degenerated model, the partially demyelinated SGN was stimulated using single pulses of 0.1 ms pulse width for both cathodic and anodic polarities to allow for comparison with thresholds and anodic/cathodic ratios from Rattay, Lutter, et al. (2001). Thresholds, DRs, and latencies are shown in Fig. 4.2.1.

Validation of the healthy SGN with biphasic stimulation in Chapter 2 showed that thresholds for the "HH" model were 77.5 µA (37.8 dB), 438.4 µA (52.8 dB), and 548.5 µA (54.8 dB) for cathodic pulses, and 144.9 µA (43.2 dB), 734.5 µA (57.3 dB), and 869.0 µA (58.8 dB) for anodic monophasic pulses at 200 µm, 500 µm and 800 µm electrode positions, respectively. Here, as shown in Fig. 4.2.1, thresholds for the partially demyelinated SGN for the biphasic stimulation conditions were very similar; 87.0 µA, 530 µA and 748.5 µA for cathodic, and 189 µA, 864 µA and 866.0 µA for anodic monophasic pulses at 200 µm, 500 µm and 800 µm electrode positions respectively.

It can then be concluded that, as the peripheral process is preserved, threshold levels for the partially demyelinated SGN remain relatively similar to the healthy SGN model. However, when examining the latencies differences between healthy and partially demyelinated SGNs, large differences are apparent. While healthy SGN latencies ranged between 1.1 and 1.2 ms in the cathodic-first condition,

partially demyelinated SGN model latencies were in the range 1.2-1.75 ms. Similarly, although in a much lesser degree, anodic-first latencies also increased in the partially demyelinated model, ranging between 1-1.2 ms for the healthy model and between 1.2-1.5 ms in the partially demyelinated case. This is in line with previous literature, reporting latencies often 3-fold larger than in a healthy SGN (Tagoe et al., 2014; Brown and Hamann, 2014).

In summary, results predict thresholds and latency changes which agree well with previous studies (animal, human, and computation models) and validate the implementation of our model. Both fully degenerated and partially demyelinated models constitute acceptable predictions for the behaviour of previously reported partial and fully degenerated SGN data.

4.3 Results

This chapter aims to characterise the response behaviour of partially demyelinated and degenerated compartment models of single human SGNs when equipped with the additional ionic channels HCN and KLT. Unhealthy human SGNs were modelled for 3 electrode positions under single pulse and pulse trains, biphasic and monophasic pulse shapes for cathodic and anodic polarities. First, single-pulse responses that provide important insight into the model's ability to exhibit basic features of the electrically stimulated SGN such as threshold shifts, polarity sensitivity, and stochasticity for both types of degeneration are presented. Second, responses to trains of pulses are described in order to characterize the behaviour of a modelled single healthy SGN subjected to a more realistic CI stimuli using two degeneration models.

4.3.1 Single Pulse Responses

Because the different ionic channel configurations present different voltage dependent characteristics, the overall threshold of the neuron can change across ionic model distributions. In addition to differences between ionic channels, the SGN also behaves differently when subjected to varying pulse types and polarities. Here, the model dependent properties for single human, partially demyelinated and degenerated SGNs when subjected to single pulse stimulation are inspected.

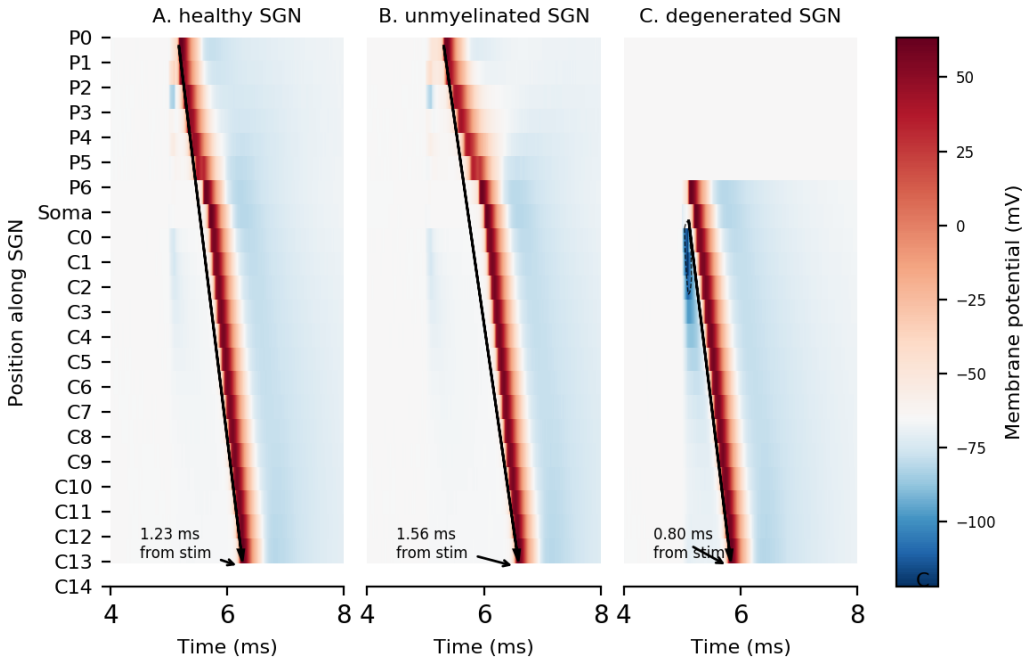

Figure 4.2.2: Effects of degeneration on single AP latency. Action potentials at threshold level for A. a healthy SGN, B. a partially demyelinated SGN and, C. a degenerated SGN). A) an AP is elicited at P0 in an healthy cell, and travels centrally in 1.32 ms from the stimulus onset. B) an AP is elicited at P0, at a similar amplitude level than A, in a partially demyelinated cell, and travels centrally in 1.64 ms from the stimulus onset. This AP will effictively arrive 0.32 ms later than the healthy cell AP. C) an AP is elicited after increasing amplitude x10 compared to healthy cell (A). Site of excitation is shifter centrally to P6, and AP travels in ms, slower than healthy cell but faster than partially demyelinated cell. Simulations were done with monophasic, cathodic pulses.

For each degeneration profile, i.e. partially demyelinated and degenerated, Firing Efficiency (FE) curves which encapsulate the stochasticity of firing rate of the SGN are simulated . Both thresholds and DRs for each simulated condition were extracted from the FE curves as described previously (see Chapter 3). Finally, mean latencies were computed by pooling and averaging latencies across the entire range of stimulating amplitudes.

4.3.1.1 Partially demyelinated SGN

Fig. 4.3.1 shows a summarised representation of the modelled FE curves for all partially demyelinated configurations. Thresholds across all electrode positions and pulse conditions ranged between 45 and 65 dB, similar to the healthy SGN model presented in Chapter 3. Also, thresholds increased with lower electrode positions, with the maximum threshold found at −800 µm, i.e. the low electrode position, for all pulse shape conditions. Differences in threshold between ionic channel models were never more than 1 dB, with the "HH+HCN+KLT" model systematically showing the higher thresholds.

DRs for the partially demyelinated neurons were between 0.45 and 1.1 dB, slightly smaller (0.5 dB) than those of healthy SGNs presented in Chapter 3. The highest DRs were found for the highest and mid electrode positions, whilst the lowest electrode position systematically showed the lowest DR values. In addition, the "HH" ionic channel model systematically showed DRs equal to, or lower than, the "HH+HCN+KLT" model, with the biggest offset (0.4 dB) occurring for the anodic monophasic condition at the highest electrode position.

Furthermore, latencies for the partially demyelinated SGN model were much larger than for healthy and degenerated models (0.2 to 1 ms larger). Because of the loss of myelin insulation, it takes more time for APs to saltate along the peripheral process, effectively increasing the AP travelling time. This is in line with the validation that was made in this chapter and with previous reports (Rattay, Lutter, et al., 2001; Frijns, de Snoo, et al., 1995) Here, AP latencies ranged between 0.95 and 1.75 This corresponds to 800 µs jitter, almost 2-folds larger than the degenerated SGN latency that was found during validation. Shorter latencies were predicted for the anodic case as the site of initiation was more central than for cathodic case. This

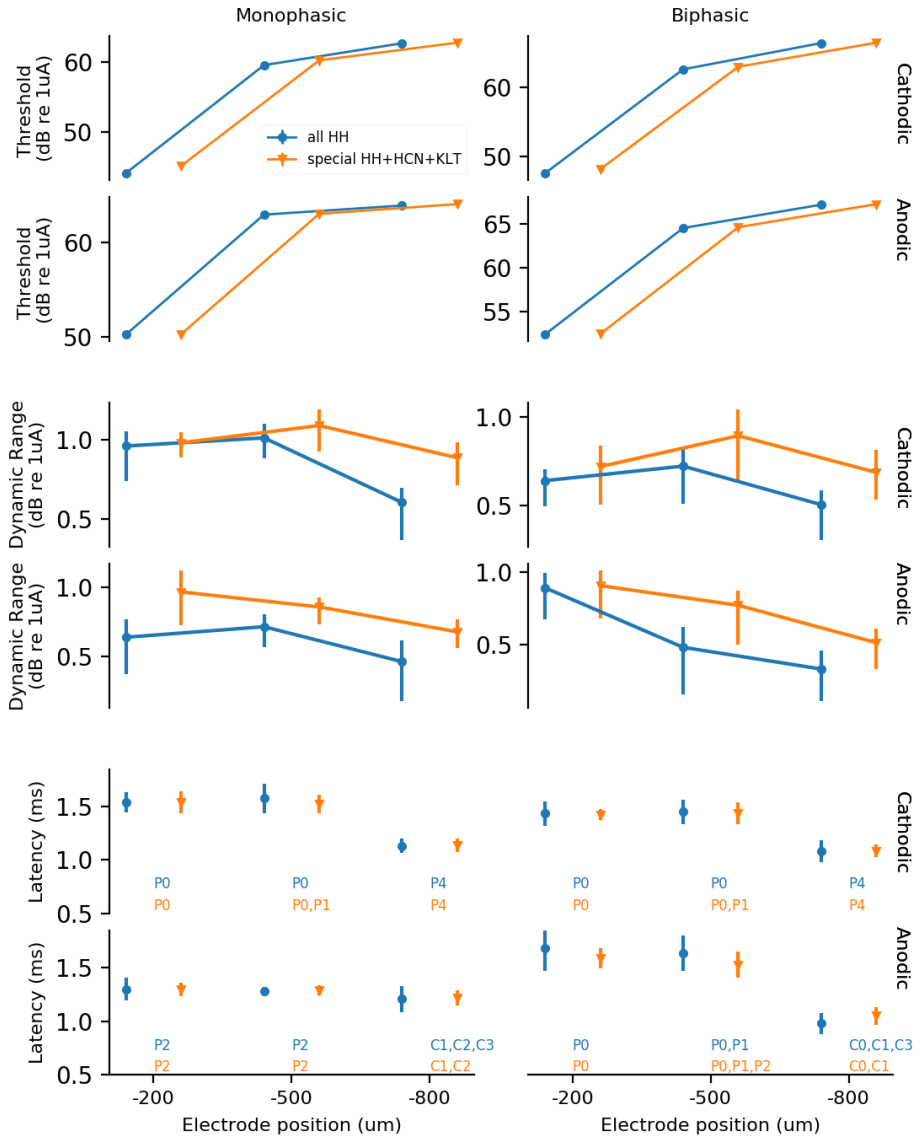

Figure 4.3.1: Summary of thresholds (top panel), dynamic ranges (middle panel), and latencies (bottom panel) estimated from FE curves in response to monophasic and biphasic single pulse stimulus for a partially demyelinated SGN. The "all-HH" model is indicated in blue whilst the "special HH+HCN+KLT" is indicated in orange. Pulse shape, polarity, and electrode position are indicated on top, right, and bottom axis, respectively. The site of excitation (denoted by the node name) is indicated in the latency panel.

increased jitter in demyelinated SGNs could be explained by the reduced myelin insulation causing a reduction in site of excitation specificity. Because of the less reliable currents at the membrane level and through the neuron, more nodes can be subject to external excitation (Resnick et al., 2018; O'Brien, 2016).

Although the partially demyelinated SGN is predicted to preserve almost normal thresholds and DRs, the important differences in latencies observed here for single pulse responses constitute a major feature. Together with the shorter latencies found for degenerated SGNs, these predictions need to be taken into account when designing stimulation strategies aiming to preserve temporal fine structure and binaural processing for bilateral CIs.

4.3.1.2 Degenerated SGN

Fig. 4.3.2 shows thresholds, DRs, and latencies derived from FE curves for all fully degenerated configurations. Threshold levels for both monophasic and biphasic pulse shapes to both polarities were high relative to the healthy SGN case (10 to 15 dB higher), ranging between 65 dB and 76 dB. Across all stimulus conditions, threshold decreased with lower electrode positions, indicative of the lack of a peripheral process. Contrary to healthy SGN responses presented in Chapter 3, the cathodic thresholds were systematically higher than the anodic for both biphasic and monophasic pulses. Biphasic thresholds were on average 2.5 dB higher than monophasic thresholds, similar to the healthy and partially demyelinated SGN models. This is similar to human data reported by Macherey, Van Wieringen, et al. (2006) where biphasic pulse thresholds were found to be on average 3.4 dB higher than pseudomonophasic pulses when presented at a pulse rate of 198 pps.

Here, the loss of peripheral process favours central AP initiation sites, more effectively elicited by anodic stimulus. As the electrode position lowers, the strength of the anodic stimulus required to elicit an AP decreases as the electrode comes closer to the soma. This is an important feature of the degenerated SGN as it implies that CI stimulation strategies should take into account the stimulus polarity required to excite the AN efficiently in cochlear regions with loss of peripheral processes.

DRs for the fully degenerated model were relatively small when compared to

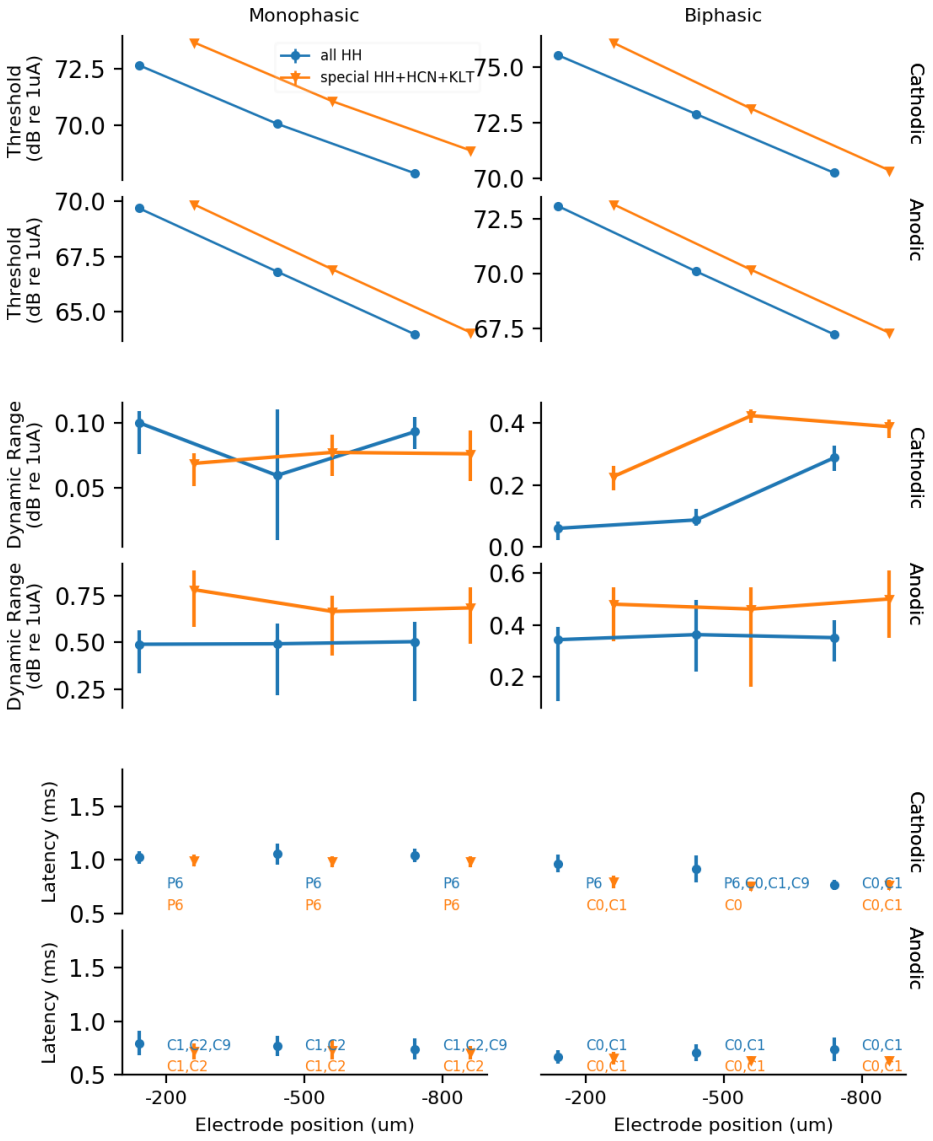

Figure 4.3.2: Firing Efficiency curves in response to monophasic and biphasic single pulse stimulus were modelled for a degenerated SGN. The 50% FE, or threshold, DR and latencies are recorded here. Different polarities, electrode positions and ionic distributions were tested to understand basic differences. Top panel shows the thresholds for both models, at 3 electrode positions, for monophasic and biphasic stimuli and for the two polarities. Mid panel shows the corresponding DRs for those conditions and bottom panel shows the corresponding latencies and observed site of excitations.

healthy and partially demyelinated SGNs. Across all conditions, the degenerated SGN model predicted DRs spanning 0.05 to 0.75 dB, definitely on the low end of realistic DRs (Javel and Viemeister, 2000). Generally, DRs for the anodic conditions were much higher than for the cathodic ones.

Furthermore, this effect seemed less important for biphasic pulses, where cathodic-first pulses showed higher DR values (by 0.2 dB) than cathodic monophasic pulses, most likely due to the presence of the counteracting anodic second phase in the biphasic case. Monophasic cathodic pulses were the least effective, with DRs below 0.1 dB, while anodic pulses showed larger values for the "HH+HCN+KLT" model with DRs from 0.5 to 0.75 dB. Similarly, biphasic anodic pulses showed better DR values ranging from 0.5 to 0.75 dB while the cathodic condition DR values ranged from 0.05 to 0.4 dB.

Differences between the two ionic channel models were apparent, with the "HH+HCN+KLT" model systematically showing higher DR values than the "HH" model DRs. DR being principally a function of the Scaling Factors (SFs) that were established in Chapter 2, the higher DRs predicted for the "HH+HCN+KLT" could mean that the inclusion of HCN and KLT channels would make the SGN slightly less sensitive to the loss of the peripheral process than the "HH" model for single pulse conditions.

Finally, latencies for the degenerated SGN were found to be relatively short with maximum values at 1.1 ms. This was expected, as the loss of peripheral process means that APs are elicited more centrally, and thus latencies are largely shortened. Shorter latencies, increased thresholds, and switches in polarity preference are perhaps the most important features of the degenerated SGN model, dramatically changing the signal being transmitted when compared to healthy and partially demyelinated SGN responses.

4.3.2 Pulse-train Responses

As indicated in Sec. 4.2, responses of SGNs to pulse trains presented at several rates were also examined. Previous studies have reported pulse-train responses of SGNs in the form of Gaussian distributions or FE curves, similar to the distributions evoked by single pulse (Badenhorst et al., 2016, 2017). However, due to the

complex stimulus interactions described in Chapter 3, the presence or absence of the SGN peripheral process, and the additional ionic channels that were added in this thesis, SGN's spike-rate functions to pulse-trains at different pulse rates, electrode positions, and pulse shapes were non-monotonic with increasing stimulus intensity. Most often, responses could not be fitted with Gaussian distributions or FE curves because of their **bimodal** behaviour. Because of this, the pulse-train responses were characterised using the principles that were described in Chapter 3. Namely, pseudo-FE curves were fitted on the first rising edge of the responses to insure homogeneity in the reported measures.

Below, a summary of spike-rate functions for a SGN subjected to a range of stimulus conditions with the aim of understanding how these responses might help predict better the overall behaviour of unhealthy SGNs is described. Then, some of the mechanisms that explain the **bimodal** behaviour above mentioned will be illustrated.

As this chapter focuses on the effect of peripheral, partial and full, degeneration on SGN responses, only the most representative spike-rate functions will be described. A detailed analysis of spike-rate functions is reported in Appendix 4.A.

4.3.2.1 Partially demyelinated SGN

As described in Sec. 4.2, partial demyelination was defined as the removal of half the number of myelin sheaths normally insulating a healthy SGN (see Sec. 4.2.4.2). As the peripheral process of the SGN is partially preserved, it is to be expected that some features found in Chapter 3 for healthy SGN will also be present for partially demyelinated SGN models.

Looking at the spike-rate functions for the partially demyelinated SGN under both monophasic and biphasic (see Appendix 4.A) pulse shapes, note that both **unimodal** and **bimodal** spike-rate functions are observed.

Values for thresholds, DRs and latencies are summarized in Fig. 4.3.3, Fig. 4.3.4, and Fig. 4.3.5.

Monophasic vs. Biphasic pulse train thresholds Overall, Fig. 4.3.3 (panels A and B) show that thresholds ranged between 39 and 65 dB across all the simulated conditions. These thresholds were very similar to the healthy threshold levels that

were presented in Chapter 3 (cf. Fig. 3.3.6), suggesting that thresholds will not be significantly affected by partial demyelination.

Effects of electrode position were found to be significant for multiple conditions. In both models, thresholds increased at lower electrode positions, indicative of the presence of the peripheral process which favours the cathodic polarity. Note that although the thresholds almost systematically increased between the mid and low position, a slight decrease was observed at 5000 pps for monophasic anodic pulses. Mid position thresholds were systematically higher than those obtained at the high (10 to 15 dB higher) and at the low (2 to 5 dB higher) electrode positions.

Moreover, pulse shape effects were similar to those from the healthy SGN (Fig. 3.3.6), with biphasic thresholds from 2 to 3 dB higher than monophasic thresholds, albeit the difference was slightly smaller than in the healthy SGN, in line with previous modelling (Rattay, Lutter, et al., 2001) and human (Macherey, Van Wieringen, et al., 2006) reports.

Polarity effects were similar to the healthy SGN (Fig. 3.3.6), with anodic thresholds being systematically higher and sometimes equal to the cathodic thresholds. Anodic thresholds were higher by 1 to 10 dB depending on the stimulation rate and electrode position. Again, these were similar to those for the healthy case reported in Chapter 3 (Fig. 3.3.6) and in line with previous literature (Rattay, Lutter, et al., 2001; Rattay, Potrusil, et al., 2013)

In addition, the effects of stimulation pulse-rate were mostly significant for cathodic polarity and conditions above 1000 pps. Mainly, cathodic monophasic thresholds were found to be 5 dB lower at 5000 pps than 1000 pps for the "HH" model, which is contrasted to a relatively smaller difference in the healthy model (2 dB smaller at 5000 pps compared to 1000 pps as per Chapter 3). In the context of the partially demyelinated SGN model, this observation makes sense as the cathodic monophasic pulse shape will elicit APs more peripherally than its anodic counterpart which elicits APs more centrally. As in the partially demyelinated SGN model only the peripheral process of the neuron is affected, the stimulation conditions that elicit APs more peripherally will be more impacted by changes in pulse rate.

Finally, differences between the two ionic models related to threshold effects become more significant with increasing pulse rate and were larger for monophasic pulse shapes. The biggest difference ("HH" model being 6 dB lower) was observed for

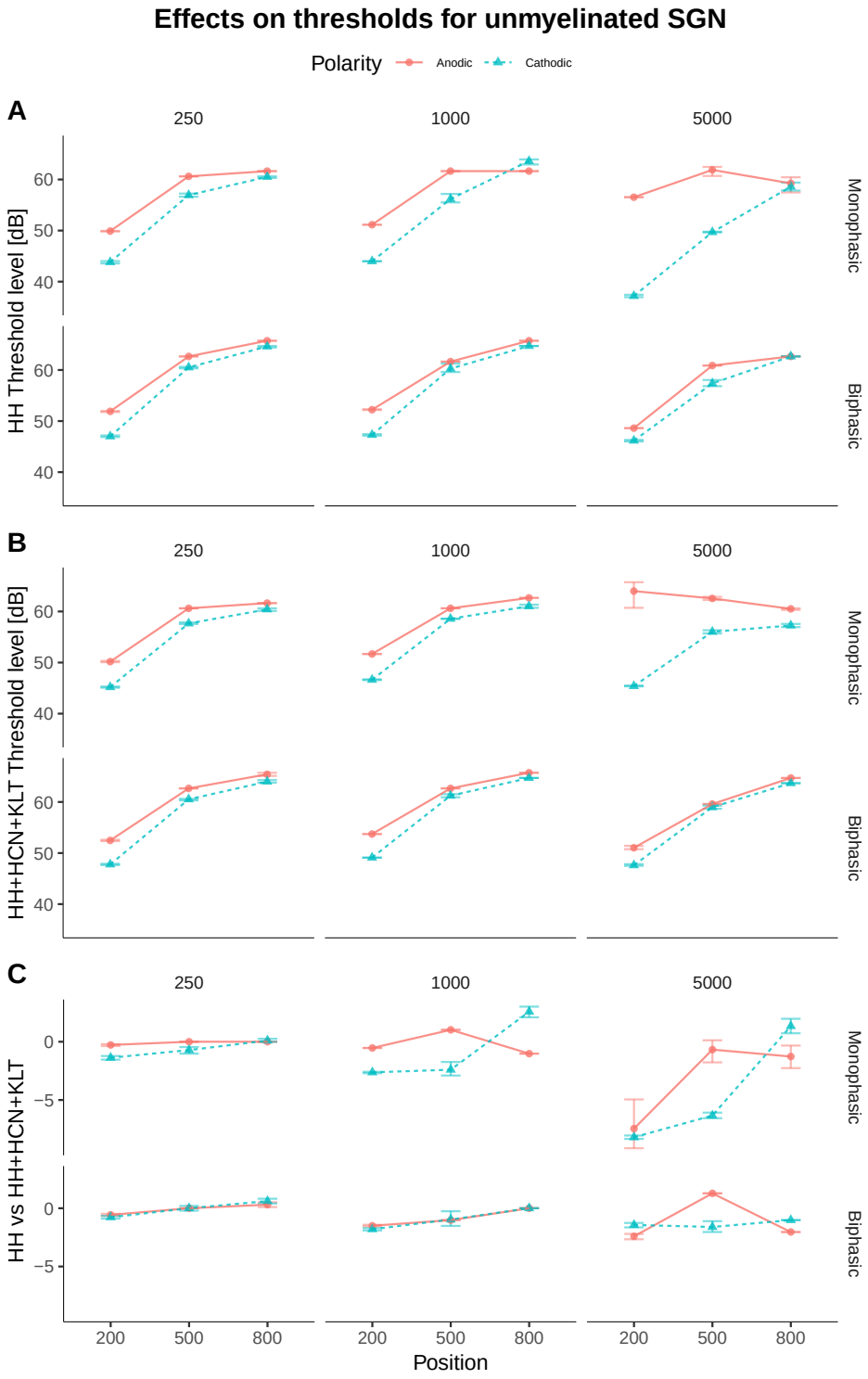

Figure 4.3.3: Threshold levels across models and stimulus conditions. A) threshold levels for the HH ionic model, B) the HH+HCN+KLT ionic model, C) the difference between the simulated threshold levels for the HH and HH+HCN+KLT.

the high electrode position at 5000 pps with an anodic monophasic pulse. This is on the higher end of the range of threshold shifts observed for the healthy SGN model (see Chapter 3) and for single-pulse responses generally. However, the thresholds are still in the range of previous reports (Rattay, Lutter, et al., 2001; Badenhorst et al., 2017)

Monophasic vs. Biphasic pulse train dynamic range The DRs shown in Fig. 4.3.4 ranged between 0.05 and 7.7 dB which is relatively smaller than healthy SGN DRs and relatively lower than the range of previous animal studies (e.g. Javel and Viemeister, 2000).

Overall, DR values were relatively variable between the monophasic and biphasic conditions. The biphasic DRs were consistently smaller or equal to the monophasic condition. Moreover, at the high electrode position, DRs were very small except for the highest pulse rate, i.e. 5000 pps. Interestingly, as shown in Fig. 4.3.4, DRs slightly increased (0.5 to 1 dB) as electrode positions was lowered.

Polarity effects on the DR values were mostly observed to be significant at the highest electrode position (around 4 dB, at 1000 pps, higher for anodic) and at high pulse rates (2 to 7.5 dB, at 5000 pps, higher for anodic polarity). For these conditions, anodic and anodic-first simulations always produced higher DRs. These results are interesting considering the fact that the peripheral process is partially demyelinated. The model suggests that for a SGN with a partially demyelinated peripheral process, anodic pulse trains could encode a wider range of intensities than cathodic ones. The opposite outcome is predicted for healthy SGNs (see Chapter 3).

Interestingly, simulations using low pulse rate predicted very low DRs at high electrode positions, and this was relatively consistent across the two ionic models. Further, at 5000 pps, some conditions for the "HH+HCN+KLT" generated a null in spiking activity due to the high pulse-rate and a potentially higher sensitivity of the HCN and KLT ionic channels to demyelination.

Fig. 4.3.4 panel C shows that differences between ionic models for DR values ranged from 1 dB to a maximum of 4 dB for the highest electrode position, for anodic polarity, and for both monophasic and biphasic conditions at 1000 pps. As the DRs of the "HH" model were lower in both cases, it can be derived that this difference was caused by the lack of the additional KLT and HCN. This indicates

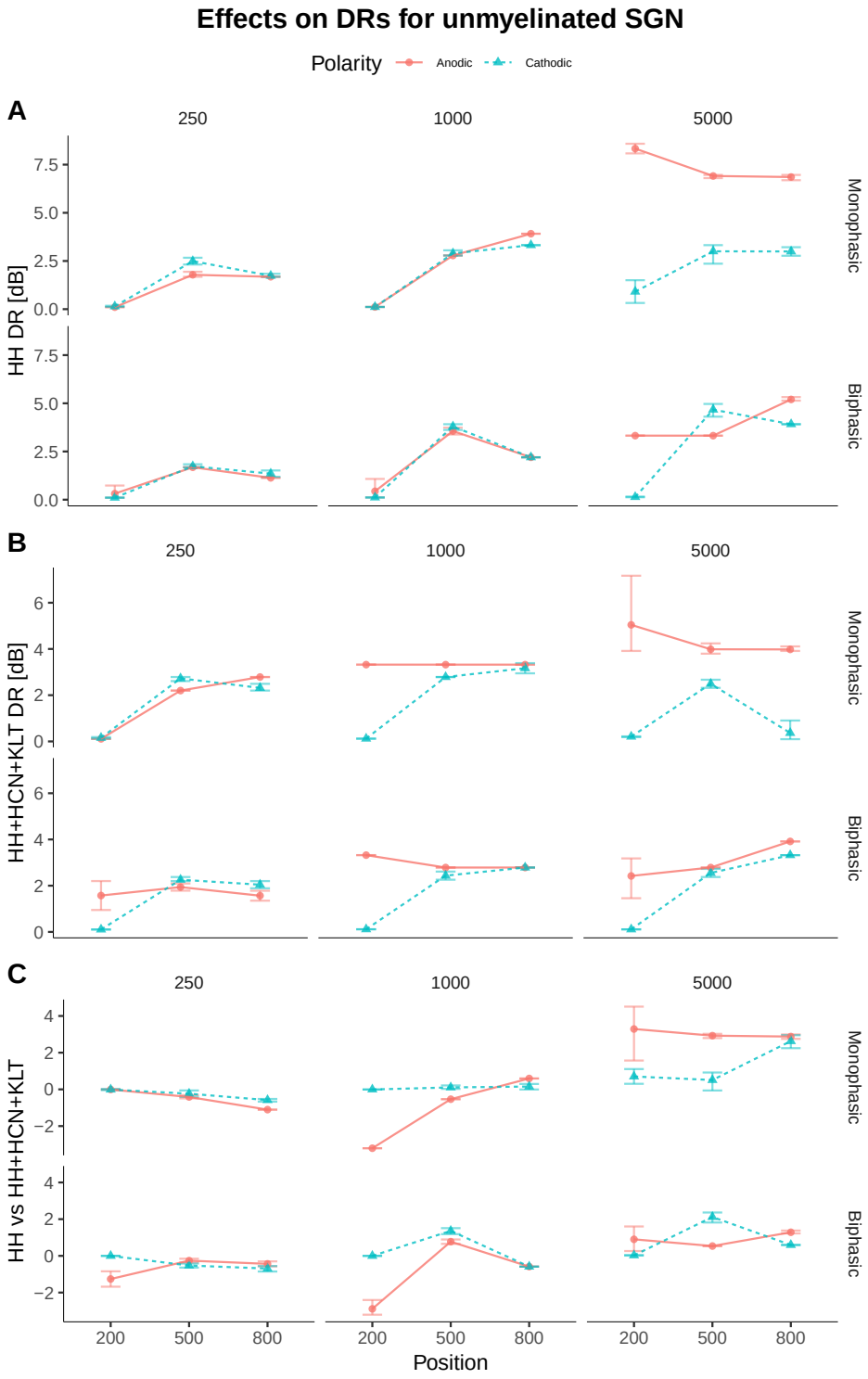

Figure 4.3.4: DR across models and stimulus conditions. A) DR for the HH ionic model, B) the HH+HCN+KLT ionic model, C) the difference between the simulated DRs for the HH and HH+HCN+KLT.

that the extra ionic channels might help increase anodic DR.

Monophasic vs. Biphasic pulse train latencies In Fig. 4.3.5 the latencies for the partially demyelinated SGN under multiple stimulation conditions were reported. In a recent study, Resnick et al. (2018) highlighted that demyelination had a strong impact on latencies. Here, the SGN model latencies ranged between 0.5 to 2.2 ms, in line with those reported by Resnick et al. (2018).

Interestingly, variability in latencies was more important in the monophasic condition than in the biphasic. Monophasic latencies ranged from 0.5 to 2.2 ms, whilst the biphasic latencies were in the range 0.5 to 1.7 ms. This is an important feature of pulse shape to consider with regards to the possibility of asymmetrical pulse shape stimulation. Here, the monophasic pulse shape shows increased differences in latencies due to the absence of the discharge phase, which is known to increase refractoriness. By changing the nature of the nodal interactions, the discharge phase increases the initiation-site specificity, in turns decreasing the variability in latencies.

Electrode position was also found to have an important effect on latencies across all conditions, where the latencies systematically decreased for lower electrode positions. This accords with the place of excitation moving towards the central axon at lowering electrode position. These significant differences ranged from 0.1 ms in monophasic conditions, to 1 ms at the high and low electrode positions, for biphasic stimulations, and both polarities. This large effect is explained by the fact that the partially demyelinated SGN has an intrinsically longer AP conduction time due to it having a less insulated peripheral process, but also because the site of excitation at the lower electrode position shifts to a more central node of Ranvier, creating a relatively large difference (Rattay, Lutter, et al., 2001; Resnick et al., 2018)

Moreover, highly significant polarity effects were observed for both monophasic (from 0.5 to 1 ms) and biphasic (from 0.1 to 0.2 ms) pulses, where the anodic polarity systematically showed shorter latencies. Again, this is not surprising as anodic and anodic-first stimulus elicit APs more centrally and in the case of partially demyelinated SGNs, this also means they bypass the relatively slowly saltating peripheral process.

A relatively large effect of pulse rate on latencies for the monophasic stimulations was also observed. First, latencies became longer between 250 and 1000 pps, but

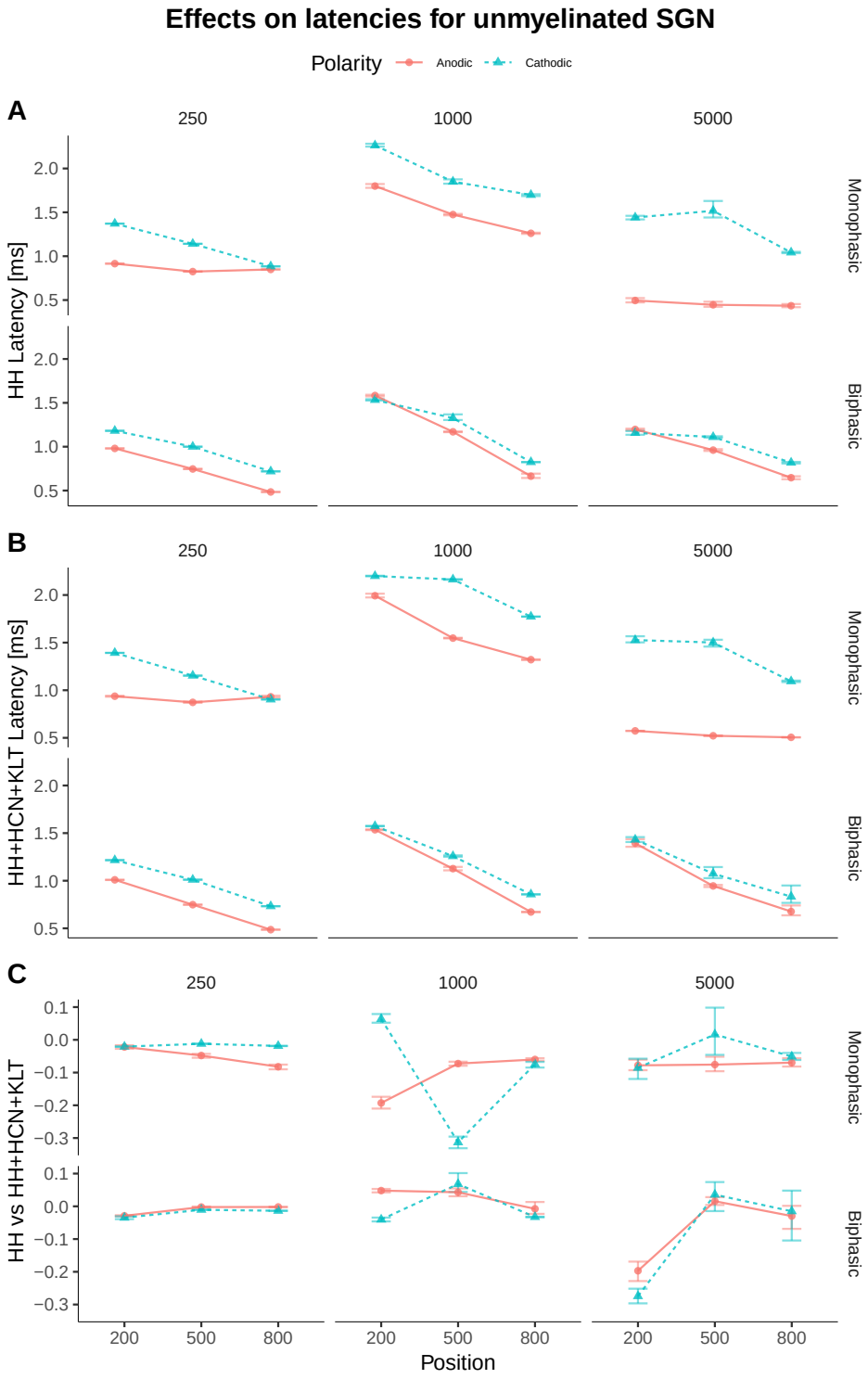

Figure 4.3.5: Latencies across models and stimulus conditions. A) Latencies for the HH ionic model, B) the HH+HCN+KLT ionic model, C) the difference between the simulated latencies for the HH and HH+HCN+KLT.

decreased again at 5000 pps to become similar to, or lower than latencies at 250 pps. This is to be expected, as the 1 ms period of 1000 pps which period is in the range of the Relative Refractory Period (RRP) (Rattay, Lutter, et al., 2001). As such, the latencies increased because the APs took longer to be elicited than at 250 pps.

Finally, differences between ionic models were mostly significant at 1000 pps, at the high electrode position for monophasic pulse shapes where the "HH" model predicted latencies 100 µs longer for the cathodic polarity and 200 µs shorter for the anodic polarity.

4.3.2.2 Degenerated SGN

Overall, as described in Sec. 4.3.1.2, thresholds for the degenerated SGN to single pulses were observed to be relatively high across all electrode positions when compared to the healthy and partially demyelinated SGN models. Similarly, pulse train thresholds for the degenerated SGN were higher than the healthy and partially demyelinated SGN and decreased with lowering electrode positions across all polarity and pulse rate conditions.

The spike-rate functions for the degenerated SGN under both monophasic and biphasic stimulation (see Appendix 4.A) were found to be either monotonic or **unimodal**, indicating that most interactions observed for healthy and partially demyelinated SGNs were due to the presence of the peripheral process. Threshold values, DRs and latencies for the degenerated SGN are summarized in Fig. 4.3.6, Fig. 4.3.7 and Fig. 4.3.8, respectively.

Monophasic vs. Biphasic pulse train thresholds Threshold levels for the degenerated SGN under pulse-train stimulation are shown in Fig. 4.3.6 A-C. Overall, threshold levels ranged from 65 to 75 dB re 1 µA (1778 to 5623 µA), definitely higher than realistic thresholds and from thresholds measured *in vivo* in humans. However, these values are a close match to previous reports on degenerated SGN modelling (Rattay, Lutter, et al., 2001; Badenhorst et al., 2017).

Degenerated SGN threshold levels were significantly higher than healthy and partially demyelinated thresholds across polarities, electrode positions, and pulse rates for both pulse shapes (between 2 and 5 dB) in line with the single pulse results.

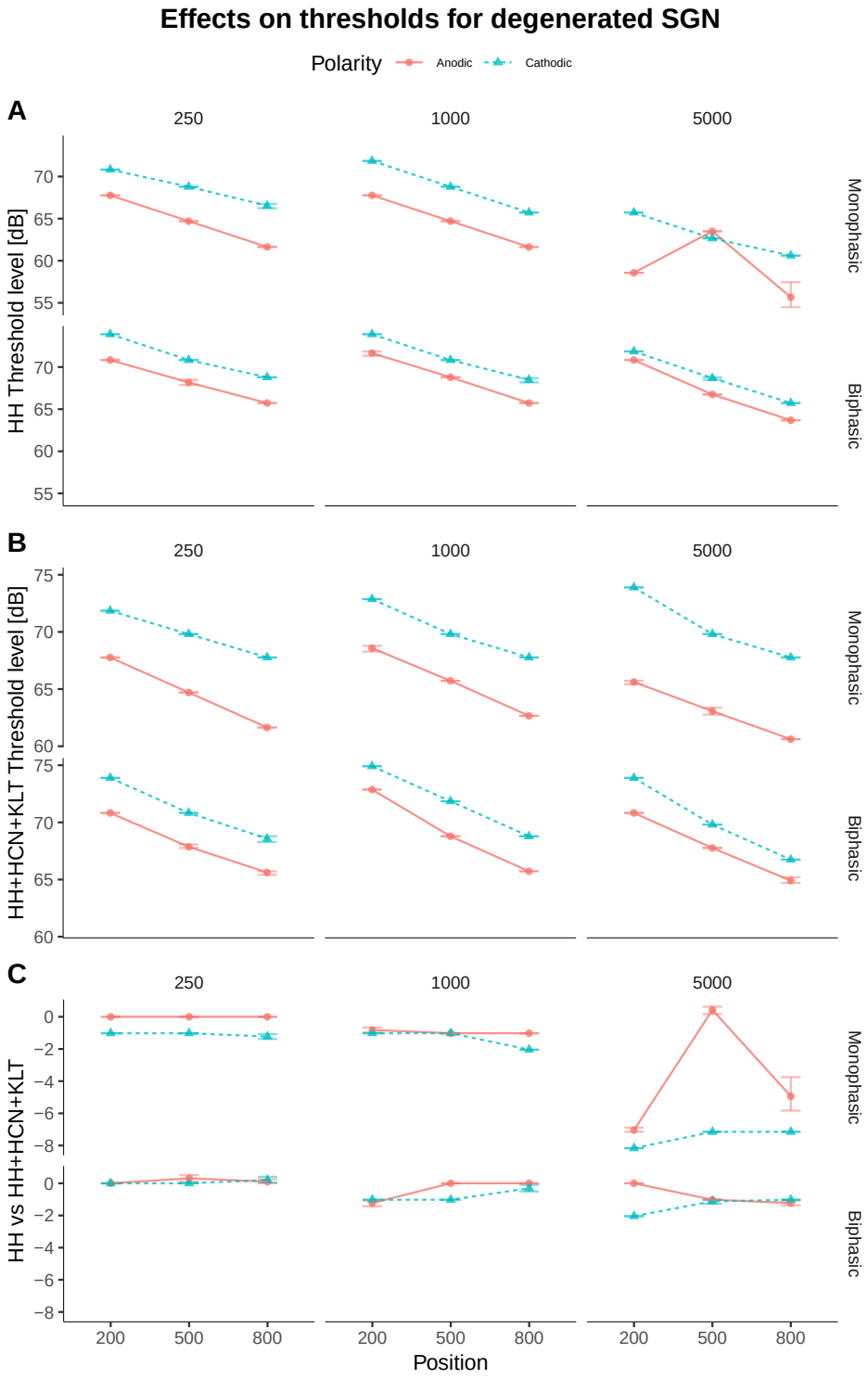

Figure 4.3.6: Threshold levels across models and stimulus conditions. A) threshold levels for the HH ionic model, B) the HH+HCN+KLT ionic model, C) the difference between the simulated threshold levels for the HH and HH+HCN+KLT.

Moreover, thresholds systematically decreased for systematically lower electrode positions, the opposite to what was observed for the partially demyelinated and healthy SGNs. This is in accordance with the morphology of the degenerated SGN which doesn't have a peripheral process. As such, lowering the electrode position effectively positions the electrode closer to the SGN.

When examining the effect of different polarities, strong and significant effects were observed: the cathodic polarity systematically produced higher thresholds than the anodic polarity. Polarity differences ranged from 2 to 7 dB across all the simulated conditions with larger differences for monophasic pulses (2 to 7 dB lower for anodic) than biphasic pulse shapes (1 to 3 dB lower for anodic). Again, this is explained by the effects of the missing peripheral process, which made the central process the most likely site to elicit APs, and the anodic polarity the most efficient stimulating polarity to depolarize the SGN membrane.

The effect of pulse-rate on thresholds was not very strong when compared to healthy and partially demyelinated SGNs. For both biphasic and monophasic pulse shapes, thresholds were either equal to, or slightly higher than, at 1000 pps (1 dB), and equal to, or slightly lower than, (less than 1 dB) at 5000 pps when compared to 250 pps. However, strong interactions between the pulse rate, electrode position and the ionic model conditions were observed. At 5000 pps, the cathodic monophasic threshold for the mid electrode position and for the "HH" ionic model appeared to be equal to the anodic polarity condition. This is in contrast with the "HH+KLT+KLT" ionic model in the same condition where the thresholds for anodic and cathodic were 5 dB different (i.e. cathodic higher than anodic).

In addition, the "HH+KLT+HCN" ionic model shows some effects of the pulse rate and electrode position. For example, at the highest electrode position for the monophasic condition, the cathodic polarity thresholds increase from 72 dB at 250 pps to 75 dB at 5000 pps. This is in contrast to the anodic polarity thresholds for monophasic pulses, which decreased from 68 dB at 250 pps to 66.5 dB at 5000 pps.

From Fig. 4.3.6 panel C, it appears that differences between thresholds were the most significant for monophasic cathodic pulses at 250 and 5000 pps (from 1 to 8 dB difference). At 250 pps, a constant 1 dB smaller threshold was measured for the "HH model", while at 5000 pps the differences varied between electrode positions and polarities (8 dB lower for cathodic and 0 to 7 dB for anodic).

Monophasic vs. Biphasic pulse train dynamic range DRs for degenerated SGNs are summarised in Fig. 4.3.7. Values ranged between 0.5 and 8.2 dB, in the range previously reported for animal studies (Javel and Viemeister, 2000)

As with thresholds, DRs were significantly higher for monophasic pulse shapes when compared to biphasic pulses (1 to 3 dB). This is in line with the previous human study from van Wieringen, Carlyon, et al. (2006) and confirms observations from the single-pulse responses (see Sec. 4.3.1.2). This also indicates that the opposite polarity phase affects the degenerated SGN similarly to the partially demyelinated and healthy SGNs with regards to DR. Also, the DRs increased with pulse rate (1 to 4 dB between 250 pps and 5000 pps across all conditions), in line with the previous report in humans by van Wieringen, Carlyon, et al. (2006).

The effect of electrode position on DR was highly variable across all conditions. Note that for low pulse rates, the electrode position did not significantly affect the DR value. Further, strong interactions between the effects of polarity, electrode position and ionic model were observed. First, exploring the "HH" model, DRs increased with increasing pulse rate and lowering electrode positions. These effects are similar across pulse-shapes, but biphasic pulse-shapes showed reduced DRs when compared to monophasic pulses. The effect of polarity was variable across pulse shape and electrode position, with the largest effect observed at 5000 pps for monophasic pulse (2 dB difference between anodic and cathodic pulses). Then, examining the "HH+KLT+HCN" ionic model, the monophasic anodic pulses thresholds were stable across electrode positions while DRs increased with rate. Cathodic pulses were more variable, probably because the excitation site is pre- or post-somatic, i.e. at locations where both HCN and KLT channels are present, whilst anodic pulse conditions, which showed lower DRs, had more central sites of excitation, i.e. where only KLT ionic channels are present, and thus are less affected by these interactions between the different channels. This variability was also observed for biphasic pulses as both polarities are present and excitation sites might also vary. Overall, both models predict that monophasic, anodic pulses are more stable across electrode position. This accords with the variable DR values that were found across electrode positions for single pulse responses.

Lastly, interactions between the ionic models and pulse-rate did have a significant effect on DR values, ranging from −2 to 4.5 dB difference between the "HH" and

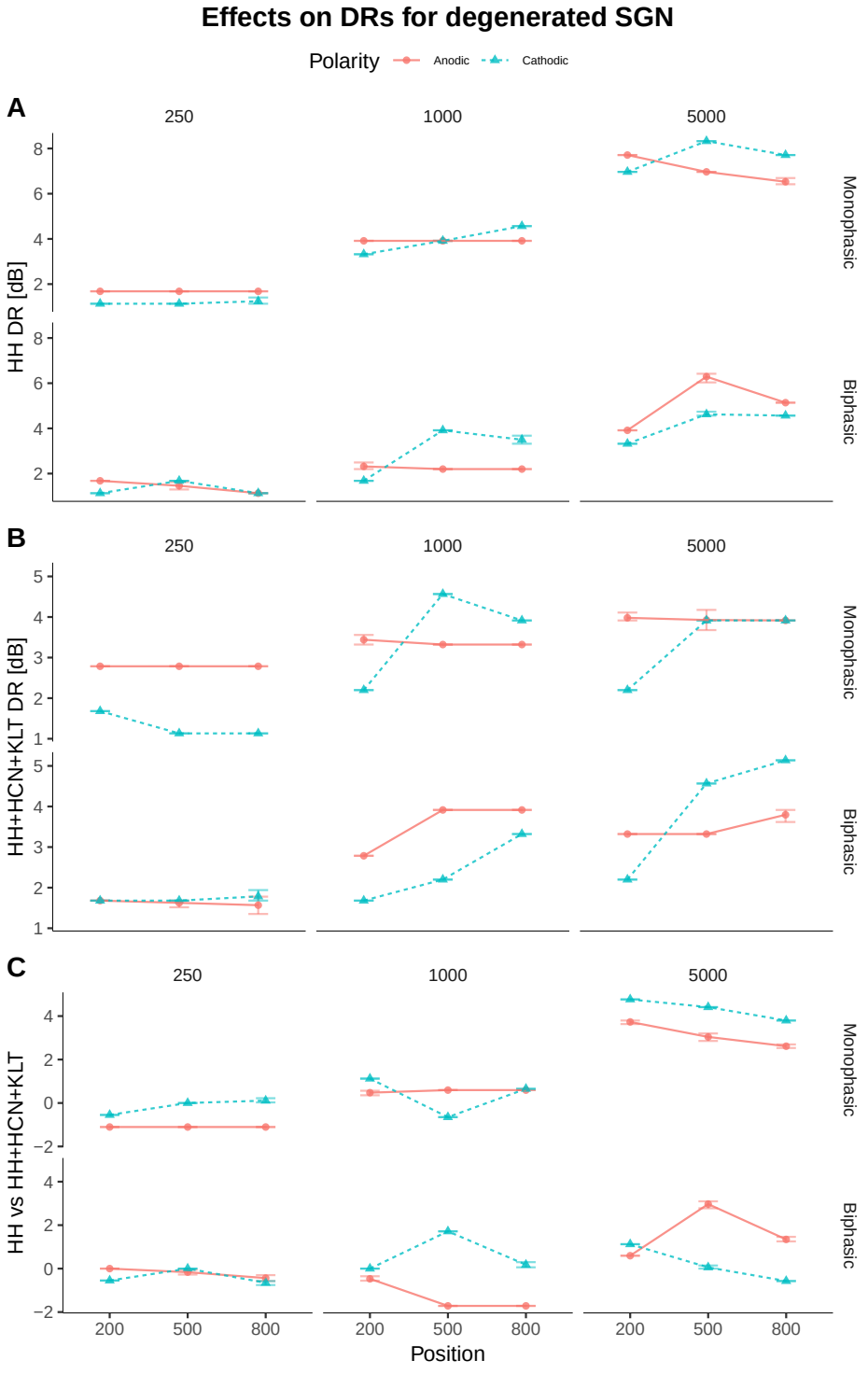

Figure 4.3.7: DR across models and stimulus conditions. A) DR for the HH ionic model, B) the HH+HCN+KLT ionic model, C) the difference between the simulated DRs for the HH and HH+HCN+KLT.

the "HH+HCN+KLT" model overall. These differences seem to be greater for monophasic pulses (3 to 5 dB difference) than biphasic pulses (0 to 2 dB) at higher pulse rates, i.e. 5000 pps. More importantly, the "HH" model showed significantly higher DRs across all electrode positions at 5000 pps (1 to 4 dB higher for "HH") while DRs were comparable at 250 pps (1 dB higher for the "HH+HCN+KLT" on average). Interestingly, this effect illustrates the main mechanism that is linked to the presence of HCN and KLT, by reducing the DR due to spike-rate adaptation when compared to the "HH" model.

Monophasic vs. Biphasic pulse train latencies Fig. 4.3.8 shows the range of latencies for the degenerated SGN model. They ranged between 0.5 and 1.3 ms in line with previous studies (Rattay, Lutter, et al., 2001; Badenhorst et al., 2017). Interestingly, the latencies seemed not to be importantly impacted by electrode position, and only slightly by polarity effects, particularly so for biphasic pulse shapes. The largest latency was found for the monophasic condition at 1000 pps (1.3 ms) while the shortest was found for anodic-first biphasic stimulations at 250 pps (0.5 ms).

Latencies for the monophasic condition were found to be systematically longer than the biphasic condition. Differences between biphasic and monophasic latencies ranged between 100 and 500 µs, which is a relatively large impact for pulse shape when compared to healthy and partially demyelinated SGN models.

The effect of electrode position on latencies was observed to be almost absent for the degenerated SGN. This is in line with the results from the single neuron responses previously described and can be explained by the missing peripheral process. Essentially, it can be assumed that because there is no peripheral process, all APs will be elicited at nodes of Ranvier that are very close together regardless of the electrode position. In the biphasic condition, only the "HH" model demonstrated significant polarity effects ranging from 100 to 200 µs. It was observed that the cathodic polarity systematically produced equal or larger latencies than the anodic condition. Also, polarity and pulse rate significantly impacted the monophasic condition for both models with differences ranging 200 to 500 µs at the 250 pps and 5000 pps pulse rates.

Finally, except for the 250 pps biphasic simulations, significant latency differences

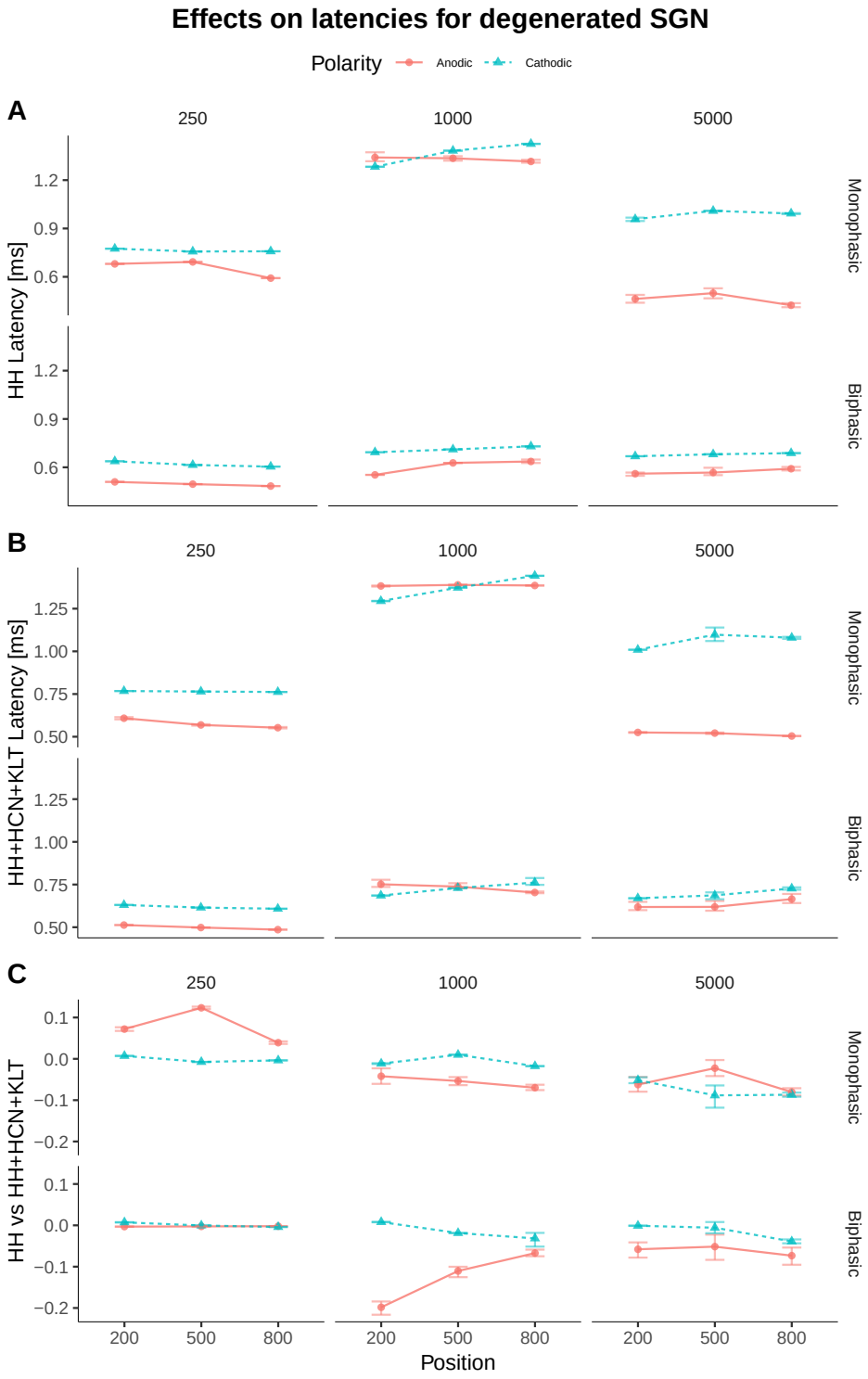

Figure 4.3.8: Latencies across models and stimulus conditions. A) Latencies for the HH ionic model, B) the HH+HCN+KLT ionic model, C) the difference between the simulated latencies for the HH and HH+HCN+KLT.

were observed between the two ionic models: the "HH" model predicted shorter latencies — 50 and 200 µs, respectively — in the anodic condition at 1000 pps for monophasic and biphasic pulses, and between 50 and 100 µs for the biphasic pulse shape at 5000 pps. This is contrasted with the 250 pps condition where the "HH" model predicted 100 µs longer latencies.

4.4 Discussion

Modelling the degeneration of SGNs is a non-trivial problem given the gradient of possible degeneration profiles that can occur in the deaf ear. Here, responses of partially and fully degenerated SGNs when subjected to both single and trains of pulses were assessed. Existing reports suggest that over the various degrees of degeneration, multiple predictions can be made as to which stimulation scenario would best encode electrically stimulated signals (Rattay, Lutter, et al., 2001; Badenhorst et al., 2017; Kalkman, Briaire, Dekker, et al., 2014; Smit, Hanekom, van Wieringen, et al., 2010).

Single-pulse responses suggest that despite the fact that partially demyelinated SGNs show similar thresholds and DRs to those of healthy SGNs, the degradation to insulating myelin causes large distortions in the timing of travelling APs. This may impact the coding of fine temporal information, which is critical for binaural processing. On the other hand, the loss of peripheral process in the fully degenerated SGN causes large upwards shifts in thresholds regardless of the electrode position and stimulus polarity. More importantly, the fully degenerated SGN has a specific characteristic that sets it aside from both healthy and partially demyelinated SGNs: whilst healthy and partially demyelinated neurons favour peripheral cathodic pulses, with greater sensitivity at electrode positions near the peripheral process, full degeneration shows higher sensitivity to anodic pulses and reduced thresholds at electrode locations near the soma. Furthemore, full degeneration implies that APs are initiated at significantly more central nodes of Ranvier, which in turns reduces the AP latencies.

Predictions from responses to pulse-trains were insightful as to how degenerated SGNs would behave under more realistic CI stimulation conditions. Interestingly, the full degenerated model demonstrated drastically reduced pulse-rate effects when

comparing with healthy and partially demyelinated models. The reduced amount of complex interactions between the electrode position and the SGN peripheral process causes the activity growth to be more linear for almost all stimulus conditions (see Appendix 4.A.10 and 4.A.6).

This is of interest as it has been shown that faster pulse-rates decreased thresholds and increased DR levels for populations responses (Macherey, Carlyon, Van Wieringen, et al., 2008).

Together, these effects make a strong case for the consideration of different degrees of degeneration in the physiological modelling of CI-stimulated SGNs.

4.4.1 Effect of pulse shape

Biphasic stimulus produced higher thresholds, lower DRs and similar latencies to monophasic pulses for both partially demyelinated and fully degenerated SGNs. Generally, it is well established that the opposite polarity phase, at least with symmetrical pulse shapes, has a negative impact on two features of CI stimulation i.e. higher thresholds and lower DRs (Eddington et al., 1994). With CI stimulation in mind, the monophasic stimulus becomes unrealistic because of pulses need to be charge-balanced to prevent damage to the cochlea (Brummer and Turner, 1977). However, this effect needs to be taken into account when designing stimulation strategies, as different SGN degeneration profiles might respond better to more complex pulse shapes and/or in combination with more focused stimulation strategies where different asymmetric charge-balanced pulse shapes can be delivered simultaneously from different electrodes.

Further, similar pulse shape effects on thresholds were previously reported by Macherey, Van Wieringen, et al. (2006) where biphasic pulses responses were compared to alternating monophasic stimulations in humans. They reported that the thresholds of the alternating monopolar pulse trains were 5 to 10 dB lower at 200 pps, 2 to 5 dB lower at 400 pps, and similar or equal at rates over 1000 pps. These results are similar to the data reported here for the effects of pulse-shapes on responses of single SGNs.

Interestingly, in a study of human CI subjects examining polarity effects on loudness growth, Macherey, Carlyon, Chatron, et al. (2017) reported that some of

the growth functions in cathodic stimulus conditions were non-monotonic. These authors also theorized that these effects observed in humans could originate from "cathodic blocking", an effect not dissimilar to the effects described here. Examining the non-monotonic single-SGN responses that were described for some stimulus conditions, and linked to cathodic blocking and spike-rate blocking, it may be that some explanation for the observations in CI listeners in Macherey, Carlyon, Chatron, et al. (2017) can be found in these mechanisms.

4.4.2 Effect of electrode position

The effects of electrode position proved to be very different across our models of degeneration: in the case of the partially demyelinated SGN, higher electrode positions meant lower thresholds and longer AP latencies. However, for the degenerated SGN, thresholds decreased at lower electrode positions and latencies were less affected.

Such a diametrical difference in the effects related to electrode position between different neural health profiles, even at the single neuron level, provides some clues as to the importance of carefully designing stimulation strategies based on those parameters. Although slightly different in terms of the quantitative aspect of the results (see Sec. 4.2.4), the data are qualitatively highly comparable to previous modelling studies which also found that thresholds and latencies were highly dependent on electrode position (Rattay, Lutter, et al., 2001; Rattay, Potrusil, et al., 2013; Smit, Hanekom, van Wieringen, et al., 2010). Here, the difference in thresholds related to electrode position is accounted for by the electrode-to-neuron distance and blocking effects. As described in Chapter 3, complex interactions can occur at different nodes of Ranvier as a function of their distance from the center of the electrode. However, it is important to note that the electrode positions represented in this thesis do not take into account the lateral changes in position which have been found to also affect the response of SGNs (Badenhorst et al., 2016).

In the context of CI candidacy and the unexplained variability in performance between implantees, the significant differences modelled between multiple degrees of degeneration could very well explain some of the underlying mechanisms that contribute to them.

4.4.3 Polarity Effects

Various studies have shown the effects of stimulus polarity and peripheral degeneration on modelled SGNs (Frijns, Mooij, et al., 1994; Badenhorst et al., 2016; Hanekom, 2001; Smit, Hanekom, van Wieringen, et al., 2010; Rattay, Lutter, et al., 2001; Rattay, Potrusil, et al., 2013) and human subjects (Undurraga, van Wieringen, et al., 2010; Undurraga, Carlyon, Macherey, et al., 2012; Undurraga, Carlyon, Wouters, et al., 2013b; Macherey, Carlyon, Van Wieringen, et al., 2008).

Typically, previous computational models have shown that partially demyelinated SGNs behave similarly to healthy SGN models with regards to polarity effects: anodic and anodic-first stimulations would have higher thresholds than cathodic and cathodic-first stimulations. This is in contrast to the fully degenerated SGN model, which has the opposite polarity sensitivity, i.e. anodic and anodic-first produce lower thresholds than cathodic and cathodic-first.

The origin of this change in threshold preference was shown to originate from the retraction of the peripheral process which causes the AP site of excitation to shift more centrally in fully degenerated SGNs, thus more sensitive to anodic polarities.

Further, it was also described that latencies for anodic and anodic-first stimulations were systematically shorter than the latencies produced by cathodic and cathodic-first stimulations for all degeneration models. This is an interesting result as it is supported by human data from previous studies (Undurraga, Carlyon, Wouters, et al., 2013b), where the wave III and V latencies from human EABRs from anodic stimulations were reported to be always shorter than for cathodic polarities.

4.4.4 Effect of pulse-rate

While SGNs were fully degenerated, single-pulse responses showed the lowest DRs, and pulse train responses showed the highest AP "activity range", i.e. the greatest total number of APs elicited for degenerated SGNs, most likely due to the lack of peripheral process interactions and higher susceptibility to facilitation. Interestingly, the low DR for degenerated SGNs induced by the reduced amount of noise at node P6 is not a limitation for the pulse train DR values.

Higher pulse rates have also been shown to reduce thresholds and increase DR values for both partially demyelinated and fully degenerated SGN models. However,

the peak activity didn't increase between 1000 pps and 5000 pps as this feature is driven by the intrinsic kinetics of the ionic channel equations used. This is represented by a larger increase in DR between 250 and 1000 pps than the increase noted between 1000 and 5000 pps.

Previous human studies have highlighted similar effects of high pulse rate on thresholds and DR (Skinner et al., 2000; Kreft et al., 2004). For example, van Wieringen, Carlyon, et al. (2006) looked at the effects of pulse-rate on thresholds and loudness for different pulse shapes in human subjects. They reported that, similar to the results present here, DRs of biphasic waveforms could increase in the range 4 to 10 dB with increasing rates in some of the patients tested.

Although the underlying mechanisms of refractoriness, facilitation and accommodation were not systematically characterized for the degeneration models of SGNs introduced here, it appears that the fully degenerated SGN would be the least subject to pulse-rate changes. This is, in part, explained by the lack of peripheral process, which drastically reduced the amount of positive, i.e. facilitation and accommodation, and negative, i.e. cathodic blocking, interactions that have been observed for the partially demyelinated and healthy SGN models.

Human subject thresholds are often reported to decrease by more that the 1 to 4 dB reported here van Wieringen, Carlyon, et al. (2006). This is an expected phenomenon as human subjects would benefit from central integration of the signals coming from other neurons while the model presented here only represents one SGN.

4.4.5 Effect of HCN and KLT ionic channels

The additional HCN and KLT ionic channels were found to change the single SGN model's behaviour both at the level of single-pulse and pulse-train responses.

For single pulses, the main difference observed was an increase in thresholds for most stimulus conditions. This effect on threshold originates in the additional current force that is required from the Na channels to elicit an AP and was to be expected due to the combined higher thresholds and reduced activity related to the additional ionic channels (Negm and Bruce, 2014; Boulet, 2016). Indeed, in the "HH" model, the "resting" equilibrium that is created between the Na, Kv, and leak, currents for the membrane potential to remain at rest is weaker than the equilibrium

created by the "HH+KLT+HCN" model. Effectively, the additional HCN and KLT channels input new currents into the system, rendering the membrane potential both more stable and more difficult to depolarize.

This interaction of channels also impacts on the pulse-train responses, where the DRs across pulse-rate and stimulus conditions for the "HH+HCN+KLT" were mostly systematically lower than the predictions for the "HH" model. Again, the additional holding force induced by the new ionic channels, i.e. HCN and KLT, makes it harder for the neuron's membrane to be depolarized and elicit APs. As explained in Chapter 2 and Chapter 3, KLT and HCN channels bring to bear new ionic currents as a response to ongoing stimulation, and this results in a reduction of AP generation in response to pulse trains when compared to the "HH" model. This effectively impacts the pulse train response DRs by reducing the range of activity of SGNs that are modelled with the "HH+HCN+KLT".

4.4.6 Effect of Degeneration

The effects of degeneration on eliciting APs by SGNs are various, and can have different degrees of importance. The latency difference induced by the reduced amount of insulating myelin in the partially demyelinated SGN or the lack of peripheral process in the fully degenerated SGN can have major implications for sound encoding. For example, if two SGNs, one partially and the other fully degenerated, abutted each other in the cochlear arrangement, they would produce tremendously different signals simply due to the differences in spike timing. A coding strategy with a built-in artificial delay map based on the health of cells facing the electrodes could help produce a more significant/homogeneous signal.

Important reductions in single pulse response DR are noticed for the cathodic monophasic pulse condition for the degenerated SGN model which is contradictory to previous animal reports where single fibre DR was found to increase with duration of deafness in guinea pigs (Sly et al., 2007). Interestingly, this stimulus conditions also coincide with the AP generation site being moved to the pre-somatic compartment (P6), behaving differently to conditions where APs are initiated in smaller nodes of Ranvier. As described in Chapter 2, the quantity of current noise that needs to be injected in each Node of Ranvier to produce a "stochastic" response was scaled for

smaller nodes. For this reason, and because node P6 is so much larger (40 times larger) than the other nodes, the effects of noise currents are much smaller, and don't generate enough stochasticity to output acceptable DRs in much larger nodes of Ranvier. Also, it was observed that for both the demyelinated and degenerated conditions, i.e. in Fig. 4.3.1, Fig. 4.3.2, Fig. 4.3.4 and Fig. 4.3.7, that anodic and anodic-first stimulations produced DRs that were sometimes larger than cathodic and cathodic-first conditions. This specific effect appears to be reversed with respect to the perceived DR when measured in human subjects (van Wieringen, Carlyon, et al., 2006; Macherey, Carlyon, Van Wieringen, et al., 2008). In the demyelinated case, the cathodic polarity DRs were also found to be relatively small. A possible explanation for this effect could be found in the variability in initiation site due to the lack of myelin insulation, causing greater interactions at the level of the peripheral process, in turns causing narrower DRs (O'Brien, 2016; Resnick et al., 2018). As for the fully degenerated case, the presence of the large pre-somatic compartment might have impacted the behavior of the SGN response to favour anodic stimulation for specific conditions. This should be studied further in order to produce more precise predictions.

In addition, an important feature of the extent of degeneration is that thresholds were higher for fully degenerated neurons than for partially demyelinated SGNs. Combined with the fact that there appeared to be smaller latency differencies, i.e. jitter, for fully degenerated SGNs (jump in site of excitation between P6 and C2 instead of P0 to C1) and the longer latencies for the partially demyelinated model (see Fig. 4.2.2), it makes a complex case as to which would be the most problematic in the context of CI stimulation. Understanding these differences might be important in the development of novel stimulation strategies that would adapt to these different physiological features, and help improve the quality of the signal encoding with respect to the degeneration status.

Resnick et al. (2018) studied the demyelination of axons and its impact on response timing. First, they reported that increasing degrees of demyelination yielded non-continuous effects on timings: while modestly demyelinated SGNs showed close to normal responses when compared to healthy responses, the strongly demyelinated fibers showed non-monotonic and stimulus-dependant behavior. This is an important effect to keep in mind and to put the results presented here into perspective, as only

one demyelination profile was simulated in this thesis. Second, they reported that those modestly demyelinated fibers were more sensitive to cathodic than anodic monophasic pulses and to cathodic-first than anodic-first biphasic pulses, however, when demyelination was more severe these relative sensitivities were reversed. This is of interest when put into perspective with the results of the fully degenerated SGN health profile, which shows a completely reversed polarity preference when compared to healthy SGNs. Finally, they reported that asymmetric demyelination introduces interaural timing difference artefacts. Placing this finding in the context of binaural hearing and binaural/bimodal CI implantation, it might be the cause of poor performance with regards to neural encoding. Typically, bimodal/bilateral CI users have little-to-no integration of cues for spatial hearing, and thresholds for discrimination of interaural time differences are always above 100 µs, compared to as low as 10 µs in normal hearing listeners.

The results reported here, and supported by Resnick et al. (2018), suggest that differences in degrees of degeneration could tremendously alter the quality of electrical signal at the SGN level. This could have detrimental effects on CI stimulation by heavily increasing latency difference compared to healthy and fully degenerated SGNs (from 50 to 500 µs). This is relevant in two different contexts: first, monaural hearing is reliant on strong timing cues for noise reduction. The spherical bushy cells are known to enhance phase in the temporal signal received from the AN (Joris and Smith, 2008; Kale et al., 2014). Second, in the context of binaural hearing, jitter could cause the loss of important temporal cues responsible for spatial grouping and in turns reduce the benefit of spatial release for hearing in noise, effectively removing the benefit of using both ears (Constan and Hartmann, 2003; Hartmann and Macaulay, 2014).

Taking into account such differences when designing more complex stimulation strategies could help CI users regain some sense of spatial hearing by assuring timely encoding of the electrical signal.

Appendix

4.A Pulse train responses

4.A.1 partially demyelinated SGN

Monophasic pulses train responses were recorded in Fig. 4.A.2 A-F for a single partially demyelinated SGN subjected to pulse trains at 3 electrode positions (high, mid, low), three pulse rates (250, 1000, 5000 pps) and for two stimulus polarities (anodic, cathodic) in the range of intensities 0 to 80 dB.

As could have been predicted due to the peripheral process, cathodic blocking effects similar to those observed in Chapter 3 were found in the monophasic pulse train simulations (e.g. Fig. 4.A.2 A and C).

In contrast with healthy SGNs, the partially demyelinated model also showed conditions where no activity was recorded at the last node of Ranvier (C14). This is illustrated here by Fig. 4.A.2 E at 5000 pps, where the "HH+HCN+KLT" predicted that no activity would travel along the partially unmyelinated SGN across the range of intensities simulated. Furthermore, although Fig. 4.A.2 A and C show that both models predicted some activity for the same pulse rate, the level of spikes was noticeably lower than for other conditions at those electrode positions.

Finally, in Fig. 4.A.2 F, the "HH" ionic channel model response did predict a pre-activity region that was assumed to not be part of the DR range (shown by the up and down blue dots). This was decided based on the fact that the "HH+HCN+KLT" did not show a similar pre-response, thus the measured DRs wouldn't have been comparable.

Biphasic pulses train responses were recorded in Fig. 4.A.4 A-F for a single partially demyelinated SGN subjected to pulse trains at 3 electrode positions (high, mid, low), three pulse rates (250, 1000, 5000 pps) and for two stimulus polarities (anodic, cathodic) in the range of intensities 0 to 80 dB.

The responses to biphasic pulse trains for the partially demyelinated SGN were

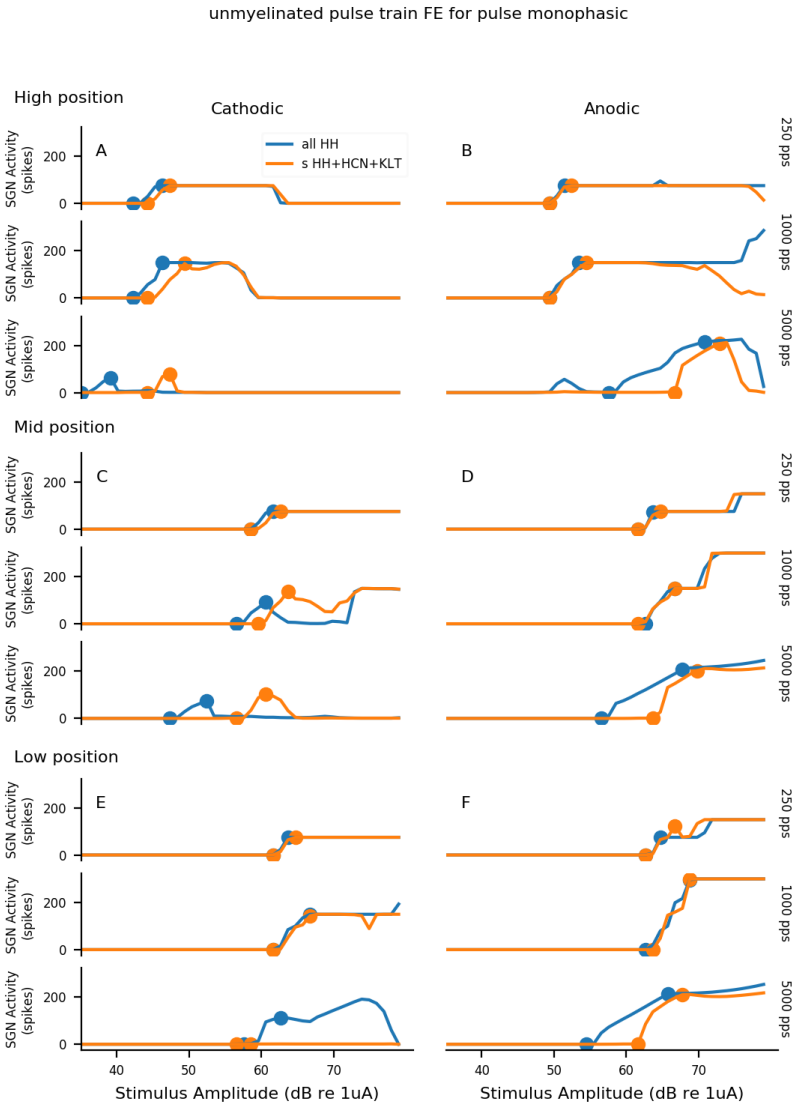

Figure 4.A.1: Monophasic pulse train response curves for an partially demyelinated SGN. Response curves for a healthy SGN to 300 ms monophasic pulse trains as a function of pulse amplitude, ionic distribution, electrode position and polarity. A, B represent the high electrode position. C,D represent the mid electrode position. E,F represent the low electrode position. A,C,E represent the cathodic condition. B,D,F represent the anodic condition. Response was calculated as the average spike activity from the SGN from 50 independent pulse train simulations.

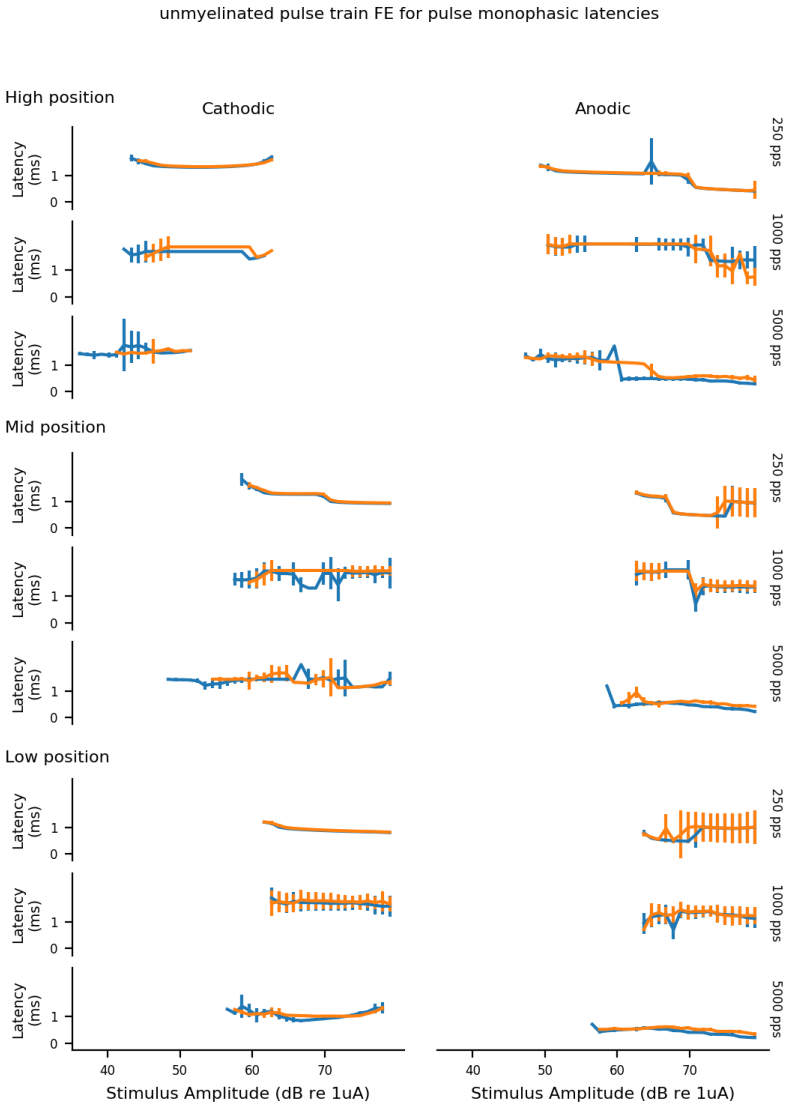

Figure 4.A.2: Monophasic pulse train latencies for an partially demyelinated SGN. Response curves for a healthy SGN to 300 ms monophasic pulse trains as a function of pulse amplitude, ionic distribution, electrode position and polarity. A, B represent the high electrode position. C,D represent the mid electrode position. E,F represent the low electrode position. A,C,E represent the cathodic condition. B,D,F represent the anodic condition. Response was calculated as the average spike activity from the SGN from 50 independent pulse train simulations.

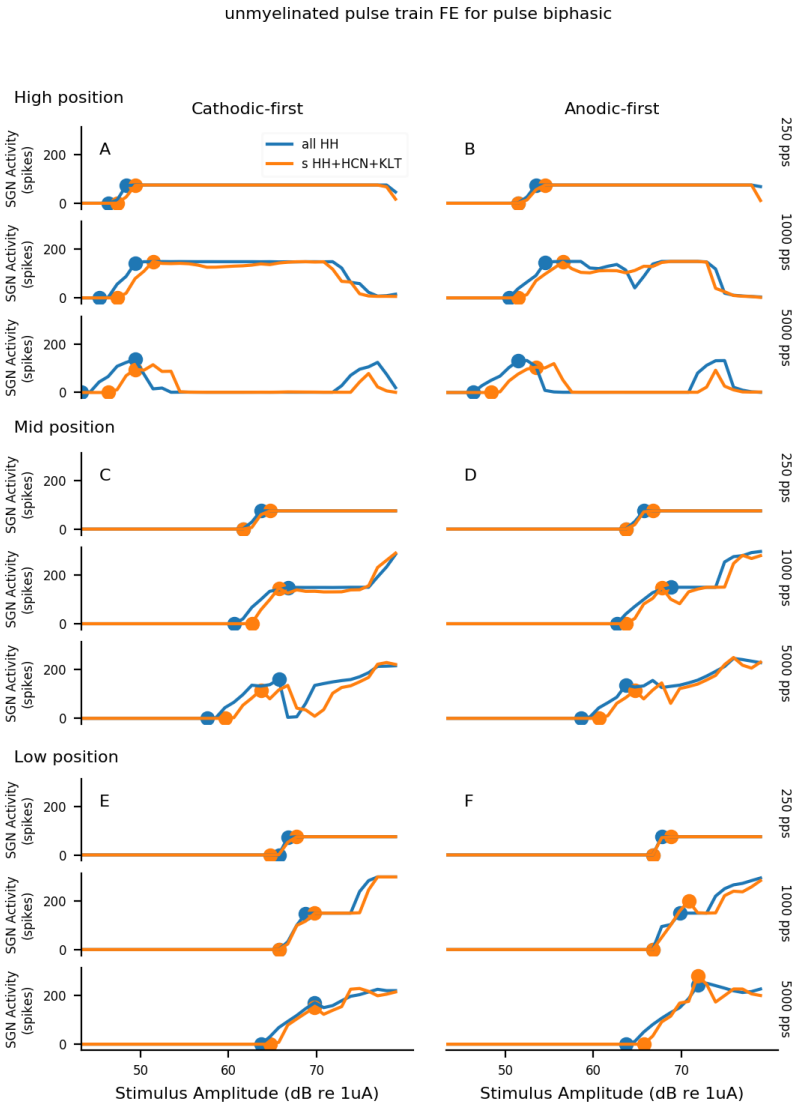

Figure 4.A.3: Biphasic pulse train response curves for an partially demyelinated SGN. Response curves for an partially demyelinated SGN to 300 ms biphasic pulse trains as a function of pulse amplitude, ionic distribution, electrode position and polarity. A, B represent the high electrode position. C,D represent the mid electrode position. E,F represent the low electrode position. A,C,E represent the cathodic condition. B,D,F represent the anodic condition. Response was calculated as the average spike activity from the SGN from 50 independent pulse train simulations.

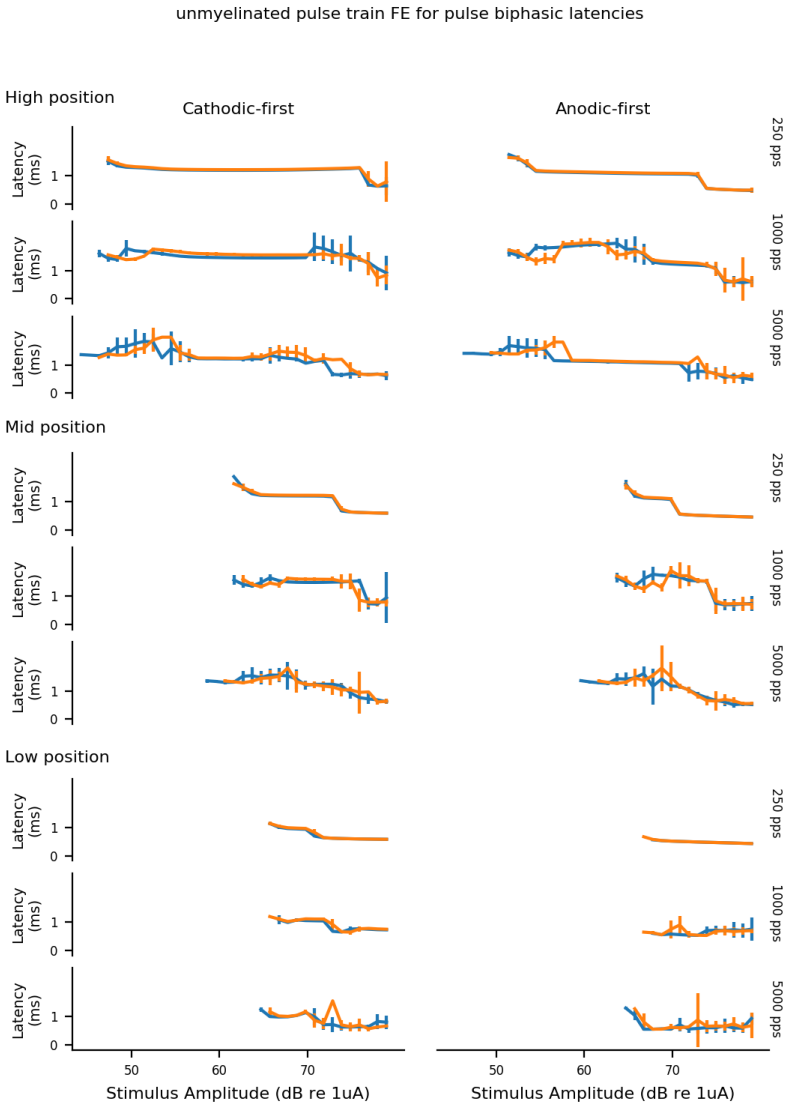

Figure 4.A.4: Biphasic pulse train latencies curves for an partially demyelinated SGN. Response curves for an partially demyelinated SGN to 300 ms biphasic pulse trains as a function of pulse amplitude, ionic distribution, electrode position and polarity. A, B represent the high electrode position. C,D represent the mid electrode position. E,F represent the low electrode position. A,C,E represent the cathodic condition. B,D,F represent the anodic condition. Response was calculated as the average spike activity from the SGN from 50 independent pulse train simulations.

relatively similar to the healthy SGN model. For pulse rates of 1000 and 5000 pps, the responses showed the characteristic gaps in activity that were also present in healthy SGN responses and are most likely explain by cathodic blocking effects and stimulus interactions at the peripheral process level. These can be observed in Fig. 4.A.4 A-C, at 1000 and 5000 pps. Interestingly, while the 1000 pps condition showed the highest throughput, reaching 1000 spikes/s for the highest intensities, the 5000 pps showed lower peak activity in the 800-900 spikes/s range.

4.A.2 Degenerated SGN

Monophasic pulses train responses were recorded in Fig. 4.A.6 A-F for a single degenerated SGN subjected to pulse trains at 3 electrode positions (high, mid, low), three pulse rates (250, 1000, 5000 pps) and for two stimulus polarities (anodic, cathodic) in the range of intensities 0 to 80 dB. Most responses were increasing with except for the 5000 pps conditions in Fig. 4.A.6 C and E. However, non-mononocities in the highest pulse-rate condition for the mid and low electrode positions were observed.

Similarly to the healthy SGN model presented in Chapter 3, Fig. 4.A.6 C and E at 5000 pps also showed effects of cathodic blocking for the mid and low electrode positions. This phenomenon was further investigated and illustrated in Fig. 4.A.7 and Fig. 4.A.8 where, as the electrode is positioned closer to the soma, the cathodic stimulation train causes a strong hyperpolarisation at node of Ranvier C0 which effectively blocks the AP from saltating over at very high intensities. The blocking effect was observed for both ionic channel models, which indicates that there was no additional adaptation blocking involved.

In addition, small differences between the two ionic channel models were observed: (i) the peak SGN activity for the "HH" model for cathodic polarity at 1000 pps in the high electrode position was higher than its "HH+HCN+KLT" counterpart. (ii) the activity of the "HH" at 250 pps followed a different pattern at all electrode positions, i.e. the activity reached a plateau at its peak prior to coming down to a similar level as the "HH+HCN+KLT". This can most likely be explained by a 'jump' in the site of excitation from P6 to a more central node, effectively increasing the activity by means of a more excitable node.

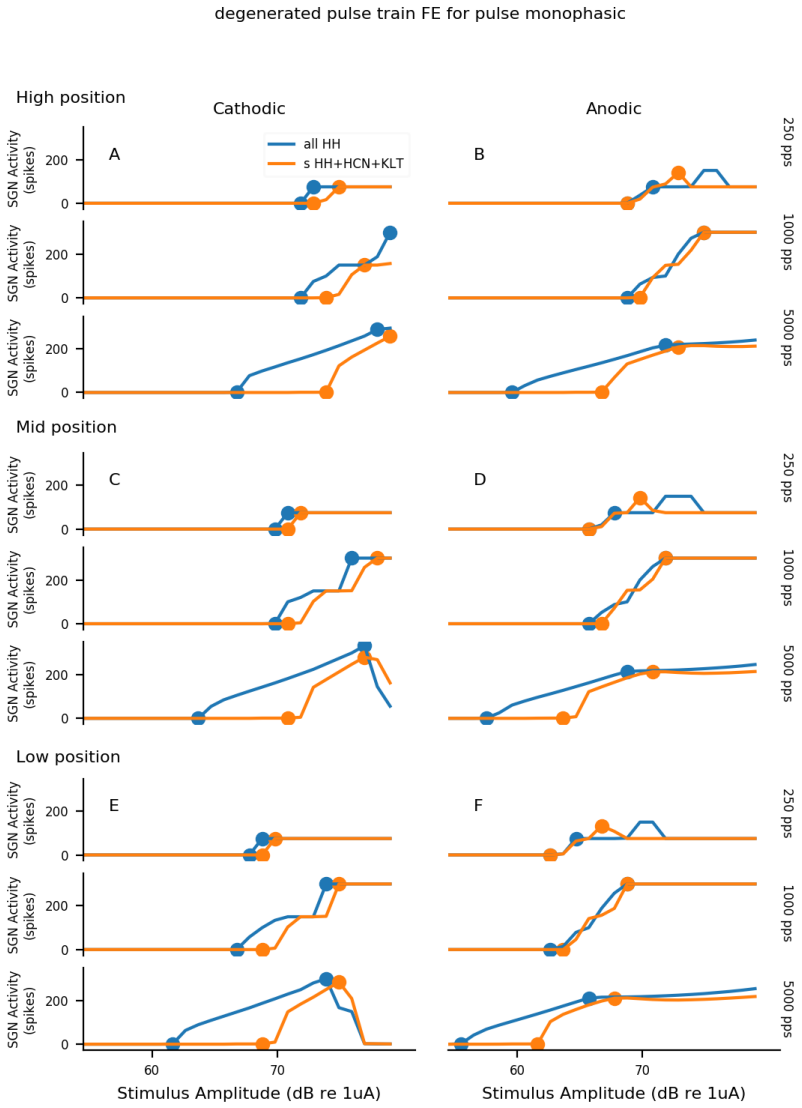

Figure 4.A.5: Monophasic pulse train response curves for a degenerated SGN. Response curves for a degenerated SGN to 300 ms monophasic pulse trains as a function of pulse amplitude, ionic distribution, electrode position and polarity. A, B represent the high electrode position. C,D represent the mid electrode position. E,F represent the low electrode position. A,C,E represent the cathodic condition. B,D,F represent the anodic condition. Response was calculated as the average spike activity from the SGN from 50 independent pulse train simulations.

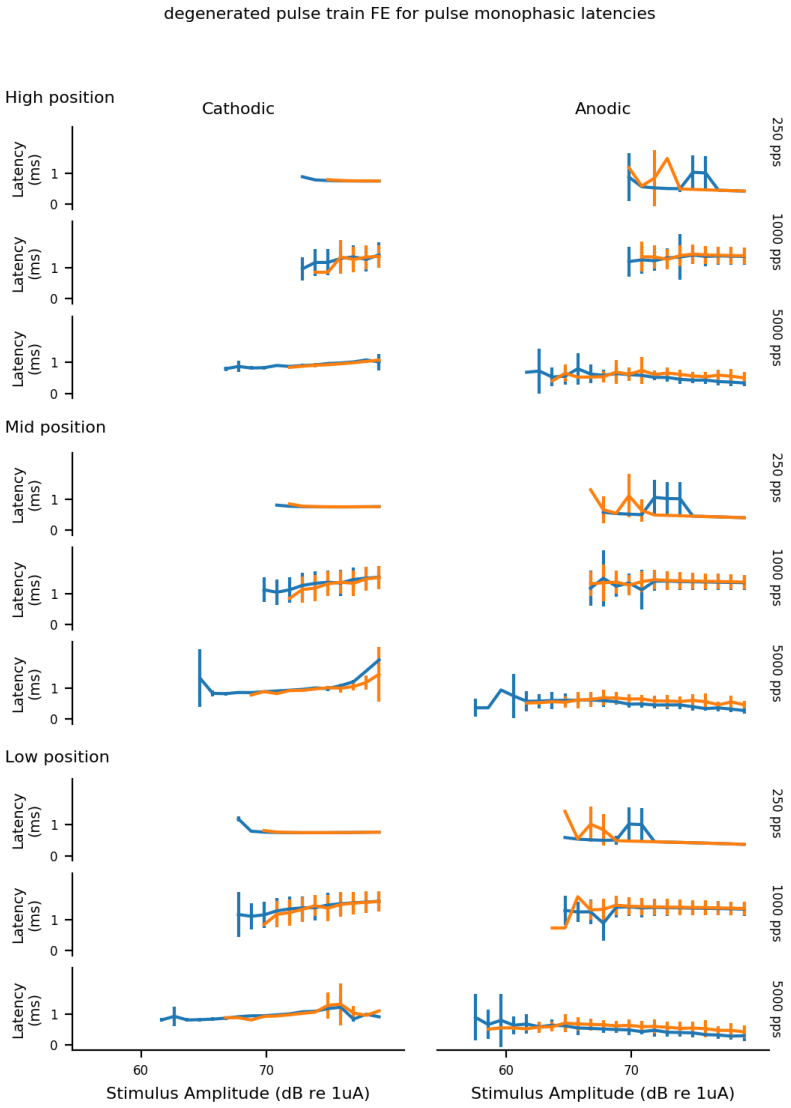

Figure 4.A.6: Monophasic pulse train latencies for a degenerated SGN. Response curves for a degenerated SGN to 300 ms monophasic pulse trains as a function of pulse amplitude, ionic distribution, electrode position and polarity. A, B represent the high electrode position. C,D represent the mid electrode position. E,F represent the low electrode position. A,C,E represent the cathodic condition. B,D,F represent the anodic condition. Response was calculated as the average spike activity from the SGN from 50 independent pulse train simulations.

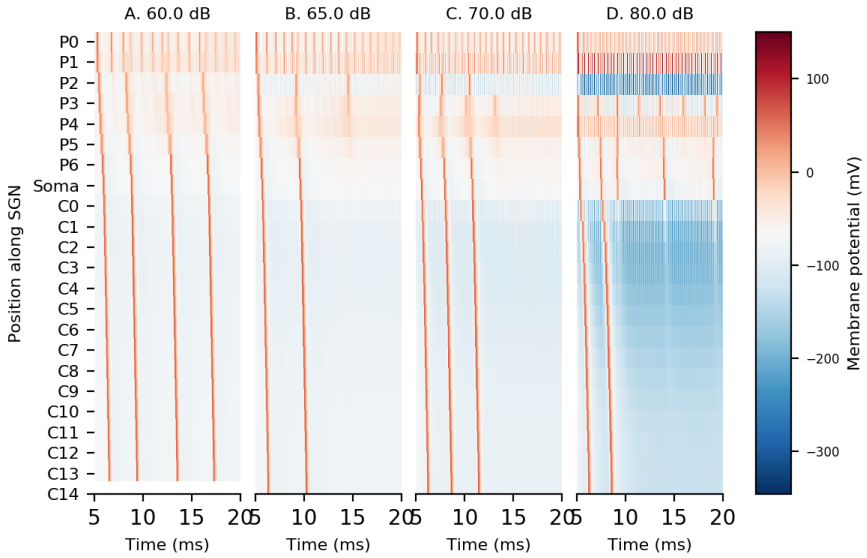

Figure 4.A.7: Cathodic blocking phenomenom. The cathodic blocking phenomenon happens when a node of Ranvier situated more centrally than the initial site of excitation is hyperpolarised by the stimulus.

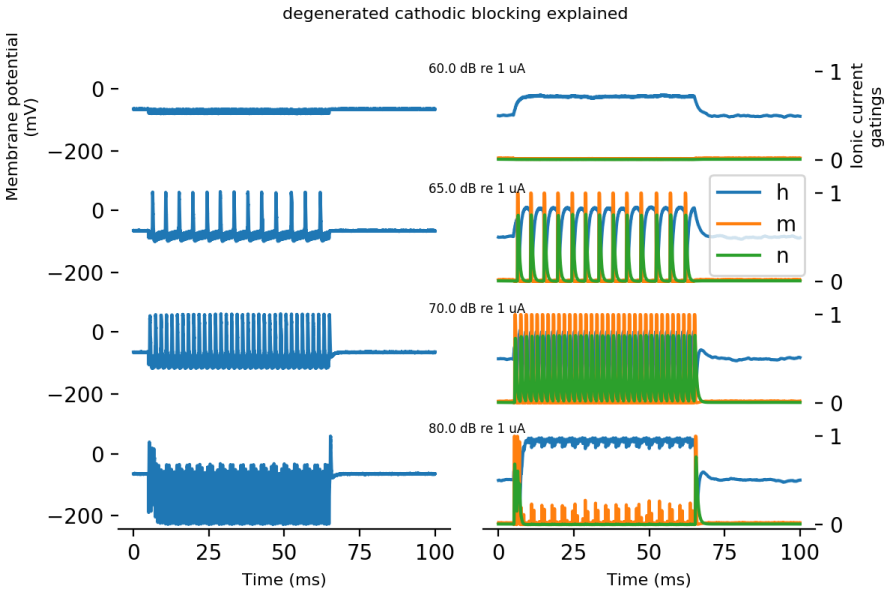

Figure 4.A.8: Bistable state illustration at node C0. Due to the high pulse-rate, the SGN membrane potential is depolarised at C0

Biphasic pulse trains responses were recorded in Fig. 4.A.10 A-F for a single degenerated SGN at 3 electrode positions (high, mid, low), three pulse rates (250, 1000, 5000 pps) and for two stimulus polarities (anodic-first, cathodic-first) in the range of intensities 0 to 80 dB. The responses to biphasic pulses were all linearly increasing with intensity, except for intermediary plateaus that can be seen in Fig. 4.A.10 D and F at 1000 pps pulse-rate. Maximum activity levels were reached under the 1000 pps pulse-rate and were electrode position non-specific.

Furthermore, except for a peak activity difference in Fig. 4.A.10 B at 1000 pps, activity levels and overall trends were almost identical for both ionic channel models presented here, indicative that the HCN and KLT channels included in the "HH+HCN+KLT" model only play a limited role in the biphasic pulse scenario.

Finally, it is interesting to note that the biphasic condition for the degenerated SGN model shows the least amount of differences between polarities, aside from a 3 to 5 dB threshold shift in favour of the anodic condition, across all electrode positions.

4.B Summary table single pulse responses

Table 4.B.1: Summary table single pulse responses partially unmyelinated

Pulse type	Polarity	Model	Electrode position	Threshold	DR	Latency
Monophasic	Cathodic	HH	High	44	0.97	1.54
			Mid	60	1.01	1.58
			Low	63	0.62	1.13
		HH+HCN+KLT	High	45	0.98	1.54
			Mid	60	1.09	1.52
			Low	63	0.88	1.14
	Anodic	HH	High	50	0.64	1.3
			Mid	63	0.72	1.28
			Low	64	0.45	1.21
		HH+HCN+KLT	High	50	0.98	1.3
			Mid	63	0.85	1.29
			Low	64	0.67	1.22
Biphasic	Cathodic	HH	High	48	0.64	1.43
			Mid	63	0.71	1.45

			Low	66	0.5	1.08
		HH+HCN+KLT	High	48	0.72	1.42
			Mid	63	0.89	1.44
			Low	66	0.68	1.08
	Anodic	HH	High	52	0.89	1.69
			Mid	65	0.49	1.64
			Low	67	0.33	0.98
		HH+HCN+KLT	High	52	0.9	1.59
			Mid	65	0.77	1.53
			Low	67	0.5	1.05

Table 4.B.2: Summary table single pulse responses degenerated

Pulse type	Polarity	Model	Electrode position	Threshold	DR	Latency
Monophasic	Cathodic	HH	High	73	0.1	0.98
			Mid	70	0.06	1.0
			Low	68	0.09	1.0
		HH+HCN+KLT	High	74	0.07	0.95
			Mid	71	0.08	0.95
			Low	69	0.08	0.95
	Anodic	HH	High	70	0.49	0.72
			Mid	67	0.5	0.71
			Low	64	0.5	0.69
		HH+HCN+KLT	High	70	0.79	0.69
			Mid	67	0.67	0.71
			Low	64	0.69	0.67
Biphasic	Cathodic	HH	High	76	0.06	0.91
			Mid	73	0.09	0.84
			Low	70	0.29	0.73
		HH+HCN+KLT	High	76	0.23	0.75
			Mid	73	0.42	0.72
			Low	70	0.39	0.73
	Anodic	HH	High	73	0.35	0.62
			Mid	70	0.36	0.66
			Low	67	0.35	0.67
		HH+HCN+KLT	High	73	0.48	0.61
			Mid	70	0.47	0.6

				Low	67	0.49	0.6

4.C Summary table pulse train responses

Table 4.C.1: Summary table pulse train responses partially unmyelinated SGN

Pulse type	Polarity	Model	Pulse rate	Electrode position	Threshold	DR	Latency
Biphasic	Cathodic	HH	250	High	47	0.79	1.19
				Mid	63	0.68	1.01
				Low	66	0.39	0.73
			1000	High	48	1.85	1.29
				Mid	63	3.39	1.23
				Low	67	1.21	0.87
			5000	High	46	3.4	1.03
				Mid	61	5.24	0.91
				Low	67	4.74	0.68
		HH+HCN+KLT	250	High	48	0.72	1.23
				Mid	63	1.16	1.02
				Low	67	0.64	0.74
			1000	High	49	2.42	1.58
				Mid	64	1.79	1.29
				Low	68	2.19	0.88
			5000	High	48	1.11	1.19
				Mid	62	1.94	0.92
				Low	67	2.76	0.68
	Anodic	HH	250	High	52	0.71	0.99
				Mid	65	0.42	0.76
				Low	67	0.24	0.5
			1000	High	53	2.9	1.25
				Mid	65	3.94	1.19
				Low	68	1.82	0.72
			5000	High	49	4	0.99
				Mid	62	3.43	0.86
				Low	69	7.05	0.63
		HH+HCN+KLT	250	High	53	1.29	1.02
				Mid	65	0.85	0.76
				Low	67	0.61	0.5
			1000	High	54	3.32	1.38

				Mid	66	2.58	1.05
				Low	69	2.6	0.68
			5000	High	51	2.4	1.23
				Mid	63	2.19	0.85
				Low	69	5.19	0.66
Monophasic	Cathodic	HH	250	High	44	1.27	1.38
				Mid	60	1.3	1.15
				Low	63	0.72	0.9
			1000	High	45	2.46	1.5
				Mid	59	2.06	1.72
				Low	64	2.81	1.58
			5000	High	38	1.6	1.41
				Mid	50	2.99	1.32
				Low	60	1.64	1.0
		HH+HCN+KLT	250	High	46	1.54	1.4
				Mid	61	1.5	1.16
				Low	63	1.26	0.91
			1000	High	47	3.08	1.48
				Mid	62	2.45	1.58
				Low	64	3.11	1.63
			5000	High	46	1.08	1.49
				Mid	59	1.6	1.39
				Low	58	0.77	1.07
	Anodic	HH	250	High	50	0.7	0.91
				Mid	63	0.66	0.84
				Low	64	0.63	0.86
			1000	High	51	3.09	1.24
				Mid	64	2.42	1.3
				Low	66	4.41	1.29
			5000	High	64	12.46	0.41
				Mid	62	9.29	0.34
				Low	60	9.11	0.33
		HH+HCN+KLT	250	High	51	1.24	0.95
				Mid	63	0.98	0.88
				Low	65	2.05	0.94
			1000	High	52	3.42	1.21
				Mid	64	3.57	1.4
				Low	67	4.52	1.31

			5000	High	68	3.77	0.47
				Mid	66	3.25	0.42
				Low	63	3.74	0.39

Table 4.C.2: Summary table pulse train responses degenerated SGN

Pulse type	Polarity	Model	Pulse rate	Electrode position	Threshold	DR	Latency
Biphasic	Cathodic	HH	250	High	75	0.24	0.65
				Mid	73	0.98	0.63
				Low	70	0.25	0.62
			1000	High	76	0.86	0.7
				Mid	76	6.13	0.72
				Low	73	4.91	0.74
			5000	High	75	4.8	0.66
				Mid	73	6.85	0.63
				Low	70	6.75	0.65
		HH+HCN+KLT	250	High	76	0.65	0.64
				Mid	73	0.63	0.63
				Low	71	0.7	0.62
			1000	High	77	0.61	0.7
				Mid	74	1.54	0.74
				Low	73	4.2	0.76
			5000	High	76	2.53	0.64
				Mid	75	6.37	0.64
				Low	72	6.56	0.64
	Anodic	HH	250	High	73	0.61	0.52
				Mid	70	0.58	0.51
				Low	67	0.25	0.5
			1000	High	74	1.39	0.56
				Mid	71	1.35	0.64
				Low	68	1.64	0.64
			5000	High	74	5.83	0.56
				Mid	72	7.94	0.59
				Low	69	7.72	0.57
		HH+HCN+KLT	250	High	73	0.62	0.52
				Mid	70	0.58	0.51
				Low	67	0.68	0.5
			1000	High	75	4.11	0.73

				Mid	73	4.97	0.73
				Low	70	4.74	0.7
			5000	High	75	4.0	0.6
				Mid	72	3.73	0.57
				Low	69	4.16	0.63
Monophasic	Cathodic	HH	250	High	72	0.29	0.79
				Mid	70	0.27	0.77
				Low	68	0.47	0.77
			1000	High	74	4.36	1.26
				Mid	74	6.51	1.36
				Low	71	7.32	1.4
			5000	High	72	10.5	0.97
				Mid	71	12.44	1.01
				Low	67	11.05	1.0
		HH+HCN+KLT	250	High	74	0.87	0.78
				Mid	71	0.25	0.78
				Low	69	0.28	0.77
			1000	High	76	1.33	1.28
				Mid	75	6.0	1.35
				Low	73	5.04	1.42
			5000	High	75	2.39	1.01
				Mid	73	3.48	1.06
				Low	71	3.94	1.08
	Anodic	HH	250	High	70	0.42	0.69
				Mid	67	0.74	0.7
				Low	64	0.65	0.6
			1000	High	72	4.47	1.17
				Mid	69	4.4	1.24
				Low	66	3.95	1.27
			5000	High	65	10.84	0.33
				Mid	63	9.8	0.33
				Low	60	9.08	0.33
		HH+HCN+KLT	250	High	71	2.52	0.62
				Mid	68	2.23	0.58
				Low	65	2.02	0.57
			1000	High	72	4.75	1.22
				Mid	69	4.63	1.27
				Low	67	4.3	1.3

5000	High	69	4.09	0.42
	Mid	66	3.59	0.41
	Low	63	3.94	0.4

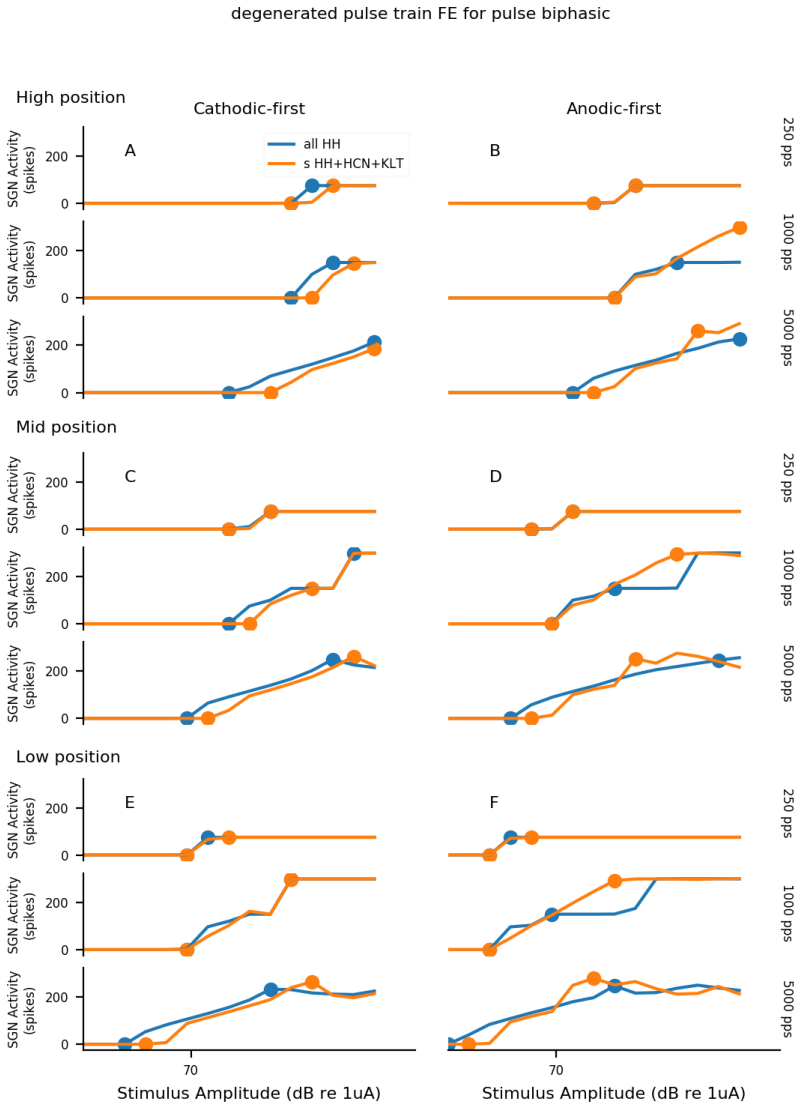

Figure 4.A.9: Biphasic pulse train response curves for a degenerated SGN. Response curves for a degenerated SGN to 300 ms biphasic pulse trains as a function of pulse amplitude, ionic distribution, electrode position and polarity. A, B represent the high electrode position. C,D represent the mid electrode position. E,F represent the low electrode position. A,C,E represent the cathodic condition. B,D,F represent the anodic condition. Response was calculated as the average spike activity from the SGN from 50 independent pulse train simulations.

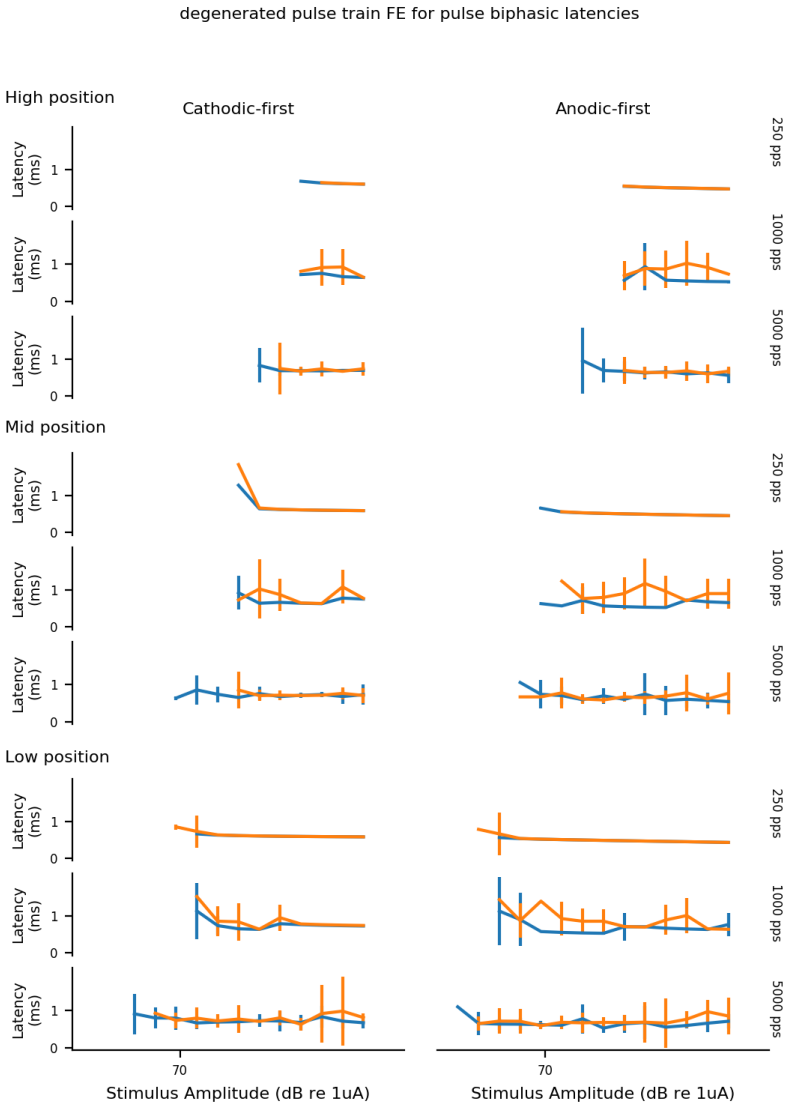

Figure 4.A.10: Biphasic pulse train latencies for a degenerated SGN. Response curves for a degenerated SGN to 300 ms biphasic pulse trains as a function of pulse amplitude, ionic distribution, electrode position and polarity. A, B represent the high electrode position. C,D represent the mid electrode position. E,F represent the low electrode position. A,C,E represent the cathodic condition. B,D,F represent the anodic condition. Response was calculated as the average spike activity from the SGN from 50 independent pulse train simulations.

5 Modelling healthy and unhealthy populations of Spiral Ganglion Neurons (SGNs) and their spread of excitation profiles

5.1 Introduction

In Chapter 3 and Chapter 4, the effects of various stimulation parameters on the response of single SGNs in the context of electrical stimulation in Cochlear Implant (CI) were investigated. Whilst these physiologically relevant single-neuron models are necessary for a basic understanding of the underlying mechanisms of neural encoding of electrical signal, they allow for only limited conclusions in terms of the response of the Auditory Nerve (AN) as a whole to electrical stimulation in CI. In order to successfully design more efficient stimulation strategies, it is necessary to understand the encoding of CI stimulations on populations of SGNs to provide an additional level of accuracy to the model predictions.

Additionally, evaluating the quality of the electrode-neuron interface by means of quantifying local neural survival is key in making CI stimulation more efficient. This information could be used to select the right stimulus parameters to reduce current spread and power consumption or to improve speech perception. Measurements of neural survival can be achieved either by subjective assessment of the CI user performance, or preferably using objective measures which are known to be better.

Objective measures have been studied in depth because of their importance in the assessment of the inner ear electrode-neuron interface (Macherey, Carlyon, Van Wieringen, et al., 2008; Undurraga, Carlyon, Wouters, et al., 2013a; Undurraga, van Wieringen, et al., 2010; Undurraga, Carlyon, Macherey, et al., 2012). When the normal ear is subjected to an acoustical stimulus, the recruitment of the population of SGNs whose Characteristic Frequency (CF) is near the stimulus frequency creates a signal called Compound Action Potential (CAP). This response is the summed

activity of many SGNs activated synchronously by the acoustic stimulus. As such, CAPs are objective electrophysiological representations of the ear response to a stimulus. Similarly, the electrical stimulation of SGN populations generates the so-called Electrically evoked Compound Action Potential (ECAP), which can be recorded by most CI devices using the intra-cochlear electrodes.

ECAP responses have become a common clinical tool since the introduction of built-in technology by manufacturers which allowed for the easy recording of ECAP responses in patients. They are commonly used to assess the response of the AN and to aid CI fitting. In the operating theatre, this objective measure is often used by the surgeon who can assess the positioning, and possible problems related to, the implant itself without the patient being conscious (Briaire and J. H. Frijns, 2005). Furthermore, ECAPs stimulated from a fixed electrode in the array can be recorded sequentially by electrodes placed further along the cochlea in order to evaluate the spread of electrical excitation (Kashio et al., 2016). In addition, ECAP can also be used in infants and children to evaluate the efficiency of the device being fitted when clinicians cannot receive perceptive feedback.

Interestingly, ECAPs responses have also been suggested by animal and computational studies as a technique to measure local neural survival by studying the changes in response to pulse shapes with variable Inter-Phase Gap (IPG) (Joshi et al., 2017; Ramekers et al., 2014; Prado-guitierrez et al., 2007) or by different polarities (Macherey, Carlyon, Van Wieringen, et al., 2008; Undurraga, van Wieringen, et al., 2010; Undurraga, Carlyon, Macherey, et al., 2012) The ECAP response morphology can be very variable according to the stimulus type and the recording locations (Macherey, Carlyon, Van Wieringen, et al., 2008; Gärtner et al., 2018). However, they are expected to have common features, similar to those schematized in Fig. 5.1.1: 1) a N1 negative peak whose latency is expected to be in the range 100 to 500 µs according to previous animal (Ramekers et al., 2014) and human reports (Undurraga, van Wieringen, et al., 2010; Undurraga, Carlyon, Macherey, et al., 2012; Macherey, Van Wieringen, et al., 2006; Kashio et al., 2016); 2) a P2 positive peak with the N1 to P2 amplitude expected to range from a few microvolts to 2 mV (Gärtner et al., 2018).

Modelling of ECAP responses can be very useful in the assessment of human SGN models as they represent a measure that can be compared with *in vivo* data

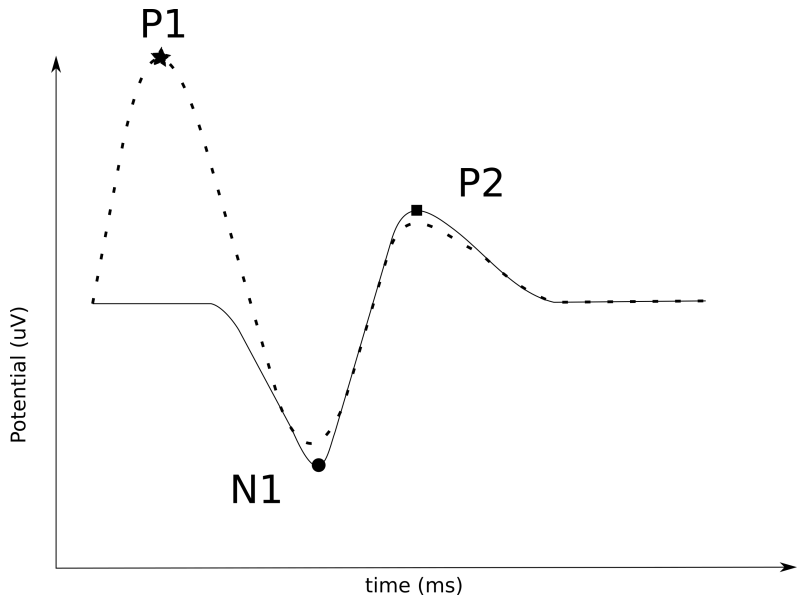

Figure 5.1.1: Basic morphology of N1-P2 (solid line) and P1-N1-P2 (dashed line) illustrated. The solid line represents a typical ECAP marked with a negative and positive maximum. The difference between those two peaks is called N1-P2 and represents the amount of neurons recruited by the stimulus that elicit this response

more easily than single SGN Action Potentials (APs) (Briaire and J. H. Frijns, 2005). The aim of Chapter 5 is to model population responses and characterize them using various SGN health profiles. In Chapter 2-Chapter 4, employing a model of single SGNs, various interactions across electrode location, polarity, pulse shape, and SGN health status were observed. The possibility of characterizing population responses to different pulse shapes and polarities could be a great clinical tool for both assessing the health status of the AN and improving CI fitting.

In this chapter, the computational resources from the National Computer Infrastructure Australia (NCI) CPU cluster were leveraged to simulate a simplified subpopulation of SGNs, with the aim of creating a more accurate predictor of the impact of different stimulation conditions on the encoding of electrical signals. The implementation of ECAP modelling will be introduced and validated. Furthermore, different types of populations of SGNs e.g. fully healthy, fully degenerated and partially demyelinated, will be modelled using several pulse shapes and polarities. The predictions made here will be assessed with regards to their utility in evaluating neural survival from ECAP measurements, and, from these predictions, to produce a more personalised

fitting of CI stimulation strategies.

5.2 Methods

In this chapter the SGN model that was presented in Chapter 2 will be used to model three different SGN populations: healthy, partially demyelinated and fully degenerated populations, all subjected to monophasic and biphasic monopolar stimulation. The electrode positions are as described previously (see Chapter 2). Due to computational limitations, ECAPs were measured from a limited number of SGNs (subpopulation response). The measurement scenario was simplified to SGNs being presented in a straight line in front of a spherical electrode, similar to the configuration presented in previous chapters (see Chapter 2). No interaction was assumed between SGNs in neighbouring areas of the populations. This simplification was also used in the previous model from Briaire and J. H. Frijns (2005).

5.2.1 Single Fibre Action Potential (SFAP) measurements

When measured *in vivo*, ECAPs represent the combined response of each individual neuron constituting the population being stimulated (Briaire and J. H. Frijns, 2005). Thus, in order to successfully model ECAP responses, it is first necessary to be able to model the response of single neurons, i.e. the SFAP. SFAPs provide the contribution, as an electrical potential, of each compartment of the neuron from the point of view of the recording electrode (Briaire and J. H. Frijns, 2005). This is achieved by using the reciprocity theorem, which states that the same transfer resistance that exists between a stimulating electrode and a particular node of Ranvier can be used to evaluate the effect of a transmembrane current through a modelled SGN compartment at the location of the electrode.

This can thus be written as:

$$SFAP = \sum i_{mem,k} \cdot R \tag{5.1}$$

where i_{mem} is the transmembrane current and R is the resistance between the compartment and the electrode. Due to the relation between media resistivity and electrode position, as well as the need for an additional set of data required

for its computation, the same electrode is used to stimulate and record SFAPs in this chapter. Thus, R is equal to the resistance used to compute the extracellular potential in the previous chapters (see Chapter 2).

Finally, the ECAP response is calculated as the sum of all individual SFAPs in the neural population (Briaire and J. H. Frijns, 2005) and can be written as:

$$ECAP = \sum SFAP_n \tag{5.2}$$

where n is the SGN index in the population.

5.2.2 Artifact removal paradigm

A major issue when measuring ECAP responses is the presence of stimulation artefacts which can be several orders of magnitude larger than the target signal. When measured *in vivo*, the masker-probe paradigm is usually considered to be the most efficient artefact removal paradigm. However, the masker-probe paradigm requires the simulation of multiple conditions which, in the case of computational models, requires an increased quantity of resources (Briaire and J. H. Frijns, 2005). Therefore, a simpler method known as the template subtraction paradigm, similar to the method described in Briaire and J. H. Frijns (2005), was chosen. Fig. 5.2.1 illustrates this paradigm which consists of three steps: first, a subthreshold artefact is recorded. Second, the sub-threshold artefact is linearly scaled to the supra-threshold pulse amplitude. Finally, the scaled artefact is subtracted from the supra-threshold response to provide a clean response.

5.2.3 Validation

5.2.3.1 ECAP measurement and precision

The cochlea is typically 30 mm long, with approximately 30000 SGNs (Felix et al., 1990; Spoendlin and Schrott, 1989), or 1 SGN for 1 µm on average in humans. In terms of the various CI devices commercially available, note that different numbers of electrodes can be found over different electrode array lengths: Advanced Bionics (AB) devices usually have 16 electrode contacts along 17 mm spacing between adjacent electrodes of 1.1 mm (center-to-center); Devices from the manufacturer

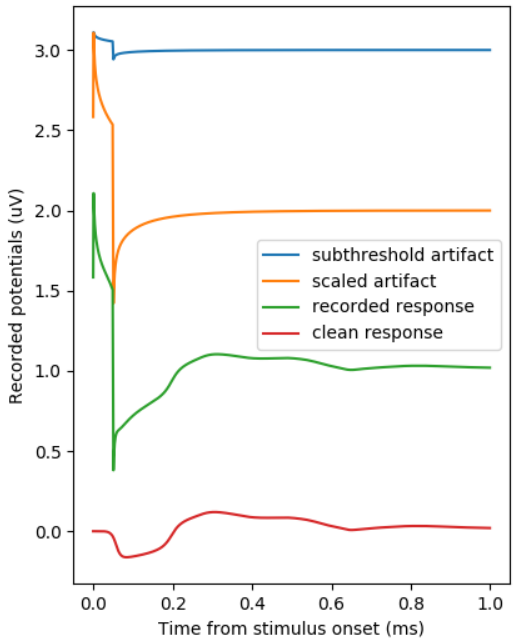

Figure 5.2.1: Template subtraction artefact paradigm illustrated on a SFAP. First the sub-threshold artefact (blue line) is recorded. Second, the sub-threshold artefact is linearly scaled to the supra-threshold amplitude (orange line). Finally, the scaled artefact is subtracted from the supra-threshold response (green line) to provide a clean response (red line).

Cochlear Ltd usually have 22 electrode contacts along 20 mm resulting in a spacing of less than 1 mm between contacts; Those of Medel have only 12 electrodes for a standard array (among several) of 26.4 mm length which makes for a 2.4 mm gap between electrodes (Eisen and Franck, 2005; Landsberger et al., 2015). Thus, the average electrode separation varies between less than 1 mm and 2.4 mm, giving an average of 1.5 mm of coverage per electrode.

In order to model a population of SGNs over the 1.5 mm of coverage per electrode, the following steps were taken. First, the SGNs were positioned along a straight line of 750 µm originating at a x position 0 on the mid-line of the stimulating and recording electrode. Second, as the model is deterministic, i.e. no noise current was injected in the nodes of Ranvier, the symmetry principle was applied to predict the response of the other side of the symmetry axis. Thus, by modelling a 750 µm linear space, the data should be meaningful for the entire theoretical electrode coverage (1500 µm).

Briaire and J. H. Frijns (2005) used a set of 299 neurons to represent the entire cochlea where each modelled SGN was later scaled in amplitude by a factor of 100 (each SGN represented a group of 100 cells). Similarly, Kalkman, Briaire, Dekker, et al. (2014) used 320 neurons in a volume conduction model of the entire human cochlea. Here, the minimum number of SGN required for an accurate model was determined by running stimulations of 1, 2, 4, 8, 15, 30, 60, 120, 240 and 480 SGNs over 750 µm to model the response of 750 SGNs, i.e. half the average electrode coverage. Neurons were equally spaced over the 750 µm distance. For each simulation the ECAP N1-P2 amplitude and number of SGNs eliciting APs were measured and scaled so that the response would represent a fixed number of 750 SGNs. For example, when modelling with 1 single neuron, the ECAP response was scaled by a factor of 750, whereas with a simulation using 8 neurons the ECAP response was scaled by a factor of 93.75. The relative scaling error was defined as the difference between the scaled ECAP amplitude from each condition and the scaled ECAP amplitude obtained with the previous number of neurons. For example, to compute the error in ECAP scaling when modelling 2 SGNs, the scaled ECAP N1-P2 amplitude modelled for 2 SGNs was subtracted from the scaled response from the model with 1 SGN. In addition the Spread of Excitation (SOE) was estimated as the scaled number of neurons which elicited an AP.

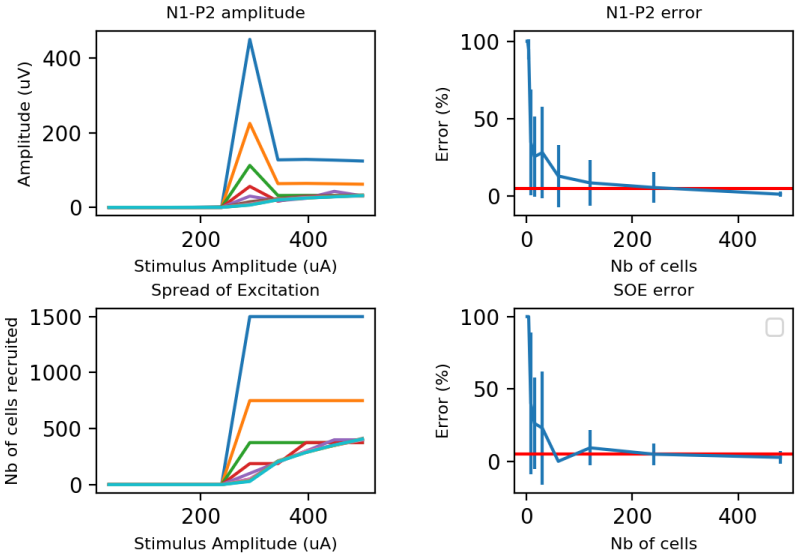

Figure 5.2.2: ECAP precision validation. The top left panel shows the scaled N1-P2 estimation as a function of amplitude for each condition of the number of neurons used in the population. The bottom left panel shows the scaled SOE estimation as a function of amplitude for each condition of the number of neurons used in the population. Both N1-P2 amplitude and SOE are evaluated as a scaled value for the population of 750 neurons. For both top left and bottom left panels blue indicates 1 neuron, orange 2 neurons, green 4 neurons, red 8, purple 15 and light blue 480 neurons. Top right panel shows the relative error in N1-P2 amplitude of each condition estimation with respect to the previous condition, i.e. lower number of neurons. Bottom right panel shows the relative error in SOE of each condition estimation with respect to the previous condition, i.e. lower number of neurons. The red line in both error plots shows the 5% error line.

Fig. 5.2.2 plots the estimate of the minimum number of SGNs needed for an accurate prediction of N1-P2 amplitude and SOE. Mainly, the non-monotonicity observed N1 P2 amplitude predictions as a function of population size is due to the poor resolution of the predictions made with small population sizes. Namely, the model fails to predict a continuum in N1-P2 amplitude increase when the number of neurons used is less than 4. The error between the predictions of the model having 480 neurons and a smaller set was computed and used to establish the minimum number of SGNs that would output predictions with less than 5% error. From the two panels on the right hand-side in Fig. 5.2.2, the 5% error line (red) for the estimate of both the N1-P2 amplitude and the neuron recruitment, i.e. SOE, estimate fell below the 5% error when the SGN population increased beyond 240 neurons. Therefore, all subsequent stimulations for this thesis were conducted with 240 neuron populations equally spaced over 750 µm and assuming symmetry on the opposite side. This morphological scenario delivered the best accuracy-to-performance ratio. All responses were elicited and recorded using the same electrode.

5.2.4 Population types

Often, simulations of ECAP responses are performed using neural populations embedded in realistic volume conduction models of the human cochlea (Frijns, de Snoo, et al., 1995; Briaire and J. H. Frijns, 2005; Hanekom, 2001; Kalkman, Briaire, Dekker, et al., 2014; Badenhorst et al., 2017). However, the focus of this thesis is to develop an effective model of the effects of stimulation parameters on the recruitment of single and populations of SGNs. With this in mind and building on the knowledge from Chapter 3 and Chapter 4 about single SGN responses, three simplified population types were simulated: the three populations were homogeneously constituted of either healthy, partially demyelinated or fully degenerated SGNs. All neurons had the same length, soma size and peripheral/central axon diameters.

5.3 Results

Three populations with different health profiles were stimulated by single pulses to model ECAP responses and the efficiency of different stimulus conditions evaluated.

Here, a summary of the ECAP measurements that were simulated for the different population health profiles is reported. The results were translated into three indicators: 1) the ECAP response morphology; 2) the mean latency of the N1 peak; 3) the mean N1-P2 amplitude. For succinctness, only the most relevant and potentially interesting effects are highlighted in this Chapter. However, complementary figures and detailed information (electrode position, ionic model, and degeneration status) can be found in the Appendix 5.A.

5.3.1 ECAP morphologies vs population health

This section summarizes typical and less-typical morphologies that were observed as a result of single pulse stimulation of the different populations. Fig. 5.3.1 to Fig. 5.3.5 show the diverse range of morphologies that were observed for ECAP responses. These figures show: 1) ECAP response (top left panel); 2) neural recruitment as a function of amplitude (top right panel); 3) normalized spike-density distribution (bottom left panel), and 4) spread of activity in population as a response to a single stimulation (bottom right panel) Normalized spike-density distributions were estimated by computing weighted histograms of AP spike-times from all neurons in the population. Weights were computed as the distance between the recording electrode and the node of Ranvier at which the latency was measured.

Although most ECAP responses were observed to be "typical" when compared to previous computational (Briaire and J. H. M. Frijns, 2000), animal (Miller, Abbas, Hay-McCutcheon, et al., 2004; Ramekers et al., 2014), and human models (Macherey, Carlyon, Van Wieringen, et al., 2008; Undurraga, van Wieringen, et al., 2010; Undurraga, Carlyon, Macherey, et al., 2012), some responses from healthy and partially demyelinated SGN populations at the mid electrode position were "atypical", presenting multiple N1 peaks (see Fig. 5.3.4). Anodic and anodic-first stimulation responses were found to produce a relatively large P1 peak. This was similar to a previous study using anodic-first symmetric pulses (Briaire and J. H. M. Frijns, 2000) and also similar to cats (Miller, Abbas, Hay-McCutcheon, et al., 2004) and humans (Macherey, Carlyon, Van Wieringen, et al., 2008; Undurraga, van Wieringen, et al., 2010) responses.

5.3.1.1 Typical morphologies

Because the ECAP response is a combination of all the individual SGN responses, i.e. SFAP, in the population, its morphology is heavily dependent on the density distribution of APs. Here, the morphologies of ECAP responses that were considered "typical" are described. These are mostly found in the high and low electrode positions and for the fully degenerated population health profile at all electrode positions.

Responses to anodic stimulus for monophasic and biphasic pulse shapes "Typical" ECAP responses were observed regardless of pulse shape in most conditions. However, only selected examples are presented and described here to highlight the features of the "typical" ECAP response.

Fig. 5.3.1 summarises a "typical" ECAP response for a monophasic anodic pulse delivered at the highest electrode position. The top left panel in Fig. 5.3.1 represents the ECAP Amplitude Growth Function (AGF) from the healthy SGN population. "Typical" ECAP response to anodic polarity stimulus, for both monophasic and biphasic pulse shapes, shows a large P1 peak, which represents the membrane current elicited by the hyperpolarization of the neurons' peripheral membrane. This peak is also represented in the bottom right panel of Fig. 5.3.1 where the red colour represents hyperpolarization of the neurons' membrane and blue represents depolarization. It can be seen that the red hyperpolarization area increases with stimulus amplitude, which is represented in the ECAP response (see top left panel in Fig. 5.3.1) by an increase in P1 with amplitude. Although Fig. 5.3.1 shows an example of a healthy SGN population profile, the P1 peak was also observed for multiple conditions in partially demyelinated and fully degenerated health profiles.

Looking at the bottom left panel of Fig. 5.3.1, it can be observed that the weighted AP density shows a peak at 0.25 ms, the same latency as the N1 peak indicated by the circled marker in Fig. 5.3.1 (top left panel). This indicates that the "typical" anodic response presented here can be correlated with one strong site of excitation across the population close to the stimulating recording electrode. Although, overall, latency was found to be stable, a more complete picture of the specific N1 latency changes is shown in the Appendix 5.B.1, 5.B.2 and 5.B.3.

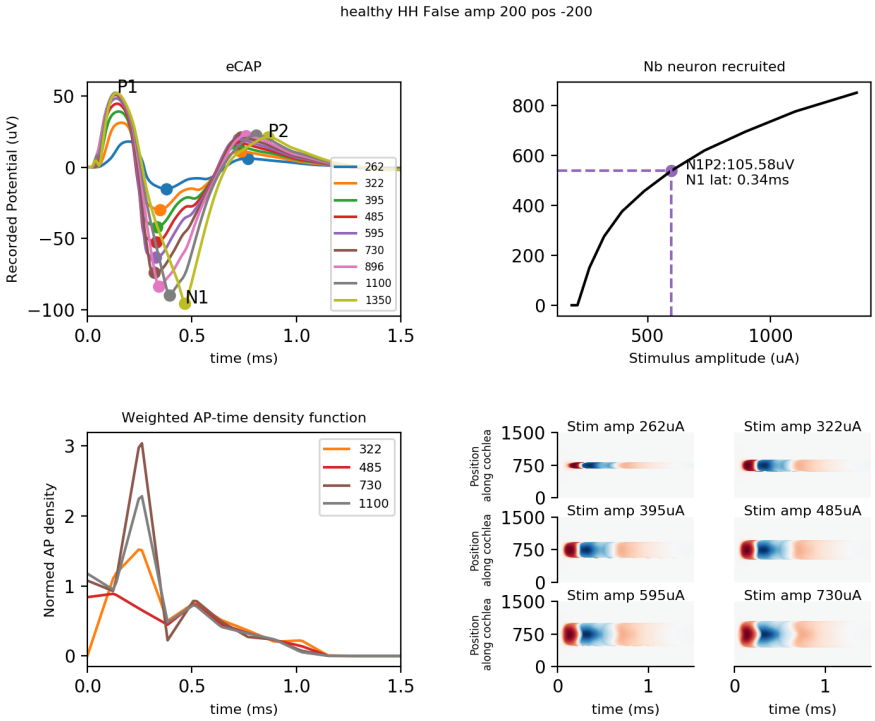

Figure 5.3.1: ECAP response summary for a healthy SGN population under monophasic anodic stimulation at high electrode position and for the "HH" ionic model. The morphology figures present four panels: 1) top left panel shows the ECAP response; 2) the top right panel shows the neural recruitment as a function of amplitude. The point highlighted on the curve represents the stimulus amplitude that produced a neural recruitment closest to 500 neurons to be used as a comparison between all the conditions. The annotations represent N1P2 amplitude and N1 latency of the ECAP response at that amplitude; 3) the bottom left panel shows the normed density distribution (sum under the curve equals 1) of the APs detected on all neurons in the population for a subset of intensity amplitudes (colors match the top left panel) and; 4) the bottom right panel shows the spread of activity in population as a response to a single stimulation. The stimulatingrecording electrode is located at 750 µm in the vertical axis. Red and blue represent high and low recorded potentials respectively.

Generally, ECAP responses of healthy neurons demonstrate N1 peak latencies that decrease with increasing stimulus amplitude. However, it is also observed that for currents above 730 µA, latencies increase, suggesting a change of excitation place. This effect is reflected in the AP density plot, e.g. Fig. 5.3.1 bottom left, by the reduction in the main density peak and the rise of a second peak, e.g. the difference between the maroon and grey density functions.

In addition, the properties of the typical ECAP morphology in the anodic condition are also present for partially demyelinated and fully degenerated population health profiles (see Appendix 5.A.1 and 5.A.2). However, the stimulation levels to evoke a response are strongly dependent on the status of the SGNs. For example, in the partially demyelinated example shown in Fig. 5.A.1, stimulation amplitude ranges from 262 to 1350 µA required to elicit an ECAP response below population saturation while the fully degenerated population (see Appendix 5.A.2) required stimulus amplitudes between 3060 µA and 4322 µA for the same simulation conditions. Overall, these differences in stimulus amplitude levels are consistent with single SGN responses shown in chapters Chapter 3 and Chapter 4.

Responses to cathodic stimulus for monophasic and biphasic pulse shapes

The top left panel in Fig. 5.3.2 represents typical ECAP responses from a healthy SGN population to cathodic pulses. Specifically, Fig. 5.3.2 shows the response of a healthy SGN population subjected to biphasic, cathodic-first stimulus at the high electrode position. A trend is observed with the N1 peak for the ECAP responses to cathodic-first stimulus being sharper than the anodic-first responses N1 peak described previously (see Sec. 5.3.1.1). The same trend is observed between cathodic monophasic mean N1 latencies and anodic monophasic mean N1 latencies. This indicates that the AP events in close vicinity to the recording electrode are highly synchronised, which is confirmed by the bottom left panel in Fig. 5.3.2. It is also the case that the P2 peak was also "multi-peaked", similar to the responses reported by Ramekers et al. (2014) where they observed two P2 peaks for responses of neurons of non-deafened or recently deafened guinea pigs. Thus, the multi-peaked P2 could originate from multiple excitation sites at the level of the peripheral process.

Similarly, as shown in Fig. 5.3.3 top left panel, the partially demyelinated population produced a comparable morphology to the healthy population profile.

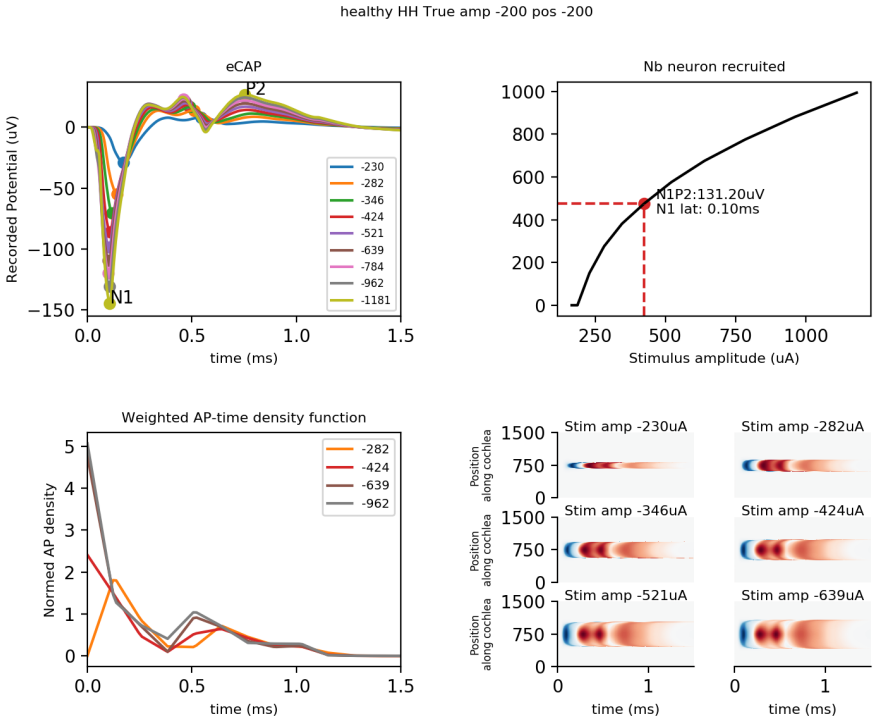

Figure 5.3.2: ECAP response summary for a healthy SGN population under biphasic cathodic stimulation at high electrode position and for the "HH" ionic model. The morphology figures present four panels: 1) top left panel shows the ECAP response; 2) the top right panel shows the neural recruitment as a function of amplitude. The point highlighted on the curve represents the stimulus amplitude that produced a neural recruitment closest to 500 neurons to be used as a comparison between all the conditions. The annotations represent N1P2 amplitude and N1 latency of the ECAP response at that amplitude; 3) the bottom left panel shows the normed density distribution (sum under the curve equals 1) of the APs detected on all neurons in the population for a subset of intensity amplitudes (colors match the top left panel) and; 4) the bottom right panel shows the spread of activity in population as a response to a single stimulation. The stimulatingrecording electrode is located at 750 µm in the vertical axis. Red and blue represent high and low recorded potentials respectively.

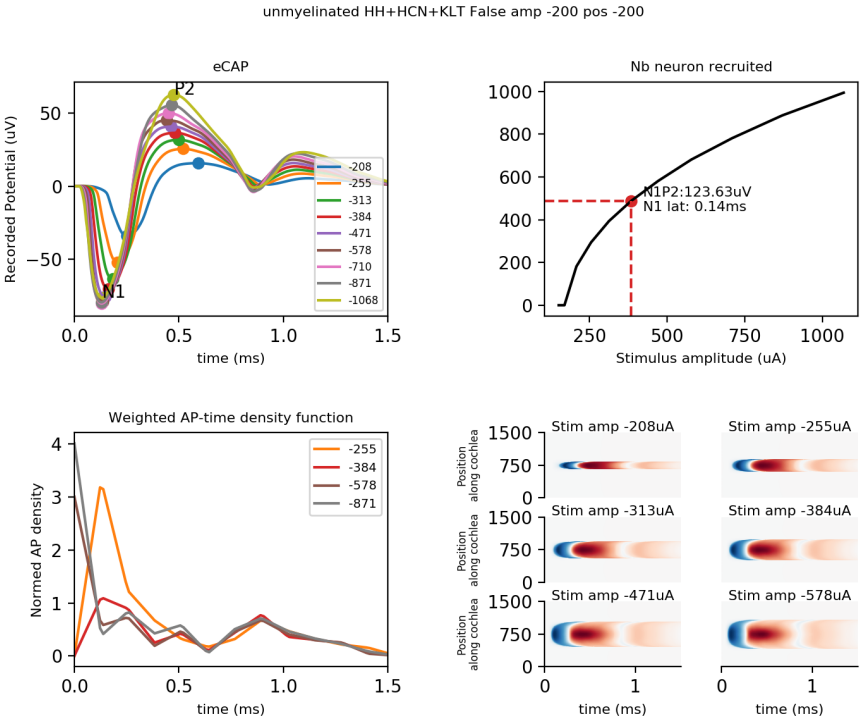

Figure 5.3.3: ECAP response summary for a partially demyelinated SGN population under monophasic cathodic stimulation at high electrode position and for the "HH+KLT+HCN" ionic model. The morphology figures present four panels: 1) top left panel shows the ECAP response; 2) the top right panel shows the neural recruitment as a function of amplitude. The point highlighted on the curve represents the stimulus amplitude that produced a neural recruitment closest to 500 neurons to be used as a comparison between all the conditions. The annotations represent N1P2 amplitude and N1 latency of the ECAP response at that amplitude; 3) the bottom left panel shows the normed density distribution (sum under the curve equals 1) of the APs detected on all neurons in the population for a subset of intensity amplitudes (colors match the top left panel) and; 4) the bottom right panel shows the spread of activity in population as a response to a single stimulation. The stimulatingrecording electrode is located at 750 µm in the vertical axis. Red and blue represent high and low recorded potentials respectively.

However, noticeable differences were observed as to the sharpness of the N1 peak and the lack of multiple P2 peaks. As reported throughout this thesis, the partial demyelination of SGNs generates important increases in AP latency, which are reflected here in the overall width of the N1 peak: it is possible that longer latencies of APs in neurons further from the stimulating/recording electrode might reduce the "sharpness" and amplitude of the N1 peak (Resnick et al., 2018).

A similar morphology is observed for the degenerated case in the low electrode position (see Fig. 5.3.5), which indicates that the morphology is highly correlated with the weighted AP density and not with the absence or presence of the peripheral process, even if pre-somatic node of Ranvier (P6) remains in the degenerated SGN model. It is also important to note that the "multi-peaked" P2 is not observed for the partially demyelinated and fully degenerated responses, which indicates that this effect is most likely caused by a healthy peripheral process interaction (Ramekers et al., 2014).

5.3.1.2 Atypical morphologies

In contrast to the previously described "typical" ECAP morphologies, less-common ECAP responses are also observed for cathodic polarities (mostly at the mid electrode position), regardless of pulse shape and for health status that still had a peripheral process, i.e. healthy and partially demyelinated. Inspecting Fig. 5.3.4 top left panel, it can be noted that the response is "multi-peaked" in the region where the N1 peak would usually be found. The reason for those peaks can be found in the AP density distribution shown in the bottom left panel of Fig. 5.3.4: when compared to AP-times density distributions which were related to more "typical" ECAP responses, e.g. in Fig. 5.3.2 bottom left panel, the distribution here is "multi-peaked", indicating multiple clusters of APs are elicited along the neurons of the population. The weighted contributions of these AP clusters change the overall morphology of the ECAP, since the activity is less synchronized. This can be explained by a complex interaction in the mid-electrode position condition where the electrode is relatively close to the peripheral process and therefore elicits APs in different nodes of the SGN, and possibly even different node sites across the population.

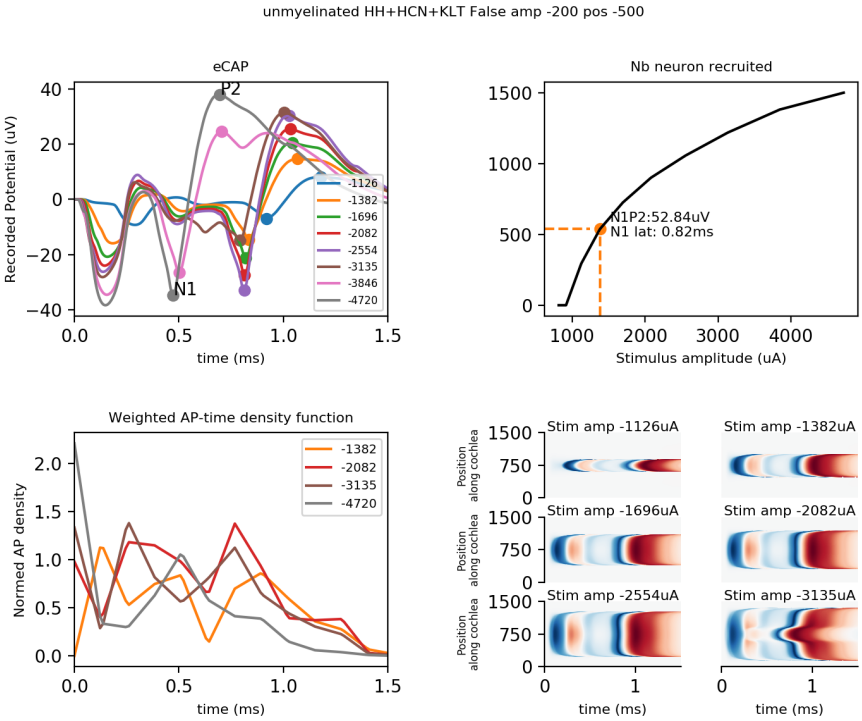

Figure 5.3.4: ECAP response summary for a partially demyelinated SGN population under monophasic cathodic stimulation at mid electrode position and for the "HH+KLT+HCN" ionic model. The morphology figures present four panels: 1) top left panel shows the ECAP response; 2) the top right panel shows the neural recruitment as a function of amplitude. The point highlighted on the curve represents the stimulus amplitude that produced a neural recruitment closest to 500 neurons to be used as a comparison between all the conditions. The annotations represent N1P2 amplitude and N1 latency of the ECAP response at that amplitude; 3) the bottom left panel shows the normed density distribution (sum under the curve equals 1) of the APs detected on all neurons in the population for a subset of intensity amplitudes (colors match the top left panel) and; 4) the bottom right panel shows the spread of activity in population as a response to a single stimulation. The stimulatingrecording electrode is located at 750 µm in the vertical axis. Red and blue represent high and low recorded potentials respectively.

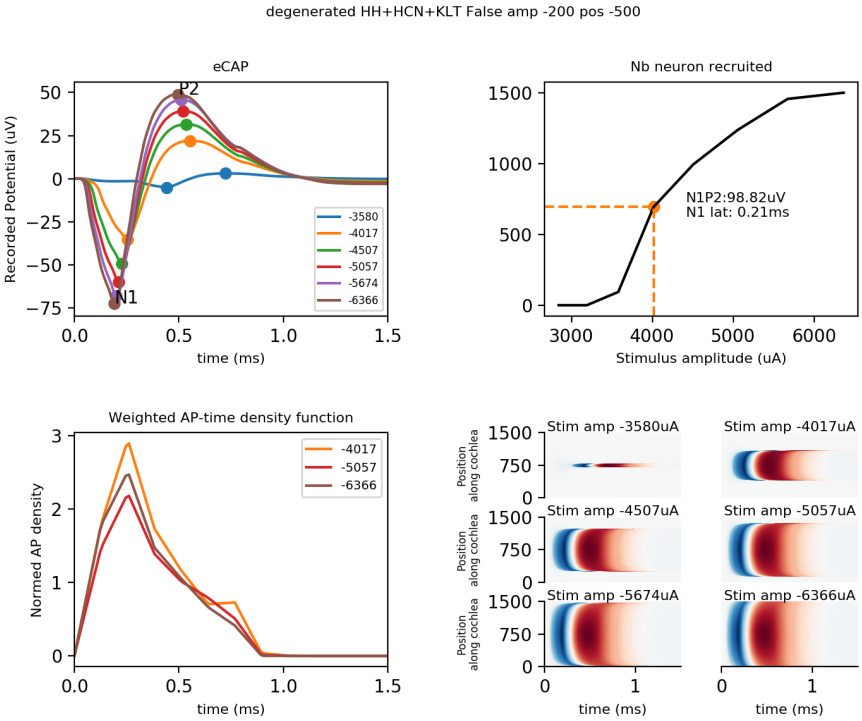

Figure 5.3.5: ECAP response summary for a fully degenerated SGN population under monophasic cathodic stimulation at mid electrode position and for the "HH+KLT+HCN" ionic model. The morphology figures present four panels: 1) top left panel shows the ECAP response; 2) the top right panel shows the neural recruitment as a function of amplitude. The point highlighted on the curve represents the stimulus amplitude that produced a neural recruitment closest to 500 neurons to be used as a comparison between all the conditions. The annotations represent N1P2 amplitude and N1 latency of the ECAP response at that amplitude; 3) the bottom left panel shows the normed density distribution (sum under the curve equals 1) of the APs detected on all neurons in the population for a subset of intensity amplitudes (colors match the top left panel) and; 4) the bottom right panel shows the spread of activity in population as a response to a single stimulation. The stimulatingrecording electrode is located at 750 µm in the vertical axis. Red and blue represent high and low recorded potentials respectively.

Fig. 5.3.5 provides further insight as to the underlying mechanism for the multiple peaks observed in Fig. 5.3.4: essentially, examining the degenerated population ECAP response for the same stimulus conditions (Fig. 5.3.5 top left panel) and the AP-time density distribution for that response (Fig. 5.3.5 bottom left panel), it is observed that the absence of the peripheral process correlates with a single-peaked N1 response. This indicates that, in the case of the partially demyelinated population response showed in Fig. 5.3.4, the "multi-peaked" morphology that was described earlier is caused by complex interactions between the stimulating electrode, the peripheral process and the sites of excitation along the neurons in the population.

The ECAPs responses showing multiple N1 peaks described in this section are somehow similar to those reported by Brown (1994), but on a much smaller scale. This effect seems to be confined to the mid-electrode position and for health profiles containing a peripheral process. Further investigation of this effect were beyond the scope of this thesis.

5.3.2 ECAP N1 latencies vs population health

For each simulation condition—across polarities, electrode positions, pulse shapes, ionic models and SGN health status—ECAP responses were recorded for 10 intensity amplitudes over a −15 dB range above the population threshold intensity, i.e. the first intensity to trigger at least 1 AP across all neurons. The plotted values represent the set of data from this threshold up to the population reached saturation, i.e. all neurons responded. The N1 latencies of the ECAP response at each intensity were systematically recorded.

Due to the large number of conditions tested (2 ionic models x 3 electrode positions x 2 polarities x 2 pulse shapes x 3 SGN health status), the results presented in this section are presented as violin plots. Violin plots are an interesting alternative to boxplots, as they display the entire set of data and its distribution at once. Whilst the focus of the descriptions in this section will be around the mean N1 latencies provided by the violin plots, these plots also give important insight as to the distribution of N1 latencies that were recorded for each simulation condition.

Although the mean N1 latencies from the violin plot accurately represent the overall behaviour between parameters, some individual differences in growth over

the range of stimulus are noted. Overall, it appears that the largest differences in N1 latencies between polarities were found at the largest stimulus amplitude assessed for each condition (see Appendix 5.B).

In Chapter 3 and Chapter 4, it was noted that the effects of ionic channel models ("HH" compared to "HH+KLT+HCN") for single pulse stimulation of the single SGN models were limited to a relatively small shift in thresholds, i.e. "HH" produced smaller thresholds than "HH+HCN+KLT". Because the ECAP measures are based on single pulse stimulation, the effects of ionic models on the ECAP responses modelled were also limited to small shifts in the ECAP thresholds. As no other significant effects were observed between the "HH" and "HH+KLT+HCN" models, the N1 latencies presented here were combined between ionic models to produce the violin plots.

In the case of "typical" ECAP morphologies, the evaluation of the N1 latency was considered to be straight-forward. However, for more complex morphologies (see Fig. 5.3.4) it is more difficult to determine which N1 peak (from the "multi-peaked" response described in Fig. 5.3.4) was the most representative of the ECAP response. In this context, the latency of the latest N1 peak from the multiple peaks seen in Fig. 5.3.4 was chosen, as the morphology of that "late response" was consistent with that from a typical response (cf. Fig. 5.3.3).

5.3.2.1 High electrode position

Mean N1 latencies measured at the high electrode position across all conditions of neural health, polarity and pulse shape were averaged across ionic models and are presented in Fig. 5.3.6. For this electrode position, the mean N1 latencies ranges from 100 µs, in the healthy condition for biphasic, cathodic pulse shape, to 700 µs in the fully degenerated health profile for monophasic, anodic pulse shape.

A trend was observed with N1 latencies for anodic (either monophasic or biphasic pulses) being longer than cathodic N1 latencies. The smallest difference occurs for the partially demyelinated population (100 µs longer for anodic-first biphasic pulse) and the largest difference for the degenerated population (450 µs longer for anodic monophasic).

The overall polarity effects appear in apparent contradiction to latency differences

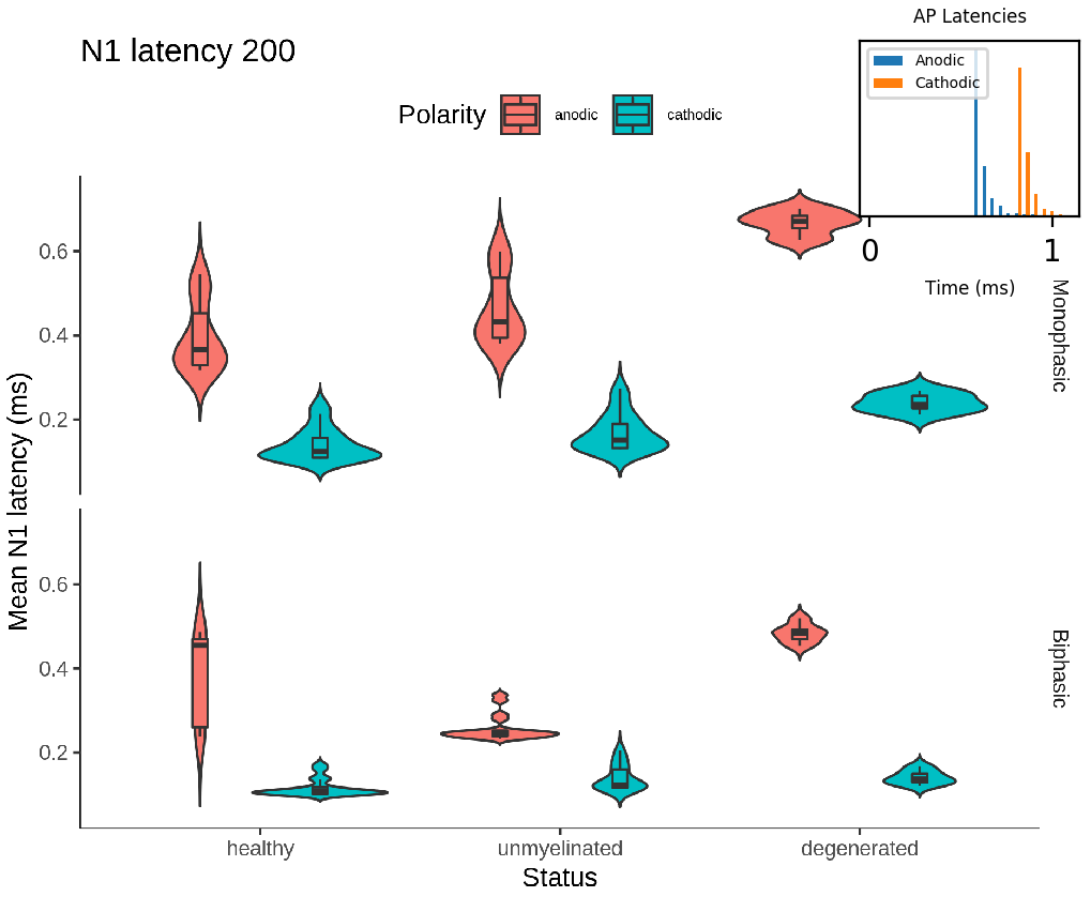

Figure 5.3.6: N1 peak latency at high electrode position (200 µm) for cathodic and anodic polarities and monophasic and biphasic pulse shapes. Latencies of "HH" and "HH+HCN+KLT" ionic models were pooled together as non-significant differences were observed. Inset represent an example of latencies distributions for cathodic and anodic monophasic pulses at the highest electrode position for the degenerated SGN health profile.

in human ECAP responses to biphasic pulse shapes from Undurraga, van Wieringen, et al. (2010), Undurraga, Carlyon, Macherey, et al. (2012) and Macherey, Carlyon, Van Wieringen, et al. (2008). Furthermore, Undurraga, Carlyon, Wouters, et al. (2013b) demonstrated differences in the range 100 to 250 µs (anodic-first shorter than cathodic-first) for human Electrically evoked Auditory Brainstem Response (EABR) responses between the two stimulus polarities. These studies all showed that the anodic-first N1 latencies, and EABR latencies, were shorter than cathodic-first, which would seem to suggest that APs were mostly elicited by the anodic phase of the pulse in both cases. However, it is interesting to note that the latency of the ECAP is decorrelated from spike latency at the most central node. As such, ECAP and EABR latencies are not really comparable. Nevertheless, from the modelling data described here, it appears that the cathodic phase of biphasic stimuli is the most AP eliciting phase.

This contradiction requires an explanation, but it could originate from the presence of the peripheral process in the healthy and partially demyelinated profiles, and the pre-somatic (P6) node of Ranvier in the fully degenerated case, which has been shown to be the main site of excitation for cathodic, biphasic and monophasic single pulses at the high electrode position (see Chapter 4 Fig. 4.3.2).

The inset to Fig. 5.3.6 provides additional insight in to this phenomenon, as it demonstrates that the latencies of APs arriving at node C14 across the degenerated SGN population model were shorter for anodic polarities than cathodic polarities. A similar relationship was also observed for the partially demyelinated and healthy population profiles, matching the single SGN data from Chapter 3 and Chapter 4. This observation would indicate that the N1 latencies from the ECAP responses are not correlated with the AP latencies of the SGN population but are rather only a representation of the AP activity local to the recording electrode.

The latency analysis also reveals an interaction between pulse shape and polarity. In the partially demyelinated case, the monophasic pulse shape generates mean N1 latencies significantly larger for the anodic polarity (450 µs compared to 250 µs for biphasic anodic), whilst the monophasic cathodic (180 µs) and biphasic cathodic-first (170 µs) are almost identical. This is interesting with regards to the eliciting phase in the biphasic condition: because the biphasic pulse essentially represents both polarities, the favoured polarity to elicit APs can vary as a function of amplitude

and distance from the stimulating electrode as well as the population health profile. Comparing the healthy population response to the partially demyelinated in the biphasic pulse shape condition, it appears that the partially demyelinated population is more sensitive to the cathodic phase, i.e. as the first or second phase in the biphasic pulse, whilst the healthy population would favour the first phase, regardless of polarity. Similar to the Inter-Phase Gap (IPG) effects that were reported by Ramekers et al. (2014) where SGNs of normal-hearing guinea pigs were found to benefit more from an increase in IPG between anodic hyperpolarising phases and cathodic depolarising phases. Here, is hypothesized that the partially demyelinated population was less affected by the hyperpolarising anodic phase from the biphasic pulses when compared to the healthy population, resulting in larger latencies for anodic-first stimulations (from 250 µs for demyelinated anodic-first to 390 µs for the healthy anodic-first).

5.3.2.2 Mid electrode position

N1 latencies measured at the mid electrode position across all conditions of neural health, polarity, and pulse shape were averaged across ionic models and are presented as violin plots in Fig. 5.3.7. Interestingly, responses showed that the two health statuses that contain peripheral processes, i.e. healthy and partially demyelinated, do show a longer mean latency for cathodic (550 to 800 µs) than anodic (400 to 650 µs) for both pulse shapes. This is in contrast with the fully degenerated SGN where cathodic latencies are much shorter (100 to 250 µs) than anodic latencies (450 to 700 µs).

The effects of polarity described here for the healthy and partially demyelinated are in line with previous reports (Undurraga, van Wieringen, et al., 2010; Undurraga, Carlyon, Macherey, et al., 2012; Undurraga, Carlyon, Wouters, et al., 2013b; Macherey, Carlyon, Van Wieringen, et al., 2008) with latencies for anodic being shorter than cathodic polarity latencies and also different from the results for mean N1 latencies observed at the high electrode position (see Sec. 5.3.2.1). This could originate from the complex interactions with the SGN peripheral process described in Chapter 3 and Chapter 4, e.g. cathodic blocking across for neurons local to the stimulating electrode. Such an effect could explain why the anodic phase becomes

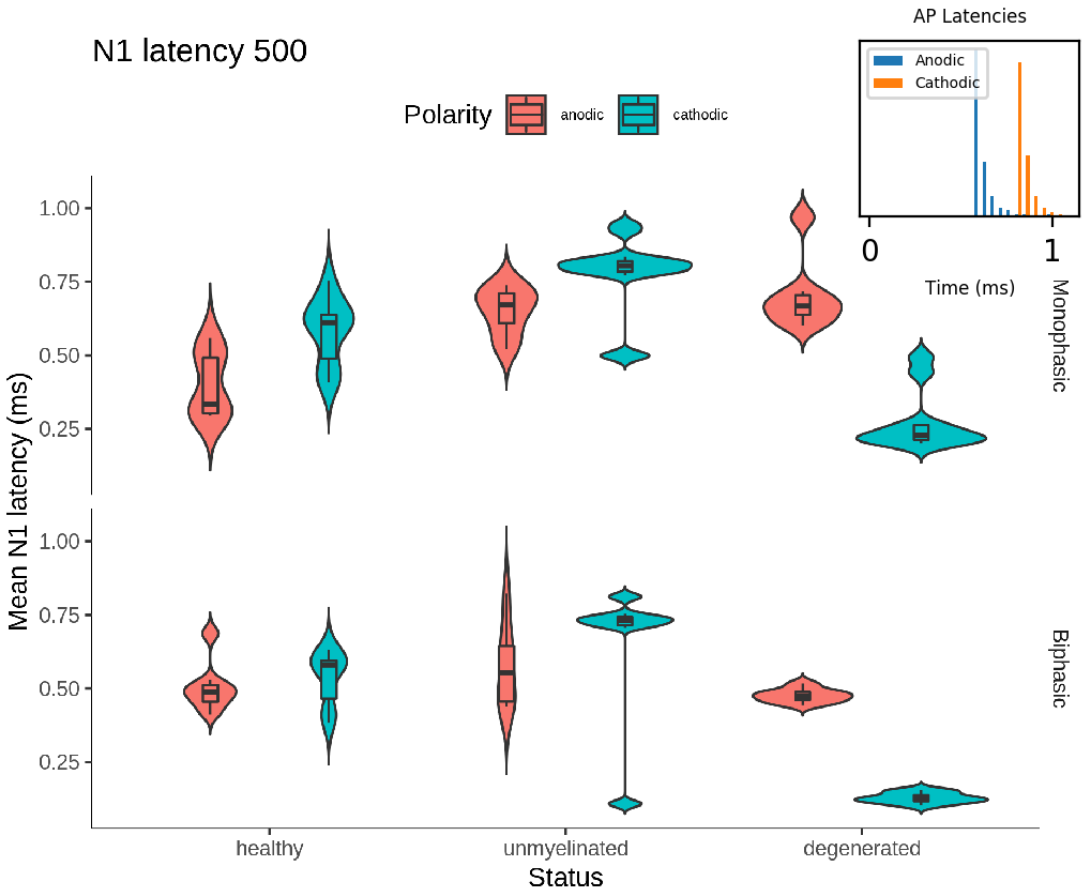

Figure 5.3.7: N1 peak latency at mid electrode position (500 µm) for cathodic (blue) and anodic (red) polarities, using monophasic (top) and biphasic (bottom) pulse shapes. Latencies of "HH" and "HH+HCN+KLT" ionic models were pooled together as non-significant differences were observed. Inset represent an example of latencies distributions for cathodic and anodic monophasic pulses at the mid electrode position for the degenerated SGN health profile.

the most likely eliciting phase for biphasic pulses, and a more efficient polarity for monophasic pulse shapes in those health status conditions (healthy and partially demyelinated) and for this electrode position.

Another possible mechanism to explain the longer mean N1 latency for cathodic than anodic is the morphology of the overall ECAP response at the middle electrode position for single healthy and partially demyelinated SGNs. As described in Sec. 5.3.1.2, the complex morphology that was observed for these conditions changes the approach to determining which N1 should be assessed. From Fig. 5.B.2 and Sec. 5.3.1.2, it is possible to assume that the mean N1 latencies would have been shorter if the initial peak from the multi-peak morphology had been chosen as reference. However, the last peak was used as a reference because of its behaviour and correlation with a typical ECAP response, i.e. a prominent N1-P2 morphology resembling typical responses as those observed at the high or low electrode positions.

For comparison, the fully degenerated population was found to contradict the polarity effects previously reported in humans (Undurraga, van Wieringen, et al., 2010; Undurraga, Carlyon, Macherey, et al., 2012; Undurraga, Carlyon, Wouters, et al., 2013b; Macherey, Carlyon, Van Wieringen, et al., 2008). Similar to the degenerated health profile in Sec. 5.3.2.1, this could be explained by the lack of peripheral process but remaining pre-somatic node of Ranvier (P6), which could make the cathodic polarity still more efficient in the absence of interaction effects, i.e. no cathodic blocking.

5.3.2.3 Low electrode position

N1 latencies from the lowest electrode position for all the simulated SGN health status are shown in Fig. 5.3.8. Overall, mean N1 latencies range from 100 µs, for the biphasic cathodic stimulus in the degenerated health profile, to 700 µs for both partially demyelinated and fully degenerated monophasic anodic stimulus. Some of the mean N1 latencies are 200 µs larger than previous reports for animals (300 to 400 µs in guinea pigs from Ramekers et al. (2014)) and humans (200 to 500 µs from Undurraga, Carlyon, Macherey, et al. (2012)). However, these studies largely reported N1 latencies for responses to biphasic stimulations and the larger latencies here were reported for monophasic stimulations.

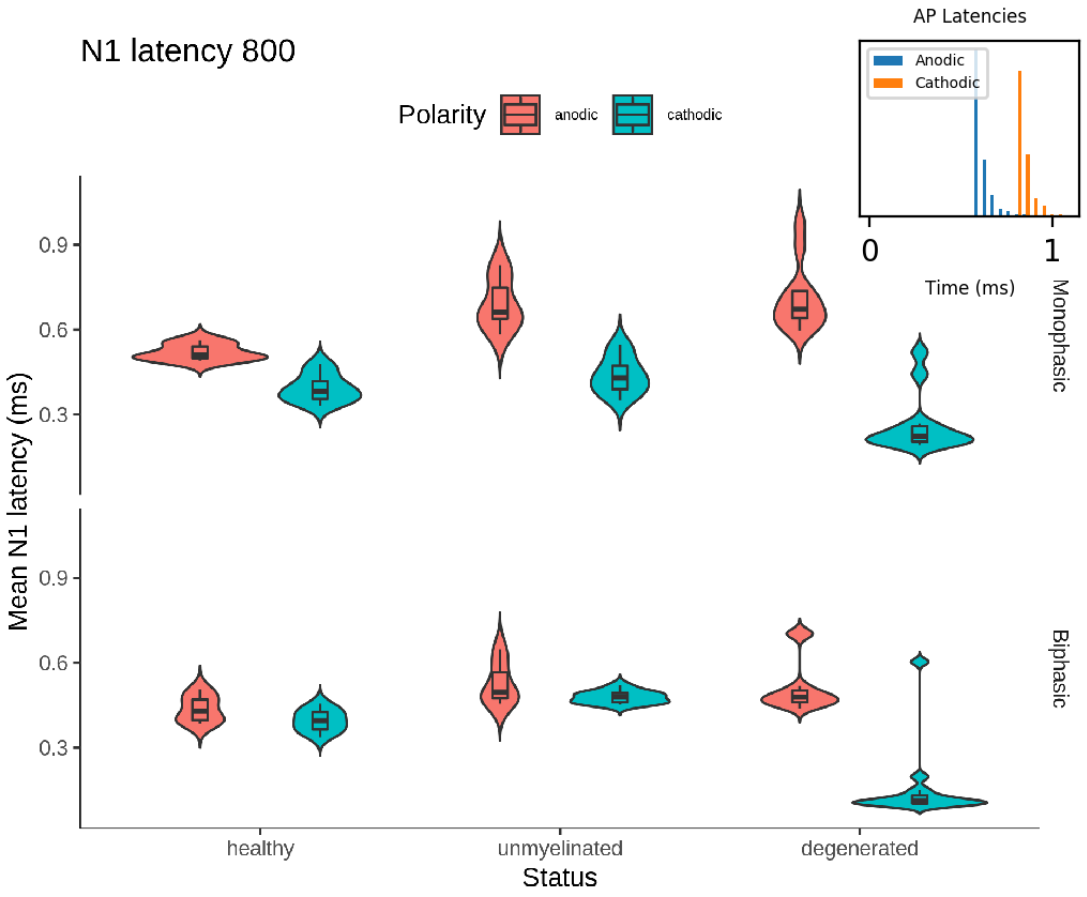

Figure 5.3.8: N1 peak latency at low electrode position (800 µm) for cathodic (blue) and anodic (red) polarities using monophasic (top) and biphasic (bottom) pulse shapes. Latencies of "HH" and "HH+HCN+KLT" ionic models were pooled together as non-significant differences were observed. Inset represent an example of latencies distributions for cathodic and anodic monophasic pulses at the lowest electrode position for the degenerated SGN health profile.

Moreover, trends in polarity effects were observed for all the health profiles for monophasic pulse shapes (150 µs, 200 µs and 450 µs differences for healthy, partially demyelinated, and fully degenerated, respectively) and for the fully degenerated using biphasic pulse shapes (400 µs). However, both healthy and partially demyelinated health profiles showed limited polarity effects (both less than 50 µs). This is found to be below the range of previous human reports (100 to 250 µs from Undurraga, Carlyon, Wouters, et al. (2013b) in EABRs) and with the results described for the high electrode position (see Sec. 5.3.2.1). Interestingly, the range of polarity effects observed for both healthy and demyelinated profiles seems to correspond to the pulse width of 50 µs which would indicate that at the lowest electrode position, the cathodic phase (second phase of an anodic-first biphasic pulse) would be the phase that elicits APs in the modelled population.

Although variable latencies across pulse shape and polarity are evident, the degenerated population shows a ratio of anodic-to-cathodic mean N1 latencies that is relatively constant between monophasic and biphasic pulse shapes (approximatively 2.3) while the ratios for the healthy and partially demyelinated conditions are significantly smaller (1.1 to 1.7) and more variable across pulse shape conditions.

5.3.3 ECAP N1-P2 amplitudes vs population health

Here are described the mean N1-P2 amplitudes that were modelled for the three population profiles and three electrode positions. Similarly to the N1 latencies results reported, N1-P2 amplitudes were recorded for each simulation condition across polarities, electrode positions, pulse shapes, ionic models and SGN health status. ECAP responses were recorded for 10 intensity amplitudes over a range of 15 dB above the population threshold intensity, i.e. the first intensity to trigger at least 1 AP across all neurons. The plotted values represent the set of data from this threshold up to the population reached saturation, i.e. all neurons responded.

Due to the large number of conditions tested the results presented in this section are presented as violin plots of all the N1-P2 amplitudes recorded for each simulation condition over the range of stimulus amplitudes. In addition, the accuracy of the N1-P2 amplitude averaging was also confirmed by comparing the N1-P2 amplitudes for the closest stimulus amplitude which recruited 500 neurons in all conditions. As

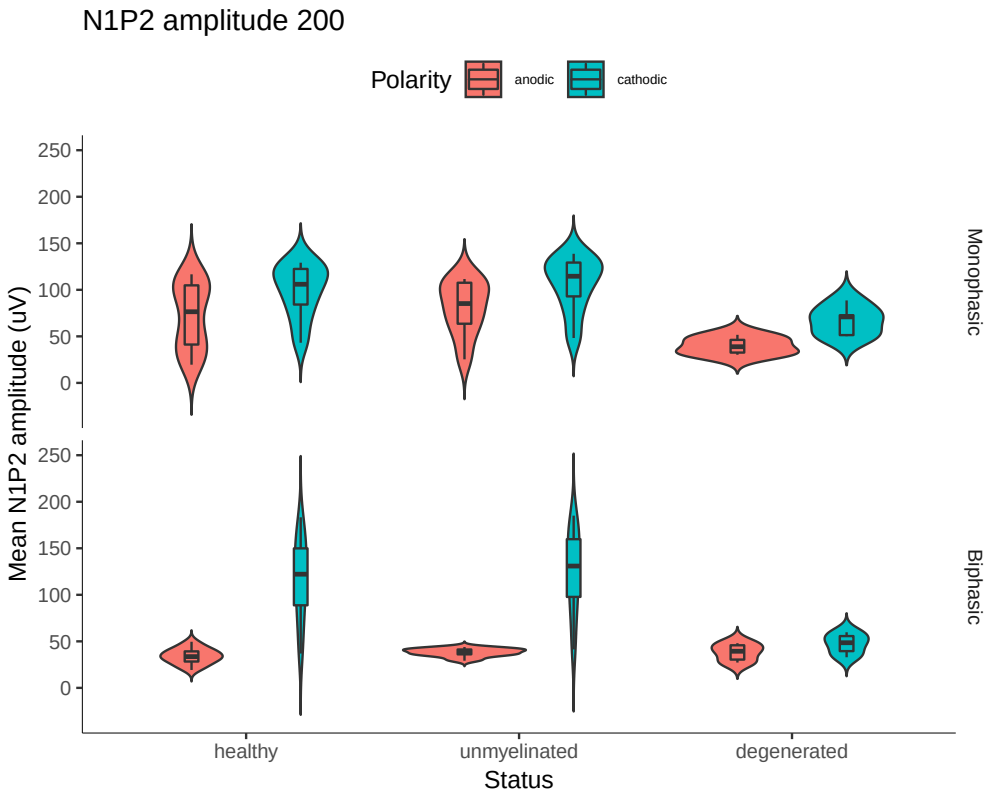

Figure 5.3.9: N1-P2 mean amplitudes at high electrode position (200 µm) for cathodic (blue) and anodic (red) polarities and monophasic (top) and biphasic (bottom) pulse shapes. Amplitudes of "HH" and "HH+HCN+KLT" ionic models were pooled together as non-significant differences were observed.

for the N1 latencies described in Sec. 5.3.2, it appears that the largest differences in N1-P2 amplitudes between polarities are found at the largest stimulus amplitude reported for each condition (see Sec. 5.C).

5.3.3.1 High electrode position

Fig. 5.3.9 shows the N1-P2 amplitudes for the different health statuses and pulse shapes at the highest electrode position. Here, mean N1-P2 amplitudes range from 30 µV for biphasic anodic-first in the healthy population to 120 µV for the cathodic-first biphasic in the partially demyelinated population.

Interactions across polarity, population health status, and pulse shape at the high electrode position are observed. For monophasic pulse shapes, the mean N1-P2

amplitude difference between stimulus polarity across all SGN profiles is similar (25 to 30 µV across all conditions). However, mean N1-P2 amplitudes for both cathodic and anodic polarities in the degenerated population are 50 to 60 µV smaller than in the healthy and partially demyelinated populations.

Biphasic responses shows larger polarity effects on the N1-P2 amplitude for both healthy and partially demyelinated SGN populations. In addition, the anodic-first stimulus N1-P2 amplitude is consistently smaller than the cathodic-first amplitude (about 80 µV smaller) for both healthy and partially demyelinated populations. This is in contrast to biphasic responses from the degenerated population which anodic-to-cathodic N1-P2 amplitude difference is relatively small (<10 µV).

5.3.3.2 Mid electrode position

Fig. 5.3.10 shows the N1-P2 amplitude for the different health status and pulse shape conditions measured for ECAP responses at the middle electrode position. N1-P2 mean amplitudes are relatively similar across both pulse shape and health status for both polarities. Overall, amplitudes range between 30 and 75 µV across pulse shapes and polarities. The smallest amplitude is observed for the partially demyelinated population using cathodic-first biphasic pulses, while the maximum amplitude is obtained for the fully degenerated SGN population with cathodic monophasic pulses.

Monophasic and biphasic N1-P2 amplitudes are similar across all conditions. Anodic and anodic-first N1-P2 mean amplitudes are similar and ranged between 30 to 50 µV while cathodic and cathodic-first amplitudes ranged between 50 to 75 µV, respectively. For both pulse shapes, the cathodic responses evoke larger N1-P2 amplitudes than the anodic ones.

The most significant effect on mean N1-P2 amplitude across health status is observed for the fully degenerated population in which the monophasic pulses resulted in a larger difference between anodic (50 µV) and cathodic (75 µV) polarities compared to partially demyelinated (40 µV anodic, 50 µV cathodic) and healthy (45 µV anodic and 55 µV cathodic).

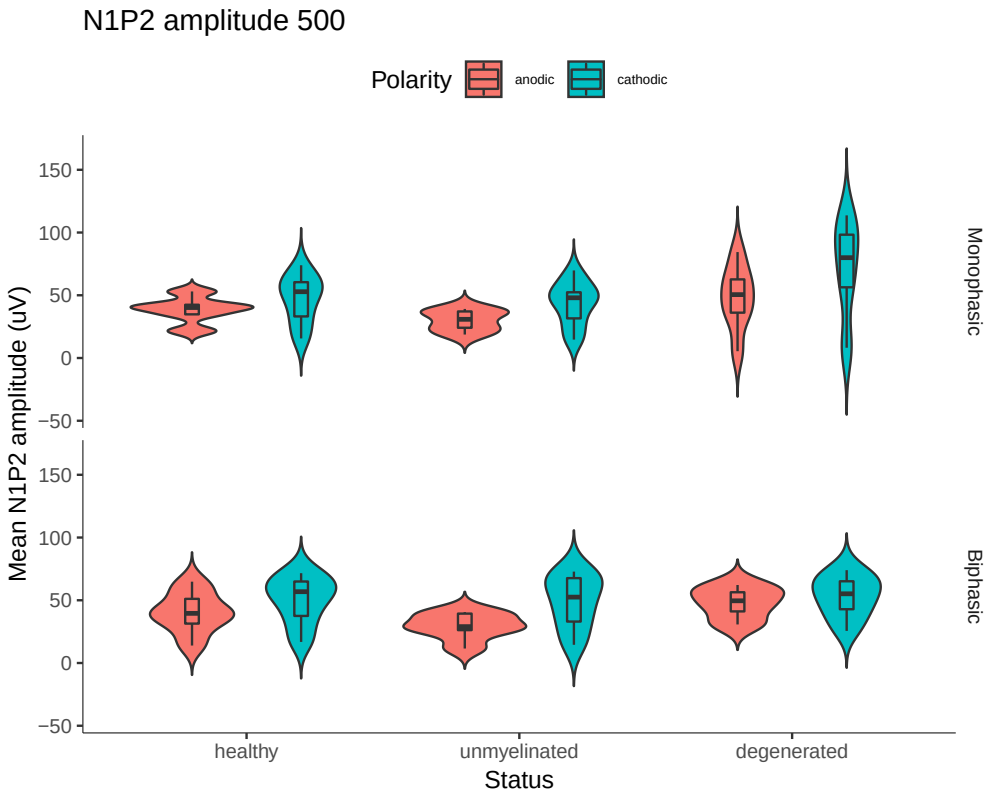

Figure 5.3.10: N1-P2 mean amplitudes at mid electrode position (500 µm) for cathodic (blue) and anodic (red) polarities using monophasic (top) and biphasic (bottom) pulse shapes. Amplitudes of "HH" and "HH+HCN+KLT" ionic models were pooled together as non-significant differences were observed.

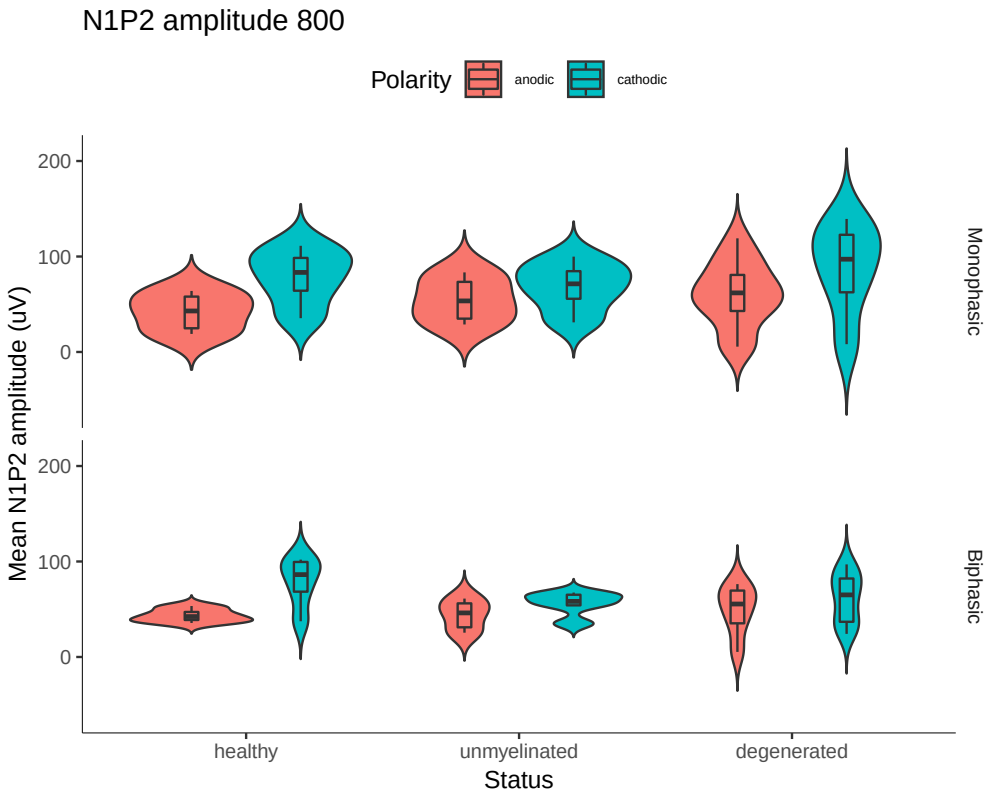

Figure 5.3.11: N1-P2 mean amplitudes at low electrode position (800 µm) for cathodic (blue) and anodic (red) polarities using monophasic (top) and biphasic (bottom) pulse shapes. Amplitudes of "HH" and "HH+HCN+KLT" ionic models were pooled together as non-significant differences were observed.

5.3.3.3 Low electrode position

Fig. 5.3.11 shows ECAP N1-P2 amplitudes for different health status and pulse shapes at the lowest electrode position. Amplitudes at this electrode position range from 40 µV, for the healthy population using monophasic anodic pulses, to 100 µV, for the fully degenerated profile using monophasic cathodic pulses.

Although no significant pulse shape effects are noted for the mean N1-P2 amplitudes, polarity differences are significant for most conditions. Amplitude differences due to polarity range from 10 µV for the biphasic pulse-shape and partially demyelinated population (cathodic-first higher), to 40 µV for monophasic pulses in the healthy population (cathodic higher). Again, even though the amplitudes reported by Miller, Abbas, Hay-McCutcheon, et al. (2004) were overall much larger than the ones reported here, they also reported that cathodic pulses produced larger N1-P2 amplitudes than anodic pulses.

5.4 Discussion

In this Chapter, ECAP responses for populations representing 1500 SGNs positioned along a 1500 µm straight line were presented. Three simplified population profiles were tested to evaluate effects of neural status: 1) healthy ; 2) partially demyelinated SGNs and; 3) fully degenerated SGNs.

The modelling data generate potentially important insights into the effectiveness of different pulse shapes and polarities on the recruitment of population of SGNs, and it appears that some features of the specific ECAP responses of these populations could be used to assess neural health using a polarity-based strategy. Polarity effects have been studied in both ECAP (Undurraga, van Wieringen, et al., 2010; Undurraga, Carlyon, Macherey, et al., 2012; Macherey, Carlyon, Van Wieringen, et al., 2008) and EABR (Undurraga, Carlyon, Wouters, et al., 2013b) as a potential tool to identify the most effective way to stimulate populations of SGNs in the context of CI stimulation. Here, population models for different neural health profiles are introduced, with the aim of identifying some of the key features that could be useful in a clinical environment to assess neural health.

First, the morphology of ECAP responses from different populations were described:

it was observed that morphologies could be considered to be either "typical", such as Fig. 5.3.1 or Fig. 5.3.2 and with comparable ECAP responses from computational (e.g. Briaire and J. H. Frijns (2005)) and human models (Macherey, Carlyon, Van Wieringen, et al., 2008; Undurraga, van Wieringen, et al., 2010; Undurraga, Carlyon, Macherey, et al., 2012). It was also shown that some electrode position and stimulus configurations produced "atypical", multi-peaked morphologies that originate from complex interactions at the peripheral level.

Two important factors of the simulation of ECAP must be considered: 1) the double-peaked morphology due to multiple sites of excitation 2) the difference in morphology related to electrode position (as the same electrode is used to stimulate and record). These generate a limitation in the analysis of ECAP N1 latencies and N1-P2 amplitudes, as strong interactions are observed between these two factors. Thus, the effects of N1 latency and N1-P2 growth can only be compared across the same electrode position condition.

An important effect was noted at the mid electrode position where neural populations with a peripheral process (healthy and partially demyelinated) had mean N1 latencies that were shorter for the anodic than the cathodic polarities for both monophasic and biphasic pulse shapes. However, the degenerated profile showed mean N1 latencies that were similar to the other two electrode position. As mentioned in Sec. 5.3.1.2 and Appendix 5.B, it is important to note that the reason for this difference in latencies could be due to the choice of N1 peak in the "atypical" ECAP morphologies that were described (see Sec. 5.3.1). This specific effect should be further investigated as previous studies in cats (Miller, Abbas, Nourski, et al., 2003) and guinea pigs (Brown, 1994) have reported double peaked "antidromic" ECAP recordings for different electrode configurations, i.e. monopolar, bipolar, tripolar, and mostly in the presence of the peripheral process, i.e. undeafened animals. The influence of the stimulating/recording electrode on the morphology of ECAP responses was beyond the scope of this thesis.

Second, the N1 latencies extracted from the ECAP responses are informative as to the overall timing of the AP events across the entire population but less so concerning the time required to travel towards the last node of Ranvier (C14). Overall, it was observed that anodic conditions had longer mean N1 latencies than cathodic pulses, which would indicate that the mean N1 latencies are mostly decorrelated from the

AP latencies. For example (see Sec. 5.3.2.1 and Fig. 5.3.6 inset), although the mean N1 latency for anodic monophasic was longer than its cathodic counterpart, the latency distribution for APs reaching node C14 in the stimulated population were shorter for the anodic stimulus. This effect raises an important consideration, as the ECAP response N1 latency should be considered decoupled from the AP events in the population and to be considered only within a fixed electrode position condition.

The mean N1 peak latencies were found to range between 100 to 800 µs which is comparable to the N1 peak latencies that were previously reported for animals (300 to 400 µs in guinea pigs (Brown, 1994; Ramekers et al., 2014), and 80 to 210 µs (Miller, Abbas, Hay-McCutcheon, et al., 2004) and 400 to 1000 µs (Miller, Abbas, Robinson, et al., 1999) in cats) and humans (200 to 500 µs, Frijns, Briaire, De Laat, et al. (2002), Undurraga, van Wieringen, et al. (2010), and Undurraga, Carlyon, Macherey, et al. (2012)). Also, long N1 peak latencies were reported here, i.e., larger than 600 µs, mostly observed for monophasic pulse shapes, which resemble more data from *in vivo* animal data than human data. Further modelling should be conducted to identify if morphological considerations, i.e. differences in SGN morphology between cats, guinea pigs and humans, could explain some of the longer N1 latencies observed.

It is also important to note that in the model with a population of fully degenerated SGNs, the pre-somatic compartment (P6) was left in place (similarly to the peripheral process truncation from Smit, Hanekom, van Wieringen, et al. (2010)) which impacted the latency differences due to polarity (anodic N1 latencies much longer than cathodic N1 latencies) as the site of excitation can still move to the remaining peripheral node of Ranvier.

Overall, the mean N1-P2 amplitudes ranged between 30 µV and 120 µV between all the simulated conditions: the smaller mean amplitudes were produced for anodic stimulus polarity conditions (30 to 80 µV) when compared to the cathodic polarity conditions (40 to 120 µV). These results are definitely on the low range of typically ECAPs responses in humans (50 to 700 µV from Macherey, Carlyon, Van Wieringen, et al. (2008) , 5 to 500 µV from Undurraga, van Wieringen, et al. (2010) and Undurraga, Carlyon, Macherey, et al. (2012)) and animals (500 to 2000 µV for guinea pigs from Ramekers et al. (2014), 500 to 10 000 µV for cats from Miller, Abbas, Hay-McCutcheon, et al. (2004)), but still in the acceptable range of expected

responses (Gärtner et al., 2018).

An explanation for the lower range of N1-P2 amplitudes described in this study could be that here are only modelled subpopulations of SGNs, organised in a linear plane, whereas the real intracochlear measurements can also be impacted by recruitment of SGNs away from the target population, i.e. stimulating neurons in other turns of the cochlea or ectopic stimulation, similar to the excitation patterns reported by Briaire and J. H. Frijns (2005).

Using the population models presented here in more realistic conditions, i.e. with 3D conduction models of the cochlea, could help explain more about these effect but is beyond the scope of this thesis.

In addition, the polarity effects observed here were similar to the differences in N1-P2 amplitude reported by Miller, Abbas, Hay-McCutcheon, et al. (2004): the responses to cathodic polarity stimulus systematically produced higher mean N1-P2 amplitudes than the responses to anodic polarity stimulus.

Importantly, the effects of ionic channel were not significant within health status and electrode position conditions. The absence of significant effects of the ionic model on population responses for single pulse stimulations, i.e. ECAP, is in line with the discussions and outcomes of Chapter 3 and Chapter 4 where the "HH+HCN+KLT" had minimal impact on single pulse stimulus apart from shifts in thresholds. Additional figures of N1-P2 amplitudes as a function of stimulus amplitude were added in the Appendix to illustrate the results that were averaged and presented here (see Appendix 5.C).

Furthermore, discussions on electrode position effects are complicated because of the multiple interactions that derive from using the same electrode for both stimulation and recording of the response. Further experiments should investigate the specific contribution of the electrode position on the recorded ECAP and its impact in the context of clinical applications.

5.4.1 Effects of pulse shape

Multiple effects related to the pulse shape were observed. First, mean N1 latencies for monophasic anodic pulses were overall larger than their biphasic counterparts. Second, large differences in N1-P2 ratios were observed between monophasic and

biphasic conditions.

From a perspective of a prediction tool, the possibility of evaluating differences between monophasic and biphasic pulse shapes is appealing because of the additional depth of information that can be extracted. As seen for the analysis of monophasic and biphasic N1 latencies and N1-P2 amplitudes, the differences between monophasic and biphasic could be used as an indicator of health status. A good illustration of how this could be used can be seen for N1 latencies at the high electrode position: with the assumption that electrode position was known, e.g. using ECAP threshold levels comparing anodic and cathodic levels or imaging techniques, the difference in N1 latencies between monophasic and biphasic pulse shapes could differentiate the target population between healthy and partially demyelinated. It is important to note that, as shown in Appendix 5.B.3, some conditions did not allow to pick a specific intensity level response to establish the N1 latency difference between polarities. As such, this data should be used as a mean of the N1 latencies over the whole range of stimulation intensities, which would encompass the latency differences.

This is possible because the partially demyelinated anodic-to-cathodic N1 latency ratio for biphasic pulses would be significantly smaller than for monophasic, while the fully degenerated and healthy population ratios would be similar to identical.

Although it is not possible to use monophasic stimulations in human CI users because of the chemical non-reversibility of those stimuli (Brummer and Turner, 1977), it is possible to use asymmetrical pulses with long discharge phases, e.g. 10 times the duration for 1/10 of the amplitude, or alternating polarity monophasic pulses with long inter-phase gaps. These are interesting pulse shapes, as results from humans (Macherey, Van Wieringen, et al., 2006; Macherey, Carlyon, Van Wieringen, et al., 2008; Undurraga, van Wieringen, et al., 2010; Undurraga, Carlyon, Macherey, et al., 2012; Undurraga, Carlyon, Wouters, et al., 2013a), suggest that they are similar to monophasic pulses. Such alternative pulse shapes could be used as a diagnostic tool to complement the information provided by biphasic pulses, comparable to the IPG technique introduced by Ramekers et al. (2014). Ideally, by evaluating the overall differences in ECAP thresholds, N1 latencies, and N1-P2 amplitudes produced by biphasic symmetric and asymmetric or alternating polarity monophasic pulses, a strong profile of neural survival could be established.

5.4.2 Effects of polarity

A combination of effects originating in stimulus polarity was also described through this thesis. First, changes in the morphology of the ECAP response were observed between anodic and cathodic pulses with anodic monophasic and biphasic pulses producing a relatively large P1 peak due to the hyperpolarization of neighbouring SGNs' membrane. Second, the ratios between the anodic and cathodic polarities seemed to be relatively constant between pulse shape conditions for the degenerated health profile. However, for the partially demyelinated profile, the ratio between the monophasic and biphasic conditions decreased in both high and low electrode positions. Similar behaviour was also observed for the healthy profile at the low electrode position. This polarity effect could be an indicator of peripheral neural survival as it mostly appears for healthy and demyelinated profiles.

As explained in Sec. 5.3.1.2, the presence of multiple N1 peaks can be ascribed to the density distribution of AP events relative to the electrode position. The most likely explanation for this effect is that the interactions occurring at the mid electrode position due to the remaining peripheral process cause this multi-site distribution of APs which, in turn, explains the ECAP morphology. Including this information in the scope of neural population health assessment, the presence of multiple peaks could be used as a strong indicator of partial to full peripheral process survival.

From the modelling data, it appears that polarity effects, when combined with information about overall thresholds or additional metrics of health status, could also be used to diagnose different health profiles based on the mean N1 latencies and mean N1-P2 amplitudes of ECAP responses. For example, referring to the results described in Fig. 5.3.8 and Fig. 5.3.11 for biphasic stimulations, the fully degenerated health profile can be distinguished from the healthy and partially demyelinated profiles by examining the combined polarity effects on N1-P2 amplitude and N1 latency; namely, a 50% larger N1-P2 amplitude for cathodic-first combined with limited to no difference in N1 latency between anodic-first and cathodic-first responses would indicate a healthy target population. Moreover, a 10 to 20% larger N1-P2 amplitude for cathodic-first combined with limited to no difference in N1 latency between anodic-first and cathodic-first responses would indicate a partially

demyelinated target population. Finally, a 10 to 20% larger N1-P2 amplitude for cathodic-first combined with a large difference (anodic-first more than 50% larger than cathodic-first) in N1 latency responses would indicate a fully degenerated target population.

These observations could be generalised to a neural health prediction model, which could be used for different pulse shapes and that would be of the form:

$$Health_{pop} = \alpha_1 Thr_- + \alpha_2 Thr_+ + \alpha_3 Morphology + \alpha_4 N1_{Lat+/-} + \alpha_5 N1P2_{Amp+/-} \tag{5.3}$$

where $Health_{pop}$ is the neural population health status, Thr_- and Thr_+ represent the anodic and cathodic thresholds respectively, $Morphology$ defines possible ECAP morphology categories, e.g. single peak vs multiple peaks, of the ECAP response, $N1_{Lat+/-}$ represents the N1 latency ratio between cathodic and anodic responses and, $N1P2_{Amp+/-}$ represents the N1-P2 amplitude ratio between anodic and cathodic responses. Such a model could be used as a prediction tool with the aim to evaluate the potential effectiveness of specific stimulation strategies with respect to the neural survival of the target SGN population. Finally, this model could be further complemented by additional effects in response to variation of other stimulus parameters such as IPG (Ramekers et al., 2014).

5.4.3 ECAP neural health prediction accuracy

After the description of the potential use of polarity effects and stimulus pulse shape as a tool for neural survival predictions, the question remains as to the accuracy of the neural survival information in the context of more CI realistic stimulus, i.e. pulse trains.

Building on the single SGN findings from Chapter 3 and Chapter 4 about the effects of ionic model (e.g. pulse-rate blocking described in Sec. 5.3.1), some preliminary investigation into pulse-train responses at the population level were introduced in this Chapter to determine whether or not the "blocking" effects at the level of single SGNs would still be observed at the population level.

Because of the time-resource required to run these computational models under pulse-trains, only the 2 conditions that showed the most interesting patterns in

single neuron scenarios (see Chapter 3 and Chapter 4) were studied.

Fig. 5.4.1 shows the overall response of a population of healthy SGNs modelled with the "HH" when subjected to cathodic-first pulse-trains stimulations at 1000 pps and at a high electrode position. This condition was chosen according to the results of the equivalent single neuron response that was previously described (see Chapter 3) in which monotonic spike-rate functions were observed for the "HH" but not for the "HH+HCN+KLT" model.

Fig. 5.4.1 top panel shows the overall population response, i.e. the sum of APs across the entire population, which was monotonic for the range of amplitudes used (35 to 60 dB).

The spread of AP activity (Fig. 5.4.1 mid panel) in response to pulse-trains was relatively condensed around the electrode location (750 µm in the vertical axis).

Latencies for this population ranged between 1 and 1.5 ms and were normally distributed around 1.2 ms. This result is in accordance with Chapter 3 where responses from single neurons (under similar conditions) also showed relatively small variability around 1.2 ms.

This can be compared with Fig. 5.4.2 which shows the overall response of a healthy SGN population using the "HH+HCN+KLT" ionic model. Here, a 1000 pps cathodic-first pulse train was delivered from an electrode located at a high position.

Fig. 5.4.2 top panel now shows a different population response to the one described in Fig. 5.4.1. The response is non-monotonous with peaks of activity occurring at 51, 70, and 78 dB and troughs at 55 and 75 dB A possible explanation of the difference in the AP activity of the population is found in the spread of AP activity (Fig. 5.4.2 mid panel). Here, the SGNs closest to the electrode start firing in response to the pulse-train, but later stop eliciting APs due to spike-rate adaptation effects that were introduced with the voltage-gated hyperpolarization-activated cation (HCN) and voltaged-gated delayed-rectifier potassium (KLT) ionic channels (Fig. 5.4.2). Then, the SGNs positioned further from the electrode start the same ON/OFF cycle until the fringing SGNs are also blocked.

Such a non-monotonic function appears to be similar to what has been previously reported by Macherey, Carlyon, Chatron, et al. (2017) who reported non-monotonic loudness growth functions in humans and theorized that they could be due to blocking effects happening at the SGN level. The trough in the population AP

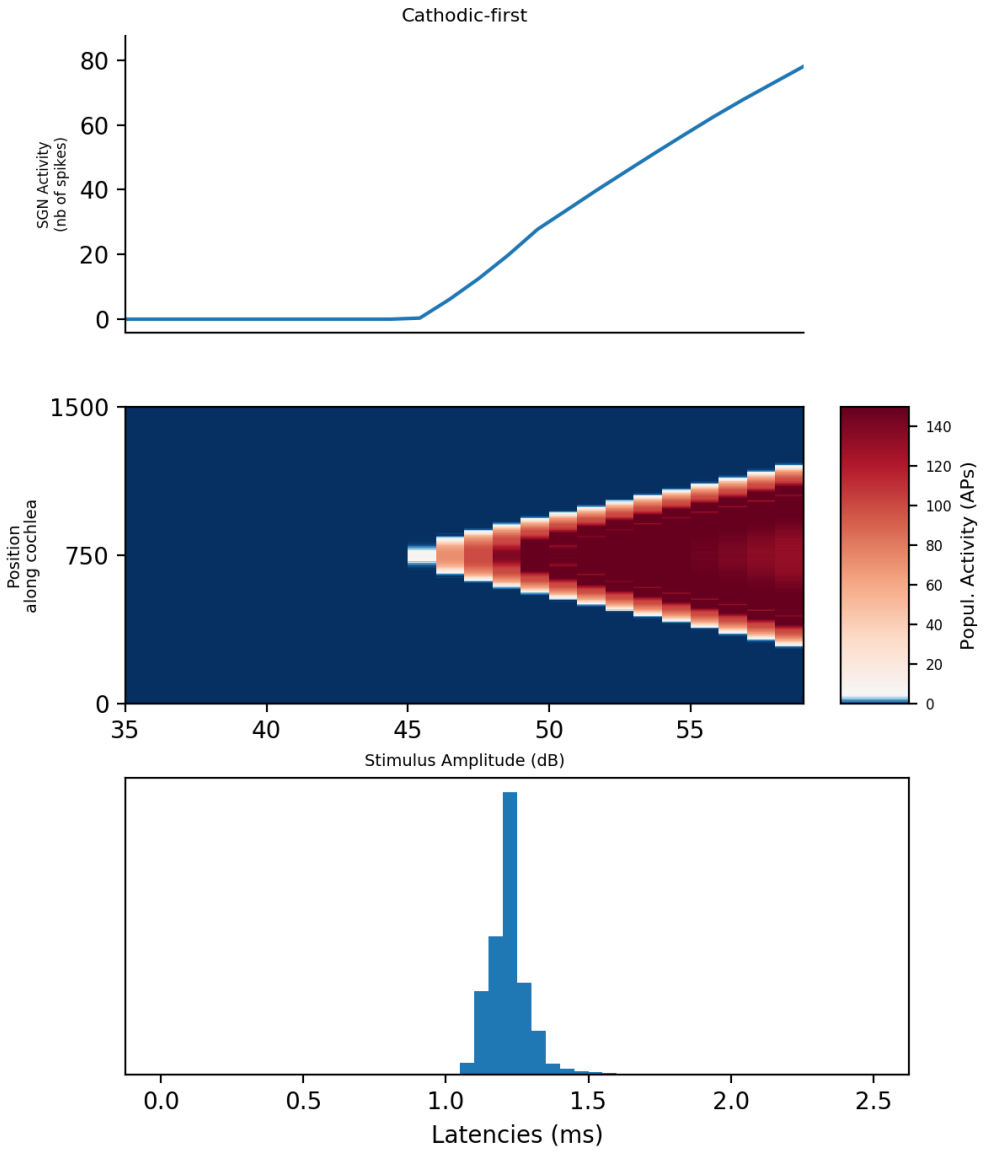

Figure 5.4.1: Population response to pulse trains for a healthy SGN health profile, the "HH" ionic model when subjected to cathodic-first pulse-trains stimulations at 1000 pps and at a high electrode position. Top panel shows the AP activity as a function of stimulus amplitude, the mid panel shows the activity spread over the population as a function of intensity and the bottom panel shows the distribution of all the latencies collected over the entire range of stimulus amplitudes.

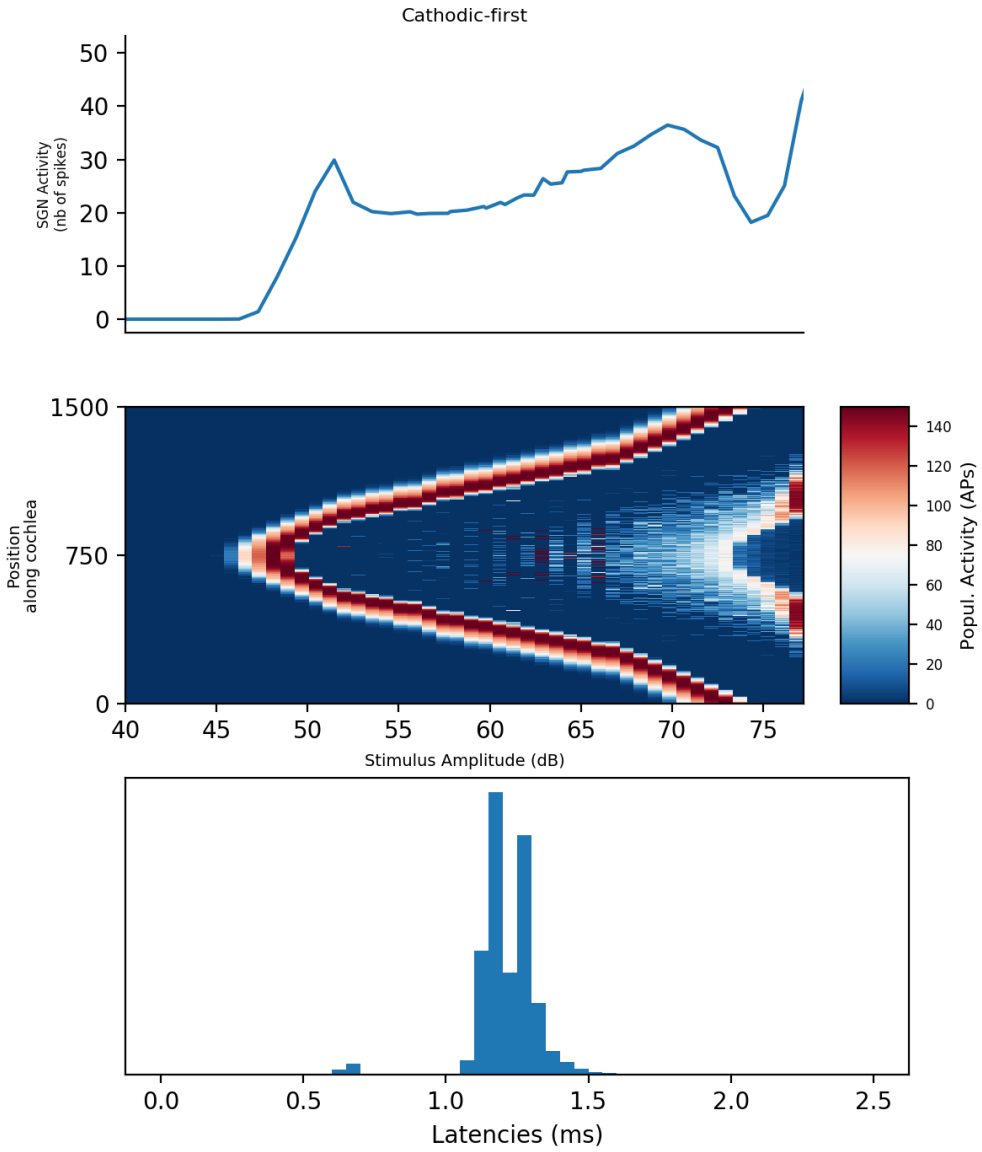

Figure 5.4.2: Population response to pulse trains for a healthy SGN health profile, the "HH+KLT+HCN" ionic model when subjected to cathodic-first pulse-trains stimulations at 1000 pps and at a high electrode position. Top panel shows the AP activity as a function of stimulus amplitude, the mid panel shows the activity spread over the population as a function of intensity and the bottom panel shows the distribution of all the latencies collected over the entire range of stimulus amplitudes.

activity due to blocking effects of the HCN and KLT ionic channels could be an additional/alternative explanation for that effect. However, it is important to note that this effect in Macherey, Carlyon, Chatron, et al. (2017) was observed at much lower pulse-rate (100pps), which would indicate the absence of spike-rate adaptation. Here, the trough in activity observed could also be explained by pure spike-rate adaptation and/or by the subpopulation characteristics, e.g. all neurons are identical which might create additional complexity. Further investigation into the nature of these non-monotonic behaviours should be conducted to make improved predictions.

There seems to be an important mismatch between the modelling prediction of neural recruitment, i.e. modelled ECAPs, and the modelled response of the same populations when subjected to pulse train simulations. In other words, it has long been assumed that a recruited neuron would be a performing neuron, i.e. a neuron properly encoding electrical signal. But the results presented here for the "HH+HCN+KLT" model seem to indicate that a population that would have been predicted to be "recruited" would not encode pulse trains properly. However, due to the heavy computational resources required to simulate the population models under pulse-trains, the scope of the results presented in this last section should be put into perspective. Further investigations into the effects of ionic channel models on SGN populations and their response to pulse train should be conducted to allow for more definitive conclusions.

To conclude, although the ECAP response would be the same for both the "HH" and "HH+HCN+KLT" models of a healthy SGN population, the encoding of pulse-trains could not have been anticipated by this measure. Although neural survival predictions are possible and undoubtedly informative, the level of information cannot directly be translated to pulse-train predictions (as suggested by the model). Further developments should investigate whether ECAP responses using pulse-trains could be useful to make such predictions. Also, further work should investigate what features of the model could explain this mismatch.

Appendix

Additional information about specific modelling results that might be of interest to the reader have been included in this section.

5.A Additional morphology figures

This section shows the additional figures with respect to the ECAP morphologies that were observed.

5.B Additional N1 latency figures

This section shows the additional figures with respect to the ECAP response N1 latency that were observed.

5.C Additional N1-P2 amplitude figures

This section shows the additional figures with respect to the ECAP response N1-P2 amplitude that were observed.

5.D Pulse-train responses

This section shows the additional figures with respect to the pulse train responses that were observed.

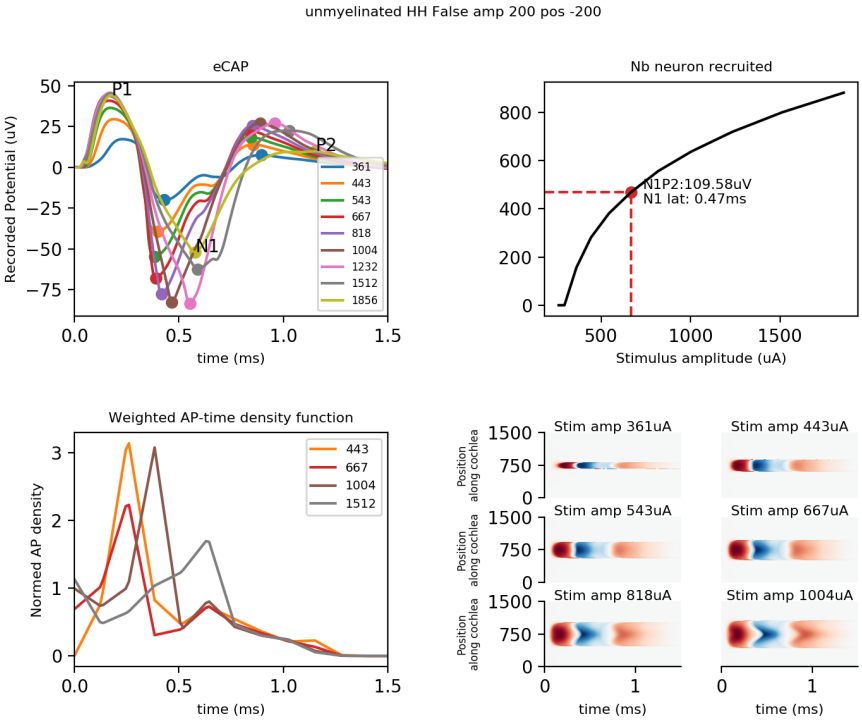

Figure 5.A.1: ECAP response summary for a partially demyelinated SGN population under monophasic anodic stimulation at high electrode position and for the "HH" ionic model. The morphology figures present four panels: 1) top left panel shows the ECAP response; 2) the top right panel shows the neural recruitment as a function of amplitude. The point highlighted on the curve represents the stimulus amplitude that produced a neural recruitment closest to 500 neurons to be used as a comparison between all the conditions. The annotations represent N1P2 amplitude and N1 latency of the ECAP response at that amplitude; 3) the bottom left panel shows the normed density distribution (sum under the curve equals 1) of the APs detected on all neurons in the population for a subset of intensity amplitudes (colors match the top left panel) and; 4) the bottom right panel shows the spread of activity in population as a response to a single stimulation. The stimulatingrecording electrode is located at 750 µm in the vertical axis. Red and blue represent high and low recorded potentials respectively.

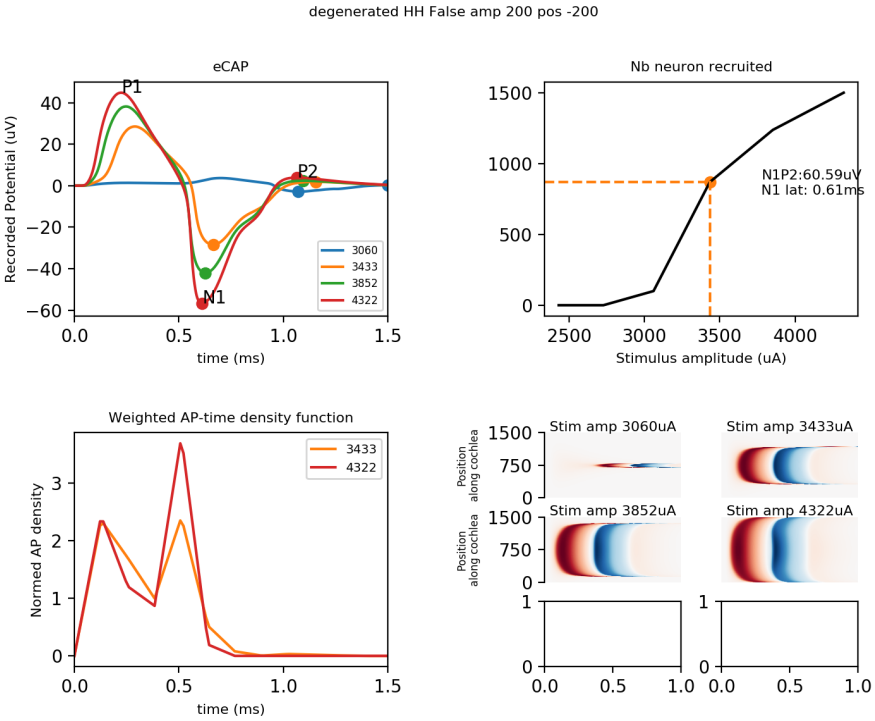

Figure 5.A.2: ECAP response summary for a fully degenerated SGN population under monophasic anodic stimulation at high electrode position and for the "HH" ionic model. The morphology figures present four panels: 1) top left panel shows the ECAP response; 2) the top right panel shows the neural recruitment as a function of amplitude. The point highlighted on the curve represents the stimulus amplitude that produced a neural recruitment closest to 500 neurons to be used as a comparison between all the conditions. The annotations represent N1P2 amplitude and N1 latency of the ECAP response at that amplitude; 3) the bottom left panel shows the normed density distribution (sum under the curve equals 1) of the APs detected on all neurons in the population for a subset of intensity amplitudes (colors match the top left panel) and; 4) the bottom right panel shows the spread of activity in population as a response to a single stimulation. The stimulatingrecording electrode is located at 750 µm in the vertical axis. Red and blue represent high and low recorded potentials respectively.

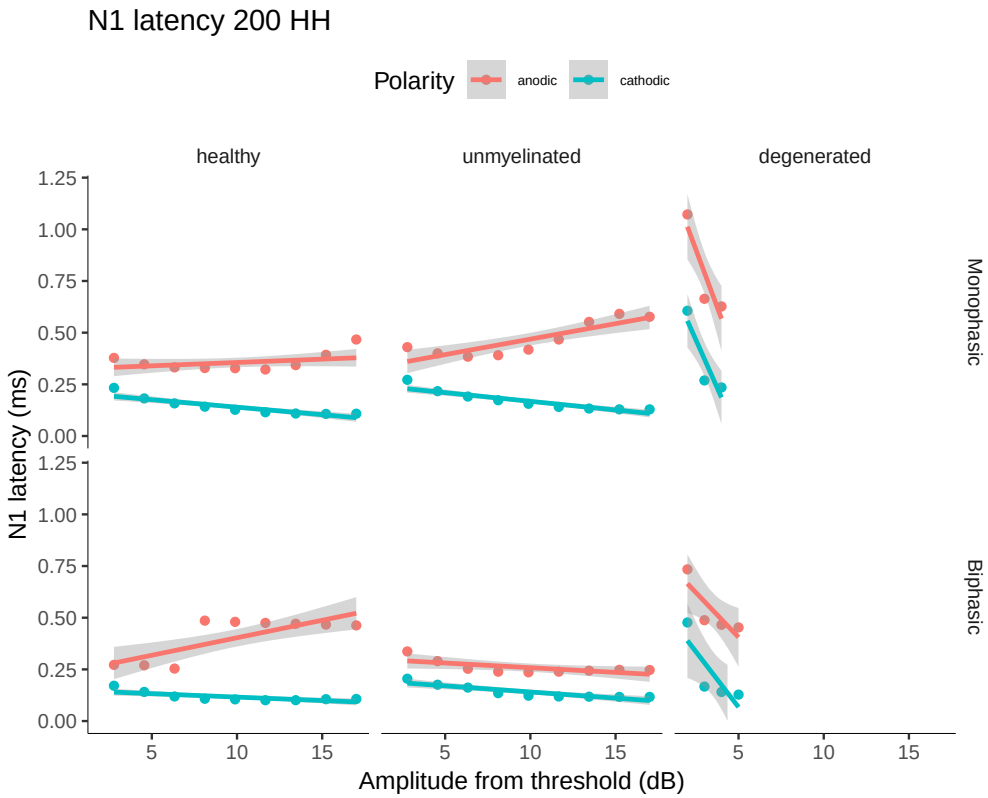

Figure 5.B.1: N1 Latency as a function of stimulus amplitude at high electrode position for the "HH" model

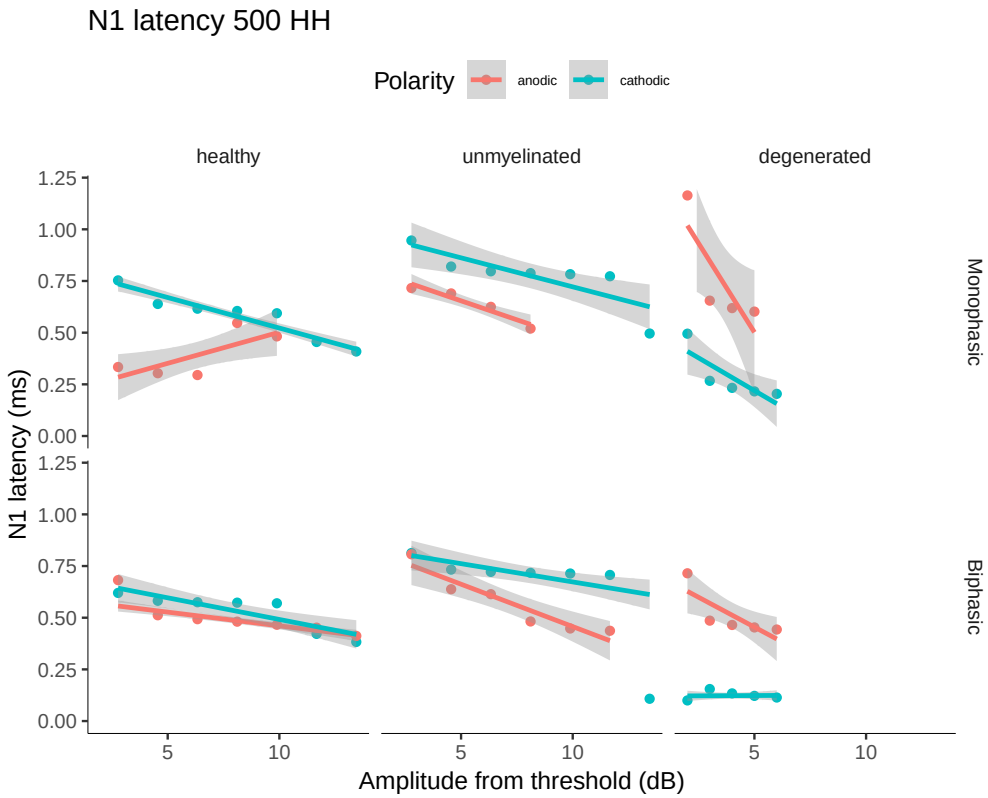

Figure 5.B.2: N1 Latency as a function of stimulus amplitude at mid electrode position for the "HH" model

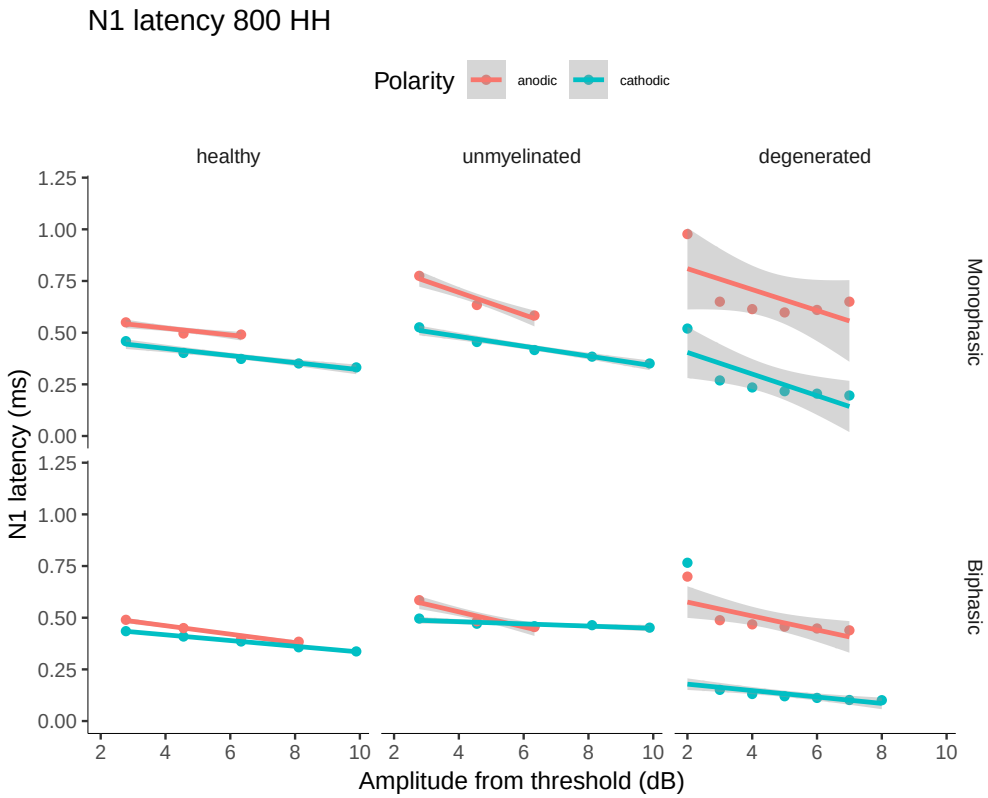

Figure 5.B.3: N1 Latency as a function of stimulus amplitude at low electrode position for the "HH" model

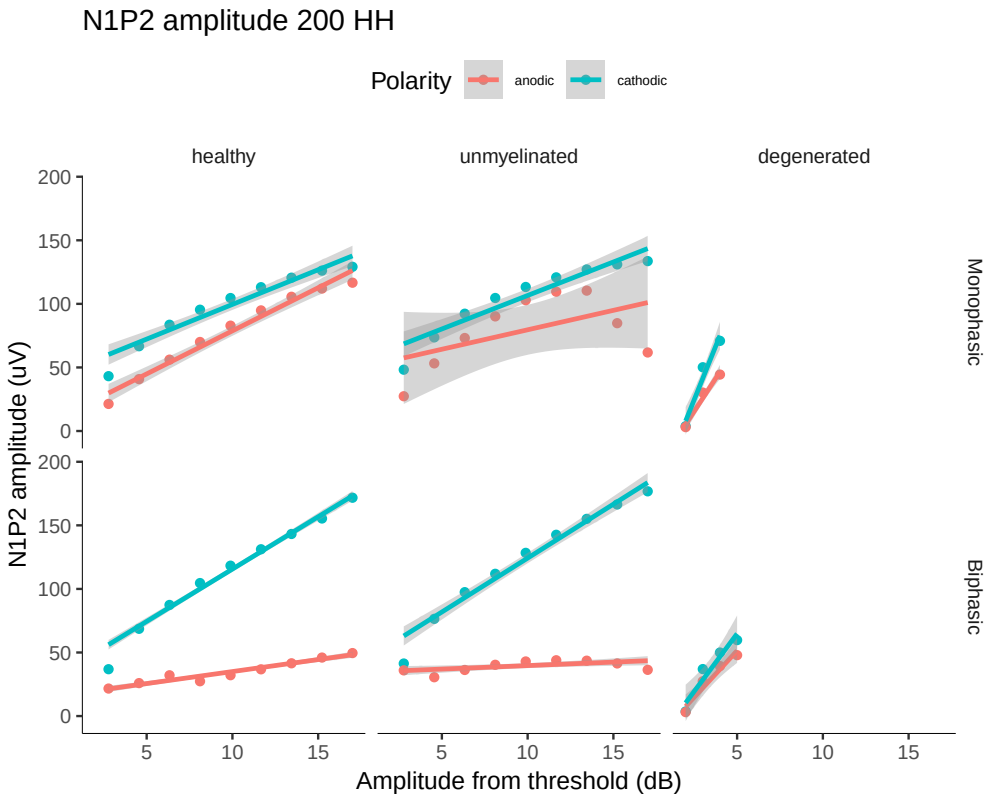

Figure 5.C.1: N1-P2 amplitude as a function of stimulus amplitude at high electrode position for the "HH" model

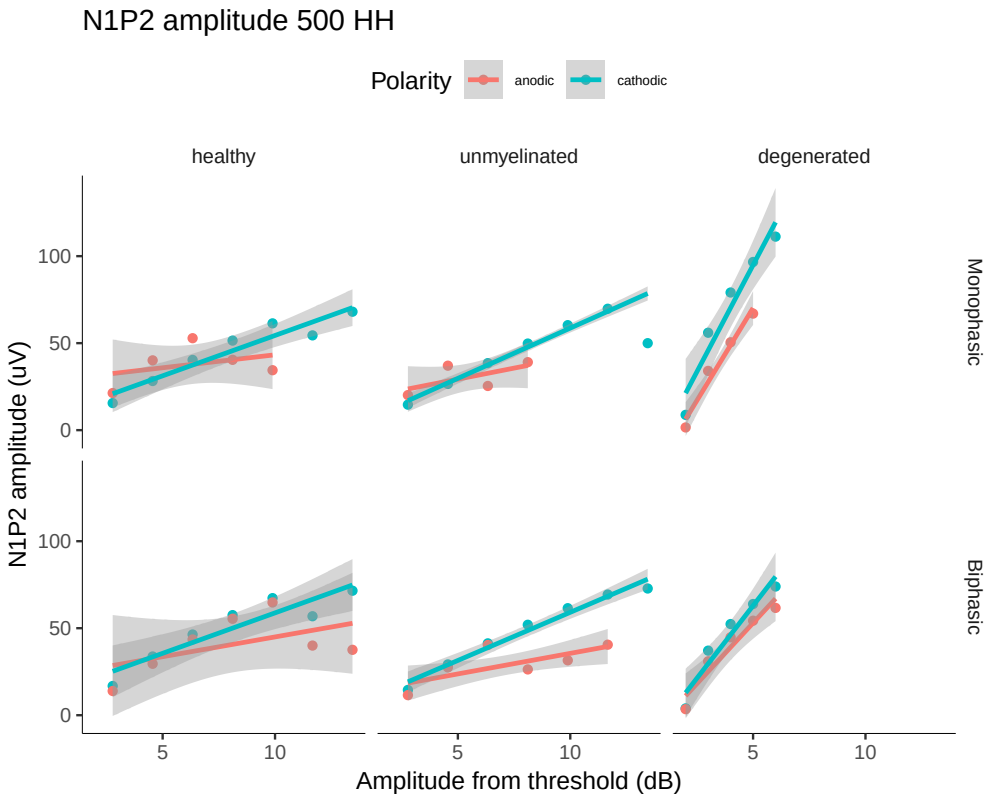

Figure 5.C.2: N1-P2 amplitude as a function of stimulus amplitude at mid electrode position for the "HH" model

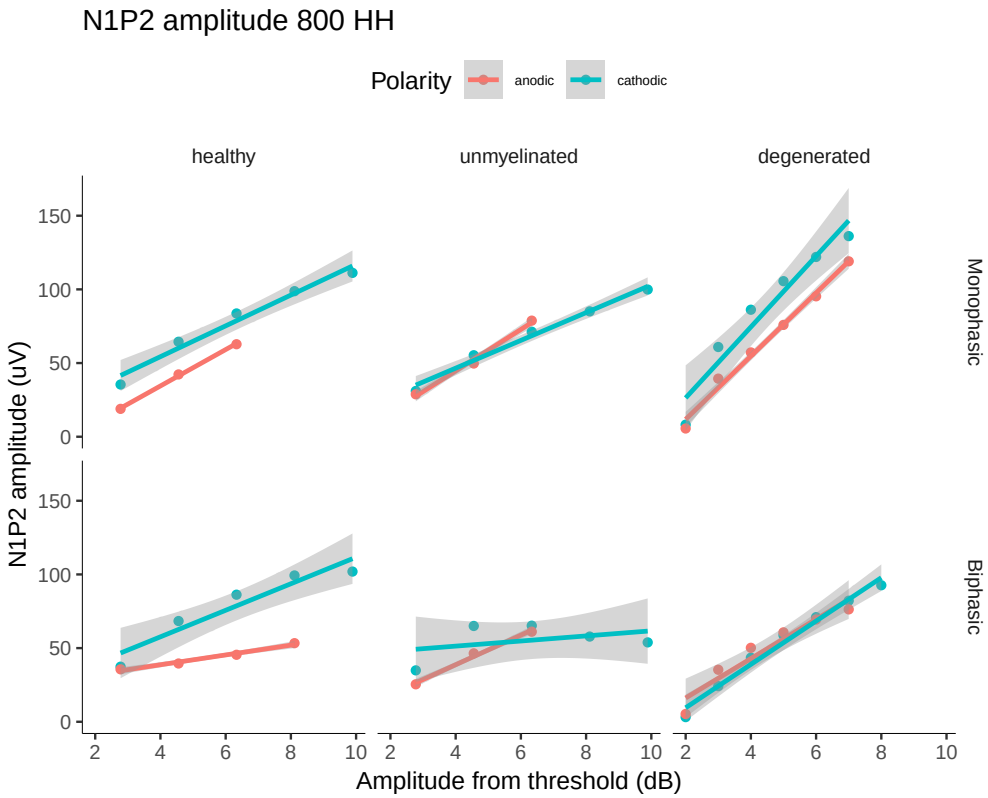

Figure 5.C.3: N1-P2 amplitude as a function of stimulus amplitude at low electrode position for the "HH" model

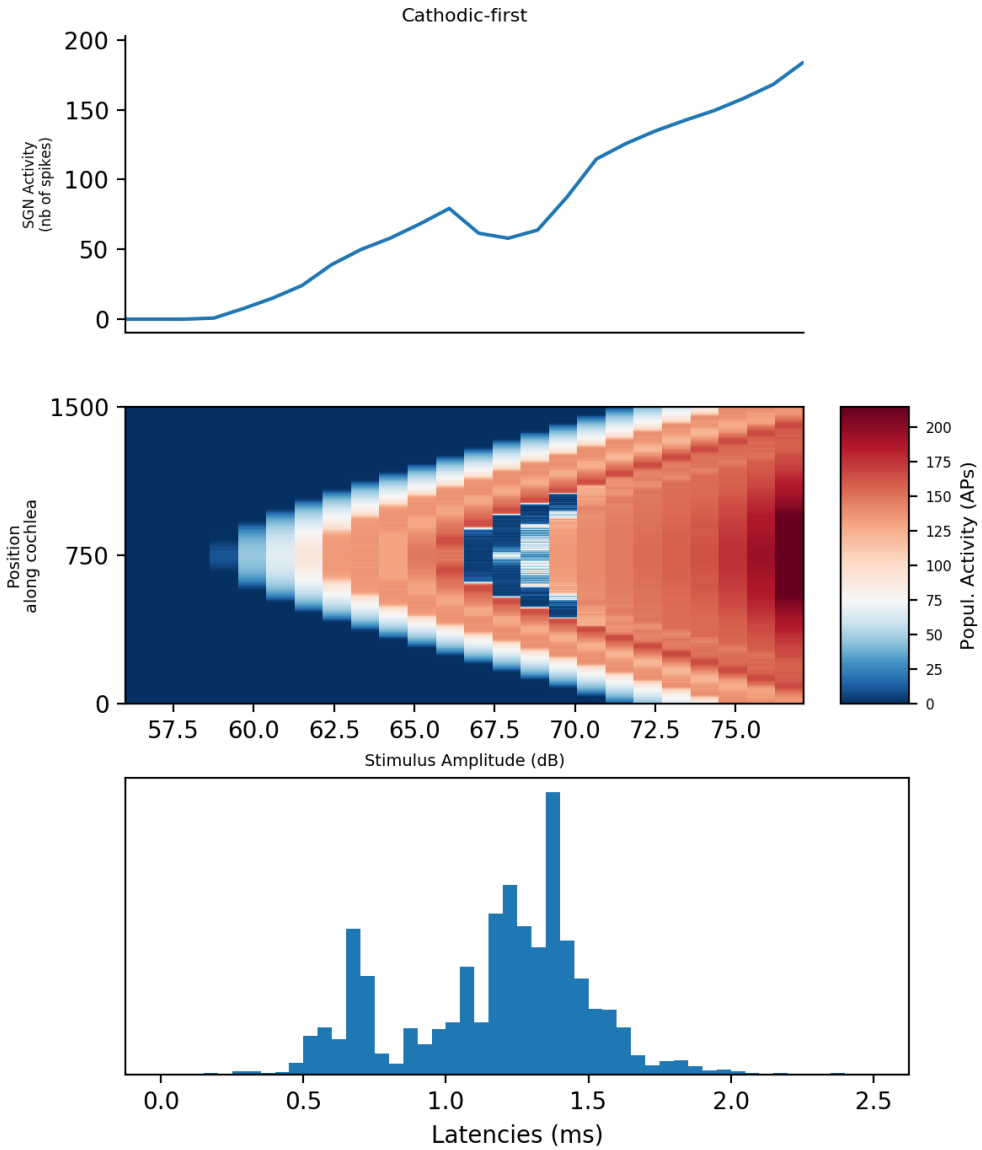

Figure 5.D.1: Population response to pulse trains for a demyelinated SGN health profile, the "HH+KLT+HCN" ionic model when subjected to cathodic-first pulse-trains stimulations at 1000 pps and at a high electrode position. Top panel shows the AP activity as a function of stimulus amplitude, the mid panel shows the activity spread over the population as a function of intensity and the bottom panel shows the distribution of all the latencies collected over the entire range of stimulus amplitudes.

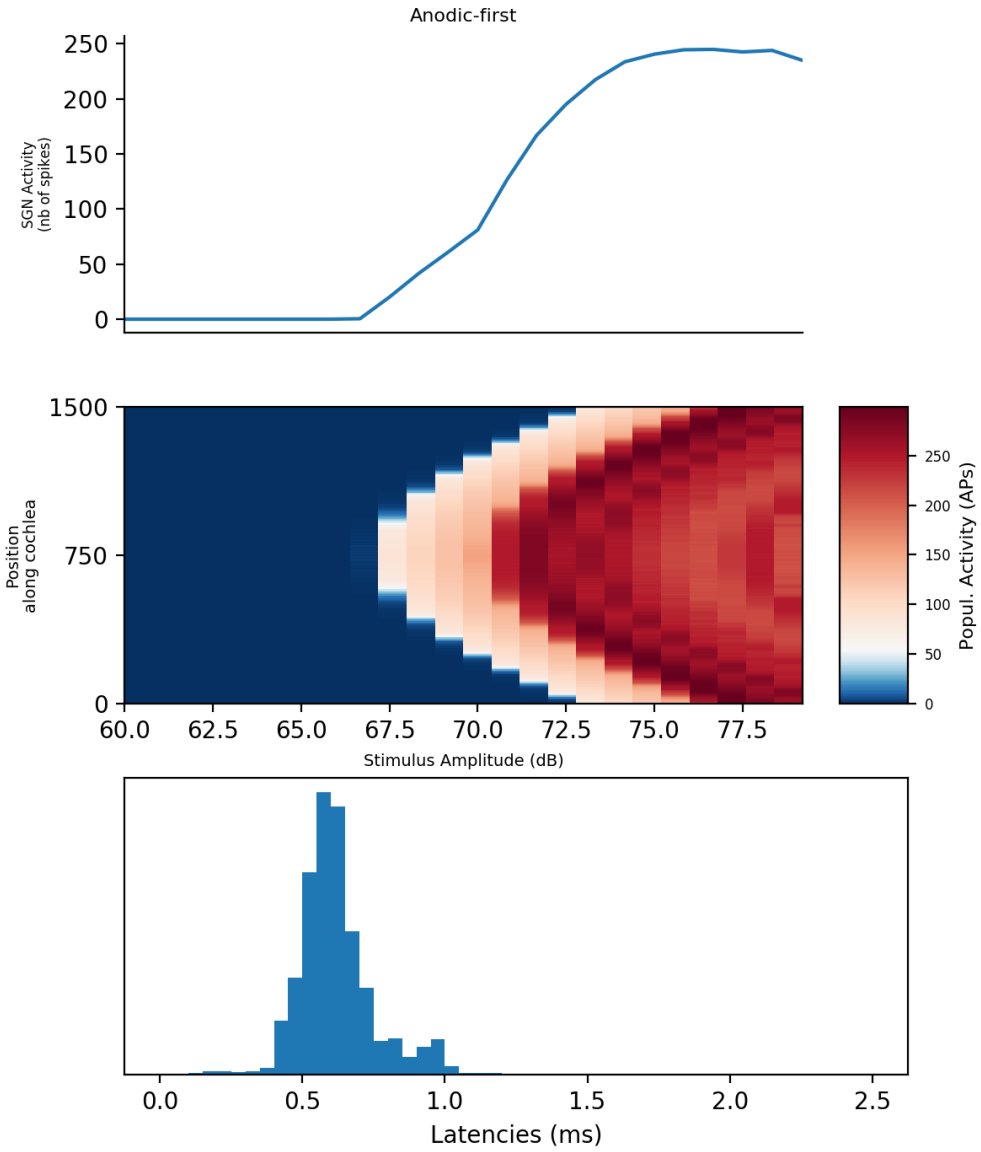

Figure 5.D.2: Population response to pulse trains for a fully degenerated SGN health profile, the "HH+KLT+HCN" ionic model when subjected to cathodic-first pulse-trains stimulations at 5000 pps and at a high electrode position. Top panel shows the AP activity as a function of stimulus amplitude, the mid panel shows the activity spread over the population as a function of intensity and the bottom panel shows the distribution of all the latencies collected over the entire range of stimulus amplitudes.

6 Modelling "atypical" pulse shapes

6.1 Introduction

For most of the past two decades, Cochlear Implants (CIs) have leveraged the efficiency of electrical stimulation in the cochlea to elicit auditory signals at the level of the Auditory Nerve (AN). The electrical stimulation is encoded by means of trains of electrical pulses, made of short, biphasic-symmetric pulses that change the membrane potential of Spiral Ganglion Neurons (SGNs) local to a stimulating electrode. Typical biphasic-symmetric pulses consist of two phases of equal width and amplitude, but with opposite polarity, in order to recover all charge that is injected in the cochlea. Despite the understanding that monophasic pulses stimulate the SGN more efficiently than biphasic, symmetric pulses are required to prevent the irreversible damage that monophasic pulses can generate in the cochlea (Brummer and Turner, 1977). As such, charge-balanced stimulation has been an essential safety requirement for CIs and biphasic-symmetric pulse shapes have been employ by almost all CI manufacturers to generate Action Potentials (APs) in the electrically stimulated cochlea without damaging it.

Nevertheless, as reported throughout this thesis, symmetric pulse shapes can have counteracting effects on the efficiency of electrical stimulation. Recent reports have theorised, and set a path for, the advent of new ramped or asymmetric, charge-balanced pulse shapes that are potentially more efficient with regards to the physiological dynamics of individual, and populations of SGNs (Van Wieringen et al., 2005; Macherey, Van Wieringen, et al., 2006; Macherey, Carlyon, Van Wieringen, et al., 2008; Smit, Hanekom, van Wieringen, et al., 2010; Undurraga, van Wieringen, et al., 2010; Undurraga, Carlyon, Macherey, et al., 2012; Undurraga, Carlyon, Wouters, et al., 2013a; Ballestero et al., 2015).

Asymmetric pulse shapes have already demonstrated clear benefits in terms of reduced thresholds and comfortable levels when compared to the common symmetric

pulses in humans (Van Wieringen et al., 2005; Macherey, Van Wieringen, et al., 2006; Macherey, Carlyon, Van Wieringen, et al., 2008; Macherey, Carlyon, Chatron, et al., 2017; Undurraga, van Wieringen, et al., 2010; Undurraga, Carlyon, Macherey, et al., 2012; Undurraga, Carlyon, Wouters, et al., 2013a). Asymmetric pulse shapes are biphasic pulse shapes where both phases have equal charge but the first phase, i.e. the eliciting phase, is short in duration and high in amplitude and the discharge phase, i.e. the recovery phase, is long in duration but low in amplitude. In essence, these asymmetric pulse shapes are thought to elicit APs similarly to monophasic pulse shapes, allowing the SGN to recover more quickly thanks to a non-eliciting discharge phase. The main hypothesis underlying the use of the asymmetric pulse shapes is that they would elicit APs at lower threshold levels than symmetric pulses.

Furthermore, a recent study has also shown that the use of ramped pulse shapes (i.e. a triangular pulse shape) in *in vitro* SGN models could reduce threshold, increase firing stochasticity and dynamic range (Ballestero et al., 2015). As with any force, the electrical forces generated by the ionic channels at each node of Ranvier are directly dependent on the electrical pulse. While square, immediate change in currents will produce strong reciprocal electrical currents from the ionic channels, the ramping of the charge phases is hypothesised to create a more natural and incremental response of the ionic channels. This technique could potentially reduce the Relative Refractory Period (RRP) and cathodic blocking effects which, in turn, would improve the encoding of electrical signals by virtue of reduced temporal and spatial interactions.

In Chapter 3 and Chapter 4, the changes in behaviour of single SGNs due to the extent of degeneration, or the distribution of ionic channels, and in response to biphasic symmetric pulses, were described. Here, the effects that modifying the pulse shape can have on responses of both single SGN and populations of fibres when subjected to pulse trains are introduced and described.

6.2 Methods

In this chapter, healthy, partially demyelinated and fully degenerated human SGNs are modelled, according to the morphology previously reported (Rattay, Lutter, et al., 2001; Rattay, Potrusil, et al., 2013; Smit, Hanekom, van Wieringen, et al.,

2010) with the parameters described in Chapter 2-Chapter 4. Healthy, partially demyelinated, and fully degenerated SGNs and populations of SGNs (similar to those from Chapter 5) are modelled and subject to biphasic monopolar stimulations of different pulse shapes. The electrode positions are the same as described in Chapter 2. Stimulations were performed for various combinations of parameters: 4 types of pulse shapes x 2 polarities (anodic and cathodic) x 3 positions (high, mid, low) x 2 ionic models.

The primary interest of this chapter being the effects of pulse shape on the response of the SGN models, only the partially demyelinated and fully degenerated models are reported here as the healthy condition did not show important differences at the single neuron level. However, the data for the healthy SGN are added in Appendix 6.A.

Two ionic channel models, both previously defined in Chapter 2, are tested here: 1) the "HH" model with the warmed fast activating sodium (Na) and voltaged-gated high-threshold inactivating potassium (Kv) channels equations from Rothman (2003); 2) the "HH+HCN+KLT" channel model adding voltage-gated hyperpolarization-activated cation (HCN) and voltaged-gated delayed-rectifier potassium (KLT) channel equations from Rothman (2003). All the effects of these conductances and temperature shifts were reported in Chapter 2.

To reduce the requirements for computational resources and focus on the effects of pulse shapes, simulation parameters for the population models were limited. The focus of this chapter being pulse shape, parameters of electrode position versus neural degeneration profiles were chosen to reduce the interactions of spike-rate adaptation and electrode position according to the knowledge from previous chapters. Two population health profiles are simulated — the healthy and the fully degenerated — to highlight the greatest differences in effects of pulse shapes. One simulation condition for the electrode position was chosen for each health profile: the healthy population was simulated with a high-electrode condition, whilst the fully degenerated population was simulated at the low-electrode position. The ionic model for each population health was chosen to reduce the degree of interactions, i.e. cathodic and spike-rate adaptation blocking, and were chosen based on the single SGN responses from Chapter 3 and Chapter 4. The healthy population was thus modelled with the "HH" ionic model, whilst the degenerated population was

modelled with the "HH+HCN+KLT" ionic model.

6.2.1 Stimulus

Pulse trains were used for single SGN and populations of SGNs. All pulse width were fixed to 50 µs and a 1 µs interphase interval was added for biphasic pulses. Biphasic pulses were either symmetric or asymmetric. Two types of asymmetric pulse shapes were used (Pseudomonophasic-Square (PSS) and Pseudomonophasic-Ramped (PSR)) which both consisted of an initial short-high amplitude phase followed by a second phase of opposite polarity which had a shorter amplitude, but a longer duration (see Fig. 6.2.2), this ensuring charge-balanced stimulation.

For the single SGN model, three different pulse rates were used, of which two were common to all models (250, 1000 pps). The effect of a third maximal pulse rate, specific to each pulse shape and the length of the second phase, was also assessed. This was 5000 pps and 1666 pps for symmetric and asymmetric pulses, respectively.

Both population models were stimulated with trains of pulses at 1000 pps only.

6.2.1.1 Pulse shapes

Fig. 6.2.2 summarizes the 4 pulse shapes x 2 polarities employed in this study. The symmetric pulse shapes were defined as Symmetric-Square (SYMS) and Symmetric-Ramped (SYMR), whilst asymmetric pulse shapes consisted of PSS, or PSR, respectively (see Fig. 6.2.2). Asymmetry was set to a fixed ratio of 1 to 10 between the first and the second phase of a pulse, and 1 to 1 for symmetric stimuli. Symmetric pulses had a pulse width of 50 µs for both phases, while asymmetric pulses had a first phase of 50 µs and a second phase that was 500 µs long, and 10 times lower in amplitude than the first phase.

SYMR and PSR were equal in charge to their square equivalent. The difference between square and ramp is illustrated in the example shown in Fig. 6.2.1. The square pulse amplitude was defined as "PA", and a "foot" amplitude, i.e. the first edge of the pulse in time, and a "peak" amplitude, the second edge of the pulse-phase in time, were considered. For the square pulse, "foot" and "peak" amplitudes are equal; for the ramp, the "foot" amplitude was defined as 10% PA and the "peak" amplitude as 190% PA, effectively producing an equal charge to the square pulse.

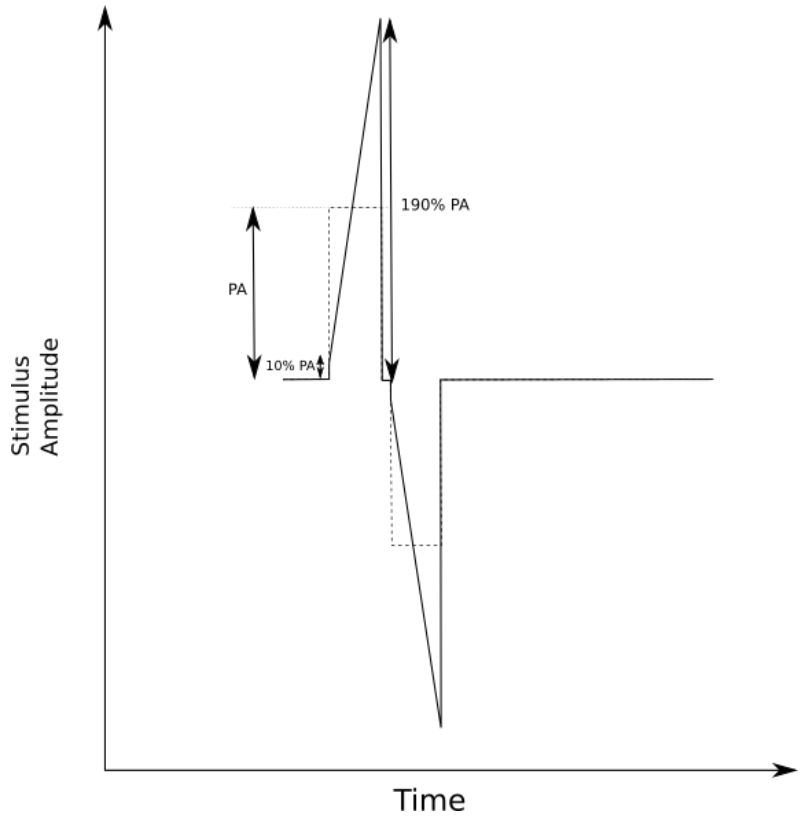

Figure 6.2.1: Ramped pulse shape parameters for equal charge. Solid line plots the ramped pulse shape, equal in charge to the square pulse shape (dashed line). 10% of the square shape Pulse Amplitude (PA) is used at the foot of the ramp. 190% of the square shape PA is used at the peak of the ramp.

To summarize, four pulse shapes are presented in this chapter: 1) the SYMS, which is a typical square biphasic symmetric (maximal pulse rate 5000 pps); 2) the SYMR which is the symmetric ramped pulse shape (maximal pulse rate 5000 pps); 3) PSS asymmetric square pulse shape (maximal pulse rate 1666 pps); 4) the PSR ramped pulse shape (maximal pulse rate 1666 pps).

Similar simulations were performed for pulse shapes with smaller asymmetry ratios, i.e. 1 to 5, and ramp percentage, i.e. 50%. These showed to be qualitatively similar to the maximum asymmetry, i.e. 1 to 10, and maximum ramp, i.e. 90%, with smaller threshold difference and spike-activity magnitudes due to their closer resemblance to the square equivalent.

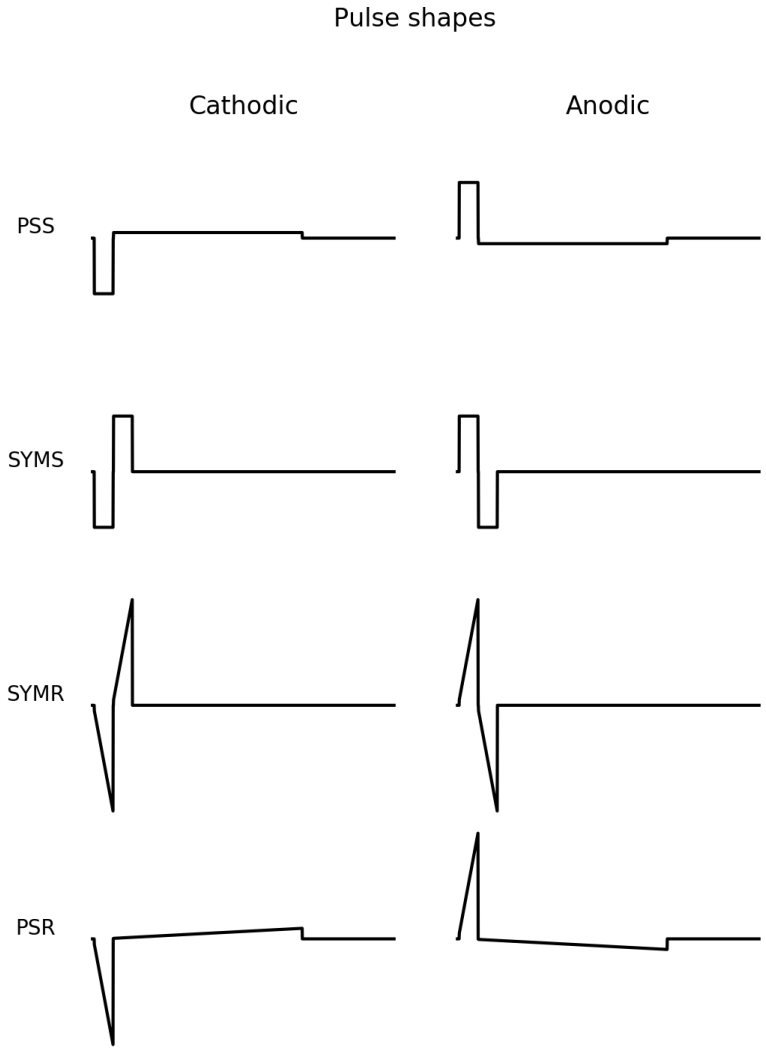

Figure 6.2.2: Symmetric and asymmetric pulse shapes used in this study. From top to bottom: PSS, SYMS, SYMR, and PSR, respectively The ratio between the first and second phase of asymmetric pulses was 1 to 10.

6.3 Results

The neural response of healthy, partially demyelinated and fully degenerated human SGN models were characterised as single and/or populations of, neurons stimulated with pulse trains using several pulse shapes. All single SGN models were subjected to stimulations from three electrode positions, biphasic symmetric and asymmetric pulse shapes for cathodic-first and anodic-first polarities. Population models were simulated in limited conditions described in Sec. 6.2. First, single SGN responses to pulse-train stimuli that provide important insight on the model's ability to show basic features of the electrically stimulated SGN such as threshold shifts, polarity sensitivity, and stochasticity for both types of degeneration are examined. Second, healthy and fully degenerated SGN population responses to pulse-train stimuli are presented for PSS, PSR, SYMS, and SYMR pulse shapes.

6.3.1 Pulse-train responses to several pulse shapes in a single SGN

Here, SGN responses to trains of electrical pulses presented at several rates are described. Similar to Chapter 3 and Chapter 4, responses to the new pulse shapes show **unimodal** as well as **bimodal** spike-rate functions. Due to the complex stimulus interactions described previously (Chapter 3 and Chapter 4), the presence or absence of the SGN peripheral process, and the additional ionic channels that were added to the models described throughout this thesis, SGN's spike-rate functions to pulse-trains at different pulse rates, electrode positions, and pulse shapes are non-monotonic with increasing stimulus intensity. Most often, responses could not be fitted with Gaussian distributions or Firing Efficiency (FE) curves because of their mixed **unimodal** or **bimodal** behaviour. Because of this, the pulse-train responses are characterised using the principles that were described in Chapter 3. Namely, pseudo-FE curves were fitted on the first rising edge of the responses to ensure homogeneity in the reported measures.

As mentioned in Sec. 6.2, the pulse rates are not homogeneous across pulse shapes. The maximum ("Max") pulse rate was 5000 pps for the two symmetric pulses and 1666 pps for PSS and PSR pulse shapes. As such, the results regarding the "Max" pulse rate are limited in the interpretation but are reported as the effect of maximal pulse-rate.

6.3.1.1 Demyelinated SGN

The effect of different pulse shapes on thresholds Fig. 6.3.1 shows the effect of pulse shape, rate, and polarity using pulse trains on single SGN threshold levels. No systematic effects of pulse rate were noted across the pulse shape conditions for pulse-rates between 250 pps and their respective "Max" value similar to previous modelling reports (Smit, Hanekom, van Wieringen, et al., 2010). Further, some effects of pulse rate and pulse shape are also found to be strongly interacting with electrode position. This appears to contradict previous reports in humans, where perceived thresholds are almost systematically found to be either monotonically or non-monotonically decreasing with increasing pulse rates (van Wieringen, Carlyon, et al., 2006). For example, van Wieringen, Carlyon, et al. (2006) reported that thresholds for trains of biphasic-symmetric pulses decreased monotonically with increasing rate, whilst the threshold function for alternating monophasic waveforms — similar to the PSS pulse shape — was non-monotonic with a maximum between 400 and 1000 pps in humans. While the results described here suggest that there is no clear and significant effect of pulse rate on thresholds for the modelled single SGNs, it is important to remember that loudness perception in humans is driven by the temporal integration of APs at higher levels of the auditory pathway (McKay, Henshall, et al., 2003; McKay and Henshall, 2010). As such, although the threshold levels for modelled single SGNs did not differ across pulse rate conditions, loudness perception might very well still be impacted by higher activity induced by higher pulse rates and for increased stimulus amplitudes.

Moreover, effects of electrode position on thresholds for each pulse shape, regardless of polarity, were found to be similar to those described in Chapter 4. Generally, the high-electrode position generates thresholds that are 10 to 15 dB lower than the mid-electrode position, whilst the mid-electrode position thresholds are 4 to 5 dB lower than the low-electrode position.

Overall, the thresholds range from 44 dB for the PSR pulse shape at 1000 pps, high electrode position and cathodic leading polarity, to 65.7 dB for the anodic-first, SYMS at the low electrode position at 1000 pps. Because of the combined effects of asymmetry and ramp, the PSR shows the largest difference with the typical SYMS pulse (44 to 62.9 dB for PSR versus 46.2 to 65.7 dB for SYMS).

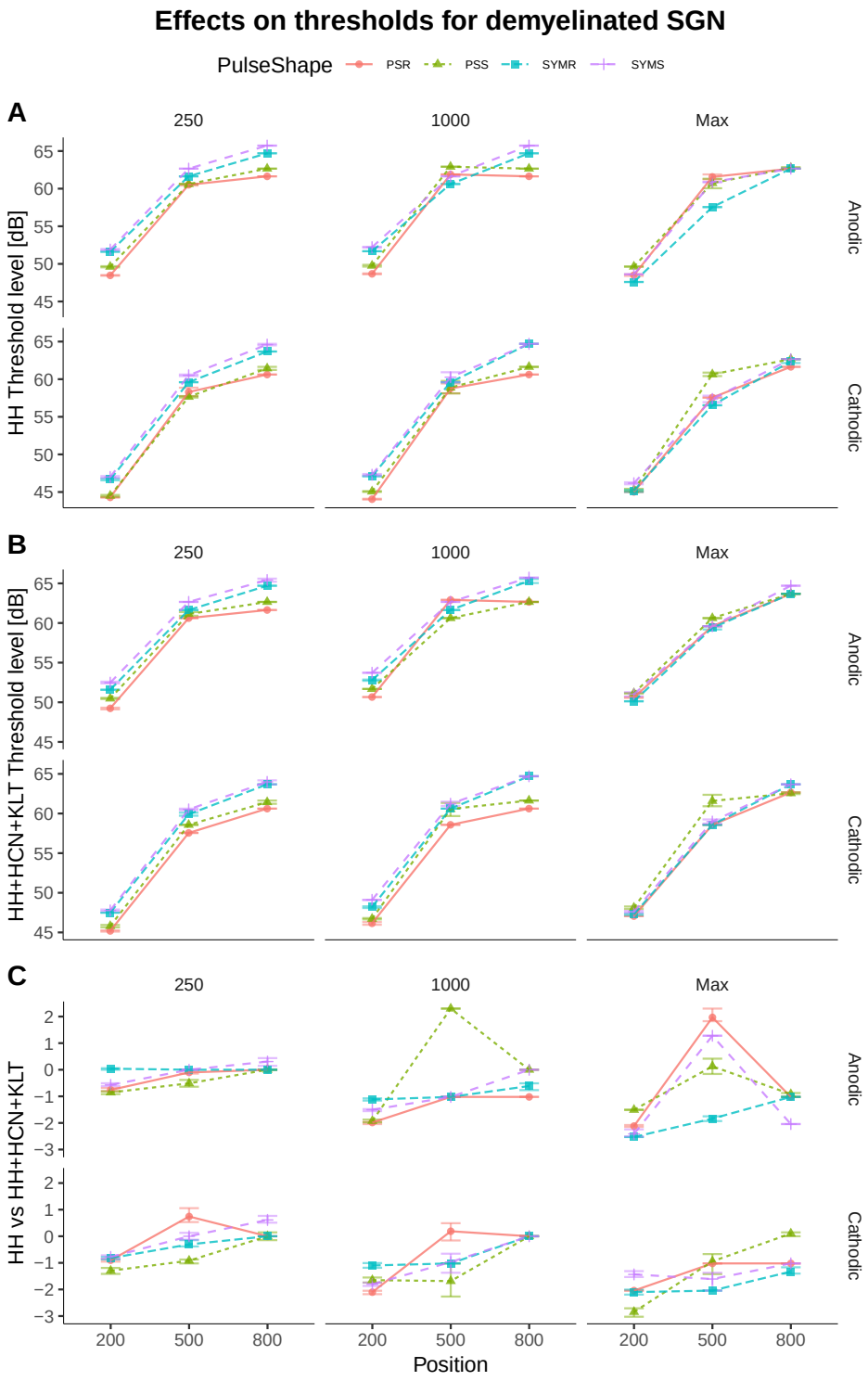

Figure 6.3.1: Threshold levels across models and stimulus conditions. A) threshold levels for the HH ionic model, B) the HH+HCN+KLT ionic model, C) the difference between the simulated threshold levels for the HH and HH+HCN+KLT.

The polarity effects on thresholds for the partially demyelinated model are similar to those introduced in Chapter 4 with anodic-first stimulation showing higher thresholds with anodic-first polarities 4 to 5 dB higher than cathodic-first for all pulse shapes. Also, the electrode position and pulse rate effects between 250 and 1000 pps are found similar to those presented previously (see Chapter 4).

Important effects of pulse shape are observed, and can be grouped into two categories: the effects of symmetry and the effects of a ramped pulse. First, PSS and PSR demonstrate generally similar or lower thresholds than the symmetric SYMS and SYMR. In the cathodic-first condition, the asymmetric pulse PSR thresholds are up to 3.3 dB lower than the SYMS pulse shape, and 3 dB lower than the SYMR pulse shape. This result is consistent with previous human reports which showed decreased thresholds of 2 dB for asymmetric pulse shapes in monopolar stimulations (Macherey, Van Wieringen, et al., 2006).

However, differences due to the ramped condition (PSR vs. PSS) are not significant, except for the mid-electrode position for cathodic-first 1000 pps pulse trains, and for the "HH+HCN+KLT" ionic model (PSR 0.5 dB lower than PSS in range with previous reports (Ballestero et al., 2015)).

The effect of different pulse shapes on DRs Fig. 6.3.2 shows the effects of the different pulse shapes on the DRs of a partially demyelinated SGN model. DRs range from 0.1 to 3.9 dB across polarity, pulse shapes, electrode positions, and for pulse rates (250 and 1000 pps). The high-electrode position generates the lowest and most variable DR values (0.1 to 3.5 dB) when compared to the mid- and low-electrode positions where DRs are higher and more stable across conditions (1 to 3.8 dB for mid and 1.1 to 3.9 dB for low electrode position).

In previous human studies using monopolar and bipolar asymmetric pulse shapes (Macherey, Van Wieringen, et al., 2006; van Wieringen, Carlyon, et al., 2006), it was found that Most Comfortable Levels (MCLs) were similarly reduced as to their relative threshold levels. Assuming MCLs-to-threshold differences can be interpreted as the DR, the data presented here—where DR is largely unchanged as a function of pulse shape—are consistent with the outcomes of these previous studies.

Strong interactions between pulse rate, electrode position, and pulse shape for both polarities and both ionic models are noted for the partially demyelinated

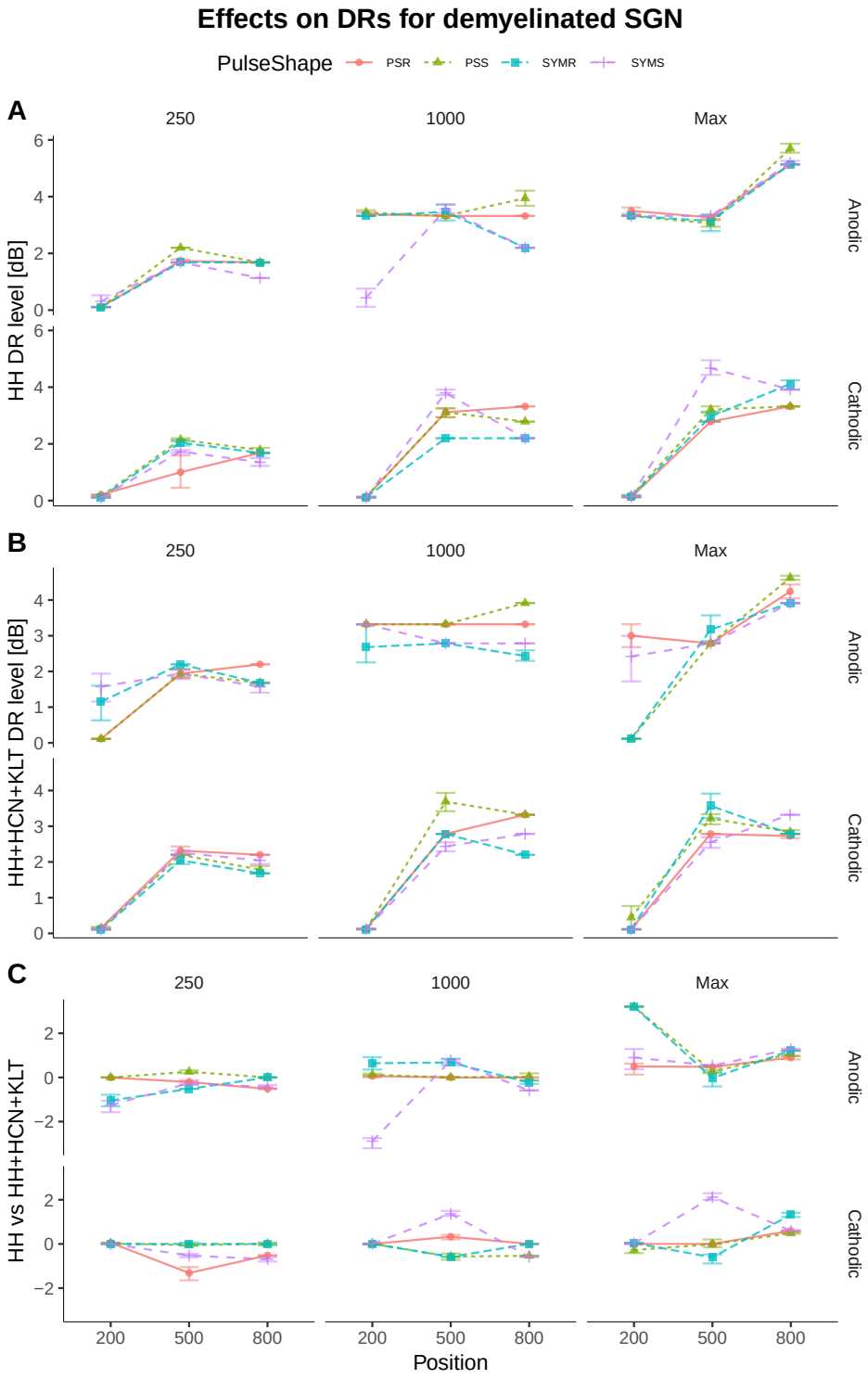

Figure 6.3.2: Dynamic Range (DR) across models and stimulus conditions. A) DR for the HH ionic model, B) the HH+HCN+KLT ionic model, C) the difference between the simulated DRs for the HH and HH+HCN+KLT.

SGN model. For example, in the anodic-first condition, asymmetric pulse shapes generate significantly higher DRs than the symmetric pulse shapes at 1000 pps for the "HH+HCN+KLT" ionic channel model, in the mid- and low-electrode position (0.5 to 1 dB higher for asymmetric pulse shapes). However, the "HH" model, for anodic-first 1000 pps, only shows significant differences at the high- and low-electrode positions (3.8 dB higher for asymmetric in for high electrode position and 1 to 1.5 dB higher for asymmetric pulse-shapes for the low electrode position).

6.3.1.2 Degenerated SGN

The effect of different pulse shapes on thresholds Important effects of pulse shape on the thresholds for the fully degenerated SGN model are noted and summarised in Fig. 6.3.3. Here, polarity, pulse rate, and electrode position interact less than in the partially demyelinated scenario.

Similar to the demyelinated SGN model, pulse rate effects are not systematically observed for all pulse shapes. Again, it is important to note that this specific effect is in apparent contradiction to previous studies in humans for bipolar stimulation (van Wieringen, Carlyon, et al., 2006), in which the thresholds for asymmetric and symmetric pulses were typically found to decrease with increasing pulse rate. Further, the thresholds for the PSR are the lowest (61.6 to 71.8 dB), whilst the SYMS generates the highest thresholds (65.7 to 73.9 dB) amongst the different pulse shapes tested. Thresholds for SYMR and PSR are equal to, or lower than, those for SYMS and PSS pulse shapes. Furthermore, larger pulse shape effects are found in the anodic-first condition at 1000 pps at all electrode positions for the "HH" model, whilst the smallest pulse shape effects are found at 250 pps for the "HH+HCN+KLT" model. Importantly, polarity effects are larger in the fully degenerated SGN model than they are in the partially demyelinated model presented above (see Sec. 6.3.1.1). Asymmetric anodic-first pulse shapes appear to be more effective than the cathodic-first ones. This is interesting, as it is observed in Chapter 4 that the fully degenerated SGN favours monophasic anodic stimulation, which closely resembles the PSS pulse shape. Interestingly, this does not necessarily match the observations from Electrically evoked Compound Action Potentials (ECAPs) made in Chapter 5 where cathodic ECAPs were larger than

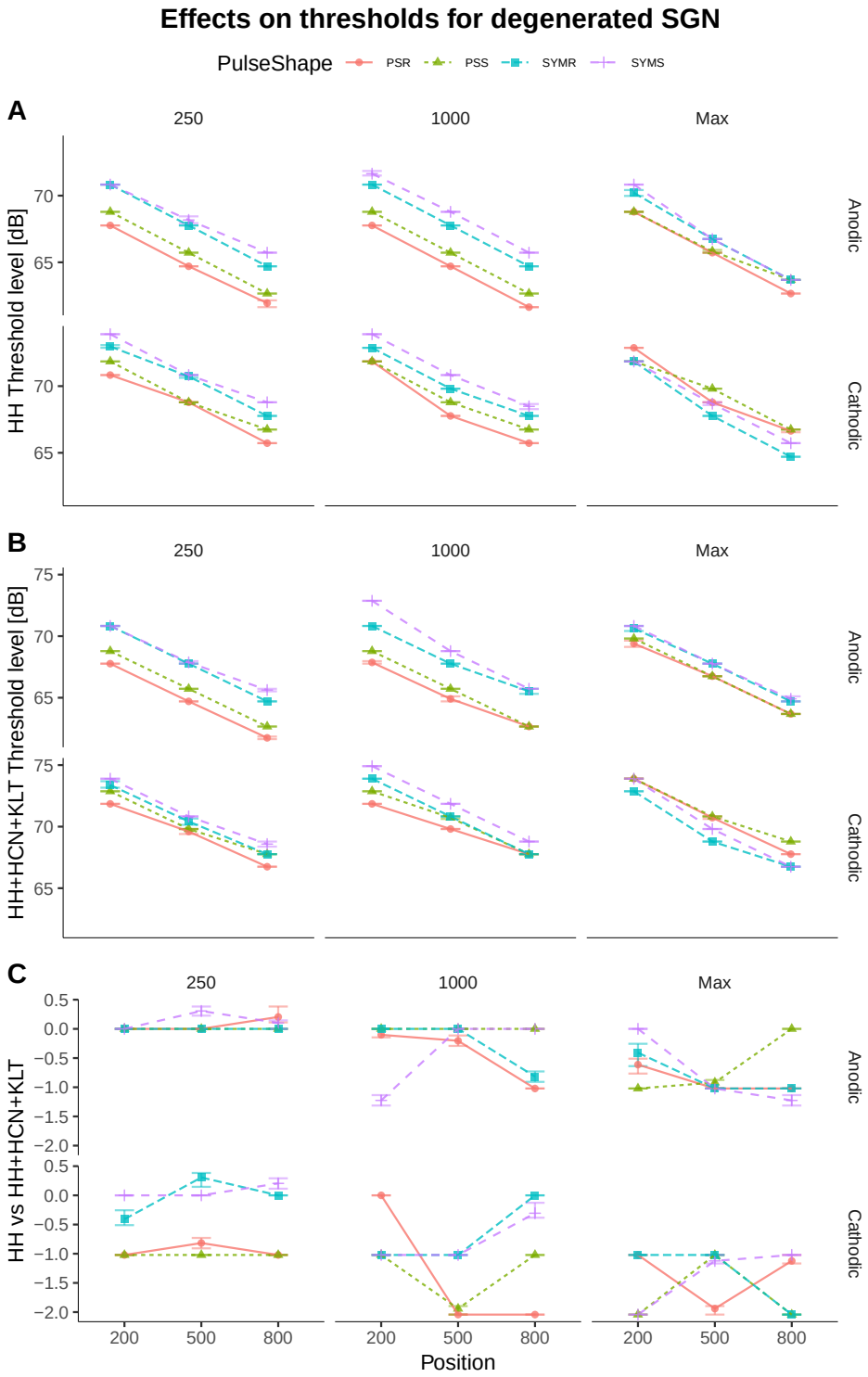

Figure 6.3.3: Threshold levels across models and stimulus conditions. A) threshold levels for the HH ionic model, B) the HH+HCN+KLT ionic model, C) the difference between the simulated threshold levels for the HH and HH+HCN+KLT.

anodic stimulations. This could be explained by the difference between the lined-up population model used in Chapter 5 and the single SGN used in this chapter. This calls for additional perspective on the interpretation of results when comparing population to single neuron simulations.

Here, because of the short amplitude and long duration second cathodic-phase, the anodic-phase becomes more effective than in the symmetric scenario. This effect is observed for both square and ramped stimulus. Ionic model effects are observed at 250 pps for asymmetric pulse shapes where the "HH+HCN+KLT" model produced thresholds that are systematically 1 dB higher than the "HH" model.

The effect of different pulse shapes on DRs Fig. 6.3.4 shows effects of pulse shapes on DR for the degenerated SGN model. The results show that pulse rate has an important interaction with pulse shape and electrode position: while the DRs are similar at 250 pps for both ionic models at all electrode positions, the 1000 pps condition show differences in DRs across pulse shape conditions and electrode position.

DRs range from 1.1 to 5 dB across all simulated conditions, which is similar to the DR values previously reported in this thesis (see Chapter 4). The lowest DRs are for cathodic-first pulse trains at 250 pps in both ionic channel models across all electrode positions. The highest DRs is found at the lowest electrode position for PSS anodic-first pulse shape at 1000 pps for the "HH" ionic channel model.

Strong interactions between pulse shape, pulse rate, polarity and ionic channel models are also noted. For example, asymmetric pulse shapes generate relatively higher DRs in the "HH" model condition when compared to the symmetric pulses. 1.5 to 2 dB higher DRs are observed when compared to SYMS for PSR and PSS, respectively, in anodic-first stimulation conditions. However, this benefit of asymmetry at 1000 pps in the anodic-first condition is not present for the "HH+KLT+HCN" model, where only the SYMS is found to be significantly lower (1 dB) at the high-electrode position, and the PSR (0.75 dB lower) at the low-electrode position.

For the cathodic-first condition, however, the benefits of asymmetry are noticeable for both PSR and PSS at mid- and low-electrode positions for the "HH" model (0.5 to 1 dB higher than SYMS for mid- and low-electrode position, respectively).

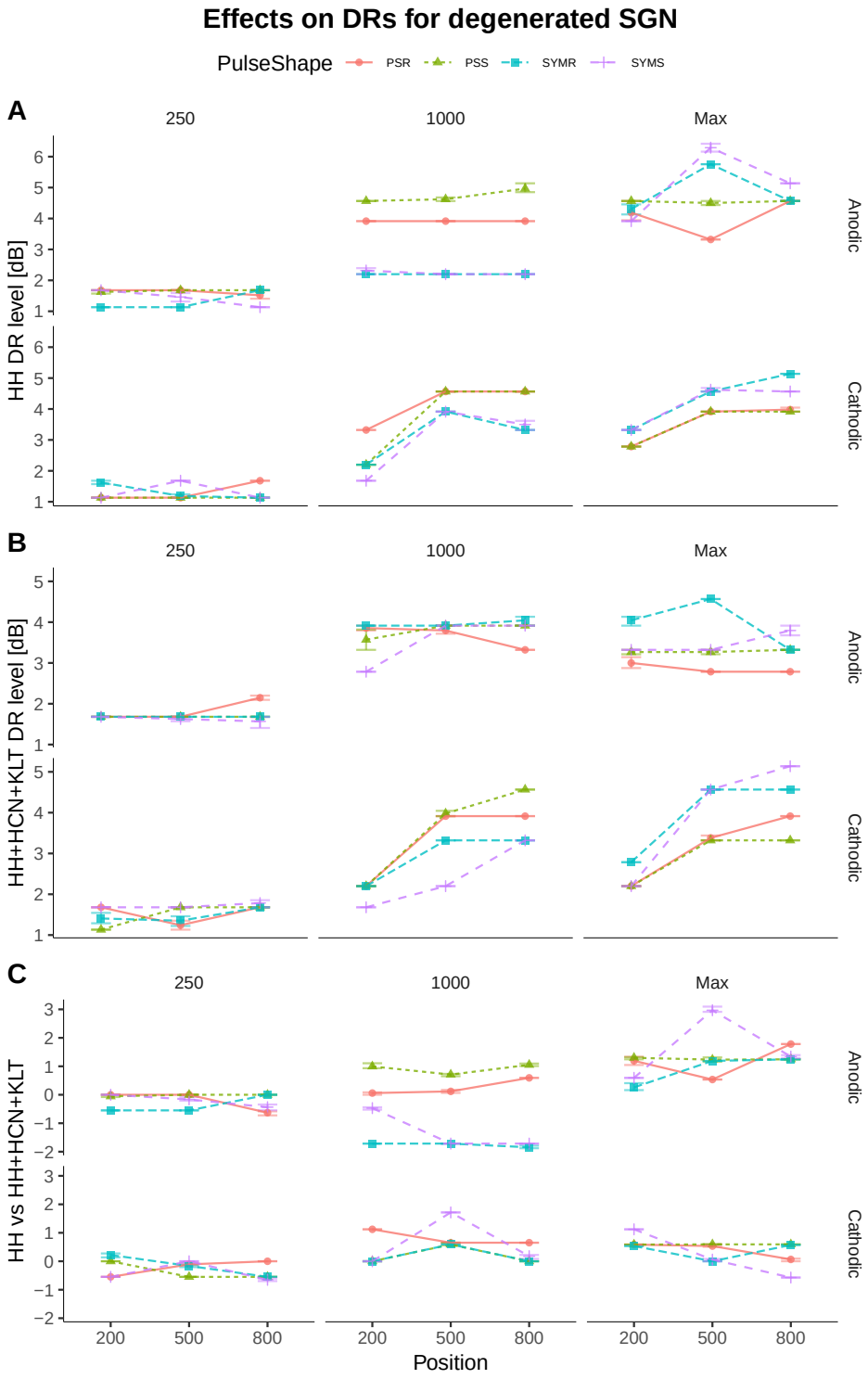

Figure 6.3.4: DR across models and stimulus conditions. A) DR for the HH ionic model, B) the HH+HCN+KLT ionic model, C) the difference between the simulated DRs for the HH and HH+HCN+KLT.

Similar effects are also observed for the "HH+HCN+KLT" model (1 to 1.8 dB higher than SYMS for PSS at mid- and low-electrode positions, respectively). Benefits at the highest electrode position for the "HH" ionic model are significant for the PSR (1 dB higher than SYMS) and both SYMR and PSS (0.5 dB higher than SYMS). This is in contrast to the "HH+HCN+KLT" ionic model are SYMR, PSS and PSR add a similar benefit compared to SYMS (0.3 dB) at the high electrode position.

In addition, small but significant effects of pulse shape are found at 250 pps for the "HH" model, for both anodic-first and cathodic-first conditions. In the anodic-first scenario, the SYMR pulse shape DR is 0.5 dB lower than all other pulse shapes at the high electrode position, whilst the SYMS DR is 0.2 dB lower than all other pulse shapes.

6.3.2 Population Pulse train responses

One of the main theorized benefits of using "ramped" pulse shape is their ability to elicit more activity local to the stimulating electrode, and/or, elicit less activity away from the stimulating electrode. Essentially, these effects of pulse shape would help reduce Spread of Excitation (SOE), and, in turn, improve spatial selectivity by reducing channel interactions. In the case of asymmetrical pulse shapes, the main benefit would be less interaction from the discharge phase of the pulse, allowing for lower thresholds and larger DRs.

To model those potential effects of "atypical" pulse-shapes, and to evaluate their predicted SOEs, two population profiles, healthy and fully degenerated, were stimulated using the same pulse shapes that are introduced in Sec. 6.2.

As mentioned in Sec. 6.2, to highlight the effect of pulse shapes without interference from other factors of the simulated SGN responses, i.e. cathodic blocking or spike-rate adaptation blocking, the results described here are simulated based on conditions of single SGN response-functions, which are found to be mostly monotonic (see Chapter 3 and Chapter 4).

In order to compare the SOE across pulse shapes, the stimulation level at which the modelled population generated the same average spike-rate was determined. The target spike-rate was then chosen as the half-point of the spike-rate function (shown in the middle panel of Fig. 6.3.5 and Fig. 6.3.6). Then, the activity density was

defined as the weighted contribution to the total AP count of each individual SGN in the population at this half-activation amplitude previously selected. This "activity density curve" is plotted for each pulse shape in the bottom panel of Fig. 6.3.5 and Fig. 6.3.6. Finally, SOE was calculated as the distance over which the AP activity was found above half the maximum activity at the half-activation amplitude.

6.3.2.1 Healthy SGN

Fig. 6.3.5 shows a summary of a healthy SGN population simulated with the "HH" ionic model when subject to four different pulse shapes: 1) SYMS; 2) SYMR; 3) PSS, and; 4) PSR, at 1000pps and for cathodic-first polarity. Anodic-first stimulations are simulated but no significant interaction between polarity and pulse shape are noted, i.e. no effect apart from polarity-related threshold differences are noted. Additional results, e.g. for anodic-first conditions are added in the appended (see Appendix 6.A.2).

The effects of pulse shape on population thresholds are similar to the effects of those for the single-neuron responses in the partially demyelinated SGN described in Sec. 6.3.1.1. However, it is important to note that saturation of the population is not reached over the 15 dB range of effective stimulus amplitudes simulated, i.e. not all neurons in the subpopulation are stimulated (see Fig. 6.3.5 top panel). In addition, it was observed that a large number of SGNs reach individual spiking saturation (see bottom panel of Fig. 6.3.5), i.e. reach their individual intrinsic spiking maximum. This shows that the healthy population has a wider range of amplitudes that could be assessed, i.e. a greater DR for the population, to assess the overall response. Due to the heavy computational resources required for such a range of stimulus amplitudes, further investigation of healthy SGN saturation amplitudes is not considered in this thesis.

The middle panel of Fig. 6.3.5 shows that the PSS pulse-shape produced the same spike-rate as SYMS pulses, except that this is shifted 3 dB down for the asymmetric condition. Similarly, the slight reduction in threshold for the SYMR stimulus is noted for the healthy SGN population (less than 0.5 dB).

From the bottom panel in Fig. 6.3.5, no significant reductions in SOE are observed for the different pulse shapes in the population of healthy SGNs: all pulse shapes

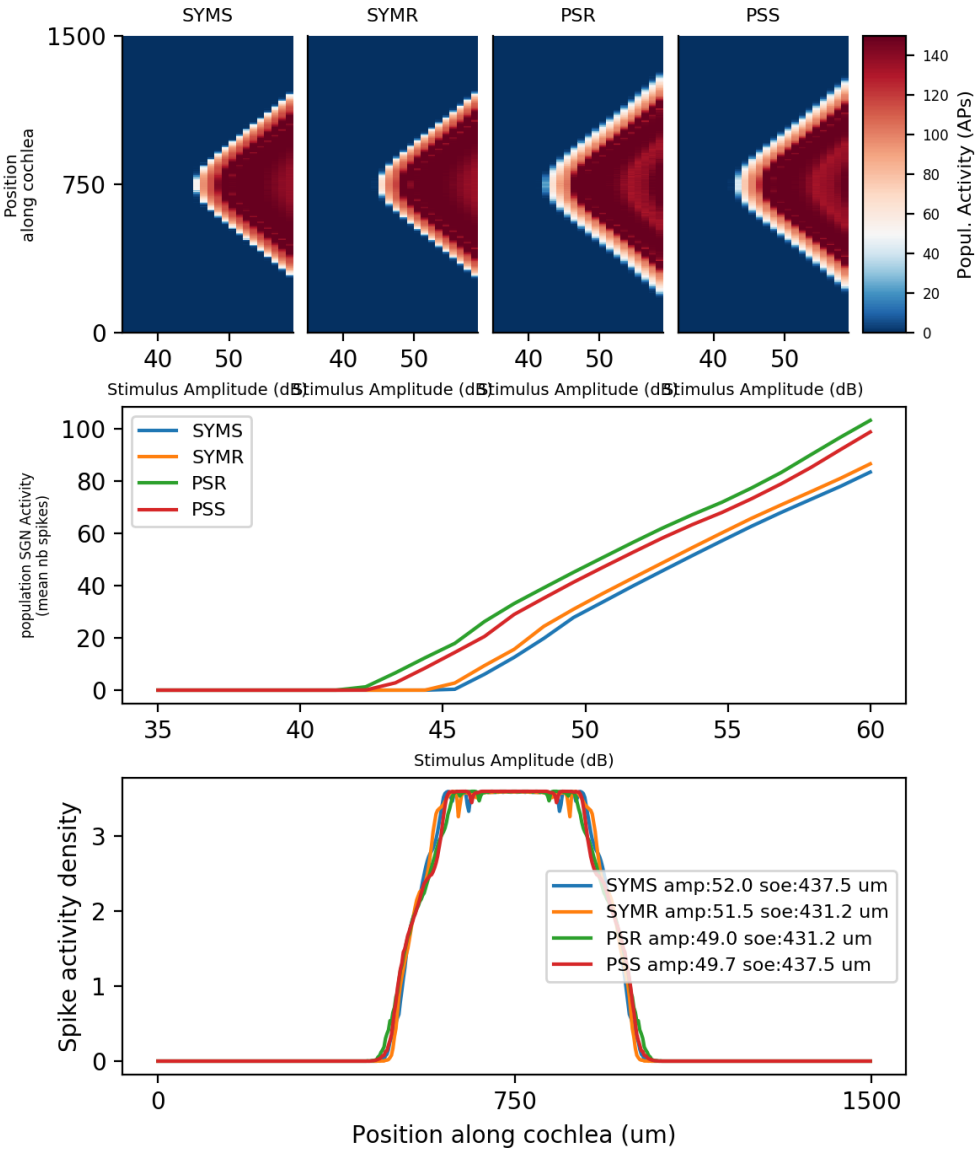

Figure 6.3.5: Population response to pulse trains for a healthy SGN health profile, the "HH" ionic model when subjected to cathodic-first pulse-trains at 1000 pps at the high electrode position. Top panel shows the AP activity as a function of stimulus amplitude, the middle panel shows the activity spread over the entire population (mean number of spikes - nb) as a function of intensity, and the bottom panel shows the density distribution of APs at the half-activation amplitude.

generate a similar SOE from 431.2 to 437.5 µm (less than 2% difference). However, amplitude benefits for asymmetry and ramp are observed to be independent of stimulus amplitude.

6.3.2.2 Degenerated SGN

In the simulations of the population of healthy SGNs, the interacting effects of pulse shape and polarity are not significant on SOE. However, the degenerated population shows significant differences in SOEs for the anodic-first and cathodic-first conditions. Here, the results for the anodic-first and cathodic-first conditions are presented, both simulated with the "HH+HCN+KLT" ionic model, at 1000 pps and at the low-electrode position.

Anodic-first stimulation Fig. 6.3.6 shows the effects of different pulse shapes on the response of a degenerated SGN population subject to trains of anodic-first electrical pulses at 1000 pps for the four pulse shapes described in Sec. 6.2. Overall, the range of stimulus amplitudes simulated for the degenerated SGN population permitted population saturation to be reached 7 dB above the respective population thresholds, i.e. all SGNs in the population were generating one or more APs at a stimulation level 7 dB above threshold (Fig. 6.3.6 top panel).

The middle panel in Fig. 6.3.6 plots the mean activity of the degenerated population when subject to stimulation by the different pulse shapes. Note that the benefits of the different pulse shapes on thresholds, e.g. a 2 dB reduction in threshold for PSS when compared to the SYMR, are independent of stimulus amplitude. This would account for the observation of only small differences in DR for the single degenerated SGN model also holding for the population model.

Finally, in contrast to the results for the healthy SGN population in Sec. 6.3.2.1, PSS and PSR pulse shapes showed different AP-activity distribution to the other two symmetric (SYMS and SYMR) pulse shapes, resulting in a significantly narrower predicted SOE close to the stimulating electrode. For the SGNs furthest from the electrode, at a distance of 750 µm, the activity first increases rapidly until reaching a "spike-rate plateau" (Fig. 6.3.6 bottom panel). Measuring the SOE for each pulse shape at the half-activity density, i.e. half-way from the peak density, it is observed that the PSS and PSR generate SOEs of 650 µm and 625 µm, respectively, whilst the

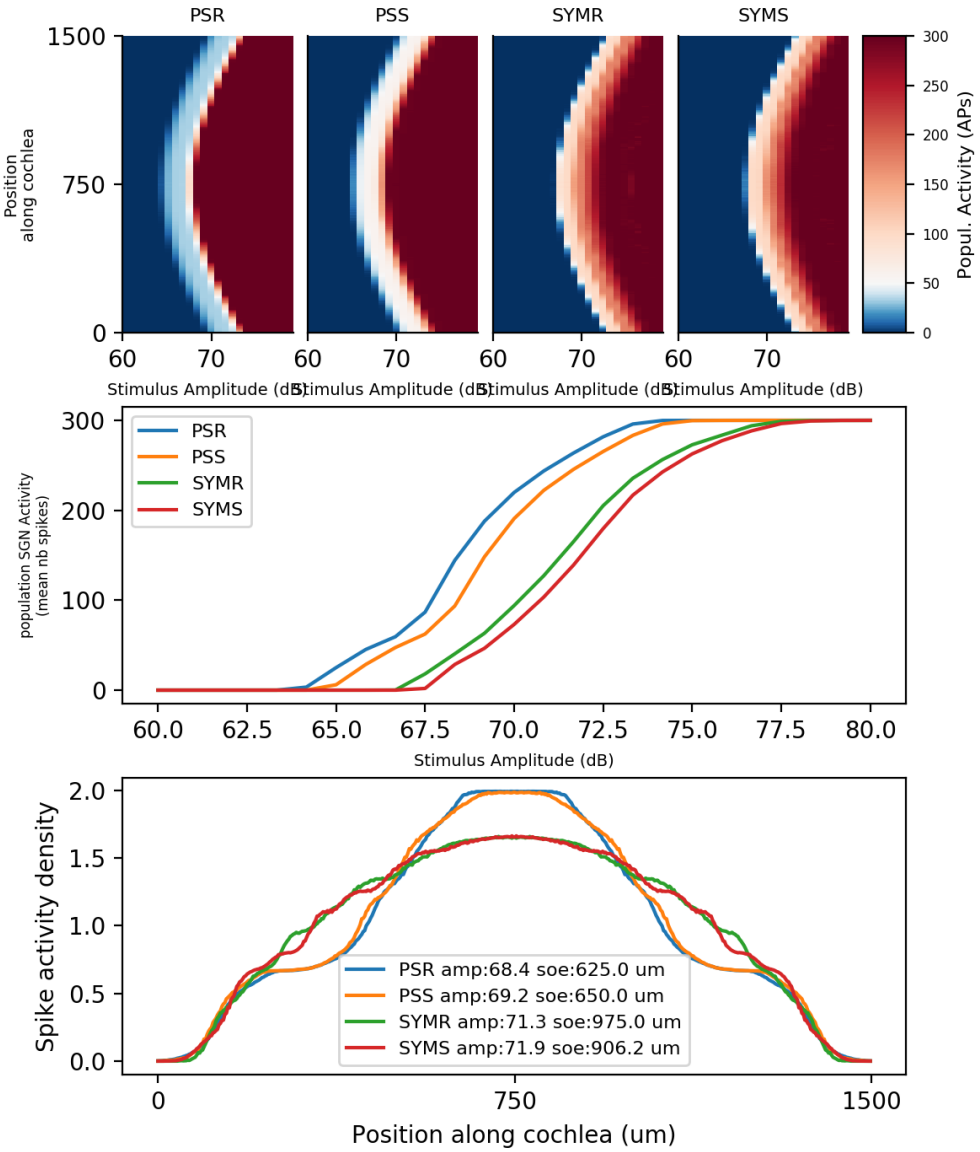

Figure 6.3.6: Population response to pulse trains for a fully degenerated SGN health profile, the "HH+KLT+HCN" ionic model when subjected to anodic-first pulse-trains stimulations at 1000 pps and at a low electrode position. Top panel shows the AP activity as a function of stimulus amplitude, the middle panel shows the activity spread over the entire population (mean number of spikes - nb) as a function of intensity, and the bottom panel shows the density distribution of APs at the half-activation amplitude.

SYMS and SYMR have SOEs of 906 µm and 975 µm respectively. When compared to the overall span of the modelled population (1500 µm), this means that the PSS (43% of population span) is 22% (23.5% for PSR) smaller than the SYMR SOE and 17% (19% for PSR) smaller than the SYMS SOE (less than 5% difference in SOE between SYMS and SYMR). This also suggests that the asymmetry of the pulse shapes is the only basis for the benefit in SOE observed in the anodic-first condition.

Cathodic-first stimulation Fig. 6.3.7 shows the effects of different pulse shapes on the response of a degenerated SGN population subject to trains of cathodic-first electrical pulses at 1000 pps for the four pulse shapes described in the methods.

The middle panel in Fig. 6.3.7 plots the mean activity of the degenerated population when stimulated by the different pulse shapes. Unlike the anodic-first condition, the benefits of asymmetry and ramp are found to be variable with stimulus amplitude. However, no shift in "best" pulse-shape with regards to stimulus amplitude is found, i.e. asymmetric pulses and ramped pulses are better than, or equal to, asymmetric alone, and ramp is better than, or equal to, square pulses.

Fig. 6.3.7 (bottom panel) shows contrasting results for the cathodic-first polarity when compared to the anodic-first condition for the degenerated SGN population described in Sec. 6.3.2.2, Here, the PSS and PSR pulse shapes have the largest predicted SOE when compared to the symmetric pulse shapes, i.e. SYMS and SYMR. Measuring the SOE showed that the PSS and PSR generated SOEs of 1056 µm and 1069 µm respectively, whilst the SYMS and SYMR have SOEs of 775 µm and 794 µm respectively. Again, comparing these SOEs to the overall span of the modelled population (1500 µm), it makes the PSS (70% of population span) 17.5% larger than the SYMR SOE (18.3% larger for PSR) and 18.8% (19.6% for PSR) larger than the SYMS SOE. Also, differences in the predicted SOEs between ramp and square conditions are not significant (less than 2% difference in SOE between SYMS and SYMR, and between PSS and PSR) suggesting that the symmetry of the pulse shapes is the only reason for SOE benefit.

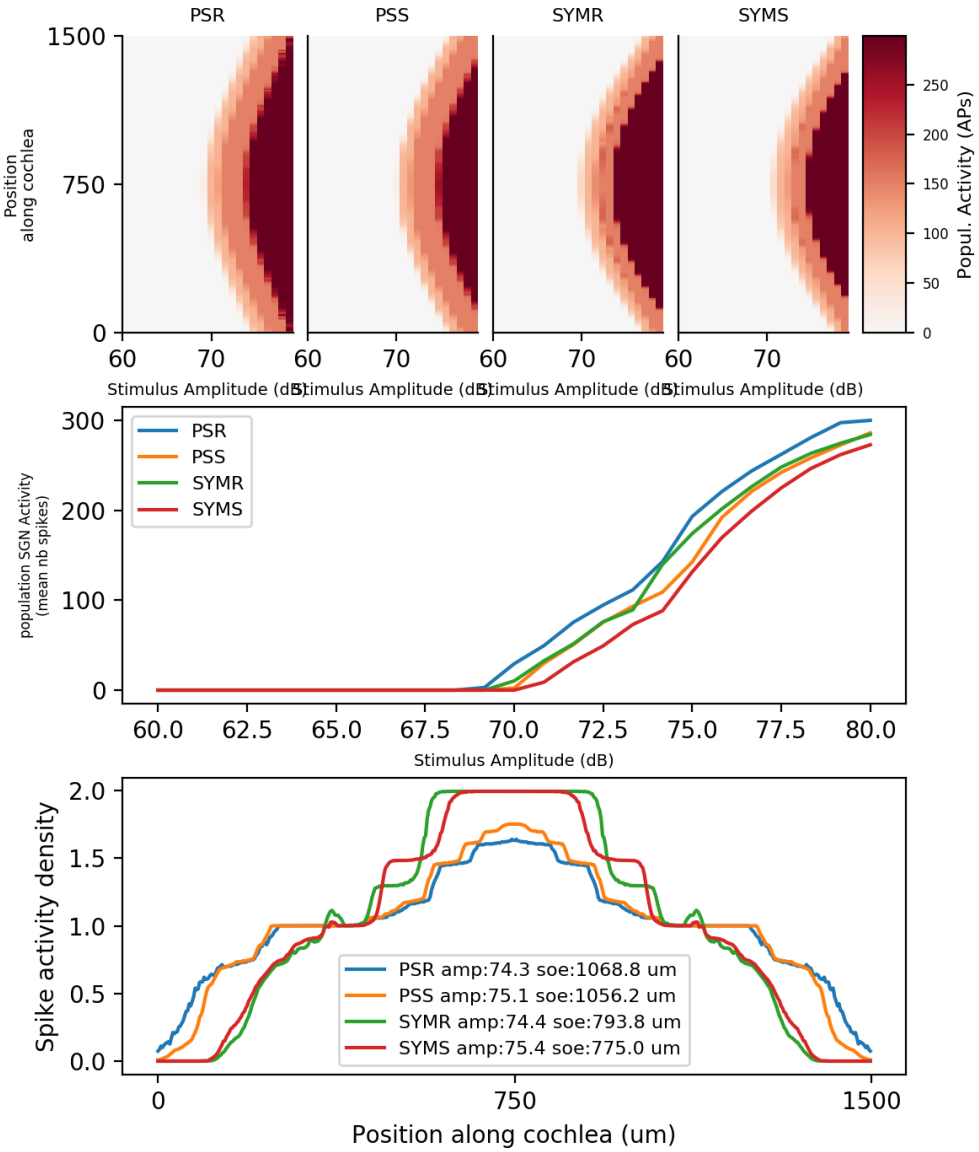

Figure 6.3.7: Population response to pulse trains for a fully degenerated SGN health profile, the "HH+KLT+HCN" ionic model when subjected to cathodic-first pulse-trains stimulations at 1000 pps and at a low electrode position. Top panel shows the AP activity as a function of stimulus amplitude, the middle panel shows the activity spread over the entire population (mean number of spikes - nb) as a function of intensity, and the bottom panel shows the density distribution of APs at the half-activation amplitude.

6.4 Discussions

Overall, this chapter introduces important effects of pulse shape and polarity. Ramp and asymmetry, when taken separately or combined (PSS, PSR, and SYMR), lower thresholds for AP generation and increase DRs, in some simulated cases for both demyelinated and fully degenerated single SGN. Those benefits are consistent with previous computational and human studies of the effects of asymmetries (Van Wieringen et al., 2005; van Wieringen, Carlyon, et al., 2006; Macherey, Van Wieringen, et al., 2006; Macherey, Carlyon, Chatron, et al., 2017; Undurraga, van Wieringen, et al., 2010; Undurraga, Carlyon, Macherey, et al., 2012; Undurraga, Carlyon, Wouters, et al., 2013a) as well as previous modelling data (Smit, Hanekom, van Wieringen, et al., 2010), and consistent with *in vitro* studies of ramp shapes (Ballestero et al., 2015). In both cases, the data presented here indicate that pulse shape could be optimized to improve CI efficiency.

Interpretations of the benefits of pulse shape effects at the level of populations of SGN were more complex. In the healthy SGN population model presented in Fig. 6.3.5, effects of asymmetry and ramp, aside from reduced thresholds, were not present. However, it was noted, in the cathodic-first condition that the amplitude benefits due to ramp and asymmetry that were observed at threshold levels for single SGN responses were still present and independent of stimulus amplitude.

More effects were observed in the degenerated SGN population model, where variation in overall spike-rate and normalized spike-rate pattern seemed to change due to the symmetry, or asymmetry, of the pulse-shape condition. A clear benefit of pulse-shape asymmetry was noted in anodic-first conditions, whilst the degenerated population subject to cathodic-first polarity stimulation benefited more from symmetry in pulse shape. Further, no significant effect of ramp in cathodic-first and anodic-first conditions were observed with regards to SOE. However, a reduction in stimulus amplitude for ramped pulse shapes, independent of amplitude and similar to that for single SGN responses, was observed in anodic-first conditions. This is in constrast to observations for the cathodic-first conditions where a similar benefit was found, but here the benefit was dependent on stimulus level.

Also, for future studies, adding a simple integration window at the output of the model to count spikes might provide further information as to the response specific

to the various parameters tested here.

6.4.1 Effects of pulse shape asymmetry

Effects of pulse shape asymmetry were observed in the different health conditions modelled in this chapter. Overall, thresholds for the SYMR pulse shape were slightly lower than the reference SYMS pulse shape, whereas both asymmetric pulses (PSS and PSR) showed significantly reduced thresholds for most anodic-first and cathodic-first conditions. Asymmetry was found to be the main driver for threshold reduction in all the conditions that were simulated.

Regarding the population response, the effects observed for the single SGN model seem to correspond to an overall reduction in threshold levels for the asymmetric pulse conditions, i.e. PSS and PSR, similar to observations reported for previous computational models (Smit, Hanekom, van Wieringen, et al., 2010) and in human listeners (Macherey, Van Wieringen, et al., 2006; Van Wieringen et al., 2005; van Wieringen, Carlyon, et al., 2006). Interestingly, the pulse-shape related SOEs for degenerated population models were found to be highly dependent on asymmetry and polarity, which was not the case for the healthy population model SOEs. In the degenerated population model, anodic-first asymmetric conditions were found to create a much narrower SOE than symmetric pulse shapes (17 to 23.5 % benefit of asymmetry). In the cathodic-first conditions, however, the opposite effect was observed: the symmetric conditions produced SOEs that were smaller than their asymmetric counterpart (17.5 to 19.6 % smaller for symmetric). This is in contradiction with previous modelling studies where asymmetry is typically found to reduce SOE (Rattay, Lutter, et al., 2001; Rattay, Potrusil, et al., 2013; Smit, Hanekom, van Wieringen, et al., 2010). However, a discrepency has previously been reported for human subjects, where the asymmetrical pulse shapes didn't always account for better specificity of excitation (Macherey, van Wieringen, et al., 2010). This has been explained by the complexity of degeneration profiles which might change the efficiency of the eliciting phase and instead favour the longer discharge phase, e.g. in the case of demyelination (Macherey, van Wieringen, et al., 2010).

Such a noticeable difference in the predicted response of SGN populations when subject to stimulation with symmetric and asymmetric pulse shapes suggest that

these have the potential to evaluate neural health. For example, in the context of perceived electrode discrimination tasks, a CI user that would perform the same way for symmetric and asymmetric pulse shapes would be most likely to have good neural health, i.e. peripheral neural survival. However, a CI user that would perform better in electrode discrimination tasks for asymmetric pulses in the anodic-first condition, and better for symmetric pulses in cathodic-first conditions could be considered to have a mostly degenerated SGN population for the tested electrode. Also, this assumes that electrode discrimination can be directly correlated to spatial selectivity, which does not currently have strong evidence in literature. For example, electrode discrimination is usually better at high than at low current levels whereas the spread is expected to increase at high current levels (Bierer, 2007). Although the effects described here are interesting, confirmation of their validity across electrode positions and more realistic modelling condition, i.e. with conduction models, would be required to define an effective strategy for evaluating neural health.

6.4.2 Effects of pulse shape ramp

While effects of ramp were not as important for the partially demyelinated single SGN responses, ramped pulse shapes showed a significant impact on the fully degenerated SGN model. Generally, it was observed that ramped pulses thresholds, both symmetric and asymmetric, were 0.5 dB lower than their square-pulse equivalent. This effect is in line with the study of Ballestero et al. (2015), which reported effects of ramp in the range of 1 to 1.5 dB in the context of *in vitro* stimulation of SGNs.

Also, it was observed that the benefits of ramp and asymmetry could be "combined" in one pulse shape, i.e. PSR, which shows promising benefits. For example, when combined with ramp, the threshold benefit brought by asymmetric pulse shapes could reduce the electrical power required to elicit efficient neural activity without deteriorating signal encoding. This is an interesting feature that should be further investigated in both models and human studies.

At the population level, ramp effects were found to be similar to those from single SGNs. While the amplitude decrease brought by the use of a ramp instead of squares in symmetric and asymmetric conditions held at the population level, it was found to interact with polarity. Similar to the asymmetry benefits, effects

of ramp were found to be amplitude independent in the anodic-first conditions for the degenerated population modelled, and stimulus dependent for the cathodic-first conditions.

Finally, one of the main suggestions that was made in Ballestero et al. (2015) was that ramped pulse shapes would improve spatial selectivity. However, the results presented here did not match this prediction. Because the main theory behind the spatial specificity argument is based on the effects of ramp on the low threshold ionic channels in the SGN, it could be that the ionic channel equations used in this thesis are not fully representative of those found in animal or human SGNs. This is further added to the effect of simplified subpopulation interactions which could account for part of the discrepency. Extended analysis of the ionic channel equations and parameters should be conducted to improve those predictions.

Appendix

6.A Pulse train responses

6.A.1 Healthy single SGN

Fig. 6.A.1 shows the results for the single, healthy SGN model when stimulated with the symmetric and asymmetric pulse-shapes introduced in Sec. 6.2. The effects of polarity, pulse shape, electrode position and pulse-rate were all found to be significant. Interaction effects between polarity, pulse shape and electrode position were also significant.

The polarity effects on thresholds were observed to be similar to the results from Chapter 3 and pulse shape differences were minimal.

6.A.2 Healthy population of SGNs

Fig. 6.A.3 shows a summary of a healthy SGN population simulated with the "HH" ionic model when subject to four different pulse shapes: 1) SYMS; 2) SYMR; 3) PSS, and; 4) PSR, at 1000pps and for anodic-first polarity. Mainly, effects of pulse shape are limited to threshold reduction for aymmetry vs symmetry, and further threshold reduction for ramped versus square. No effects of pulse shapes on SOE are noted for this polarity, similar to the results reported in Sec. 6.3.2.1.

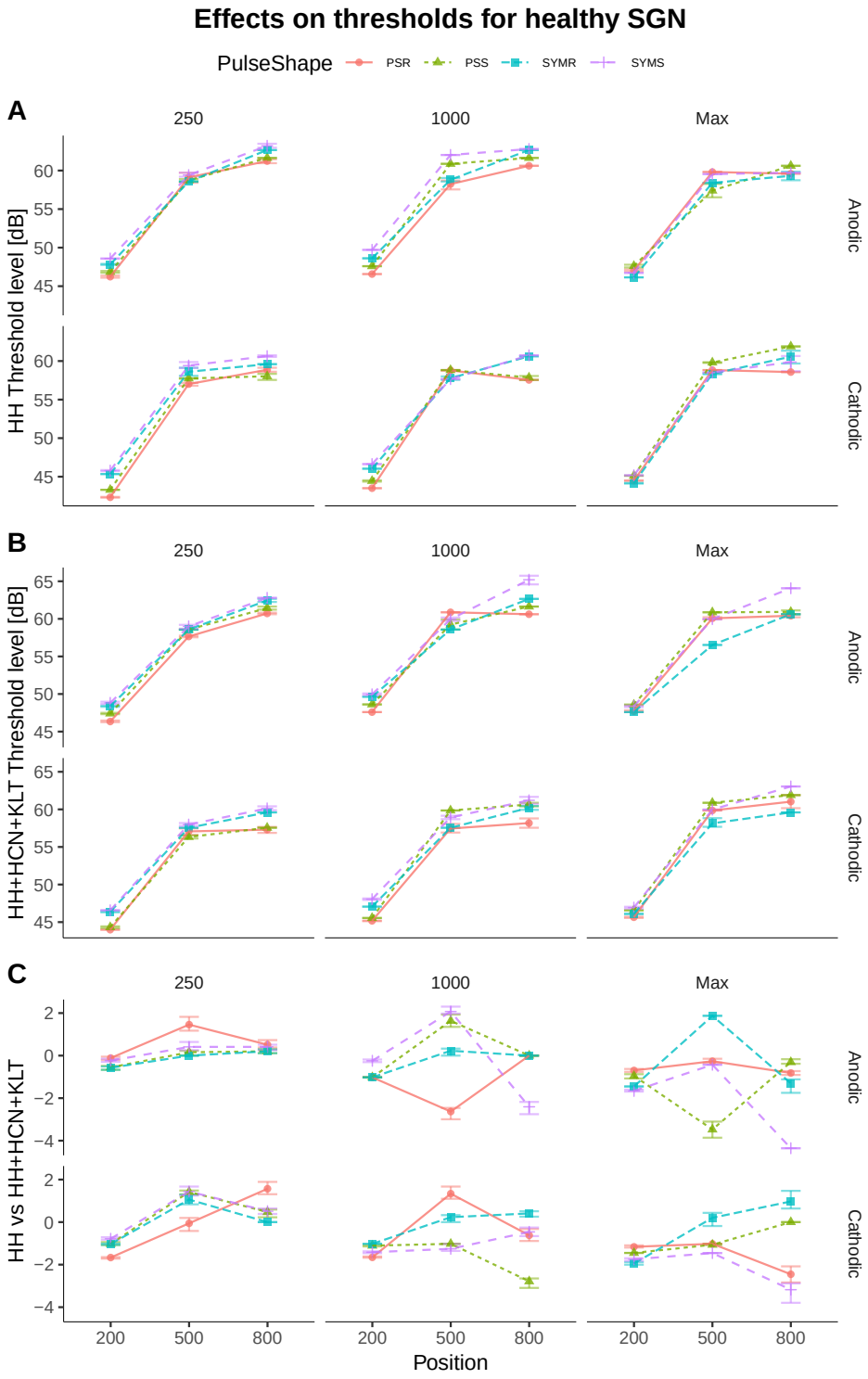

Figure 6.A.1: Threshold levels across models and stimulus conditions. A) threshold levels for the HH ionic model, B) the HH+HCN+KLT ionic model, C) the difference between the simulated threshold levels for the HH and HH+HCN+KLT.

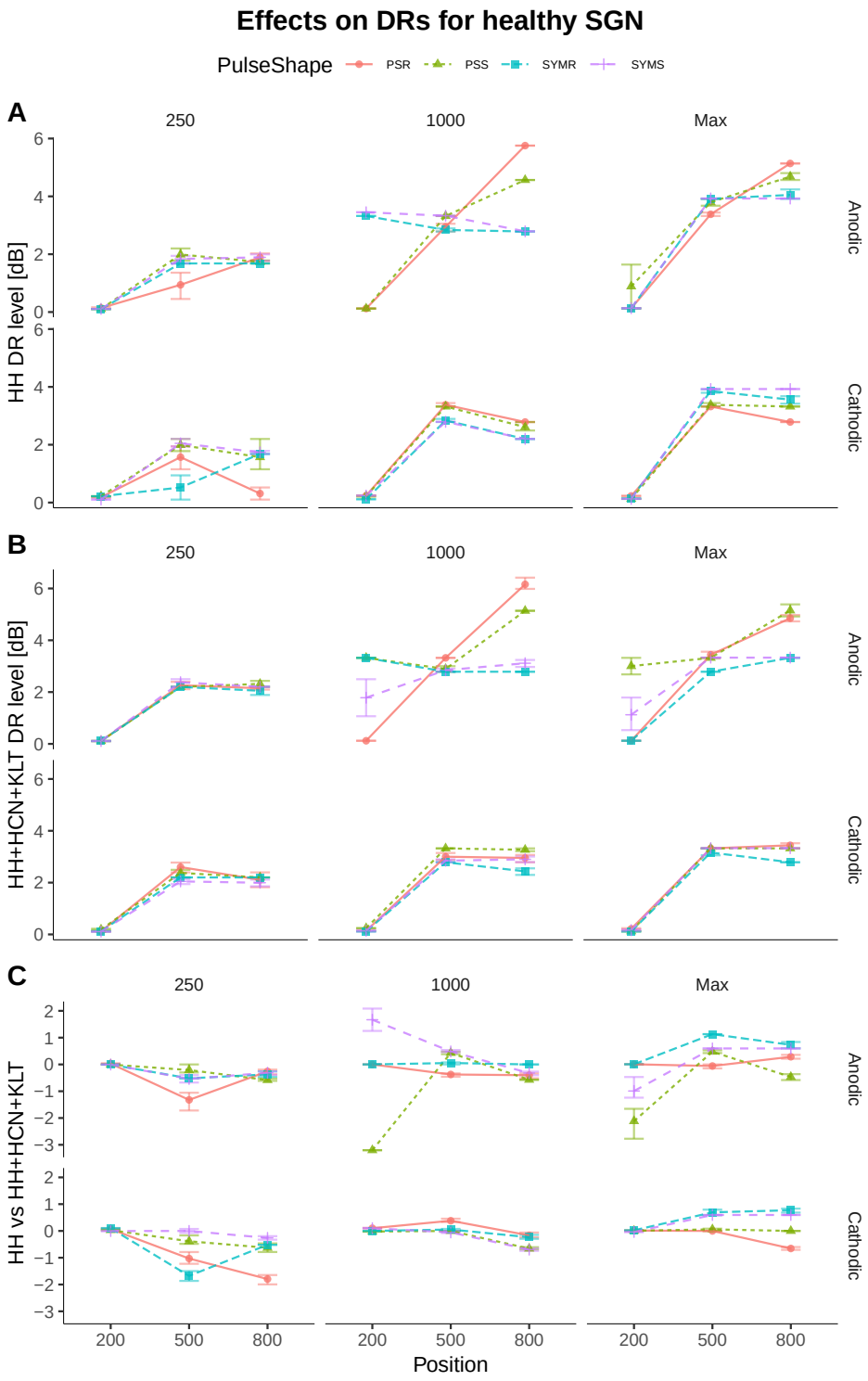

Figure 6.A.2: DR across models and stimulus conditions. A) DR for the HH ionic model, B) the HH+HCN+KLT ionic model, C) the difference between the simulated DRs for the HH and HH+HCN+KLT.

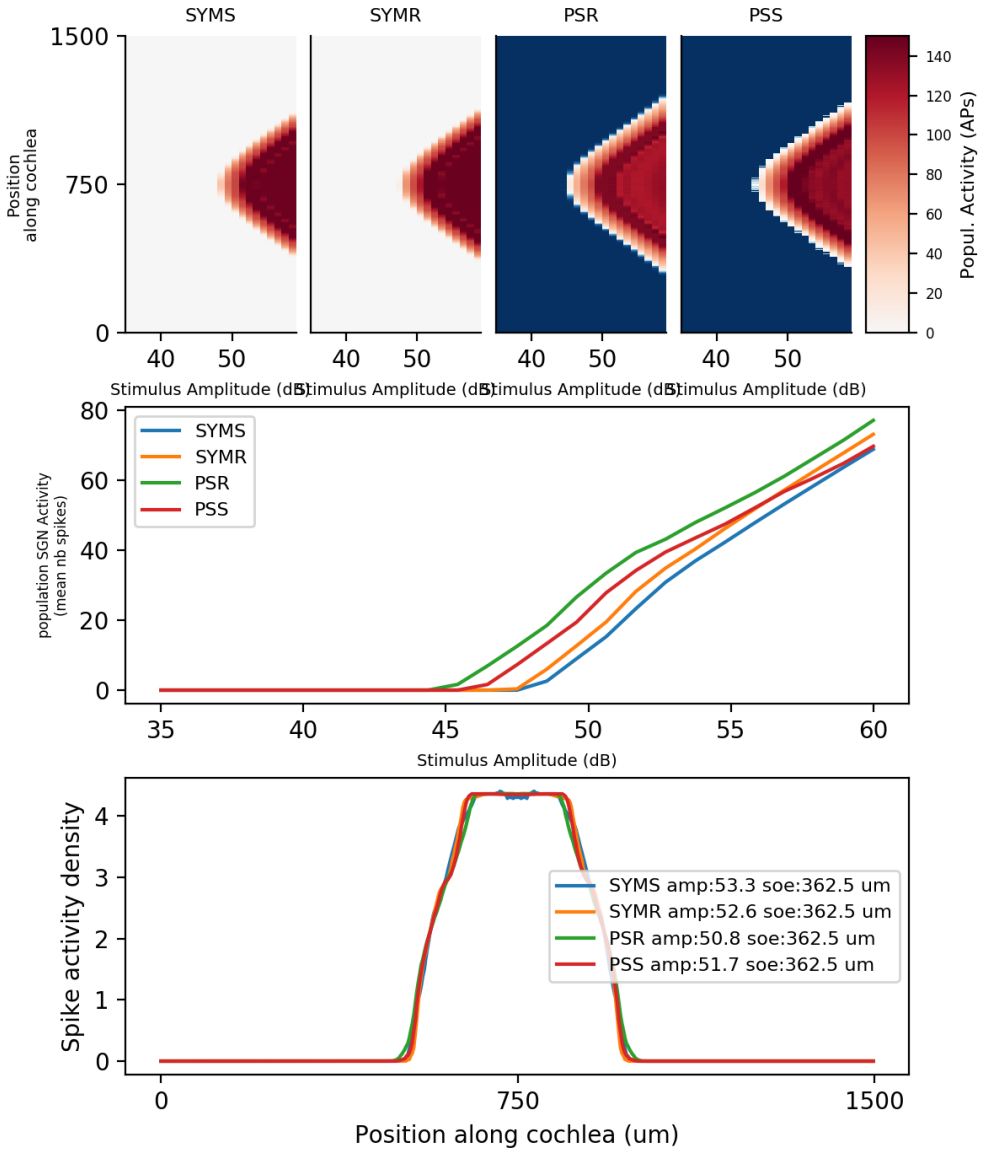

Figure 6.A.3: Population response to pulse trains for a healthy SGN health profile, the "HH" ionic model when subjected to anodic-first pulse-trains at 1000 pps at the high electrode position. Top panel shows the AP activity as a function of stimulus amplitude, the middle panel shows the activity spread over the entire population (mean number of spikes - nb) as a function of intensity, and the bottom panel shows the density distribution of APs at the half-activation amplitude.

7 Discussion

The aim of this thesis was to develop more realistic, physiologically based, models of single and populations of Spiral Ganglion Neurons (SGNs). These models would be used to demonstrate that stimulation strategies adapted to specific patient profiles could provide better encoding of speech information by restoring important temporal and spatial information or, by minimizing unwanted temporal and spatial interactions of electrical stimulation.

Further, this thesis also aimed to explore how a pulse shape designed according to the physiological properties of SGNs could help restore some level of stochasticity to neural firing and increase the spatial selectivity of electrical stimulation. To assess this, Chapter 3 examined an implementation of the Rattay, Lutter, et al. (2001) model extended with voltaged-gated delayed-rectifier potassium (KLT) and voltage-gated hyperpolarization-activated cation (HCN) ionic channels similar to those of Rothman (2003) and Negm and Bruce (2014). Introducing new types of ionic channels helped model more closely the behaviour of SGNs with regards to spike-rate adaptation. Two ionic models were tested: the standard Hodgkin-Huxley (HH) equations for fast activating sodium (Na) and voltaged-gated high-threshold inactivating potassium (Kv), and a more complex and realistic model which included KLT and HCN ionic channels. Modelling the degeneration of SGNs is not a trivial problem given the gradient of possible degeneration profiles that can occur in the deaf ear. Chapter 4 presented model responses of partially demyelinated and fully degenerated single SGNs when subjected to both single and trains of pulses. In Chapter 5, modelled Electrically evoked Compound Action Potential (ECAP) responses for populations representing 1500 SGNs positioned along a 1500 µm straight line were assessed. Three simplified population profiles were tested to evaluate effects of neural status: 1) healthy, 2) partially demyelinated SGNs, and 3) fully degenerated SGNs. Finally, Chapter 6 studied the effects of pulse shape on modelled responses, when asymmetry and ramp were parameters.

7.1 Effects of HCN and KLT ionic channels

Two ionic-channels distributions were used throughout this thesis: the "HH" model with all nodes of Ranvier containing Na and Kv channels which served as a control model, and the "HH+HCN+KLT" model with KLT channels co-located with Kv and additional HCN channels in the post-synaptic as well as pre and post-somatic nodes of Ranvier. The model successfully demonstrated both stochastic and spike-rate adaptation features.

By introducing KLT and HCN channels, the aim was to test the hypothesis that Auditory Nerve (AN) responses would resemble closer neural activity recorded from animal models than those from HH ionic-channel based models. Cochlear Implant (CI) stimulation strategies encode sounds by means of amplitude-modulated pulse trains at rates where spike-rate adaptation and accommodation are important features expected in the SGN response.

In Chapter 3 and Chapter 4, it was observed that the introduction of KLT and HCN did change the preferred pulse-rate for highest Dynamic Range (DR) at specific electrode positions and polarities. Namely, because of spike-rate adaptation, the higher pulse-rate was not necessarily found to have the highest DR, responses also being dependent on peripheral survival and electrode position. This indicates that KLT and HCN can impact encoding of monophasic electrical impulses at the SGN level, rendering them important parameters to be considered when simulating SGN pulse-train responses. Although the effects of KLT and HCN with regards to threshold were also apparent for biphasic stimulations, the difference was not statistically significant.

Importantly, the effects of ionic channels were not significant across health status and electrode position conditions, for the single pulse ECAPs modelled in Chapter 5. The absence of significant effects of ionic model on population responses for single pulse ECAP, is in line with the discussions and outcomes of Chapter 3 and Chapter 4 where the "HH+HCN+KLT" had minimal impact on single pulse stimulus apart from shifts in thresholds.

7.2 Effects of degeneration, electrode position and pulse rate

Existing literature shows that over the various degrees of SGN degeneration associated with hearing loss, multiple predictions can be made as to which stimulation scenario would best encode electrically stimulated signals (Rattay, Lutter, et al., 2001; Badenhorst et al., 2017; Kalkman, Briaire, Dekker, et al., 2014; Smit, Hanekom, van Wieringen, et al., 2010). Overall, peripheral survival was seen to induce a cathodic polarity preference, whilst full degeneration showed the opposite preference to anodic polarity stimulus. Also, a high electrode position would generate lower thresholds for SGNs with a peripheral process, whilst the degenerated SGN would show lower thresholds for a low electrode position.

Single pulse responses suggest that despite the fact that partially demyelinated SGNs showed similar thresholds and DRs than healthy SGNs, the degradation to insulating myelin causes large distortions in the timing of travelling Action Potentials (APs). This may impact the coding of temporal fine structure, which is critical for speech understanding in noise and binaural processing. On the other hand, the loss of peripheral process in the fully degenerated SGN causes large upwards shifts in thresholds regardless of the electrode position and stimulus polarity.

It is important to note that for the model presented in this thesis the choice of morphological parameters, specifically those of the pre-somatic compartment, might have impacted the results. Access to systematic evidence of the morphological parameters of human SGNs is still limited, which produces a need to sometimes derive morphological values from other mammals or amphibians (Rattay, Potrusil, et al., 2013; Boulet, 2016; Cartee, 2006). In modelling of the SGN, the length of the pre-somatic compartment, regardless of the degeneration status, is highly correlated with the degree of myelination of the cell body (Rattay, Potrusil, et al., 2013). Lower degrees of myelination would require longer pre-somatic compartments to achieve the level of current necessary for an AP to saltate the cell body. In Cartee (2006), the modelled human-like SGN was presumed to have a 50 µm cell body, with a 15 µm, which was possible with a relatively high degree of myelination (0.5 µm of myelin thickness). In comparison, with the relatively low degree of the myelination used in this thesis, based on the previous studies Rattay, Lutter, et al. (2001), Rattay, Potrusil, et al. (2013), and Smit, Hanekom, van Wieringen, et al.

(2010), a 100 µm was required. Although these two approaches are very different, they seem to be equally acceptable due to the fact that different degrees of cell body myelination can be found across the cochlea (Rattay, Potrusil, et al., 2013).

Predictions of responses to pulse-trains were insightful for understanding how degenerated SGNs might behave under more realistic CI stimulation conditions. Interestingly, the full degenerated model demonstrated drastically reduced pulse-rate effects when compared to healthy and partially demyelinated models. The reduced degree of complexity between the electrode position and the SGN peripheral process causes neural response-growth functions to be more linear for almost all stimulus conditions.

Further, discussions on electrode position effects in the context of ECAP modelling are complex because of the multiple interactions that derive from using the same electrode for both stimulation and recording of the response. Nevertheless, the result suggests that differences in N1 latencies and N1-P2 could be used to evaluate the neural health of the population local to the electrode. Healthy populations would show shorter N1 latencies and larger N1-P2 amplitudes for cathodic-first stimulations while the opposite would be true for degenerate populations. Further experiments should investigate the specific contribution of the electrode position on the recorded ECAP and its impact in the context of clinical applications.

7.3 Effects of polarity

The fully degenerated SGN has a specific characteristic that sets it apart from both healthy and partially demyelinated SGNs: whilst healthy and partially demyelinated neurons favour peripheral excitation to cathodic pulses with greater sensitivity at electrode positions near the peripheral process, full degeneration shows higher sensitivity to anodic pulses and reduced thresholds at electrode locations near the soma. Further, full degeneration implies that APs are initiated at significantly more central nodes of Ranvier, which in turns reduces APs latencies.

The results described in Chapter 5 generated important insights into the effectiveness of different pulse shapes and polarities on population recruitment, and it appears that some features of their specific ECAP responses could be used to assess neural health using a polarity-based strategy. Polarity effects have been studied in both

ECAP (Undurraga, van Wieringen, et al., 2010; Undurraga, Carlyon, Macherey, et al., 2012; Macherey, Carlyon, Van Wieringen, et al., 2008) and Electrically evoked Auditory Brainstem Response (EABR) (Undurraga, Carlyon, Wouters, et al., 2013b) as a potential tool to identify the most effective way to stimulate populations of SGNs in the context of CI stimulation.

For example, although the mean N1 latency for anodic monophasic was longer than its cathodic counterpart, the latency distribution for APs reaching node C14 in the stimulated population were shorter for the anodic stimulus. This effect highlights an important consideration, as the ECAP response N1 latency is always to be considered decoupled from the AP events in the population and to be considered only within the condition of a fixed electrode position.

7.4 Modelling ECAPs

Regarding the morphology of ECAP responses from different populations, it was observed that morphologies could be considered to be either "typical", such as Fig. 5.3.1 or Fig. 5.3.2 and comparable ECAP responses from computational (e.g. Briaire and J. H. Frijns (2005)) and human models (Macherey, Carlyon, Van Wieringen, et al., 2008; Undurraga, van Wieringen, et al., 2010; Undurraga, Carlyon, Macherey, et al., 2012). It was also shown than some electrode position and stimulus configurations produced "atypical", multi-peaked morphologies that originate from complex interactions at the peripheral level.

Differences in morphology related to electrode position (as the same electrode is used to stimulate and record) limited the analysis, as strong interactions were observed between these two factors. Thus, the effects of N1 latency and N1-P2 growth can only be compared across the same electrode-position condition.

An important effect was noted at the mid-electrode position, where neural populations with a peripheral process (healthy and partially demyelinated) had mean N1 latencies that were shorter for the anodic than the cathodic polarities for both monophasic and biphasic pulse shapes. However, the degenerated profile showed mean N1 latencies that were similar to the other two electrode position.

The specific effects causing "atypical" ECAP morphologies should be further investigated as previous studies in cats (Miller, Abbas, Nourski, et al., 2003)

and guinea pigs (Brown, 1994) have reported double peaked "antidromic" ECAP recordings for different electrode configurations, i.e. monopolar, bipolar, tripolar, and mostly in the presence of the peripheral process, i.e. undeafened animals. The influence of the stimulating/recording electrode on the morphology of ECAP responses will be further characterised in following studies but was left outside the scope of this thesis.

An explanation for the lower range of N1-P2 amplitudes described in this study could be that here only modelled subpopulations of SGNs were assessed, arranged in a linear plane, whereas the real intracochlear measurements can also be impacted by recruitment of SGNs away from the target population, i.e. stimulating neurons in other turns of the cochlea or ectopic stimulation, similar to the excitation patterns reported by Briaire and J. H. Frijns (2005).

7.5 Effects of pulse shape

Different pulse shapes were tested: polarity and pulse shape are known to play an important role in the efficacy of SGN recruitment in CI, often considered as a possible explanation for the large variability in performance observed clinically (Undurraga, Carlyon, Wouters, et al., 2013a; Macherey, Carlyon, Chatron, et al., 2017). Perhaps the first important point to discuss would be the relevance of using monophasic stimulations in Chapter 3 and Chapter 4. As shown by Macherey, Carlyon, Van Wieringen, et al. (2008) and van Wieringen, Carlyon, et al. (2006), the use of asymmetrical pulses can dramatically change the subjective response of CI users. This indicates that part of the discharge phase of biphasic pulses, regardless of polarity, would impact the stimulation of SGNs.

As shown in Chapter 6, ramped pulses and asymmetries in pulse shapes can lower thresholds and increase DRs, in some demyelinated conditions, and in models of fully degenerated single SGNs. Generally, it was observed that thresholds for ramped pulses were lower than their square-pulse equivalent, in line with *in vitro* data (Ballestero et al., 2015). In addition, simulations of a degenerated population of SGNs showed that asymmetry could reduce Spread of Excitation (SOE) for anodic-first stimulation, whilst symmetric pulse shapes had reduced SOEs for cathodic-first conditions.

It was also noted that the amplitude benefits due to ramp and asymmetry that were observed at threshold levels for single SGN responses were still present at the population level. However, these effects of pulse shape could be found either dependent on, or independent of, stimulus amplitude, depending on neural health and stimulus polarity.

When combined with ramp shapes, the threshold benefit brought by using asymmetric pulse shapes could reduce the electrical power required to elicit efficient neural activity without deteriorating the signal encoding. This is an interesting feature that should be further investigated in both models and human studies.

7.6 Model limitations

Throughout this thesis, various features of the modelling of single and population of SGNs were described and discussed. Similarly to most computational models, the different degrees of simplification and parametrisation cause the model to present multiple limitations that should be discussed.

First, the choice of electrode positions used for the simulations, i.e. the high, mid and low positions from Rattay, Lutter, et al. (2001), was found to impact the predictions made. The model introduced here is limited in that the electrode positions were derived from previous studies and are not fully representative of *in-vivo* scenarios. It has been shown previously that the relevant effects of electrode-to-neuron distance were more variable for lateral than vertical changes (Frijns, Briaire, and Grote, 2001; Briaire and J. H. Frijns, 2006). Furthermore, Badenhorst et al. (2017) reported that the main differences in modelled SGN responses were accounted for by the electrode position relative to the cell body. Because electrode position is such an important parameter of SGN, further studies should be conducted on this limitation to present more realistic predictions. In addition to electrode position, other computational models of the electrically stimulated inner ear often incorporate volume conduction models to accurately represent the complexity of the cochlear structure and the different media it contains. For this thesis, as mentioned in Chapter 2, the model is considered to be in an idealised conductive medium, which represents a limitation of the realistic projection of current spread in the cochlea. Due to the idealised conductive medium, it was theorised and demonstrated

in Chapter 3 and Chapter 4 that changes in distance between the electrode and neuron would mainly affect threshold levels relative to the degeneration profile. However, a more complex electrical field simulated with a conductive volume model would be more realistic and should be used with this model in future studies.

In Chapter 5, SGNs were combined in order to model a subpopulation of neurons in the cochlea. In the ear, the AN is constituted of SGNs placed in the cochlear spiral with variable morphological parameters, such as length of the peripheral and central processes or the position and diameter of the soma. In this thesis, the modelled subpopulation was built with two simplifications: 1) the neurons were placed side-by-side on a straight line; 2) the neurons were all assumed to have the exact same morphology. This is an important limitation of the model as the encoding of different intensities and temporal features is supported by this variability in the SGN population (Spoendlin and Schrott, 1989; Finley et al., 1990; Joris and Smith, 2008). With this model now developed and the availability of systematic studies of the variation in morphology across the cochlea, the model could be improved further by modelling morphologically distributed population of SGNs.

In Chapter 3, the bistable state of the Na gating equation was introduced as a limitation of the model introduced in this thesis. This specific prediction was not reported by any of the previous SGN modelling specific literature (Rattay, Lutter, et al., 2001; Rattay, Potrusil, et al., 2013; Smit, Hanekom, van Wieringen, et al., 2010; Frijns, de Snoo, et al., 1995; Negm and Bruce, 2014). However, the reports were made for stimulations at either lower pulse rates, lower temperature (i.e. slower kinetics), or for single node morphology. This feature of the model introduced in this thesis should definitely be investigated further to explain this new outcome. The bistable limitation is also highly correlated with the large amounts of parameters needed for this model. As shown in **??**, the parameters that where chosen for the models presented in this thesis were derived from previous studies (Rattay, Lutter, et al., 2001; Rattay, Potrusil, et al., 2013; Smit, Hanekom, van Wieringen, et al., 2010; Frijns, de Snoo, et al., 1995; Negm and Bruce, 2014). However, their origin often differs, from amphibians to mammals reports, and some adjustments where often made to produce more relevant results. This limitation should be considered further in future work, and a parameter sensitivity study should be conducted with physiological boundaries.

Also, as mentioned in Chapter 6, a mismatch exists between the predicted neuron recruitment (ECAPs) and the encoding of pulse trains for specific population conditions related to the 'HH+HCN+KLT' ionic channel model was observed. This is a major limitation in the model predictions which is hypothesized to originate from a more general charateristic of the spike-rate adaptation and the implementation of the equations for HCN and KLT ionic channels from Negm and Bruce (2014), Boulet (2016) and Rothman (2003). As described and validated in Chapter 2, the spike-rate adaptation profile of the model was defined as weak when compared to animal data (Zhang et al., 2007). Furthermore, it was observed in some of the responses described in Chapter 3 and Chapter 4 that at 5000pps, some stimulation intensity conditions only produced one AP, i.e. the initial AP, before stopping activity, i.e. spike-rate adaptation blocking. This effect has not been previously reported by Negm and Bruce (2014), Boulet (2016) nor Rothman (2003), and could have an important impact on responses at higher pulse rates, e.g. beyond 1000pps, warranting further investigation. The model has shown some promising spike-rate adaptation features which were previously lacking from SGN computational models using human morphology. However, the spike-rate adaptation feature was mostly observed for monophasic stimulation conditions, and was not found to be consistent across degeneration profiles. Thus, adapting the equations and parameters of HCN and KLT ionic channels through a more detailed study would greatly improve the model predictions with regard to spike-rate adaptation.

The pulse width for all eliciting phases in the pulse shapes used in this thesis were 50 µs in duration. Although this duration is not outside the possible range of electrical stimulation in CIs, 25 µs is more commonly used in clinical setting (van Wieringen, Carlyon, et al., 2006). In addition, the range of stimulation intensities that were used in the thesis were also found to be very high and, most of the time, well beyond the realistic range of intensities used in clinical setting. This was found to be similar to previous modelling studies, but is nevertheless an important limitation of the current models of the SGN. One possible explanation can be found in the complex dynamics of the ionic channels that might not always be well represented. Improving the prediction

Finally, the analysis of the responses for Chapter 3, Chapter 4 and Chapter 6 focused on the effects of polarity at threshold levels for single SGN simulations.

However, it is important to note that those effects of polarity are only present in humans at suprathreshold levels or Most Comfortable Levels (MCLs) (van Wieringen, Carlyon, et al., 2006; Macherey, Carlyon, Van Wieringen, et al., 2008). This constitutes a limitation of the predictions made by the model, as there is no human data that shows evidence of such effects at threshold levels. However, this could be explained by the intrinsic difference of single SGN modelling and the behaviour of a realistic population of SGNs. Given that the subpopulation modelled in Chapter 5 was simplified, further investigation into the impact of realistic population modelling on polarity effects should be conducted to improve the model predictions.

Table 7.6.1: Summary of experimental findings and corresponding model predictions

Clinical or experimental findings	Model predictions	Rating
Animal studies show SGN stochasticity (Javel and Viemeister, 2000)	Model provides control over stochasticity	Excellent
Cat SGNs show weak to strong spike-rate adaptation (Zhang et al., 2007)	Model predicts limited features of spike-rate adaptation and categorizes as weak	Poor
ECAPs N1 latencies are longer for cathodic-first than anodic-first pulses (Undurraga, van Wieringen, et al., 2010)	Model predicts that polarity effects on N1 latency are electrode postion dependent	Poor to good
Asymmetrical pulses show polarity effects at MCL but not at threshold levels (Macherey, Carlyon, Van Wieringen, et al., 2008)	Model predicts polarity effects at threshold level for single SGN	Good
Ramped pulse shapes could produce APs (Ballestero et al., 2015)	Model predicts ramped pulses generate APs at lower thresholds than square pulse	Excellent

7.7 Future work

The findings presented in this thesis allow for a neural survival estimation framework based on ECAP thresholds and morphology in response to various polarities to be laid out. Knowledge from different simulation scenarios in Chapter 3, Chapter 4 and Chapter 5 can be leveraged to predict the stimulation that would provide the

best outcome. For example, this would mean to use cathodic-first polarity in cases with peripheral survival or use built-in pulse delays, i.e. virtually advance pulses in time on purpose, for electrodes facing partially demyelinated populations of SGN.

Provided with a more realistic idea of the electrode-to-SGN distance using imaging of the implanted cochlea, e.g. Cone Beam Computed Tomography (CBCT) scans similarly to Badenhorst et al. (2017), further work will aim to match known ECAP responses with modelled responses from volume conduction models like Badenhorst et al. (2017). Using the population models presented in this thesis in more realistic conditions, i.e. with 3D conduction models of the cochlea, could help explain more about the effects generally observed with regards to thresholds and DR.

Fig. 7.7.1 illustrates the flow to be followed to predict the best stimulation strategy based on ECAP measured for both anodic-first and cathodic-first asymmetric pulse shapes. The outcome of such a flowchart would be to have a preferred stimulation strategy based on the predicted neural survival similar to what was described in the Discussion of Chapter 5. However, as mentioned in Chapter 5, single pulse ECAPs appear not to be useful indicators of pulse-train encoding. As such, additional research into the subjective performance related to the predicted neural survival and its correlation to stimulation strategy should be conducted.

The consistent ability of the SGNs, and by extension of the AN, to generate APs in phase with a stimulus is known as phase locking. Although AP latencies as a function of stimulus were not systematically studied in this chapter, a difference in AP phase-locking was noted between the symmetric and asymmetric pulses. To assess the phase locking of a neuron, the distribution of timing of the generated APs, also called phase histogram, can be evaluated over a cycle of the size of the stimulus period (1 ms in this case). In Chapter 6, the consideration of how pulse shape affects the phase locking and entrainment of SGNs was beyond the scope of research. However, analysing some preliminary data from the simulations that were done in Chapter 6, it seems that asymmetry could reduce phase-locking.

Fig. 7.7.2 shows the phase histogram (for more details see Rubinstein, Wilson, et al. (1999) and Shepherd and Javel (1999)) for APs at the last node (C14) of a single degenerated SGN under anodic-first pulse train stimulation at 1000 pps at 5000 µA (74 dB) at the lowest electrode position. Here, the PSS pulse-shape produced a vector strength of 0.892, whilst the SYMS showed a vector strength of

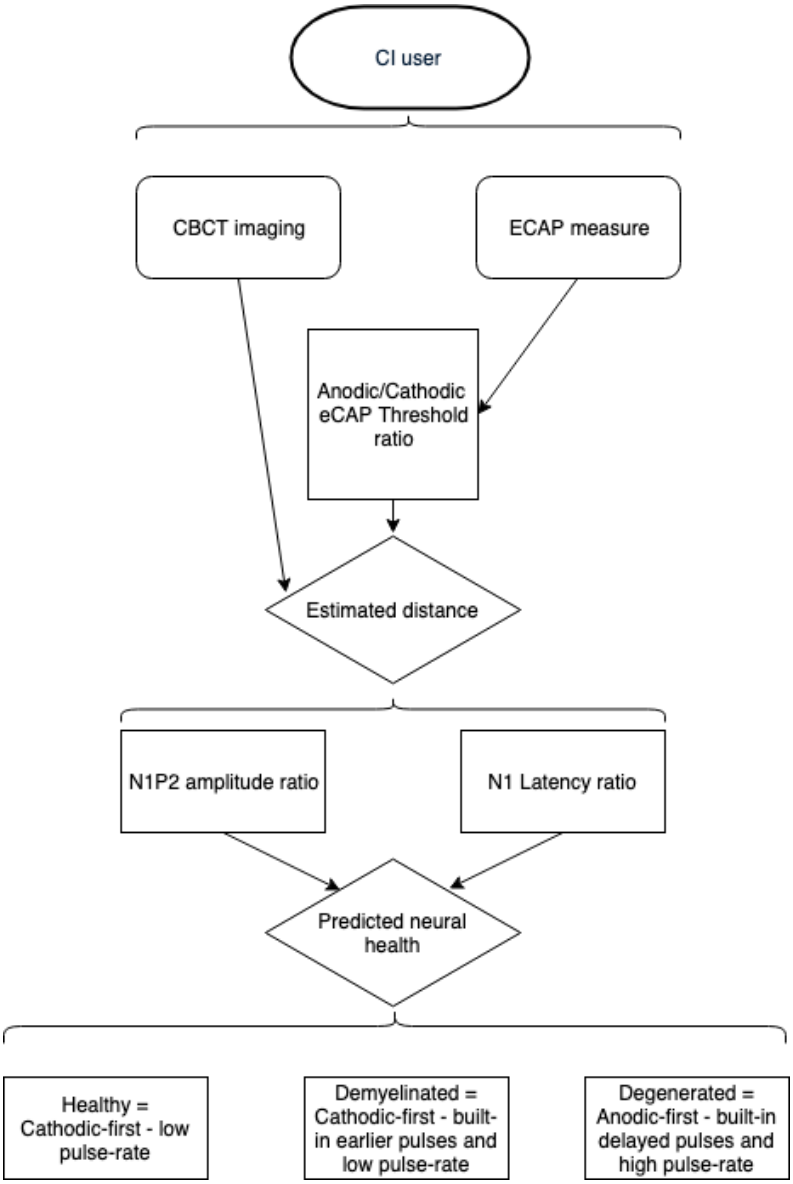

Figure 7.7.1: Flowchart for ECAP based neural survival prediction.

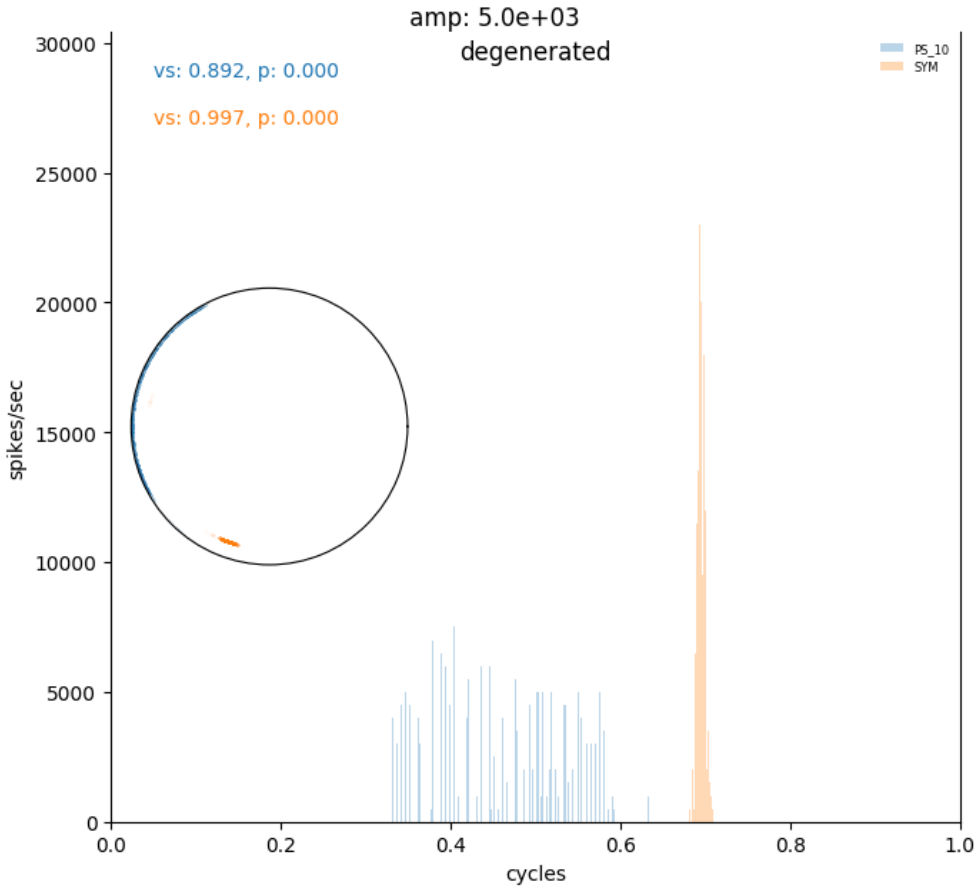

Figure 7.7.2: Phase histogram of spikes at C14 for a fully degenerated SGN and for the "HH+KLT+HCN" ionic model when subjected to anoodic-first pulse-trains stimulations at 1000 pps and at a low electrode position. The phase histograms presented are for the Symmetric-Square (SYMS) and Pseudomonophasic-Square (PSS) (PS_10) pulse shapes. A vector strength (vs) was calculated from the phase distribution of APs (inset). Bin size for the histogram was 200 µs.

0.997. Although the SYMS showed a large vector strength, both pulse shapes were strongly phased-locked to the pulse train. However, it is also noted that the PSS was relatively more dispersed in its probability of firing in the phase cycle when compared to the SYMS pulse shape. Similarly, looking at entrainment (not shown here), which measures the ability of the SGN to respond to each pulse in a pulse train, it appeared that the PSS pulse-shape entrained more effectively than did the SYMS. That is, the single SGN could respond to almost every pulse of the PSSs, but to only every second pulse in the SYMS pulse-trains. Similar responses were observed across the range of amplitudes, polarity and degeneration profiles. This result suggests that PSS pulse-shapes may reduce the degree of phase locking in the electrically stimulated SGN, a response feature that has been suggested to be overrepresented by electrical stimulation (Rubinstein, Wilson, et al., 1999; Shepherd and Javel, 1999).

Future work should be conducted to evaluate the impact of pulse shape on phase locking, and evaluate its impact on perceived signals when encoded via CI stimulation

Bibliography

Adamson, Crista L., Reid, Michael A., Mo, Zun Li, Bowne-English, Janet, and Davis, Robin L. (2002). "Firing features and potassium channel content of murine spiral ganglion neurons vary with cochlear location". In: *Journal of Comparative Neurology* 447.4, pp. 331–350.

Badenhorst, Werner, Hanekom, Tania, and Hanekom, Johan J. (2016). "Development of a voltage-dependent current noise algorithm for conductance-based stochastic modelling of auditory nerve fibres". In: *Biological Cybernetics* 110.6, pp. 403–416.

Badenhorst, Werner, Hanekom, Tania, and Hanekom, Johan J. (2017). "Analysis of a purely conductance-based stochastic nerve fibre model as applied to compound models of populations of human auditory nerve fibres used in cochlear implant simulations". In: *Biological Cybernetics* 111.5-6, pp. 439–458.

Ballestero, Jimena, Recugnat, Matthieu, Laudanski, Jonathan, Smith, Katie E., Jagger, Daniel J., Gnansia, Daniel, and McAlpine, David (2015). "Reducing Current Spread by Use of a Novel Pulse Shape for Electrical Stimulation of the Auditory Nerve". In: *Trends in hearing* 19.

Bierer, Julie Arenberg (2007). "Threshold and channel interaction in cochlear implant users: Evaluation of the tripolar electrode configuration". In: *Citation: The Journal of the Acoustical Society of America* 121, p. 1642.

Blamey, Peter, Arndt, Patti, Brimacombe, Judy, Staller, Steven, Bergeron, François, Facer, George, Bergeron, François, Lindström, Bo, Petersone, Ann, Larkyi, Jan, Nedzelski, Julian, Shipp, David, and Whitford, Leslie (1996). "Factors affecting auditory performance of postlinguistically deaf adults using cochlear implants". In: *Audiology and Neuro-Otology* 1.5, pp. 293–306.

Boulet, Jason (2016). "Biophysical and phenomenological models of cochlear implant stimulation". In:

Briaire, Jeroen J. and Frijns, Johan H.M. (2005). "Unraveling the electrically evoked compound action potential". In: *Hearing Research* 205.1-2, pp. 143–156.

Briaire, Jeroen J. and Frijns, Johan H.M. (Apr. 2006). "The consequences of neural degeneration regarding optimal cochlear implant position in scala tympani: A model approach". In: *Hearing Research* 214.1-2, pp. 17–27.

Briaire, Jeroen J. and Frijns, Johan H.M. M (Apr. 2000). "3D mesh generation to solve the electrical volume conduction problem in the implanted inner ear". In: *Simulation Practice and Theory* 8.1-2, pp. 57–73.

Brown, Angus M. and Hamann, Martine (2014). "Computational modeling of the effects of auditory nerve dysmyelination". In: *Frontiers in Neuroanatomy* 8.August, p. 73.

Brown, M. Christian (1994). *The Antidromic Compound Action Potential of the Auditory Nerve*. Tech. rep. 5.

Bruce, Lan C., White, Mark W., Irlicht, Laurence S., O'Leary, Stephen J., Dynes, Scott, Javel, Eric, and Clark, Graeme M. (1999). "A stochastic model of the electrically stimulated auditory nerve: Single-pulse response". In: *IEEE Transactions on Biomedical Engineering* 46.6, pp. 617–629.

Brummer, S B and Turner, M J (1977). "Electrochemical considerations for safe electrical stimulation of the nervous system with patinum electrodes". In: *IEEE*, pp. 59–63.

Carlyon, Robert P., MacHerey, Olivier, Frijns, Johan H.M., Axon, Patrick R., Kalkman, Randy K., Boyle, Patrick, Baguley, David M., Briggs, John, Deeks, John M., Briaire, Jeroen J., Barreau, Xavier, and Dauman, René (Dec. 2010). "Pitch comparisons between electrical stimulation of a cochlear implant and acoustic stimuli presented to a normal-hearing contralateral ear". In: *JARO - Journal of the Association for Research in Otolaryngology* 11.4, pp. 625–640.

Carlyon, Robert P., Van Wieringen, Astrid, Deeks, John M., Long, Christopher J., Lyzenga, Johannes, and Wouters, Jan (July 2005). "Effect of inter-phase gap on the sensitivity of cochlear implant users to electrical stimulation". In: *Hearing Research* 205.1-2, pp. 210–224.

Carlyon, Robert P, Long, Christopher J, and Deeks, John M (Apr. 2008). "Pulse-rate discrimination by cochlear-implant and normal-hearing listeners with and without binaural cues." In: *J Acoust Soc Am* 123.4, pp. 2276–2286.

Cartee, Lianne A. (May 2006). "Spiral ganglion cell site of excitation II: Numerical model analysis". In: *Hearing Research* 215.1-2, pp. 22–30.

Cartee, Lianne A., Miller, Charles A., and van den Honert, Chris (2006). "Spiral ganglion cell site of excitation I: Comparison of scala tympani and intrameatal electrode responses". In: *Hearing Research* 215.1-2, pp. 10–21.

Cartee, Lianne A., Van Den Honert, Chris, Finley, Charles C., and Miller, Roger L. (2000a). "Evaluation of a model of the cochlear neural membrane. I. Physiological measurement of membrane characteristics in response to intrameatal electrical stimulation". In: *Hearing Research* 146.1-2, pp. 143–152.

Cartee, Lianne A., Van Den Honert, Chris, Finley, Charles C., and Miller, Roger L. (2000b). "Evaluation of a model of the cochlear neural membrane. I. Physiological measurement of membrane characteristics in response to intrameatal electrical stimulation". In: *Hearing Research* 146.1-2, pp. 143–152.

Constan, Zachary A. and Hartmann, William M. (2003). "On the detection of dispersion in the head-related transfer function". In: *The Journal of the Acoustical Society of America* 114.2, pp. 998–1008.

Crozier, R. A. and Davis, R. L. (2014). "Unmasking of Spiral Ganglion Neuron Firing Dynamics by Membrane Potential and Neurotrophin-3". In: *Journal of Neuroscience* 34.29, pp. 9688–9702.

Dorman, Michael F., Dankowski, Korine, McCandless, Geary, and Smith, Luke (1989). "Consonant recognition as a function of the number of channels of stimulation by patients who use the symbion cochlear implant". In: *Ear and Hearing* 10.5, pp. 288–291.

Dorman, Michael F., Loizou, Philipos C., Kemp, Lauren L., and Iler Kirk, Karen (Dec. 2000). "Word recognition by children listening to speech processed into a small number of channels: Data from normal-hearing children and children with cochlear implants". In: *Ear and Hearing* 21.6, pp. 590–596.

Eddington, Donald K., Noel, V., Rabinowitz, W., Svirsky, M., Tierney, J., and Zissman, M. (1994). *Speech Processors for Auditory Prostheses, Eighth Quarterly Progress Report*.

Eisen, Marc D. and Franck, Kevin H. (2005). "Electrode interaction in pediatric cochlear implant subjects". In: *JARO - Journal of the Association for Research in Otolaryngology* 6.2, pp. 160–170.

Felix, H, Johnsson, L G, Gleeson, M, and Pollak, A (1990). "Quantitative analysis of cochlear sensory cells and neuronal elements in man." In: *Acta oto-laryngologica. Supplementum* 470, pp. 71–9.

Finley, Charles C., Wilson, Blake S., and White, Mark W. (1990). "Models of Neural Responsiveness to Electrical Stimulation". In: *Cochlear Implants*. New York, NY: Springer New York, pp. 55–96.

Friesen, Lendra M., Shannon, Robert V., Baskent, Deniz, and Wang, Xiaosong (Aug. 2001). "Speech recognition in noise as a function of the number of spectral channels: Comparison of acoustic hearing and cochlear implants". In: *The Journal of the Acoustical Society of America* 110.2, pp. 1150–1163.

Frijns, J. H.M., De Snoo, S. L., and Ten Kate, J. H. (May 1996). "Spatial selectivity in a rotationally symmetric model of the electrically stimulated cochlea". In: *Hearing Research* 95.1-2, pp. 33–48.

Frijns, J. H.M., de Snoo, S. L., and Schoonhoven, R. (1995). "Potential distributions and neural excitation patterns in a rotationally symmetric model of the electrically stimulated cochlea". In: *Hearing Research* 87.1-2, pp. 170–186.

Frijns, Johan H.M., Briaire, Jeroen J., De Laat, Jan A.P.M., and Grote, Jan J. (June 2002). "Initial evaluation of the Clarion CII cochlear implant: Speech perception and neural response imaging". In: *Ear and Hearing* 23.3, pp. 184–197.

Frijns, Johan H.M., Briaire, Jeroen J., and Grote, Jan J. (2001). "The importance of human cochlear anatomy for the results of modiolus-hugging multichannel cochlear implants". In: *Otology and Neurotology* 22.3, pp. 340–349.

Frijns, Johan H.M., Mooij, Jaap, and ten Kate, Jaap H. (1994). "A Quantitative Approach to Modeling Mammalian Myelinated Nerve Fibers for Electrical Prosthesis Design". In: *IEEE Transactions on Biomedical Engineering* 41.6, pp. 556–566.

Gärtner, Lutz, Lenarz, Thomas, and Büchner, Andreas (Dec. 2018). "Fine-grain recordings of the electrically evoked compound action potential amplitude growth function in cochlear implant recipients". In: *BioMedical Engineering Online* 17.1, p. 140.

Goldman, L. and Albus, James S. (1968). "Computation of Impulse Conduction in Myelinated Fibers; Theoretical Basis of the Velocity-Diameter Relation". In: *Biophysical Journal* 8.5, pp. 596–607.

Gulya, Julianna (1996). "The scala vestibuli for cochlear implantation". In: pp. 5–7.

Hales, John Paul, Lin, Cindy Shin Yi, and Bostock, Hugh (2004). "Variations in excitability of single human motor axons, related to stochastic properties of nodal sodium channels". In: *Journal of Physiology* 559.3, pp. 953–964.

Hanekom, T. (2001). "Three-dimensional spiraling finite element model of the electrically stimulated cochlea". In: *Ear and Hearing* 22.4, pp. 300–315.

Hartmann, William M. and Macaulay, Eric J. (2014). "Anatomical limits on interaural time differences: An ecological perspective". In: *Frontiers in Neuroscience* 8.8 FEB, pp. 1–13.

Hatsushika, Shin Ichi, Shepherd, Robert K., Tong, Yit C., Clark, Graeme M., and Funasaka, Sotaro (1990). "Dimensions of the scala tympani in the human and cat with reference to cochlear implants". In: *Annals of Otology, Rhinology & Laryngology* 99.11, pp. 871–876.

Heffer, Leon F., Sly, David J., Fallon, James B., White, Mark W., Shepherd, Robert K., and O'Leary, Stephen J. (2010). "Examining the Auditory Nerve Fiber Response to High Rate Cochlear Implant Stimulation: Chronic Sensorineural Hearing Loss and Facilitation". In: *Journal of Neurophysiology* 104.6, pp. 3124–3135.

Hines, M L and Carnevale, N T (2003). "The NEURON simulation environment". In: *The Handbook of Brain Theory and Neural Networks* 9.6, pp. 1–24.

Hinojosa, Raäl and Marion, Mitchell (June 1983). "Histopathology of Profound Sensorineural Deafness". In: *Annals of the New York Academy of Sciences* 405.1, pp. 459–484.

Hodgkin, a L and Huxley, a F (1952). "A quantitative description of membrane current and its applicaiton to conduction and excitation in nerve". In: *J Physiol* 117.4, pp. 500–544. arXiv: NIHMS150003.

Holmes, A E, Kemker, F J, and Merwin, G E (May 1987). "The effects of varying the number of cochlear implant electrodes on speech perception." In: *The American journal of otology* 8.3, pp. 240–6.

Hossain, Waheeda a, Antic, Srdjan D, Yang, Yang, Rasband, Matthew N, and Morest, D Kent (2005). "Where is the spike generator of the cochlear nerve? Voltage-gated sodium channels in the mouse cochlea." In: *The Journal of neuroscience : the official journal of the Society for Neuroscience* 25.29, pp. 6857–6868.

Javel, Eric and Viemeister, Neal F. (Feb. 2000). "Stochastic properties of cat auditory nerve responses to electric and acoustic stimuli and application to intensity discrimination". In: *The Journal of the Acoustical Society of America* 107.2, pp. 908–921.

Joris, P. X. and Smith, P. H. (June 2008). "The volley theory and the spherical cell puzzle". In: *Neuroscience* 154.1, pp. 65–76.

Joshi, Suyash Narendra, Dau, Torsten, and Epp, Bastian (Apr. 2017). "A Model of Electrically Stimulated Auditory Nerve Fiber Responses with Peripheral and Central Sites of Spike Generation". In: *JARO - Journal of the Association for Research in Otolaryngology* 18.2, pp. 323–342.

Kale, Sushrut, Micheyl, Christophe, and Heinz, Michael G. (2014). "Implications of within-fiber temporal coding for perceptual studies of F0 discrimination and discrimination of harmonic and inharmonic tone complexes". In: *JARO - Journal of the Association for Research in Otolaryngology* 15.3, pp. 465–482.

Kalkman, Randy K., Briaire, Jeroen J., Dekker, David M T, and Frijns, Johan H M (2014). "Place pitch versus electrode location in a realistic computational model of the implanted human cochlea". In: *Hearing Research* 315, pp. 10–24.

Kalkman, Randy K., Briaire, Jeroen J., and Frijns, Johan H.M. (2016). "Stimulation strategies and electrode design in computational models of the electrically stimulated cochlea: An overview of existing literature". In: *Network: Computation in Neural Systems* 27.2-3, pp. 107–134.

Kashio, Akinori, Tejani, Viral D, Scheperle, Rachel A, Brown, Carolyn J, and Abbas, Paul J (2016). "Exploring the Source of Neural Responses of Different Latencies Obtained from Different Recording Electrodes in Cochlear Implant Users." In: *Audiology & neuro-otology* 21.3, pp. 141–9.

Kreft, Heather A., Donaldson, Gail S., and Nelson, David A. (2004). "Effects of pulse rate on threshold and dynamic range in Clarion cochlear-implant users (L)". In: *The Journal of the Acoustical Society of America* 115.5, pp. 1885–1888.

Kroon, Steven, Ramekers, Dyan, Smeets, Emma M., Hendriksen, Ferry G.J., Klis, Sjaak F.L., and Versnel, Huib (2017). "Degeneration of auditory nerve fibers in guinea pigs with severe sensorineural hearing loss". In: *Hearing Research* 345, pp. 79–87.

Landsberger, David M, Svrakic, Svrakic, Roland, J Thomas, and Svirsky, Mario (2015). "The Relationship between Insertion Angles, Default Frequency Allocations, and Spiral Ganglion Place Pitch in Cochlear Implants HHS Public Access". In: *Ear Hear* 36.5, pp. 207–213.

Loeb, Gerald E., White, Mark W., and Jenkins, William M. (1983). "Biophysical Considerations in Electrical Stimulation of the Auditory Nervous System". In: *Annals of the New York Academy of Sciences* 405.1, pp. 123–136.

Loizou, Philipos C. (1998). "Mimicking the human ear". In: *IEEE Signal Processing Magazine* 15.5, pp. 101–130. arXiv: arXiv:1011.1669v3.

Macherey, Olivier, Carlyon, Robert P., Chatron, Jacques, and Roman, Stéphane (2017). "Effect of Pulse Polarity on Thresholds and on Non-monotonic Loudness Growth in Cochlear Implant Users". In: *JARO - Journal of the Association for Research in Otolaryngology* 18.3, pp. 513–527.

Macherey, Olivier, Carlyon, Robert P., Van Wieringen, Astrid, Deeks, John M., and Wouters, Jan (June 2008). "Higher sensitivity of human auditory nerve fibers to positive electrical currents". In: *JARO - Journal of the Association for Research in Otolaryngology* 9.2, pp. 241–251.

Macherey, Olivier, Van Wieringen, Astrid, Carlyon, Robert P., Deeks, John M., and Wouters, Jan (Sept. 2006). "Asymmetric pulses in cochlear implants: Effects of pulse shape, polarity, and rate". In: *JARO - Journal of the Association for Research in Otolaryngology* 7.3, pp. 253–266.

Macherey, Olivier, van Wieringen, Astrid, Carlyon, Robert P., Dhooge, Ingeborg, and Wouters, Jan (Jan. 2010). "Forward-masking patterns produced by symmetric and asymmetric pulse shapes in electric hearing". In: *The Journal of the Acoustical Society of America* 127.1, pp. 326–338.

Malherbe, T. K., Hanekom, T., and Hanekom, J. J. (2016). "Constructing a three-dimensional electrical model of a living cochlear implant user's cochlea". In: *International Journal for Numerical Methods in Biomedical Engineering* 32.7. arXiv: NIHMS150003.

McKay, Colette M. and Henshall, Katherine R (2010). "Amplitude modulation and loudness in cochlear implantees". In: *JARO - Journal of the Association for Research in Otolaryngology* 11.1, pp. 101–111.

McKay, Colette M., Henshall, Katherine R, Farrell, Rebecca J, and McDermott, Hugh J. (2003). "A practical method of predicting the loudness of complex electrical stimuli". In: *The Journal of the Acoustical Society of America* 113.4, pp. 2054–2063.

McKay, Colette M., Lim, Hubert H., and Lenarz, Thomas (2013). "Temporal processing in the auditory system: Insights from cochlear and auditory midbrain implantees". In: *JARO - Journal of the Association for Research in Otolaryngology* 14.1, pp. 103–124.

Miller, Charles A., Abbas, Paul J., Hay-McCutcheon, Marcia J., Robinson, Barbara K., Nourski, Kirill V., and Jeng, Fuh Cherng (Dec. 2004). "Intracochlear and extracochlear ECAPs suggest antidromic action potentials". In: *Hearing Research* 198.1-2, pp. 75–86.

Miller, Charles A., Abbas, Paul J., and Robinson, Barbara K. (Sept. 2001). "Response Properties of the Refractory Auditory Nerve Fiber". In: *Journal of the Association for Research in Otolaryngology* 2.3, pp. 216–232.

Miller, Charles A., Abbas, Paul J., Robinson, Barbara K., Rubinstein, Jay T., and Matsuoka, Akihiro J. (1999). "Electrically evoked single-fiber action potentials from cat: Responses to monopolar, monophasic stimulation". In: *Hearing Research* 130.1-2, pp. 197–218.

Miller, Charles A, Abbas, Paul J, Nourski, Kirill V, Hu, Ning, and Robinson, Barbara K (2003). *Electrode configuration influences action potential initiation site and ensemble stochastic response properties*. Tech. rep.

Mino, Hiroyuki, Rubinstein, Jay T., and White, John A. (2002). "Comparison of algorithms for the simulation of action potentials with stochastic sodium channels". In: *Annals of Biomedical Engineering* 30.4, pp. 578–587.

Nayagam, Bryony A., Muniak, Michael A., and Ryugo, David K. (2011). "The spiral ganglion: Connecting the peripheral and central auditory systems". In: *Hearing Research* 278.1-2, pp. 2–20.

Negm, Mohamed H. and Bruce, Ian C. (Nov. 2014). "The effects of HCN and KLT ion channels on adaptation and refractoriness in a stochastic auditory nerve model". In: *IEEE Transactions on Biomedical Engineering* 61.11, pp. 2749–2759.

O'Brien, Gabrielle (2016). "Biophysical Population Models of the Auditory Nerve". In:

O'Connell, Brendan P., Hunter, Jacob B., and Wanna, George B. (2016). "The importance of electrode location in cochlear implantation". In: *Laryngoscope Investigative Otolaryngology* 1.6, pp. 169–174.

Pfingst, Bryan E, Zhou, Ning, Colesa, Deborah J, Watts, Melissa M, Strahl, Stefan B, Garadat, Soha N, Schvartz-Leyzac, Kara C, Budenz, Cameron L, Raphael, Yehoash, and Zwolan, Teresa A (2015). "Importance of cochlear health for implant function". In: *Hearing Research* 322, pp. 77–88.

Prado-guitierrez, Pavel, Fewster, Leonie M, Heasman, John M, Mckay, Colette M, and Shepherd, Robert K (2007). "Effect of interphase gap and pulse duration on electrically evoked potentials Is Correlated With Auditory Nerve Survival". In: *Victoria* 215, pp. 47–55.

Ramekers, Dyan, Versnel, Huib, Strahl, Stefan B., Smeets, Emma M., Klis, Sjaak F L, and Grolman, Wilko (2014). "Auditory-nerve responses to varied inter-phase gap and phase duration of the electric pulse stimulus as predictors for

neuronal degeneration". In: *JARO - Journal of the Association for Research in Otolaryngology* 15.2, pp. 187–202.

Rattay, F. (Mar. 1999). "The basic mechanism for the electrical stimulation of the nervous system". In: *Neuroscience* 89.2, pp. 335–346. arXiv: arXiv:1011.1669v3.

Rattay, Frank (1989). "Analysis of Models for Extracellular Fiber Stimulation". In: *IEEE Transactions on Biomedical Engineering* 36.7, pp. 676–682.

Rattay, Frank, Lutter, Petra, and Felix, Heidi (Mar. 2001). "A model of the electrically excited human cochlear neuronI. Contribution of neural substructures to the generation and propagation of spikes". In: *Hearing Research* 153.1-2, pp. 43–63.

Rattay, Frank, Potrusil, Thomas, Wenger, Cornelia, Wise, Andrew K., Glueckert, Rudolf, and Schrott-Fischer, Anneliese (2013). "Impact of morphometry, myelinization and synaptic current strength on spike conduction in human and cat spiral ganglion neurons". In: *PLoS ONE* 8.11.

Resnick, J.M., O'Brien, G.E., and Rubinstein, J.T. (2018). "Simulated auditory nerve axon demyelination alters sensitivity and response timing to extracellular stimulation". In: *Hearing Research* 361, pp. 121–137.

Rothman, J. S. (2003). "The Roles Potassium Currents Play in Regulating the Electrical Activity of Ventral Cochlear Nucleus Neurons". In: *Journal of Neurophysiology* 89.6, pp. 3097–3113.

Rubinstein, J T (1995). "Threshold Fluctuations in an N Sodium Channel Model of the Node of Ranvier". In: *Biophysical Journal* 68.March, pp. 779–785.

Rubinstein, J. T. and Rubinstein, J. T. (July 1993). "Axon Termination Conditions for Electrical Stimulation". In: *IEEE Transactions on Biomedical Engineering* 40.7, pp. 654–663.

Rubinstein, J. T., Wilson, B S, Finley, C C, and Abbas, P J (1999). "Pseudospontaneous activity: Stochastic independence of auditory nerve fibers with electrical stimulation". In: *Hearing Research* 127.1-2, pp. 108–118.

Schmiedt, Richard A. (1989). "Spontaneous rates, thresholds and tuning of auditory-nerve fibers in the gerbil: Comparisons to cat data". In: *Hearing Research* 42.1, pp. 23–35.

Schwarz, Jürgen R. and Eikhof, Gesa (1987). "Na currents and action potentials in rat myelinated nerve fibres at 20 and 37° C". In: *Pflügers Archiv European Journal of Physiology* 409.6, pp. 569–577.

Shepherd, Robert K. and Javel, Eric (1997). "Electrical stimulation of the auditory nerve. I. Correlation of physiological responses with cochlear status". In: *Hearing Research* 108.1-2, pp. 112–144.

Shepherd, Robert K. and Javel, Eric (Apr. 1999). "Electrical stimulation of the auditory nerve: II. Effect of stimulus waveshape on single fibre response properties". In: *Hearing Research* 130.1-2, pp. 171–188.

Skinner, M.W., Holden, L.K., Holden, T., and Demorest, M.E. (2000). "Effect of stimulation rate on cochlear implant recipients' thresholds and maximum acceptable loudness levels." In: *Journal of the American Academy of Audiology* 11.4, pp. 203–213.

Sly, David J, Heffer, Leon F, White, Mark W, Shepherd, Robert K, Michael, G J, Minter, Ricki L, Nelson, Niles E, Wise, Andrew K, and Leary, Stephen J O (2007). *Deafness aleters auditory nerve fibre responses to cochlear Implant Stimulation.* Tech. rep. 2, pp. 510–522.

Smit, J. E., Hanekom, T., and Hanekom, J. J. (2008). "Predicting action potential characteristics of human auditory nerve fibres through modification of the Hodgkin-Huxley equations". In: *South African Journal of Science* 104.7-8, pp. 284–292.

Smit, Jacoba E., Hanekom, Tania, and Hanekom, Johan J. (2009). "Modelled temperature-dependent excitability behaviour of a single ranvier node for a human peripheral sensory nerve fibre". In: *Biological Cybernetics* 100.1, pp. 49–58.

Smit, Jacoba E., Hanekom, Tania, van Wieringen, Astrid, Wouters, Jan, and Hanekom, Johan J. (2010). "Threshold predictions of different pulse shapes using a human auditory nerve fibre model containing persistent sodium and slow potassium currents". In: *Hearing Research* 269.1-2, pp. 12–22.

Spelman, F.A., Clopton, B.M., and Pfingst, B.E. (1982). "Tissue Impedance and Current Flow in the Implanted Ear Implications for the Cochlear Prosthesis". In: *Annals of Otology, Rhinology and Laryngology* suppl.98, pp. 3–8.

Spoendlin, H. (1975). "Retrograde degeneration of the cochlear nerve". In: *Acta Oto-Laryngologica* 79.3-6, pp. 266–275.

Spoendlin, H. and Schrott, A. (Dec. 1989). "Analysis of the human auditory nerve". In: *Hearing Research* 43.1, pp. 25–38.

Svirskis, G. (2004). "Sodium Along With Low-Threshold Potassium Currents Enhance Coincidence Detection of Subthreshold Noisy Signals in MSO Neurons". In: *Journal of Neurophysiology* 91.6, pp. 2465–2473.

Tagoe, T., Barker, M., Jones, A., Allcock, N., and Hamann, M. (2014). "Auditory Nerve Perinodal Dysmyelination in Noise-Induced Hearing Loss". In: *Journal of Neuroscience* 34.7, pp. 2684–2688.

Undurraga, Jaime A. (2013). *Basic Neural Mechanisms of the Electrically Stimulated Auditory Nerve Doctoral Thesis in Biomedical Sciences*, p. 245.

Undurraga, Jaime A., Carlyon, Robert P., Macherey, Olivier, Wouters, Jan, and van Wieringen, Astrid (Aug. 2012). "Spread of excitation varies for different electrical pulse shapes and stimulation modes in cochlear implants". In: *Hearing Research* 290.1-2, pp. 21–36.

Undurraga, Jaime A., Carlyon, Robert P., Wouters, Jan, and Van Wieringen, Astrid (June 2013a). "The polarity sensitivity of the electrically stimulated human

auditory nerve measured at the level of the brainstem". In: *JARO - Journal of the Association for Research in Otolaryngology* 14.3, pp. 359–377.

Undurraga, Jaime A., Carlyon, Robert P., Wouters, Jan, and Van Wieringen, Astrid (June 2013b). "The polarity sensitivity of the electrically stimulated human auditory nerve measured at the level of the brainstem". In: *JARO - Journal of the Association for Research in Otolaryngology* 14.3, pp. 359–377.

Undurraga, Jaime A., van Wieringen, Astrid, Carlyon, Robert P., Macherey, Olivier, and Wouters, Jan (Oct. 2010). "Polarity effects on neural responses of the electrically stimulated auditory nerve at different cochlear sites". In: *Hearing Research* 269.1-2, pp. 146–161.

Van den Honert, C. and Stypulkowski, P. H. (1987). "Single fiber mapping of spatial excitation patterns in the electrically stimulated auditory nerve". In: *Hearing Research* 29.2-3, pp. 195–206.

Van Wieringen, Astrid, Carlyon, Robert P., Laneau, Johan, and Wouters, Jan (Feb. 2005). "Effects of waveform shape on human sensitivity to electrical stimulation of the inner ear". In: *Hearing Research* 200.1-2, pp. 73–86.

Van Wieringen, Astrid, Carlyon, Robert P., Macherey, Olivier, and Wouters, Jan (Oct. 2006). "Effects of pulse rate on thresholds and loudness of biphasic and alternating monophasic pulse trains in electrical hearing". In: *Hearing Research* 220.1-2, pp. 49–60.

Van Wieringen, Astrid, Macherey, Olivier, Carlyon, Robert P., Deeks, John M., and Wouters, Jan (Aug. 2008). "Alternative pulse shapes in electrical hearing". In: *Hearing Research* 242.1-2, pp. 154–163.

Verveen, A A (1962). "Axon diameter and fluctuation in excitability". In: *Acta Morphologica Neerlando-Scandinavica* 5.1, pp. 79–85.

Verveen, A. A. and Derksen, H. E. (1965). "Fluctuations in membrane potential of axons and the problem of coding". In: *Kybernetik* 2.4, pp. 152–160.

Verveen, A. A. and Derksen, H. E. (1968). "Fluctuation Phenomena in Nerve Membrane". In: *Proceedings of the IEEE* 56.6, pp. 906–916.

Wikipedia contributors (2003). *Human ear anatomy with detailed diagram. Attributed to Iain. Released under the GNU Free Documentation License.* [Online; accessed 22-July-2004].

Wikipedia contributors (2005). *Illustration of cochlear implant from the National Institute on Deafness and Other Communication Disorders at the National Institutes of Health. Attributed to Maxim Razin. Released under the GNU Free Documentation License.* [Online; accessed 22-July-2004].

Wikipedia contributors (2007). *Illustration of a typical action potential. Attributed to Chris73. Released under the GNU Free Documentation License.* [Online; accessed 22-July-2004].

Wilson, Blake S., Finley, Charles C., Lawson, Dewey T., Wolford, Robert D., Eddington, Donald K., and Rabinowitz, William M. (July 1991). "Better speech recognition with cochlear implants". In: *Nature* 352.6332, pp. 236–238.

Yi, E., Roux, I., and Glowatzki, E. (2010). "Dendritic HCN Channels Shape Excitatory Postsynaptic Potentials at the Inner Hair Cell Afferent Synapse in the Mammalian Cochlea". In: *Journal of Neurophysiology* 103.5, pp. 2532–2543.

Ylikoski, J., Wersäll, J., and Björkroth, B. (Jan. 1974). "Degeneration of neural elements in the cochlea of the Guinea-pig after damage to the organ of corti by ototoxic antibiotics". In: *Acta Oto-Laryngologica* 78.S326, pp. 23–41.

Zeng, Fan Gang (Dec. 2002). "Temporal pitch in electric hearing". In: *Hearing Research* 174.1-2, pp. 101–106.

Zeng, Fan Gang and Shannon, Robert V. (July 1992). "Loudness balance between electric and acoustic stimulation". In: *Hearing Research* 60.2, pp. 231–235.

Zhang, Fawen, Miller, Charles A., Robinson, Barbara K., Abbas, Paul J., and Hu, Ning (2007). "Changes across time in spike rate and spike amplitude of auditory nerve fibers stimulated by electric pulse trains". In: *JARO - Journal of the Association for Research in Otolaryngology* 8.3, pp. 356–372.